University of Roma La Sapienza

DEPARTMENT OF MECHANICAL AND AEROSPACE ENGINEERING

Ph.D. degree in Theoretical and Applied Mechanics

Direct numerical simulation of internal compressible flows at high Reynolds number: numerical and physical insight

Candidate:
Davide Modesti

Thesis advisor:
Prof. Sergio Pirozzoli

Thesis submitted in 2016

Alla mia famiglia.

Acknowledgements

Firstly, I would like to express my sincere gratitude to my advisor Professor Sergio Pirozzoli, because he introduced me to the field of research and with his support and advice made this work possible. His everyday guidance during the last three years has been of immense value, and the daily discussions with him have always been a great source of inspiration. Secondly, I want to thank Prof. Matteo Bernardini, for his scientific, moral and financial support, and because he made me discover that typing with a mechanical keyboard may totally change your life. Besides, I am very thankful to Prof. Paolo Orlandi, for his advice and for the frequent and nice talks about turbulence. I further acknowledge that most of the results reported in this work have been achieved using the PRACE Research Infrastructure resource FERMI based at CINECA, Casalecchio di Reno, Italy.

Abstract

This work reports results of direct numerical simulations (DNS) of compressible internal flows. For this purpose three internal flow geometries of increasing complexity are considered, namely planar channel, pipe and rectangular duct flow. The work focuses on both numerical and physical issues related to wall-bounded turbulent flows. In the first part of the work some numerical issues concerning the solution of compressible wall-bounded flows, both in Cartesian and cylindrical coordinates, are addressed. Attention is focused on the acoustic time-step limitation which, in the case of wall-bounded flows, is restrictive across all Mach numbers. For this reason we develop a semi-implicit algorithm for time-accurate simulation of the compressible Navier-Stokes (N-S) equations. The method is based on linearization of the partial convective fluxes associated with acoustic waves, in such a way to suppress, or at least mitigate the acoustic time step restriction. Together with replacement of the total energy equation with the entropy transport equation, this approach avoids the inversion of block-banded matrices involved in classical methods [8], which is replaced by less demanding inversion of standard banded matrices [92]. This novel implementation, in which only Acoustic Terms are Implicit (ATI), is more efficient than previous approaches [8, 122], barely requiring the inversion of a banded scalar system in each coordinate direction. All available data support higher computational efficiency than existing methods, and saving of resources ranging from 85% under low-subsonic flow conditions, to about 50% in supersonic flow. Numerical issues arising from the use of cylindrical coordinates are also discussed. We show that N-S equations in cylindrical coordinates can be conveniently recast to guarantee discrete conservation of total kinetic energy [111]. The ATI approach is extended to the cylindrical case to deal with the severe time-step limitation in the azimuthal direction. In the second part of the work attention is focused on the effects of Mach and Reynolds number variation for the three flow geometries considered. DNS of planar channel, pipe and rectangular duct flow at bulk Mach number $M_b = 0.2, 1.5, 3$ and up to $Re_\tau \approx 1000$ are presented. A long-standing topic in compressible flows is the relevant Reynolds number for comparing flow cases across the Mach number range [28]. At this purpose, different compressibility transformations [142, 148] are compared to incompressible datasets at matching relevant Reynolds number [91]. All data show that the Trettel-Larsson transformation allows excellent collapse of the compressible statistics on the

incompressible ones, thus supporting the validity of semi-local scaling and Morkovin hypothesis. The size of the typical turbulent eddies is studied through spanwise spectral densities of the velocity field, which support validity of a scaling based on the local mean shear and the local friction velocity, with the main conclusion that the actual size of the eddies does not vary with the Mach number, at a fixed outer wall distance. Passive scalar transport is also studied across Mach and Reynolds number. Eventually, similarities and differences between compressible channel, pipe and rectangular duct flow are investigated.

Contents

List of Figures

List of Tables

Nomenclature

α	Passive scalar diffusivity
α_ℓ	Coefficient for the ℓ-th Runge-Kutta stage
$\mathcal{AR}$	Aspect ratio
β_ℓ	Coefficient for the ℓ-th Runge-Kutta stage
Δt	Time-step
Δx	Mesh spacing in x direction
Δy	Mesh spacing in y direction
Δz	Mesh spacing in z direction
δ_v	Viscous length scale
ℓ	Compressible scaling for the integral length scales
ℓ	Incompressible scaling for the integral length scales
η	Wall distance normalized with the channel half width
γ	Specific heat ratio
γ_ℓ	Coefficient for the ℓ-th Runge-Kutta stage
$\hat{E}_\varphi(k_z)$	One dimensional normalized spectrum of φ
$\hat{f}^i_{j+1/2}$	Numerical flux at the interface $j+1/2$ in the i-th direction
Λ^i_φ	Integral length scale of φ in the i-th direction
λ_z	Wavelength in the spanwise direction
$\mathbf{A}^a_i$	Acoustic Jacobian the i-th direction
$\mathbf{f}_i$	Vector of Eulerian fluxes in the i-th direction
$\mathbf{f}^a_i$	Acoustic part of the Eulerian flux in the i-th direction
$\mathbf{f}^c_i$	Convective part of the Eulerian flux in the i-th direction
$\mathbf{f}^v_i$	Vector of viscous fluxes in the i-th direction
$\mathbf{P}^a_i$	Jacobian primitive to conservative variable transformation
$\mathbf{S}$	Vector of viscous source terms in Cartesian coordinates
$\mathbf{S}_e$	Vector of Eulerian source terms in cylindrical coordinates
$\mathbf{S}_v$	Vector of viscous source terms in cylindrical coordinates
$\mathbf{v}$	Vector of primitive variables
$\mathbf{w}$	Vector of conservative variables

μ	Dynamic viscosity
μ_w	Dynamic viscosity at the wall
ν	Kinematic viscosity
ν_t	Eddy viscosity
ν_w	Kinematic viscosity at the wall
ω_i	Vorticity component
ω_i^*	Vorticity component in Huang scaling
$\overline{\phi}$	Generic mean quantity averaged according to Reynolds
Φ	Forcing term in the passive scalar equation
ϕ	Passive scalar
Π	Forcing term (pressure gradient) in the momentum equation
Re_λ	Reynolds number based on the Taylor microscale
Re_τ	Friction Reynolds number
Re_b	Bulk Reynolds number
Re_v	Vortex Reynolds number
$Re_{\tau B}$	Equivalent friction Reynolds number for Brun transformation
$Re_{\tau H}$	Equivalent friction Reynolds number for Huang transformation
$Re_{\tau I}$	Equivalent friction Reynolds number for generic transformation
$Re_{\tau T}$	Equivalent friction Reynolds number for Trettel transformation
ρ	Density
ρ_b	Bulk density
ρ_w	Density at the wall
Sc	Schmidt
σ_i	Viscous stress tensor
τ	Eddy turnover time
τ_w	Viscous stress at the wall
τ_{ij}	Reynolds stress tensor
Θ	Dilatation
θ	Azimuthal spatial coordinate
φ	Generic convected quantity
$\widetilde{\phi}$	Generic mean quantity averaged according to Favre
$\widetilde{u''v''}$	Reynolds stress component $tau_1 2$
A	Area of the duct section
B	Additive logarithmic constant in the law of the wall
B_q	Heat flux coefficient
c	Speed of sound
c_μ	Suitable constant to express the eddy viscosity in the outer wall layer region
C_f	Friction coefficient

c_p	Specific heat at constant pressure
c_v	Specific heat at constant volume
$C_{\varphi\varphi}$	Two point correlation function of φ
E	Total energy
$E(k)$	Three dimensional energy spectrum
$E_\varphi(k_z)$	One dimensional energy spectrum of φ
f_B	Brun's transforming function for wall distance
f_D	van Driest transforming function for wall distance
f_I	Generic transforming function for wall distance
f_T	Trettel-Larsson transforming function for wall distance
g_B	Brun's transforming function for velocity
g_D	van Driest transforming function for velocity
g_I	Generic transforming function for velocity
g_T	Trettel-Larsson transforming function for velocity
H	Hydraulic diameter
H	Total enthalpy
h	Channel/duct half height
j	Generic mesh node
J_i	Scalar diffusion flux vector
k	Thermal conductivity
k	von Karman constant
k_z	Fourier wavenumber in the spanwise direction
L_x	Length of computational domain in x direction
L_y	Length of computational domain in y direction
L_z	Length of computational domain in z direction
M	Size of the block in block-banded matrices
M_τ	Friction Mach number
M_b	Bulk Mach number
M_e	Mach number at the channel centerline
M_t	Turbulent Mach number
M_v	Vortex Mach number
N	Number of grid points in a given coordinate direction
N_θ	Number of grid points in θ direction
N_x	Number of grid points in x direction

N_y	Number of grid points in y direction
N_z	Number of grid points in z direction
ng	Number of ghost nodes
P	Perimeter of the duct section
p	Pressure
q_i	Heat flux vector
q_w	Wall heat flux
R	Gas constant
R	Pipe radius
r	Radial spatial coordinate
r	recovery factor
r_v	Vortex radius
s	Entropy
T	Temperature
T_τ	Friction temperature
T_e	Temperature at the channel centerline
T_r	Recovery temperature
T_w	Temperature at the wall
u	Velocity component in the streamwise direction
u^+	Mean velocity in wall units
u_τ	Friction velocity
u_τ^*	Local friction velocity
u_θ	Velocity component in the azimuthal direction
u_B	Mean velocity transformed with Brun transformation
u_b	Bulk velocity
u_D	Mean velocity transformed with the van Driest transformation
u_e	Streamwise velocity at the channel centerline
u_I	Mean velocity transformed with a generic transformation
u_i	Velocity vector
u_r	Velocity component in the radial direction
u_T	Mean velocity transformed with Trettel-Larsson transformation
u_V	Velocity transformed according to the viscous sublayer transformation
u_v	Maximum tangential velocity of a vortex
u_x	Velocity component in the streamwise direction
v	Velocity component in the wall-normal direction
w	Velocity component in the spanwise direction
x	Streamwise spatial coordinate

y	Wall-normal spatial coordinate
y^+	Wall distance in wall units
y_B	Wall distance transformed with Brun transformation
y_D	Wall distance transformed with the van Driest transformation
y_I	Wall distance transformed with a generic transformation
y_T	Wall distance transformed with Trettel-Larsson transformation
z	Spanwise spatial coordinate
Δt_I^+	Incompressible time-step in wall units
Δt_x^+	Compressible time-step in wall units in x direction
Δt_y^+	Compressible time-step in wall units in y direction
Δt_z^+	Compressible time-step in wall units in z direction
Δt_{av}	Averaging time interval
Δt_{yv}^+	Viscous time-step in wall units in y direction
Δy_w	Mesh spacing at the wall in y direction
τ_{Bij}	Reynolds stress component transformed according to Brun
τ_{Dij}	Reynolds stress component transformed according to van Driest
τ_{Iij}	Generic incompressible Reynolds stress component
τ_{Tij}	Reynolds stress component transformed according to Trettel-Larsson

Chapter 1

Introduction

Compressible wall-bounded turbulent flows are of obvious importance in mechanical and aerospace engineering and have been extensively studied in the past [18]. Many reviews on the compressibility effects on turbulence are present in literature [18, 39, 81, 97, 134], although some basic issues as Mach and Reynolds number effects on the mean velocity profile and on the Reynolds stresses distribution are not fully settled yet. Most early studies were based on experimental approaches, as thoroughly reviewed by Bradshaw [18], Gatski and Bonnet [48], Sandborn [126], Smits and Dussauge [129]. However, growth of available computational power has recently made the numerical solution of the full compressible Navier-Stokes equation feasible, and direct numerical simulation (DNS) has become an important tool in turbulence research. The effects of finite flow compressibility on turbulence have been traditionally divided into indirect effects due to mean density and temperature variations, and genuine effects caused by dilatational velocity fluctuations and thermodynamic fluctuations. Morkovin [97] postulated that for non-hypersonic boundary layers (say, $M < 5$), genuine effects of compressibility are negligible, hence the mean flow profiles are expected to collapse to the corresponding incompressible distributions, provided mean density and viscosity variations are suitably taken into account. Morkovin's hypothesis also subtends earlier theoretical findings, as the celebrated van Driest transformation for the mean velocity profile [146], and led to relations between temperature and velocity fluctuations for adiabatic boundary layers, collectively known as strong Reynolds analogies (SRA) [49, 62, 97]. Many studies of compressible boundary layers support the validity of Morkovin's hypothesis, at least for adiabatic walls, whereas the original SRA relationships turned out not to be very robust [55, 116, 165].

Morkovin's hypothesis, has been validated for adiabatic boundary layers up to $M_\infty \approx 5$ both in experiments [126, 131] and numerical simulations [36, 55, 117]. On the other hand it has been shown [28, 35] that in the case of cold walls van Driest transformation fails at much lower Mach number ($M_b = 1.5$ in Coleman et al. [28]), so that Morkovin's hypothesis does not seem to apply to cold walls. One of the aims of this work is to investigate the validity of Morkovin's hypothesis in the presence of wall heat flux. For this purpose direct numerical simulations (DNS) of internal flows are performed, where the wall is necessarily cooler than the bulk. The internal flow configuration is preferred with respect to the boundary layer (BL), since the generation of inflow boundary condition in the case of isothermal BL is not trivial. Three different flow geometries of increasing complexity are taken into account in this work, namely planar channel, circular pipe and rectangular duct. This work addresses both numerical and physical aspects that arise from the solution of wall-bounded compressible flows. An extensive literature review of the physical and numerical aspects in compressible wall-bounded flows is presented in this chapter. As discussed in Section 1.4 DNS of wall-bounded compressible flows is more expensive than the incompressible case, mostly due to the acoustic time step limitation. This led us to develop a novel semi-implicit algorithm for the treatment of acoustic waves, which allow to mitigate this restriction across all Mach numbers. The main advantage of the method, described in Section 2.1.2, is the trifling number of floating point operations required by it. Moreover a simple wall treatment that allows to double the time step restriction in the case of co-located flow solvers is also described in Section 2.1.3. Numerical issues that emerge from discretization of Navier-Stokes (N-S) equations in cylindrical coordinates are also described specifically in Section 2.2. The novel time-stepping algorithm is validated in Section 2.3 using homogeneous isotropic turbulence, planar channel and square duct as test cases. In the second part of this work the results of DNS of planar channel, circular pipe and rectangular duct are analyzed, Sections 3.1-3.2-3.3. The simulations here presented involve bulk Mach numbers $M_b = 0.1, 0.2, 1.5, 3$ spanning a friction Reynolds number in the range $Re_\tau = 180 - 1000$. Attention is focused on the effects of Mach and Reynolds number as well as the flow geometry.

1.1 Compressible channel flow

Planar channel is the simplest prototype of wall-bounded internal flows. Since the pioneering work of Kim et al. [71], many DNS studies of incompressible channel

flows have appeared, and Reynolds numbers have been reached at which a sizeable layer with near-logarithmic variation of the mean velocity emerges [11, 60, 79]. Pioneering studies of turbulent channel flow at supersonic conditions ($M_b = 1.5$, $Re_b = 3000$ being the bulk Mach ad Reynolds number, respectively) were carried out by Coleman et al. [28], Huang et al. [62]. Those authors studied compressible channel flows between isothermal walls, in which the wall is necessarily cooler than the bulk fluid, and found that the van Driest-transformed velocity follows only approximately the incompressible law-of-the-wall, with differences attributed to low-Reynolds-number effects. Those authors also showed that density and temperature fluctuations are indeed small as compared to their mean values, thus substantiating Morkovin's hypothesis. The turbulent stresses were found to collapse fairly well on incompressible data when scaled with the mean density ratio, but better agreement was observed when 'semi-local' units are used, based on a local friction velocity and viscous length scale. Lechner et al. [77] reproduced the flow case considered by Coleman et al. [28] using a pressure-velocity-entropy formulation with governing equations cast in characteristic form, and discretized with fifth-order compact upwind formulas. Good agreement was observed with the results of Coleman et al. [28], and higher values of the density-scaled normal Reynolds stresses were observed as compared to the incompressible case, whereas the transformed turbulent shear stress was found to be lower. Morinishi et al. [95], Tamano and Morinishi [138] carried out DNS of compressible channel flow between both isothermal and adiabatic walls using a Fourier/Galerkin B-spline discretization [94], confirming the validity of Huang's semi-local scaling for the turbulent stresses. Foysi et al. [42] performed DNS spanning bulk Mach numbers in the range between 0.3 and 3.5. Consistent with previous works, they found that the density-scaled turbulent stresses collapse on the incompressible distributions sufficiently far from the wall when reported in outer scaling, whereas Huang's semi-local scaling yields better accuracy than van Driest in inner scaling. Brun et al. [21] developed an extensive large-eddy simulation database of compressible channel flows, and noticed that as the Mach number is increased for given bulk Reynolds number the flow tends to relaminarize, although the friction Reynolds number increases, thus raising the important question of which is the relevant Reynolds number for comparing flow cases across the Mach number range. Brun et al. [21] also proposed a modified form of mean velocity scaling which explicitly takes into account mean viscosity variations, and which was found to yield better collapse on incompressible data than semi-local scaling. Wei and Pollard [157, 158] used a discontinuous Galerkin

solver to develop a DNS dataset of compressible channel flows spanning the bulk Mach number range between 0.2-1.5. As in previous studies, they found that as the bulk Mach number increases the transformed turbulent stresses do not follow the incompressible profiles when reported in wall units. In a recent work, Trettel and Larsson [141, 142] further investigated failure of the van Driest transformation in the case of cold walls. They showed that the semi-local scaling of Huang et al. [62] is actually rooted in arguments of mean momentum balance, and they derived a novel velocity transformation which by construction satisfies universality of the turbulent stresses. The novel transformation was shown to yield satisfactory agreement of the mean velocity profiles with incompressible distributions in a reasonably wide range of Reynolds and Mach numbers. Recently Patel et al. [106, 107] derived Trettel-Larsson (TL) transformation from arguments similar to the ones by Trettel and Larsson [142], and tested it in the low Mach number case finding good agreement with incompressible data. One of the uses of 'compressibility transformations' consists in the derivation of predictive relations for the friction coefficient, such as the popular van Driest II transformation [148]. In order to derive such friction relations a temperature-velocity relation is also needed. For that purpose, a typical choice is Walz relation [156], which has been found to work well for adiabatic boundary layers [35, 36]. An empirical correction to Walz formula was proposed by Duan and Martin [34], and generalized by Zhang et al. [165], to explicitly account for finite wall heat flux. A frequently debated issue in the compressible flow community is the effect of flow compressibility on the typical length scales in wall turbulence [129, 134]. Although there is a general consensus that the integral scales of fluid motion sufficiently away from the wall do not vary substantially with the Reynolds number, the dependence on the Mach number is still largely unclear. Furthermore, most available experimental data only refer to the streamwise length scales, which can be easily estimated from one-point measurements, upon use of Taylor's hypothesis. In this respect, Demetriades and Martindale [31] found that the streamwise integral length scales in a Mach 3 boundary layer are about half as in incompressible boundary layers. Smits et al. [130] also observed that the streamwise length scales sensibly decrease with the Mach number, whereas the spanwise length scales are almost unchanged. On the other hand, Spina et al. [134] claimed that the integral length scales increase with the Mach number both in inner and outer units, being weakly affected by the Reynolds number. Recent measurements by Ganapathisubramani et al. [47] at M = 2 seem to suggest substantial increase of the eddy size in both the streamwise and in the spanwise direction with the Mach

number, whereas recent DNS [116] at M = 2 support insensitivity on the Mach number, at least for adiabatic boundary layers. To shed more light on the open issues outlined above, we have developed a novel database of compressible channel flow in the range of bulk Mach numbers from $M_b = 1.5$ to 3, and bulk Reynolds numbers up to $Re_b \approx 34000$, which significantly extends the range of previous DNS. In order to precisely gauge the importance of compressibility effects and directly assess the validity of the compressibility transformations, a series of companion incompressible DNS have been performed so as to exactly match the relevant Reynolds number (see the later discussion), thus avoiding ambiguities and uncertainties of previous studies. Results of DNS of compressible channel flow are reported in Section 3.1.

1.2 Compressible pipe flow

The study of compressible fully developed pipe flow is particularly important since it represents the first prototype of air intake and nozzle/diffuser used in the aeronautical industry. Despite the fact that usually the flow in air intakes and nozzles is far from being fully developed, the pipe flow is a simple model to understand the effect of cylindrical geometries on compressible turbulence. Many DNS of incompressible pipe flow appeared in literature, ranging from low [37, 154] to moderately high Reynolds number [2, 26]. The first DNS of incompressible pipe flow was performed by Eggels et al. [37] who successfully compared their data with the experimental ones. Orlandi and Fatica [103] and Fukagata and Kasagi [45] repeated Eggels simulations finding good agreement with their data. Higher Reynolds number simulations in longer domains have also been accomplished [1, 2, 26, 27, 38, 78, 160, 161], up to $Re_\tau \approx 3000$ and $L_x = 30R$. Experiments are typically carried out in a higher range of Reynolds number, $Re_\tau \sim 10^3 - 10^5$. [46, 86, 162, 163]. Wu et al. [161] performed DNS of incompressible pipe flow with streamwise length $L_x = 30R$. Their data show evidence of a minor peak in the streamwise energy spectra at small-wavenumbers, which is interpreted as an evidence of very-large-scale motions (VLSM). Nevertheless comparison with experiments at matching Reynolds number confirms the findings by Alamo and Jiménez [3], that the small-wavenumbers peak is overestimated by the use of Taylor's hypothesis. Ahn et al. [1] performed DNS of incompressible pipe flow spanning a friction Reynolds number $Re_\tau \approx 180 - 1000$. They use over-resolved discretization at the lowest Reynolds number and find differences with previous results, thus highlighting higher sensibility of the flow statistics to the mesh resolution, with

respect to channel flow. Those authors also focused attention on the increase of the streamwise velocity variance peak with Reynolds number. Many studies observed the increase of the streamwise velocity fluctuations peak with Reynolds number both for boundary layer and channel flow [11, 84, 127]. On the other hand Princeton Superpipe experiments reported insensitivity of the peak with Reynolds number, which highlights differences in the interaction of the outer and near wall region in pipe with respect to channel. On the contrary Ahn et al. [1] dataset clearly shows a dependence of the streamwise velocity fluctuations peak with Reynolds number hence supporting the thesis that the interaction between outer and inner wall layer is similar in pipe, channel and boundary layer. A longstanding topic regarding the pipe flow is whether the log law applies or not. Mckeon et al. [86] observed both power law and log law at $Re_\tau > 5000$, depending on y^+. Wu et al. [161] observed power law at $Re_\tau \approx 1100$ and Chin et al. [26] did not inspect log low at $Re_\tau \approx 2000$. Recent DNS of channel flow up to $Re_\tau = 4000$ [11] support the hypothesis of a linear variation of the log law indicator, whereas plateau indicating the von Karman constant can only be reached in the limit of infinite Reynolds number [67]. Ahn et al. [2], Lee et al. [78] showed that large scale motions (LSMs), which are responsible for the overlap region survive for shorter time in pipe than in channel, due to the wall confinement thus leading to different universal laws in the overlap region. It seems that even if many experimental and numerical studies appeared concerning incompressible pipe flow, some basic issues are not fully settled. Despite the relevant role that compressible pipe flow may play in the understanding of wall turbulence, few numerical studies appeared in literature which involve fully developed flows in cylindrical geometries [51, 52, 53, 125]. Experiments of compressible internal flows are difficult to perform, and only an experimental study of compressible pipe $M_b = 0.1 - 0.3$ appears in literature [72]. To our knowledge the only DNS of compressible pipe flow was carried out by Ghosh et al. [52], using a fifth order upwind scheme. Their study is limited to a single Mach number $M_b = 1.3$ and relatively low Reynolds number, $Re_\tau \sim 240$, focusing on differences with channel flow. One of their main findings is that the transverse curvature of the pipe affect mean flow statistics, but its role is expected to decrease with increasing Reynolds number. Those authors also extended their study to fully developed nozzles and diffusers using DNS and LES [51, 53]. As in the case of channel flow Ghosh et al. [52] observed inaccuracy of the van Driest transformation, whereas the semi-local scaling yield better collapse of the Reynolds stresses. As in the case of channel flow we focus our attention on the accuracy of the compressibility transformations for velocity and Reynolds

stresses. The effect of Mach and Reynolds number on the turbulent scales is studied using spanwise spectra as for the channel flow. In the case of pipe flow we also put under scrutiny passive scalar transport, which has been widely study in the case of homogeneous and free shear turbulence [12, 44], while fewer examples can be found in compressible wall-bounded flows [41]. Comparison with incompressible statistics is performed using incompressible data available in literature at approximately matching Reynolds number. We show that compressibility transformations which hold for velocity (e.g. van Driest), also work out for the passive scalar fields, by comparison with incompressible channel flow data [118] and with experimental fittings Kader [68]. Results of DNS of compressible pipe flows are presented in Section 3.2.

1.3 Compressible duct flow

Internal flows with rectangular section are common in many engineering applications, such as water draining or ventilation systems. Moreover it represents the simplest prototype of internal flow for which 3D effects appear in the mean flow. Secondary flows which appear in non-circular ducts can be classified into two kinds, depending on the generation mechanism. Variations to the mean streamwise vorticity are due to skew-induced contributionand stress-induced contribution [19]. The skew-induced contribution is responsible for Prandtl's secondary motions of first kind, while the stress-induced contribution is responsible for secondary motions of second kind [19]. In straight ducts only secondary motions of second kind are present, that is the mean streamwise vorticity can only be generated gradients of Reynolds stresses. Moreover, while secondary motions of first kind may occur both in laminar and turbulent flows, motions of second kind only characterize turbulent flows. Rectangular duct flow is therefore particularly interesting due to the occurrence of Prandtl's second motions of second kind. A first DNS of incompressible duct flow has been performed by Gavrilakis [50] who simulated the flow in a square duct at $Re_b = 2hu_b/\nu = 4410$ (where h is the duct half side), corresponding to a friction Reynolds number of $Re_\tau = hu_\tau/\nu = 150$. Gavrilakis used a second-order staggered finite differences solver, in which Poisson equation for pressure was solved using cyclic reduction algorithm. Secondary motions were observed in the cross-stream plane, formed by four pairs of statistically stationary counter rotating vortices directed to the duct corners. Despite the secondary motions, the mean flow at the bisectors was found to be similar as in a planar

channel. Gavrilakis [50] reported an averaging interval of five turn over times, but realized that statistics were not fully converged, thus quadrant averages were used to increase statistical convergence. Huser and Biringen [63] performed DNS with a spectral solver increasing the Reynolds number up to $Re_\tau = 300$. They collected statistics for a time interval $\Delta t_{av} u_e/(2h) = 330$ and averaged over the eight triangles. Pinelli et al. [110], Uhlmann et al. [145] used a spectral solver to study transition in duct flow, spanning friction Reynolds number from laminar to $Re_\tau = 150$. They found differences between their data and the ones by Gavrilakis [50]. They observed that a very long averaging time is necessary to collect reliable mean flow statistics, reporting $\Delta t_{av} u_b/h = 8000$. Zhang et al. [164] performed DNS of square duct up to $Re_\tau = 600$, which is the highest friction Reynolds number reached up to now in DNS. They repeated the simulation performed by Huser and Biringen [63] and found differences with their results, which they attributed to the low mesh resolution used by those authors. More recent studies [137, 153] focused on the effect of the aspect ratios and differences with planar channel flow both in the transitional and fully turbulent regime. Vinuesa et al. [153] performed DNS of duct flow with aspect ration $Æ = 1-7$ at $Re_\tau = 180$ using the spectral element solver Nek5000. They also reported long averaging time $\Delta t_{av} u_b/h = 400 - 7000$ depending on the case. They found differences with the planar channel, persisting up to $Æ = 7$. Duct flow is also interesting for turbulence modeling. Secondary motions in fact cannot be predicted by any turbulence models based on Boussinesq hypothesis which rely on isotropy of turbulent stresses. LES of turbulent duct flow were performed by Breuer and Rodi [20], Madabhushi and Vanka [82] at $Re_\tau = 150$ and $Re_\tau = 180$ respectively. From previous studies clear difficulties in the simulation of duct flow emerge. The inhomogeneity in the spanwise direction does not allow to use direct methods for the solution of Poisson equation for pressure, thus increasing the computational cost. Besides, ensemble averages can only be collected in the streamwise direction and in time, thus very long time averaging intervals are required to collect meaningful statistics. These two issues seem to have limited the maximum achievable Reynolds number in duct flow with respect to channel and pipe. To date,the only study of compressible duct flow was carried out by Vázquez and Métais [149], who performed LES of an isothermal square duct at $M_b = 0.5$, also changing the wall temperature on one side of the duct. They achieved good agreement with previous DNS data for the uniformly cooled case, while no compressibility effect was reported, due to the relatively low Mach number. It turns out that Mach number effects has never been investigated in literature and Reynolds number dependence studies are also

limited. For this purpose we performed DNS of rectangular duct flow at different Mach and Reynolds number. DNS of square duct flow in the incompressible regime, at $M_b = 0.2$ $Re_\tau = 1000$ is performed and compared to previous data at lower Reynolds number. Supersonic duct flow at $M_b = 1.5$, $Re_\tau = 220$ and $\mathcal{AR} = 1 - 4$ is presented to study the effect of side walls and differences with the planar channel case. As for channel and pipe flow a single DNS at $M_b = 3$ is also carried out.

1.4 Numerical issues in compressible flows

In this Section some of the main difficulties which arise in the solution of compressible flows are addressed. Since we consider both flows in Cartesian geometries (planar channel and duct) and in cylindrical coordinates (pipe), this Section is divided into two parts to separately introduce numerical issues and techniques for Cartesian and polar coordinates. As we will show, compressible flows in cylindrical coordinates share intrinsic difficulties with the Cartesian ones, namely the acoustic time step limitation, but they also poses challenges associated with the pole singularity.

1.4.1 Cartesian coordinates

It is known that the numerical solution of the compressible Navier-Stokes equations is significantly more time consuming than their incompressible counterpart, partly owing to the inherently higher number of floating point operations (flops) per grid point, but mainly because of the much smaller time step imposed by the acoustic stability restriction. In free-shear flows, conventional explicit algorithms can still be used efficiently as long as the typical Mach number is of the order of unity. However, wall-bounded flows inevitably include regions with near stagnant flow and tiny grid spacing adjacent to solid surfaces, which makes the acoustic time step limitation in the wall-normal direction dominant, even at high bulk Mach numbers. Besides being dictated by stability considerations, time step limitations in turbulent flows also have a physical interpretation, as in order to capture the relevant physics of transport phenomena with given speed (say U) on a mesh with given size (say Δ), time steps no larger than Δ/U should be used. Hence, CFL numbers (defined as the ratio of the time advancement step to the maximum allowed time step for explicit time integration) should always be of the order of unity for genuine DNS. In compressible flows, information simultaneously propagate at the hydrodynamic and at the acoustic speed. However, acoustic waves typically make

a negligible contribution to the overall energetics of turbulent flows [81]. Hence, with the obvious exception of cases where acoustic instabilities play an important role, such as in certain combustion applications [120] or in direct simulation of aerodynamic noise [29], using a time step which allows to resolve the hydrodynamic (vortical) mode while giving up accurate representation of acoustic phenomena may be a legitimate choice, which actually subtends much of the research carried out for low-speed solvers. It is the goal of this work to develop a numerical algorithm for direct numerical simulation of compressible flow which is capable of seamless efficient operation throughout the Mach number range, down to nearly incompressible conditions. The algorithm is at the same time meant to remove or at least alleviate the acoustic time step limitation in the presence of solid boundaries. To gain a clearer perception for the problem, we refer to a canonical compressible boundary layer flow over a flat surface, or flow in a planar channel. Let Δx, Δz be the mesh spacings in the streamwise and spanwise directions, respectively, and let Δy be the minimum mesh spacing in the wall-normal direction, assuming unit CFL number, the time step limitations associated with the discretization of the convective terms in the coordinate directions are

$$\begin{aligned} \Delta t_x^+ &= \frac{\Delta x^+}{\max(u_0^+ + c_0^+, c_w^+)} = \Delta x^+ M_0 \sqrt{C_f/2} \min\left(1, \frac{1}{1+M_0}\sqrt{T_w/T_0}\right), \\ \Delta t_y^+ &= \frac{\Delta y^+}{c_w^+} = \Delta y^+ M_0 \sqrt{C_f/2} \\ \Delta t_z^+ &= \frac{\Delta z^+}{\max(c_0^+, c_w^+)} = \Delta z^+ M_0 \sqrt{C_f/2} \min\left(1, \sqrt{T_w/T_0}\right), \end{aligned} \tag{1.1}$$

where the '+' superscript is used to denote quantities made nondimensional with respect to local wall units, namely the friction velocity $u_\tau = (\tau_w/\rho_w)^{1/2}$, and the viscous length scale $\delta_v = \nu_w/u_\tau$, the subscript 0 is used to denote flow properties at the centerline (for channels) and at the free-stream (for boundary layers), and w to denote wall properties, with $C_f = 2\tau_w/(\rho_0 u_0^2)$. It should be noted that if acoustic waves are suppressed, as is the case of strictly incompressible flow, the time step is controlled by the streamwise direction, and

$$\Delta t_I^+ = \Delta x^+ \sqrt{C_f/2}. \tag{1.2}$$

The viscous time step limitation is mainly effective in the wall-normal direction, and in wall units one has

$$\Delta t_{yv}^+ = \Delta {y^+}^2. \tag{1.3}$$

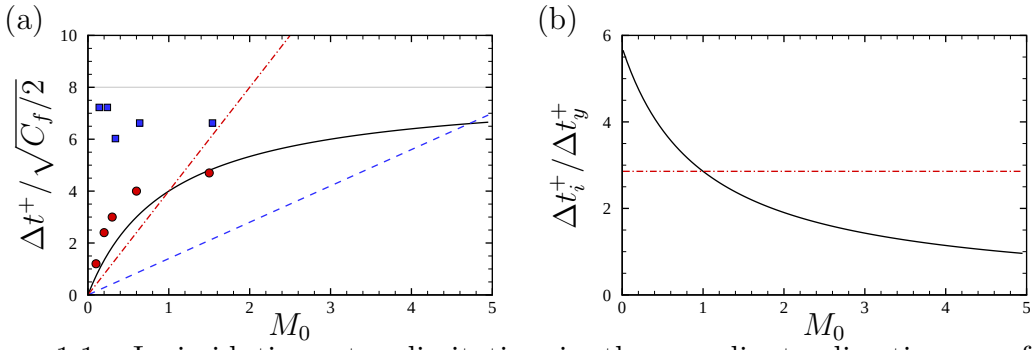

Figure 1.1: Inviscid time step limitation in the coordinate directions as from Eqn. (1.1) as a function of the reference Mach number M_0. In panel (a) we show Δt_x (solid), Δt_y (dashed), Δt_z (dot-dashed). In panel (b) we show the ratios $\Delta t_x/\Delta t_y$ (solid), $\Delta t_z/\Delta t_y$ (dot-dashed). For reference, in panel (a) we report with a grey line the 'incompressible' time limitation given in Eqn. (1.2). The symbols denote the time step limits for the ATI algorithm as dictated by accuracy (circles) and stability (squares), as discussed in Section 2.3.2.

For the sake of graphical representation of the above formulas, we assume: i) the distance of the first point from the wall is $\Delta y_w^+ \approx 0.7$, which is the maximum value for which accurate turbulence statistics are obtained [91]; ii) the minimum mesh spacing in the wall-normal direction is $\Delta y = 2\Delta y_w$, which can be achieved by staggering the mesh in the vertical direction, thus alleviating the stability restrictions [91]; iii) the wall-parallel mesh spacings are $\Delta x^+ = 8$, $\Delta z^+ = 4$, which is typical for DNS; iv) the wall is isothermal, with $T_w = T_0$. Figure 1.1 shows the inviscid time step restrictions according to Eqn. (1.1) as a function of the reference Mach number M_0, scaled by $\sqrt{C_f/2}$ (panel a), and as a fraction of the wall-normal allowed time step (panel b). Inefficiency of explicit compressible solvers is apparent in the low-Mach-number regime, where vanishingly small time steps are required. Time steps comparable to those achievable in incompressible flow are only possible starting at $M_0 \approx 3$. With the exception of hypersonic flow, the most restrictive time limitation is that associated with the vertical direction, and an increase by at least a factor of two can be gained by removing it (see panel b). It is also interesting to note that the acoustic time limitation in the spanwise size is more restrictive than the streamwise limitation up to $M_0 \approx 1$, whereas at supersonic Mach numbers the convective limitation in x is controlling. Removing the wall-normal acoustic time limitation in supersonic flow is sufficient to achieve a similar time step as in incompressible flow, whereas in subsonic flow it is also necessary to remove the acoustic time restriction in the wall-parallel directions. We further note that the normalized viscous time limitation $\Delta t_{yv}^+/\sqrt{C_f/2}$, with Δt_{yv}^+ given in Eqn. (1.3) is always much weaker than

the convective ones, provided $\Delta y^+ \sim 1$, and considering that the range of friction coefficients typically accessed by DNS is $2 \times 10^{-3} \leq C_f \leq 6 \times 10^{-3}$. While the above estimates are reported for typical DNS mesh spacings, the case of wall-resolved RANS, LES and DES is even more severe, as the aspect ratio of near-wall cells is substantially higher, hence making suppression of the wall-normal time step restriction mandatory for any practical calculation. All the above-mentioned difficulties are well know to the CFD community, and a variety of techniques have been developed to cope with the numerical stiffness of the compressible Navier-Stokes equations. The chief choice in this respect has traditionally been the use of (semi-)implicit time integration schemes. A landmark contribution in this sense was given by Beam and Warming [8, 9], who proposed a time-implicit algorithm for the solution of the Navier-Stokes equations in conservative form based on linearization of the convective and viscous flux vectors, coupled with approximate factorization [33] to handle multiple space dimensions. However, the method is computationally expensive as it requires the inversion of 5×5 block-banded systems of equations, which is more expensive than, e.g. standard banded systems. In this respect we note that, whereas the classical Thomas algorithm for tridiagonal matrices requires a number of floating point operations (flops) of $O(6N)$ (where N is the number of grid points in a given coordinate direction), its block-tridiagonal version requires $O(3N(M^3 + M^2))$ flops, where M ($= 5$ in the Beam-Warming algorithm) is the size of each block [66]. The computational cost is about twice as much in the case of periodic boundary conditions [7]. Pulliam and Chaussee [122] developed a variant of the Beam-Warming algorithm which involves the inversion of standard tridiagonal systems rather than block matrices, with large saving of computer time, but with loss of accuracy and stability in the case of unsteady simulations [57]. Algorithms of the Beam-Warming family are at the heart of highly successful aerospace CFD software [24, 121]. Algorithms which avoid inversion of banded systems of equations have also been designed [83], which may be useful for efficient parallel implementation. However, those algorithms require point-wise iterative procedures whereby the right-hand-side of the equations must be evaluated several times per time step, with unclear outcome in terms of overall efficiency. Alternative approaches to circumvent the stiffness of compressible Navier-Stokes equations rely on the use of pre-conditioning techniques, based on the attempt to change the eigenvalues of the system of equations in order to remove the large disparity of wave speeds. This is accomplished by pre-multiplying the time derivatives by a matrix that slows the speed of the acoustic waves down toward the fluid speed [143, 144].

Preconditioning is the choice of election for steady-state application, however its extension to unsteady flow problem is not straightforward, requiring the use of dual time stepping techniques, namely inner iterations in terms of a pseudo-time [104, 105, 150]. However, the number of iterations per physical time step can be very large, with subsequent loss of computational efficiency. Specialized algorithms for the Navier-Stokes equations have been also developed for the low-Mach number regime, which allow to account for temperature-dependent density variations, as is typically the case in combustion. All these variable-density algorithms are based on the idea the only the terms which bring an acoustic contribution should be advanced implicitly in time, in such a way that the acoustic time limitation is removed. Numerical schemes of this kind were pioneered by Casulli and Greenspan [25], who proposed to treat implicitly only the pressure term in the momentum equation and the dilatation term in the internal energy equation, which results in having to solve an elliptic equation for pressure, with large incurred overhead. Pierce [109], Wall et al. [155] extended the classical pressure-correction method [70] to variable-density flows by solving a Helmholtz equation for the pressure correction, and the use of sub-iterations. LES results were carried out in which a time step forty times larger than the explicit case was achieved, with modest computational cost overhead. Moureau et al. [98] developed an implicit scheme for the removal of the acoustic limitation which also relies on the solution of a Helmholtz equation, however without reverting to sub-iterations, with an overhead CPU time of about 25% with respect to standard incompressible solvers. Hence it appears that, in one way or another, algorithms tailored for the near-incompressible regime involve either iterative procedures and/or the inversion of elliptic systems of equations. The latter can only be carried out efficiently in the case that periodic directions are present, which allows for the use of direct solvers [133]. In this work we develop a novel semi-implicit algorithm for the compressible Navier-Stokes equations based on a modification of the basic Beam-Warming linearization, thus avoiding any iterative procedure. The algorithm is presented in Section 2.1.2, which also includes a discussion of the treatment of viscous terms, accurate time integration, and extension to multiple space dimensions. Numerical examples are given in Section 2.3, which include DNS of turbulent flows from the low subsonic to the supersonic regime.

1.4.2 Cylindrical coordinates

In recent years much effort has been dedicated to the development of numerical schemes for the convective terms in the Navier-Stokes(N-S) equations that discretely preserve the kinetic energy in the inviscid incompressible limit [13, 69, 99, 111, 112, 136]. The discrete conservation of the kinetic energy allows numerical stability without the use of upwinding, artificial dissipation or filtering which are common practices in the compressible flow community. Despite the attention devoted to the topic, most compressible energy-consistent solvers are limited to Cartesian coordinates. Notoriously jet and pipe flows are naturally studied in cylindrical coordinates, and in fact many studies have appeared concerning the discrete conservation of the kinetic energy in cylindrical coordinates [32, 45, 96, 101, 102, 103, 151], but they are all limited to the incompressible and variable density case. On the other hand, all compressible studies involving cylindrical geometries deal with non-linear instabilities using upwinding of filtering [15, 17, 22, 23, 52, 88, 125], which tend to dump turbulent fluctuations. Hence, energy-preserving schemes are advisable for turbulent flow simulations, especially for direct and Large Eddy Simulations (LES). The numerical solution of the Navier-Stokes equations in cylindrical coordinates poses some intrinsic difficulties with respect to Cartesian coordinates. One complication is the inherent singularity of cylindrical coordinate systems, which is numerically treated using different approaches [30, 43, 93, 96, 124, 139, 151]. In the case of staggered meshes the singularity can be elegantly avoided rewriting the equations in terms of $q_x = u$, $q_r = rv$ $q_\theta = w$ so that q_r, the only quantity evaluated at the axis, is identically zero [151]. Another approach, also used in compressible flows, consists in solving the Cartesian equations at the axis [43], thus getting rid of the singularity. Constantinescu and Lele [30] obtained an exact equation for the axis, which can be used both for co-located and staggered meshes, which can be generalized singularities arising in spherical and elliptical coordinates. Despite the solid foundation of the method, its implementation is not straightforward, and the simpler approach of Mohseni and Colonius [93], who simply stager the first point off the axis $\Delta r/2$, is frequently preferred [15]. A further difficulty comes from the time step restriction. The inviscid time step limitations in the streamwise, wall-normal and azimuthal direction can in fact be cast as in Eqn. (1.1), with the only difference that $\Delta z_c^+ = \Delta r_0^+ \Delta\theta = \Delta r_0^+ 2\pi/N_z$ is the mesh spacing at the axis in the azimuthal direction. Repeating the analysis performed for channel flow in Section 1.4.1, and assuming standard mesh spacing used in DNS of wall bounded

flows, namely $\Delta x^+ = 8$, $\Delta y^+ = 2\Delta y_w^+ = 1.4$, $\Delta r_0^+ = 4$ and $N_z = 1280$ one obtains the time step limitation as a function of the bulk Mach number.

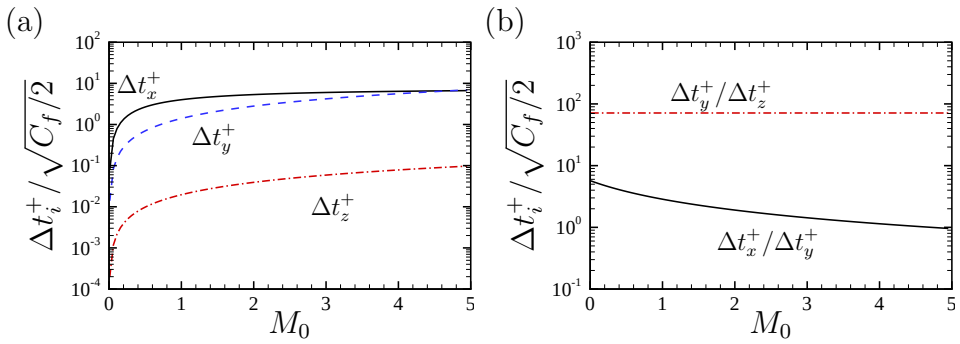

Figure 1.2: Time step limitation as a function of the bulk Mach number M_0 in cylindrical coordinates as in Eqn. (1.1). Panel (a) shows time step limitation in wall-normal (black solid), azimuthal (red dashed) and streamwise (green dash-dotted). Panel (b) shows $\Delta t_y^+/\Delta t_z^+$ (dot-dashed) and $\Delta t_x^+/\Delta t_y^+$ (solid).

It is easy to understand from Fig. 1.2 that for azimuthal spacing of practical interest the time step limitation in θ direction is the most restrictive across all Mach numbers. Although the azimuthal mesh spacing considered is moderately fine it is immediate to realize that the ratio $\Delta t_y^+/\Delta t_z^+$ hardly becomes smaller than 10 even on coarse meshes. Note that in Eqn. (1.1) the spanwise velocity w has been neglected, nevertheless the azimuthal velocity at the axis can be finite, as in the pipe flow, so that the convective limitation at the axis can also become relevant. The viscous limitation in in the azimuthal direction is also restrictive, in fact in wall units we get

$$\Delta t_{zv}^+ = \Delta {z_0^+}^2 = \left(\frac{\Delta r_0^+ 2\pi}{N_z} \right)^2 . \tag{1.4}$$

In the incompressible case the time step limitation at the axis is removed by treating both convective and viscous terms implicitly [56, 96, 151, 160]. In the compressible case the time step limitation is even more restrictive because of the acoustic time step constraint, and this difficulty is usually tackled by skipping nodes when computing derivatives in θ direction [16]. The main disadvantage of this approach is the natural chess-boarding of the computational stencil, which causes odd-even decoupling unless the variables are explicitly filtered. In this work we apply the locally conservative, energy-consistent splitting developed by Pirozzoli [111] to cylindrical coordinates, together with the singularity treatment of Mohseni and Colonius [93], which allows to formally preserve the kinetic energy. The acoustic

time step limitation in the azimuthal and wall normal direction is removed using the novel approach introduced in Section 2.1.2, although the use of the implicit integration formally destroys the conservation of the kinetic energy, inviscid test cases show that the scheme retains excellent conservation properties also at realistic CFL numbers.

Chapter 2

Numerical approach

In this work both Navier-Stokes equations in Cartesian and cylindrical coordinates are considered. The discretization of the compressible Navier-Stokes equations in Cartesian and polar coordinates poses different difficulties, thus requiring specialized techniques for the two cases In Section 2.1 the equations and numerical techniques for Cartesian coordinates are introduced. All simulations presented in this work are performed using the entropy equation, but for the sake of completeness the total energy equation is also reported, since it is the common choice in compressible flow solvers. The use of the entropy equation is a building block for the development of a novel semi-implicit algorithm for the treatment of the acoustic terms, described in Section 2.1.2. Issues related to the flow initialization and boundary conditions are also addressed in Section 2.1.3-2.1.4. Section 2.2 focuses on issues specific of the compressible N-S equations in polar coordinates. A simple approach that allows the discrete conservation of the kinetic energy is described together with an approach to relax the severe time step limitation in the azimuthal direction and a proper axis treatment.

2.1 Governing equations in Cartesian coordinates

The Navier-Stokes equations for a perfect heat-conducting gas in terms of total energy or entropy equation with passive scalar transport are,

$$\frac{\partial \rho}{\partial t} + \frac{\partial \rho u_i}{\partial x_i} = 0, \tag{2.1a}$$

$$\frac{\partial \rho u_i}{\partial t} + \frac{\partial \rho u_i u_j}{\partial x_j} = -\frac{\partial p}{\partial x_i} + \frac{\partial \sigma_{ij}}{\partial x_j} + \Pi \delta_{i1}, \tag{2.1b}$$

$$\frac{\partial \rho E}{\partial t} + \frac{\partial \rho u_j H}{\partial x_j} = -\frac{\partial q_j}{\partial x_j} + \frac{\partial \sigma_{ij} u_i}{\partial x_j} + \Pi u_1, \tag{2.1c}$$

$$\frac{\partial \rho s}{\partial t} + \frac{\partial \rho u_j s}{\partial x_j} = \frac{1}{T}\left(-\frac{\partial q_j}{\partial x_j} + \sigma_{ij}\frac{\partial u_i}{\partial x_j}\right) \tag{2.1d}$$

$$\frac{\partial \rho \phi}{\partial t} + \frac{\partial \rho u_j \phi}{\partial x_j} = \frac{\partial}{\partial x_j}\left(\rho \alpha \frac{\partial \phi}{\partial x_j}\right) + \Phi \tag{2.1e}$$

where u_i, $i = 1, 2, 3$, is the velocity component in the i-th direction. The velocity components in x, y z direction will be denoted as u, v, w respectively. ρ is the density, p the pressure, $E = c_v T + u_i u_i/2$ the total energy per unit mass, and $H = E + p/\rho$ is the total enthalpy and $s = c_v \ln(p\rho^{-\gamma})$ the entropy per unit mass, $\gamma = c_p/c_v = 1.4$ is the specific heat ratio, q_j and σ_{ij} are the components of the heat flux vector and the viscous stress tensor respectively,

$$\sigma_{ij} = \mu\left(\frac{\partial u_i}{\partial x_j} + \frac{\partial u_j}{\partial x_i} - \frac{2}{3}\frac{\partial u_k}{\partial x_k}\delta_{ij}\right), \tag{2.2}$$

$$q_j = -k\frac{\partial T}{\partial x_j}, \tag{2.3}$$

where the dependence of the viscosity coefficient on temperature is accounted for through Sutherland's law and $k = c_p\mu/Pr$ is the thermal conductivity, with $Pr = 0.71$. Equation (2.1e) represents the transport of a passive scalar ϕ which will also be considered in this work. The passive scalar diffusivity is $\alpha = \mu/(\rho Sc)$, with Sc the Schmidt number. Note that Eqn. (2.1c) and (2.1d) are the total energy and entropy equation, which are of course interchangeable. The total energy equation is usually the natural choice in the compressible flow community, since it allows to derive the correct Rankine-Hugoniot jump conditions, while the entropy does not [123]. Despite that, as we will see in Section 2.1.2, the entropy formulation allows to derive efficient semi-implicit schemes which can be used for smooth flows, which are the focus of this work. In the case of internal flows the system must

be forced in order to keep turbulence alive. The forcing term Π in Eqn. (2.1b) is evaluated at each time step in order to discretely enforce constant mass-flow-rate in time, and the corresponding power spent is added to the right-hand-side of the total energy equation. No forcing term is needed for the entropy equation, Eqn. (2.1d). In the case of internal flows, depending on the boundary conditions, a forcing term Φ is added to the passive scalar equation, Eqn. (2.1e), to enforce a constant bulk scalar flux in time. The compressible Navier-Stokes equations can be cast in compact vector form for later use,

$$\frac{\partial \mathbf{w}}{\partial t} = -\sum_{i=1}^{3} \frac{\partial \mathbf{f}_i}{\partial x_i} + \sum_{i=1}^{3} \frac{\partial \mathbf{f}_i^v}{\partial x_i} + \mathbf{S} + \mathbf{F} = \mathbf{R}(\mathbf{w}), \tag{2.4}$$

where $\mathbf{w}$ is the vector of conservative variables, $\mathbf{f}_i$ and $\mathbf{f}_i^v$ are the Eulerian and viscous fluxes in the i-th direction, with x, y, z the streamwise, wall normal and spanwise directions and $\mathbf{S}$ the source terms in the entropy equation, namely

$$\mathbf{w} = \begin{Bmatrix} \rho \\ \rho u_j \\ \rho s \\ \rho \phi \end{Bmatrix}, \ \mathbf{f}_i = \begin{Bmatrix} \rho u_i \\ \rho u_i u_j + p\delta_{ij} \\ \rho u_i s \\ \rho u \phi \end{Bmatrix}, \ \mathbf{f}_i^v = \begin{Bmatrix} 0 \\ \sigma_{ij} \\ -q_i/T \\ \rho\alpha \frac{\partial \phi}{\partial x_i} \end{Bmatrix}, \ \mathbf{S} = \begin{Bmatrix} 0 \\ 0 \\ 0 \\ 0 \\ \frac{\sigma_{\ell m}}{T}\frac{\partial u_\ell}{\partial x_m} - \frac{q_\ell}{T^2}\frac{\partial T}{\partial x_\ell} \\ 0 \end{Bmatrix}, \tag{2.5}$$

and $\mathbf{F} = \begin{Bmatrix} 0 \\ \Pi\delta_{1j} \\ 0 \\ \Phi \end{Bmatrix}$ is the vector of forcing terms.

2.1.1 Space discretization

The nonlinear terms in the Navier-Stokes equations in Cartesian coordinates are discretized using locally conservative, energy-consistent formulas of arbitrary order of accuracy which guarantee that the total kinetic energy is discretely preserved from the convective terms in the limit case of inviscid flow [111]. Let us consider the Eulerian flux in one direction (say y) $f_y = \rho v \varphi$, where φ is the transported quantity in the Euler equations, $\varphi = 1$ for the mass equation, $\varphi = u_j$ for the momentum

H for the total energy, $\varphi = s$ for the entropy equation and ϕ for the passive scalar transport. As it is customary in the compressible flow community we recast finite difference derivative approximations of order of accuracy $2\,L$ in terms of numerical fluxes,

$$\left.\frac{\partial f_y}{\partial y}\right|_j = \frac{1}{\Delta y}\sum_{l=-L}^{L} a_l f^y_{j+l} = \frac{1}{\Delta y}\left(\hat{f}^y_{j+1/2} - \hat{f}^y_{j-1/2}\right), \tag{2.6}$$

and a_l are the coefficients for the central first derivative of order of accuracy $2\,L$.

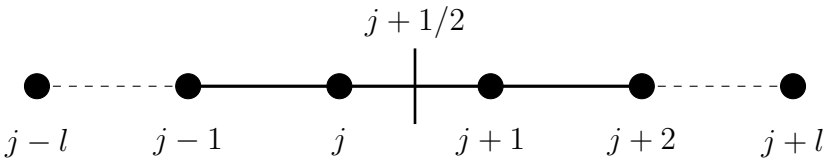

Figure 2.1: Sketch of the computational stencil in one direction. Computational nodes are denoted by bullets.

Let us consider the computational stencil in Fig. 2.1.1, the numerical flux $f^y_{j+1/2}$ for a $2\,L$ order of accuracy at the interface $j + 1/2$ is,

$$\hat{f}^y_{j+1/2} = 2\sum_{l=1}^{L} a_l \sum_{m=0}^{l-1} \left(\widetilde{\rho, v, \varphi}\right)_{j-m,l}. \tag{2.7}$$

We also introduced the three-point averaging operator,

$$\left(\widetilde{f, g, h}\right)_{j,l} = \frac{1}{8}\left(f_j + f_{j+l}\right)\left(g_j + g_{j+l}\right)\left(h_j + h_{j+l}\right), \tag{2.8}$$

The finite difference approximation of the Eulerian fluxes in Eqn. (2.4) at node (i, j, k) is

$$\mathbf{H}_{i,j,k} \approx \frac{\partial \mathbf{f}_x}{\partial x} + \frac{\partial \mathbf{f}_y}{\partial y} + \frac{\partial \mathbf{f}_z}{\partial z}, \tag{2.9}$$

$$\begin{aligned}\mathbf{H}_{i,j,k} = \Bigg[&\frac{1}{\Delta x_i}\left(\hat{\mathbf{f}}^x_{i+1/2,j,k} - \hat{\mathbf{f}}^x_{i-1/2,j,k}\right) + \frac{1}{\Delta y_j}\left(\hat{\mathbf{f}}^y_{i,j+1/2,k} - \hat{\mathbf{f}}^y_{i,j-1/2,k}\right) + \\ &\frac{1}{\Delta z_k}\left(\hat{\mathbf{f}}^z_{i,j,k+1/2} - \hat{\mathbf{f}}^z_{i,j,k-1/2}\right)\Bigg].\end{aligned} \tag{2.10}$$

This approach allows conservation of the quantity φ^2 in the inviscid limit, that

is the discrete kinetic energy and the entropy variance s^2, thus avoiding the introduction of any artificial viscosity for numerical stabilization, as done in most existing compressible flow solvers. The viscous fluxes in Eqn. (2.4) are expanded as Laplacians in order to benefit of a higher dissipation in the wavenumber space and avoid odd-even decoupling phenomena and approximated with the same order of accuracy of convective terms,

$$\frac{\partial}{\partial x}\left(\mu\frac{\partial u}{\partial x}\right) = \frac{\partial \mu}{\partial x} + \mu\frac{\partial^2 u}{\partial x^2}. \tag{2.11}$$

In the case of wall-bounded flows the mesh is usually uniform in wall-parallel direction and stretched towards the wall, so that the wall-normal logical coordinate η is mapped to physical space through $y(\eta)$. A detailed description on how non-uniform meshes are handled is reported in the Appendix 5.1.

2.1.2 Time integration

In this Section a novel semi-implicit algorithm for the treatment of acoustic waves is introduced. As shown in the following, the use of the entropy equation in System (2.4) is instrumental to achieving efficient implicit treatment of the acoustic terms, and also yield benefits in terms of increased robustness as compared to algorithms solving for the energy equation [58]. On the other hand, this setting precludes the possibility to directly capture shock waves [123], hence in the following we restrict ourselves to discussing the case of shock-free flows. Implicit treatment of viscous terms is also described, since in some cases viscous time step limitation may become relevant.

Implicit treatment of acoustic waves

In order to remove the time acoustic time step limitation in the generic coordinate direction (say, y), we proceed by splitting the convective flux vector into a purely advective part, and a part which supports acoustic fluctuations, namely

$$\mathbf{f}_y = \mathbf{f}_y^c + \mathbf{f}_y^a, \quad \mathbf{f}_y^c = \begin{Bmatrix} 0 \\ \rho u v \\ \rho v^2 \\ \rho v w \\ \rho v s \end{Bmatrix}, \quad \mathbf{f}_y^a = \begin{Bmatrix} \rho v \\ 0 \\ p \\ 0 \\ 0 \end{Bmatrix}. \tag{2.12}$$

This approximate splitting is made possible by the use of the entropy equation instead of the energy equation, and in a linearized setting it yields full decoupling of the acoustic, vortical and entropy modes [76]. The main advantage for later purposes is that the acoustic partial flux Jacobian has a simple structure,

$$\mathbf{A}_y^a = \frac{\partial \mathbf{f}_y^a}{\partial \mathbf{w}} = \begin{bmatrix} 0 & 0 & 1 & 0 & 0 \\ 0 & 0 & 0 & 0 & 0 \\ \frac{p}{\rho}\left(\gamma - \frac{s}{C_v}\right) & 0 & 0 & 0 & \frac{p}{\rho C_v} \\ 0 & 0 & 0 & 0 & 0 \\ 0 & 0 & 0 & 0 & 0 \end{bmatrix}. \tag{2.13}$$

For completeness acoustic and full Jacobians in the three coordinate directions are also reported in the Appendix 5.2. Splitting of the flux vectors into pressure and velocity contributions was previously considered by Barth and Steger [6], Steger [135], based on the attempt to reduce the block size in the implicit operator as compared to the Beam-Warming algorithm. In essence, these decompositions amounted [121] to isolating the pressure gradient in the momentum equation and the pressure flux in the total energy equation. However, besides being consistent with wave decomposition in a linear setting, we find the splitting (2.13) to be vastly more robust in practice. We proceed to discretize Eqn. (2.4) between two time levels n and $n+1$, by evaluating explicitly the convective partial flux, and evaluating the acoustic partial flux in fully implicit fashion upon linearization about time level n, namely

$$\mathbf{f}_y^{an+1} = \mathbf{f}_y^{an} + \mathbf{A}_y^{an}\left(\mathbf{w}^{n+1} - \mathbf{w}^n\right) + O(\Delta t^2), \tag{2.14}$$

thus obtaining

$$\left(\mathbf{I} + \Delta t \frac{\partial}{\partial y}\mathbf{A}_y^{an}\right)\Delta \mathbf{w}^n = -\Delta t \frac{\partial \mathbf{f}_y^N}{\partial y} + \Delta t \mathbf{F}_{xz}^n = \Delta t\, \mathbf{RHS}^n, \tag{2.15}$$

where $\Delta \mathbf{w}^n = \mathbf{w}^{n+1} - \mathbf{w}^n$, and where for convenience all terms containing transverse flux derivatives as well as all viscous fluxes are lumped together into the term $\mathbf{F}_{xz}$. All the convective derivatives at the right-hand-side of Eqn. (2.15) are discretized using conservative, energy-preserving discretizations as in Eqn. (2.10), and viscous terms are expanded to Laplacian form and discretized with central formulas [80] as described in Section 2.1.1. In the explicit case this discretization allow to exactly

conserve the total kinetic energy as well as the entropy variance in the inviscid incompressible limit, hence providing strong nonlinear stability to the algorithm without introducing any numerical diffusion [58, 112]. It is important to note that, because of the special structure of the acoustic flux Jacobian, the inversion of Eqn. (2.15) is much simpler than in the case of the standard Beam-Warming algorithm [8]. Component-wise, Eqn. (2.15) reads

$$\begin{cases} \Delta w_1^n + \Delta t \dfrac{\partial}{\partial y} \Delta w_3^n = \Delta t RHS_1^n & \text{(2.16a)} \\ \Delta w_2^n = \Delta t RHS_2^n & \text{(2.16b)} \\ \Delta w_3^n + \Delta t \dfrac{\partial}{\partial y} (A_{y31}^{an} \Delta w_1^n) + \Delta t \dfrac{\partial}{\partial y} (A_{y35}^{an} \Delta w_5^n) = \Delta t RHS_3^n & \text{(2.16c)} \\ \Delta w_4^n = \Delta t RHS_4^n & \text{(2.16d)} \\ \Delta w_5^n = \Delta t RHS_5^n & \text{(2.16e)} \end{cases}$$

Hence, the time increments of entropy and of the transverse velocity components can be explicitly evaluated, thus effectively reducing the system of equations to be solved to

$$\begin{cases} \Delta w_1^n + \Delta t \dfrac{\partial}{\partial y} \Delta w_3^n = \Delta t RHS_1^n & \text{(2.17a)} \\ \Delta w_3^n + \Delta t \dfrac{\partial}{\partial y} (A_{y31}^{an} \Delta w_1^n) = \Delta t RHS_3^n - \Delta t \dfrac{\partial}{\partial y} (A_{y35}^{an} \Delta w_5^n) = \Delta t \widehat{RHS}_3^n & \text{(2.17b)} \end{cases}$$

which, upon discretization of the space derivative operators, gives rise to a block-banded system of equations in which each block has 2×2 size, whose solution yields the time increments of ρ and ρv. Equation (2.17b) can be further rearranged by formally solving for Δw_1^n in (2.17a), to obtain

$$\left(1 - \Delta t^2 A_{y31}^{an} \frac{\partial^2}{\partial y^2} - \Delta t^2 \frac{\partial A_{y31}^{an}}{\partial y} \frac{\partial}{\partial y} \right) \Delta w_3^n = \Delta t \widehat{RHS}_3^n - \Delta t^2 \frac{\partial}{\partial y} \left(A_{y31}^{an} RHS_1^n, \right), \tag{2.18}$$

whose solution requires the inversion of an ordinary banded system of equations with bandwidth depending on the accuracy in the approximation of the first and second space derivative operators. Back substitution into (2.17a) then yields the time increment of density. Although apparently cumbersome, we find the latter formulation to be more computationally efficient than the solution of the 2×2 block system given by Eqn. (2.17b), while the performance is nearly identical. Hence,

Eqn. (2.18) is used in all the forthcoming implicit numerical applications.

Implicit treatment of viscous terms

If needed, viscous terms can also be handled implicitly, using approximate factorization. For that purpose, we split the viscous flux derivatives in Eqn. (2.4) into a Laplacian term and a difference thereof

$$\frac{\partial \mathbf{f}_y^v}{\partial y} = \boldsymbol{\mu}\frac{\partial^2 \mathbf{v}}{\partial y^2} + \boldsymbol{\varphi}_y^v, \tag{2.19}$$

where $\mathbf{v}$ is the vector of the primitive variables, $\mathbf{v} = [\rho, u, v, w, T]$, and $\boldsymbol{\mu}$ is the viscosity matrix,

$$\boldsymbol{\mu} = \begin{bmatrix} 0 & 0 & 0 & 0 & 0 \\ 0 & \mu & 0 & 0 & 0 \\ 0 & 0 & \mu & 0 & 0 \\ 0 & 0 & 0 & \mu & 0 \\ 0 & 0 & 0 & 0 & \frac{\mu Cp}{PrT}. \end{bmatrix} \tag{2.20}$$

Freezing for simplicity the viscosity matrix at time step n, the following linearization is considered,

$$\left(\boldsymbol{\mu}\frac{\partial^2 \mathbf{v}}{\partial y^2}\right)^{n+1} \approx \left(\boldsymbol{\mu}\frac{\partial^2 \mathbf{v}}{\partial y^2}\right)^{n} + \boldsymbol{\mu}^n \frac{\partial^2 \mathbf{P}\Delta \mathbf{w}^n}{\partial y^2}, \tag{2.21}$$

where $\mathbf{P}$ is the Jacobian of the conservative-to-primitive variables transformation

$$\mathbf{P} = \frac{\partial \mathbf{v}}{\partial \mathbf{w}} = \begin{bmatrix} 1 & 0 & 0 & 0 & 0 \\ -\frac{u}{\rho} & \frac{1}{\rho} & 0 & 0 & 0 \\ -\frac{v}{\rho} & 0 & \frac{1}{\rho} & 0 & 0 \\ -\frac{w}{\rho} & 0 & 0 & \frac{1}{\rho} & 0 \\ \frac{-Ts}{\rho c_v} & 0 & 0 & 0 & \frac{T}{\rho c_v} \end{bmatrix}. \tag{2.22}$$

Similar to what done to arrive at Eqn. (2.15), the previous linearization yields

$$\left(\mathbf{I} + \Delta t \frac{\partial}{\partial y}\mathbf{A}_y^{an} - \Delta t \boldsymbol{\mu}^n \frac{\partial^2}{\partial y^2}\mathbf{P}^n\right)\Delta \mathbf{w}^n = \Delta t\, \mathbf{RHS}^n, \tag{2.23}$$

which can be factorized as follows

$$\left(\mathbf{I}+\Delta t\frac{\partial}{\partial y}\mathbf{A}_y^{an}\right)\left(\mathbf{I}-\Delta t\boldsymbol{\mu}^n\frac{\partial^2}{\partial y^2}\mathbf{P}^n\right)\Delta\mathbf{w}^n=\Delta t\,\mathbf{RHS}^n. \tag{2.24}$$

Inversion of Eqn. (2.24) can be be then carried out into two sequential sub-steps, application of the inversion procedure for

$$\left(\mathbf{I}+\Delta t\frac{\partial}{\partial y}\mathbf{A}_y^{an}\right)\widetilde{\Delta\mathbf{w}}^n = \Delta t\mathbf{RHS}^n, \tag{2.25}$$

$$\left(\mathbf{I}-\Delta t\boldsymbol{\mu}^n\frac{\partial^2}{\partial y^2}\mathbf{P}^n\right)\Delta\mathbf{w}^n = \widetilde{\Delta\mathbf{w}}^n, \tag{2.26}$$

whereby the provisional time increment $\widetilde{\Delta\mathbf{w}}^n$ is first computed through the inversion procedure for the convective fluxes described in Section 2.1.2. The time increment is then evaluated by inverting the viscous implicit operator at the left-hand-side of Eqn. (2.26), which, accounting for the special structure of the Jacobian matrix given in Eqn. (2.22), can be carried out in cascade, as follows

$$\begin{cases}
\Delta w_1^n=\widetilde{\Delta w_1}^n & \text{(2.27a)}\\
\left(1-\mu_{22}^n\Delta t\frac{\partial^2}{\partial y^2}P_{22}^n\right)\Delta w_2^n=\widetilde{\Delta w_2}^n+\mu_{22}^n\Delta t\frac{\partial^2}{\partial y^2}\left(P_{21}^n\Delta w_1^n\right) & \text{(2.27b)}\\
\left(1-\mu_{33}^n\Delta t\frac{\partial^2}{\partial y^2}P_{33}^n\right)\Delta w_3^n=\widetilde{\Delta w_3}^n+\mu_{33}^n\Delta t\frac{\partial^2}{\partial y^2}\left(P_{31}^n\Delta w_1^n\right) & \text{(2.27c)}\\
\left(1-\mu_{44}^n\Delta t\frac{\partial^2}{\partial y^2}P_{44}^n\right)\Delta w_4^n=\widetilde{\Delta w_4}^n+\mu_{44}^n\Delta t\frac{\partial^2}{\partial y^2}\left(P_{41}^n\Delta w_1^n\right) & \text{(2.27d)}\\
\left(1-\mu_{55}^n\Delta t\frac{\partial^2}{\partial y^2}P_{55}^n\right)\Delta w_5^n=\widetilde{\Delta w_5}^n+\mu_{55}^n\Delta t\frac{\partial^2}{\partial y^2}\left(P_{51}^n\Delta w_1^n\right) & \text{(2.27e)}
\end{cases}$$

The inversion of four standard narrow-banded systems of equations is thus required for the purpose. We point out that the present procedure is different than the original Beam-Warming procedure, which relies on linearization of the full viscous flux vectors, and which again requires the inversion of block-banded systems. However, we have found the robustness to be very weakly affected by the approximations herein made.

Multiple space dimensions

As done for the case of one space dimension, the acoustic and viscous time limitations can be effectively removed through direction-wise factorization of the implicit

operators. Assuming that all directions are handled in semi-implicit fashion, we obtain

$$\mathbf{L}^n \Delta \mathbf{w}^n = \mathbf{R}(\mathbf{w}^n), \tag{2.28}$$

where

$$\begin{aligned} \mathbf{L}^n = \quad & \left(\mathbf{I} + \Delta t \frac{\partial}{\partial x}\mathbf{A}_x^{an}\right)\left(\mathbf{I} + \Delta t \frac{\partial}{\partial y}\mathbf{A}_y^{an}\right)\left(\mathbf{I} + \Delta t \frac{\partial}{\partial z}\mathbf{A}_z^{an}\right) \cdot \\ & \left(\mathbf{I} - \Delta t \boldsymbol{\mu}^n \frac{\partial^2}{\partial x^2}\mathbf{P}^n\right)\left(\mathbf{I} - \Delta t \boldsymbol{\mu}^n \frac{\partial^2}{\partial y^2}\mathbf{P}^n\right)\left(\mathbf{I} - \Delta t \boldsymbol{\mu}^n \frac{\partial^2}{\partial z^2}\mathbf{P}^n\right). \end{aligned} \tag{2.29}$$

Hence, repeated application of the procedures developed in the previous two sections is needed. the Appendix 5.2.

Accurate time integration

Time accuracy and stability enhancement is typically obtained by Runge-Kutta schemes as wrapper to one-step implicit procedures outlined in the previous paragraphs. Low-storage algorithms are a popular choice, and here we consider for example Wray's three-stage, third-order scheme [102], adapted to semi-implicit integration of the convective terms,

$$\mathbf{L}^{(\ell)} \Delta \mathbf{w}^{(\ell)} = \alpha_\ell \Delta t \mathbf{R}^{(\ell-1)} + \beta_\ell \Delta t \mathbf{R}^{(\ell)}, \quad \ell = 0, 1, 2, \tag{2.30}$$

where $\Delta \mathbf{w}^{(\ell)} = \mathbf{w}^{(\ell+1)} - \mathbf{w}^{(\ell)}$, $\mathbf{w}^{(0)} = \mathbf{w}^n$, $\mathbf{w}^{n+1} = \mathbf{w}^{(3)}$, the left-hand-side implicit operator is a generalization of Eqn. (2.29), namely

$$\begin{aligned} \mathbf{L}^{(\ell)} = \quad & \left(\mathbf{I} + \gamma_\ell \Delta t \frac{\partial}{\partial x}\mathbf{A}_x^{a(\ell)}\right)\left(\mathbf{I} + \gamma_\ell \Delta t \frac{\partial}{\partial y}\mathbf{A}_y^{a(\ell)}\right)\left(\mathbf{I} + \gamma_\ell \Delta t \frac{\partial}{\partial z}\mathbf{A}_z^{a(\ell)}\right) \cdot \\ & \left(\mathbf{I} - \gamma_\ell \Delta t \boldsymbol{\mu}^{(\ell)} \frac{\partial^2}{\partial x^2}\mathbf{P}^{(\ell)}\right)\left(\mathbf{I} - \gamma_\ell \Delta t \boldsymbol{\mu}^{(\ell)} \frac{\partial^2}{\partial y^2}\mathbf{P}^{(\ell)}\right)\left(\mathbf{I} - \gamma_\ell \Delta t \boldsymbol{\mu}^{(\ell)} \frac{\partial^2}{\partial z^2}\mathbf{P}^{(\ell)}\right), \end{aligned}$$

and the integration coefficient are $\alpha_\ell = (0, 17/60, -5/12)$, $\beta_\ell = (8/15, 5/12, 3/4)$, $\gamma_\ell = \alpha_\ell + \beta_\ell$. We have found this time stepping scheme to work well in practice, however because of the partial flux linearization, the method is only formally first-order accurate in time. A genuinely third-order accurate semi-implicit Runge-Kutta

scheme was derived by Nikitin [100], which can be conveniently cast as follows

$$\begin{cases} \mathbf{L}^n \Delta \mathbf{w}^{(1)} = \dfrac{2}{3}\Delta t \mathbf{R}^n & \text{(2.31a)} \\ \mathbf{L}^{(1)} \Delta \mathbf{w}^{(2)} = -\left(\mathbf{w}^{(1)} - \mathbf{w}^n\right) + \dfrac{1}{3}\Delta t \mathbf{R}^n + \dfrac{1}{3}\Delta t \mathbf{R}^{(1)} & \text{(2.31b)} \\ \Delta \mathbf{w}^{(3)} = \dfrac{1}{2}\left(\mathbf{w}^{(2)} - \mathbf{w}^n\right) - \dfrac{3}{2}\alpha \Delta \mathbf{w}^{(2)} & \text{(2.31c)} \\ \mathbf{L}^{(3)} \Delta \mathbf{w}^{(4)} = -\left(\mathbf{w}^{(3)} - \mathbf{w}^n\right) + \dfrac{1}{4}\Delta t \mathbf{R}^n + \dfrac{3}{4}\Delta t \mathbf{R}^{(1)} & \text{(2.31d)} \\ \mathbf{L}^{(4)} \Delta \mathbf{w}^{(5)} = -\left(\mathbf{w}^{(4)} - \mathbf{w}^n\right) + \dfrac{1}{4}\Delta t \mathbf{R}^n + \dfrac{3}{4}\Delta t \mathbf{R}^{(2)}, & \text{(2.31e)} \end{cases}$$

where $\gamma_\ell = \gamma$ is the same for all sub-steps, and α are free parameters (hereafter, we assume $\alpha = 1$, $\gamma = 0.6$). With respect to Wray's algorithm, Eqn. (2.31) is not in low-storage form (although it can be implemented using three arrays only), and it involves an additional inversion, but no additional evaluation of the explicit operator. Despite the slight computational overhead, all the following analysis and numerical experiments are carried out with algorithm (2.31) because of its higher formal accuracy.

Stability analysis

The stability of the semi-implicit algorithm herein developed is here analyzed within the simplified setting of the linearized inviscid acoustic equations in the presence of a mean flow u_0, which can be cast as

$$\frac{\partial \mathbf{v}}{\partial t} + \mathbf{A}\frac{\partial \mathbf{v}}{\partial x} = 0, \quad \mathbf{v} = \begin{bmatrix} \rho' \\ u' \end{bmatrix}, \quad \mathbf{A} = \begin{bmatrix} u_0 & \rho_0 \\ c_0^2/\rho_0 & u_0 \end{bmatrix}, \tag{2.32}$$

where the subscript 0 refers to the unperturbed state, and primes to fluctuations thereof. A semi-implicit discretization of Eqn. (2.32) can be obtained by considering the linearized counterpart of the partial flux Jacobian (2.13), namely

$$\mathbf{A}^a = \begin{bmatrix} u_0 & \rho_0 \\ c_0^2/\rho_0 & 0 \end{bmatrix}. \tag{2.33}$$

Backward Euler discretization of Eqn. (2.32) then yields

$$\left(\mathbf{I} - \Delta t \mathbf{A}^a \frac{\partial}{\partial x}\right) \Delta \mathbf{v}^n = -\Delta t \mathbf{A} \frac{\partial \mathbf{v}^n}{\partial x}. \tag{2.34}$$

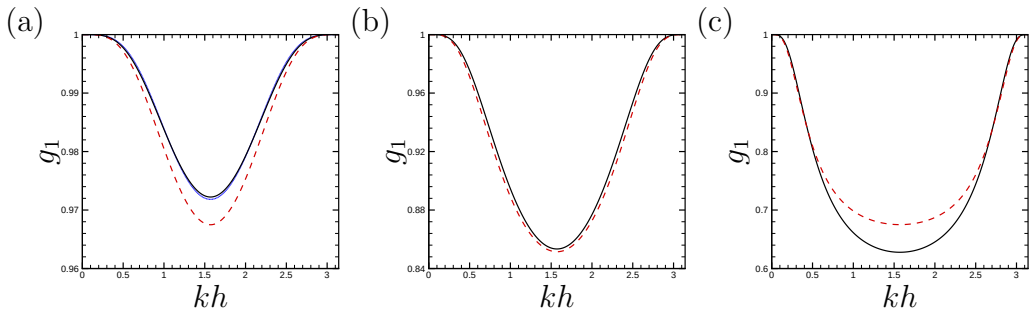

Figure 2.2: Smallest eigenvalue of amplification matrix at CFL = 1 (a), CFL = 2 (b), CFL = 5 (c), for explicit Runge-Kutta time integration (dotted lines), semi-implicit time integration (with $\alpha = 1$, $\gamma = 0.6$, solid lines), and fully implicit Beam-Warming scheme (dashed lines), at Mach number $M_0 = 0.3$. Curves are only shown for stable schemes.

Transforming Eqn. (2.34) to Fourier space with the token $\mathbf{v}(x,t) = \hat{\mathbf{v}}(t)e^{ikx}$ yields the amplification matrix of the scheme

$$\mathbf{G} = \mathbf{I} - \left(\mathbf{I} - i\Delta t\tilde{k}\mathbf{A}^a\right)^{-1} i\Delta t\tilde{k}\mathbf{A}, \tag{2.35}$$

where $\mathbf{v}^{n+1} = \mathbf{G}\mathbf{v}^n$, and $\tilde{k}$ is the modified wavenumber corresponding to the discretization of the space first derivative operator [152]. Von Neumann's stability condition requires that both eigenvalues of $\mathbf{G}$ are no larger than unity in modulus. Assuming for instance second-order central differencing (i.e. $\tilde{k}h = \sin(kh)$), it turns out that the scheme (2.34) is unconditionally stable for $M_0 = u_0/c_0 \lesssim 1$. A similar analysis can be carried out (details are omitted) for the Runge-Kutta time stepping scheme of Eqn. (2.31). In the case of explicit time integration (i.e. $\gamma = 0$) the scheme is stable for CFL $\lesssim \sqrt{3}$, where CFL $= (u_0 + c_0)\Delta t/h$. In the case of semi-implicit time integration (with $\gamma = 0.6$, $\alpha = 1$) unconditional stability is achieved for $M_0 \lesssim 0.525$. To provide an idea of the accuracy of the algorithm, in Fig. 2.2 we show the smallest eigenvalues of the amplification matrix at various Courant numbers for explicit and semi-implicit Runge-Kutta time integration. For reference, the amplification factor of the baseline Beam-Warming algorithm is also shown. At CFL numbers lower than the stability limit for explicit discretization (panel (a)), the semi-implicit and the fully explicit algorithms have similar performance, whereas the Beam-Warming algorithm has somewhat higher diffusion. At higher Courant numbers the explicit scheme goes unstable, and semi-implicit and fully implicit scheme have similar performance, with slightly less diffusive behavior of Beam-Warming at higher CFL. Notably, all schemes have unit amplification factor at the Niquist limit ($kh = \pi$), hence they are not dissipative in the sense of Kreiss.

This is the reason why schemes of the Beam-Warming family are typically used with explicit addition of artificial diffusion terms [8, 57]. We note that the semi-implicit algorithms herein dealt with have zero numerical diffusion at the highest resolved wavenumbers. For this reason Beam-Warming scheme is often used in conjunction to additional numerical diffusion terms. On the other hand we found that no artificial diffusion is necessary, due to the space discretization here used which allows to exactly preserve the total kinetic energy from convection, and conserve the entropy variance in the inviscid limit, hence providing strong nonlinear stability to the algorithm without introducing any numerical diffusion.

Computational efficiency

Scheme	CPU/CPU_{EXPL}
EXPL	1.
ATI	1.14
ATI-CYC	1.16
AVTI	1.32
AVTI-CYC	1.37
BW	1.67
BW-CYC	2.21
BWV	1.87
BWV-CYC	2.33

Table 2.1: Computational cost for implicit schemes compared to fully explicit discretization. Figures refer to implicit treatment of a single space direction.

Achieving higher computational efficiency is obviously the main motivation for using implicit algorithms, which are inherently more computationally intensive than explicit ones. Computational cost figures for the present semi-implicit algorithm and for the Beam-Warming scheme are listed in Tab. 2.1, as a fraction of the cost for the baseline explicit algorithm. Cost estimates are given for implicit treatment of convective terms only, and for simultaneous treatment of convective and viscous terms, referring to a single space direction. Also for ease of later reference, we use the following notation to distinguish the various schemes. The semi-implicit scheme herein developed is referred to as either ATI (acoustic terms-implicit, as in Eqn. (2.15)), or ATVI in the case that both convective and viscous terms are handled implicitly (Eqn. (2.23)). As a basis of comparison, cost figures for the Beam-Warming (BW) scheme, also with implicit treatment of the viscous terms (BWV) are reported. Cost figures are provided for both the case of periodic (CYC)

and non-periodic boundary conditions. It should be noted that the cost estimates refer to actual parallel computations, and also include the computational overhead for data transposition across processors in non-contiguous space directions. Of course, precise figures may change depending on the specific implementation of the algorithm and/or machine architecture, but we trust that the numbers listed in the table provide a reasonably robust estimate. It appears that the computational overhead of the ATI algorithm is rather limited, hence implicit treatment of a given space direction is computationally advantageous provided the attainable time step is at least 20% higher than for fully explicit. Substantial improvement of computational efficiency over standard Beam-Warming discretization is also apparent, for comparable expected accuracy (recalling Fig. 2.2).

2.1.3 Boundary closure

In order to evaluate central spatial derivatives as described in Section 2.1.1 nodes $j-l$ and $j+l$ are needed which clearly poses issues at the exterior boundaries, or at the block boundaries where nodes outside the domain are required. In present computations the ghost nodes approach is used for all boundaries. The number of ghost nodes n_g is proportional to the order of accuracy of the scheme $n_g = L$. In the simulation of wall-bounded internal flows one direction (streamwise in duct) or two directions (streamwise and spanwise in channel and pipe) are periodic. In periodic directions the solution in the ghost nodes (say $i = N_x + l$, $l = 1 \ldots, ng$) is taken from the inner nodes on the opposite boundary, $(i = l)$. The treatment of the wall boundary conditions for compressible internal flows may be more critical. Most compressible flow solvers use co-located meshes and only few examples or staggered compressible solvers are available in literature [14, 99]. The presence of the wall in co-located meshes, in which the wall coincides with a node, may lead to lack of total mass conservation in the case of internal flows. This can be easily understood computing the total mass $\sum_{i,j,k}^{N_x,N_y,N_z} \rho_{i,j,k}$, which can only vary due to the Eulerian flux in Eqn. (2.10), thus summing $\mathbf{H_{i,j,k}}$ on all nodes and using $\Delta x_i = \Delta x$, $\Delta z_k = \Delta z$, $\Delta y_{N_y} = \Delta y_1$,

$$\sum_{i,j,k}^{N_x,N_y,N_z} \mathbf{H}_{i,j,k} = \left[\frac{1}{\Delta x} \left(\hat{\mathbf{f}^x}_{N_x+1/2,j,k} - \hat{\mathbf{f}^x}_{-1/2,j,k} \right) + \frac{1}{\Delta y_{N_y}} \left(\hat{\mathbf{f}^y}_{i,N_y+1/2,k} - \hat{\mathbf{f}^y}_{i,-1/2,k} \right) + \frac{1}{\Delta z} \left(\hat{\mathbf{f}^z}_{i,j,N_z+1/2} - \hat{\mathbf{f}^z}_{i,j,-1/2} \right) \right] = \frac{1}{\Delta y_{N_y}} \left(\hat{\mathbf{f}^y}_{i,N_y+1/2,k} - \hat{\mathbf{f}^y}_{i,N_y-1/2,k} \right).$$

(2.36)

Equation (2.36) shows that mass is not conserved in the case of co-located walls, since in general $\hat{\mathbf{f}^y}_{i,N_y+1/2,k} \neq \hat{\mathbf{f}^y}_{i,N_y-1/2,k}$. This issue was solved in previous studies [28, 28, 96] by adding a source term to the continuity equation at the wall nodes so that the net mass variation is zero. In this work we prefer to stagger the first node off the wall in such a way that the latter coincides with an intermediate node (see Fig. 2.3), where the convective fluxes $\hat{\mathbf{f}^y}_{i,N_y+1/2,k} = \hat{\mathbf{f}^y}_{i,N_y-1/2,k} = 0$ are identically zero.

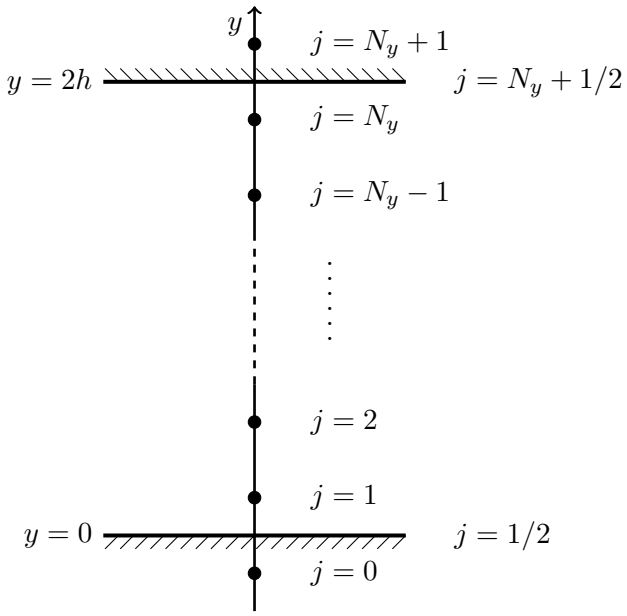

Figure 2.3: Distribution of collocation points in wall-normal direction. Walls are made to coincide with the intermediate nodes $j = 1/2$, $j = N_y + 1/2$, where the numerical convective fluxes are set to zero.

Hence, correct telescoping of the numerical fluxes is guaranteed, and no net mass variation can occur. A further benefit of this approach is that, for given distance of the first grid point from the wall, the maximum allowable time step associated with the vertical mesh spacing is doubled. The only minor difficulty that arises from staggering is the enforcement of the impermeability and wall thermal condition. Hence we simply reflect pressure from the interior nodes and extrapolate

temperature and velocity,

$$p\left(i,1-l,k\right)=p\left(i,l,k\right) \tag{2.37a}$$
$$T\left(i,1-l,k\right)=2\,T_{wall}-T\left(i,l,k\right) \tag{2.37b}$$
$$\rho\left(i,1-l,k\right)=p\left(i,1-l,k\right)/\left(RT\left(i,1-l,k\right)\right) \tag{2.37c}$$
$$u\left(i,1-l,k\right)=2\,u_{wall}-u\left(i,l,k\right) \tag{2.37d}$$
$$v\left(i,1-l,k\right)=-v\left(i,l,k\right) \tag{2.37e}$$
$$w\left(i,1-l,k\right)=-w\left(i,l,k\right), \tag{2.37f}$$

with $i=1,\ldots,N_x$ $l=1,\ldots,N_g$ $k=1,\ldots,N_z$. In all simulations considered in this work the wall is isothermal, since this is the only realistic scenario in the case of internal flows. Adiabatic wall condition would require the addition of a sink term to the total energy/entropy equation, in order to reach a statistically stationary state. All simulations are performed in a convective frame of reference, in which the flow bulk velocity is zero, normally we set $u_{wall}=-u_b$, where u_b is the bulk velocity of the flow. As pointed out by Bernardini et al. [10] finite difference discretization is not Galilean invariant, with an error that is proportional to the mesh spacing and inversely proportional to the bulk velocity of the flow, thus using a frame of reference in which the flow bulk velocity is close to zero reduces this error.

2.1.4 Flow initialization

The choice of the initial conditions is also a non-obvious choice in DNS of wall-bounded flows, since not all initial conditions yield properly developed turbulence. If possible, the best option would be interpolating from a coarser turbulent solution, or from a previously obtained solution at different Reynolds number. A more straightforward, frequently used approach is to initialize the flow with a laminar velocity profile (i.e. a parabolic profile for Poiseuille flow), with superposed random fluctuations. In our experience this approach should be discarded, as it may fail to trigger transition, since if the mesh is fine enough, the small-scale fluctuations are immediately damped by physical viscosity. A recommended approach is to augment the initially laminar profile with more or less physical deterministic disturbances, as obtained for instance with the digital filtering technique [73]. A compromise between effectiveness and simplicity is to add an array of longitudinal rollers, which are extremely effective in redistributing momentum, hence triggering transition to

a turbulent state. A simple prescription is as follows,

$$v\,(y,z) = A_v \sin\,(\pi y/2)\cos\,(2\pi z L_z), \tag{2.38a}$$

$$w\,(y,z) = A_w \cos\,(\pi y/2)\sin\,(2\pi z L_z), \tag{2.38b}$$

where $A_w = -A_v L_z/4$, with A_v an arbitrary amplitude (a few percent of the bulk velocity is sufficient). The difference of adding deterministic disturbances is illustrated in Fig. 2.4, where we show the time history of the friction coefficient for purely random initial conditions (solid lines) and with added longitudinal rollers (dashed lines). It is clear that transition only occurs in the latter case on a time scale $tu_\tau/h \approx 10$, which is typical to achieve a fully turbulent state.

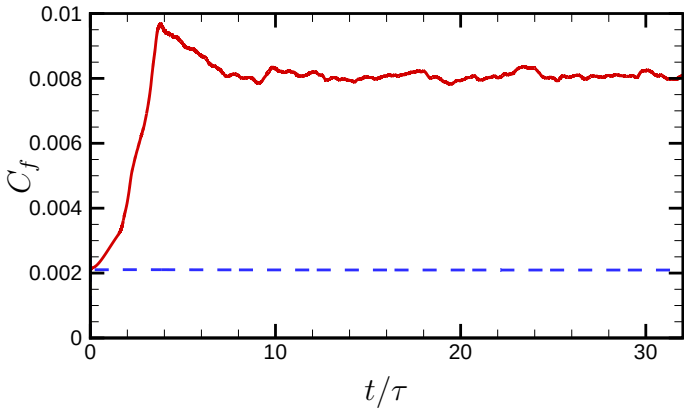

Figure 2.4: Channel flow at $Re_b = 5700$, $M_b = 0.1$: time history of friction coefficient $C_f = 2(u_\tau/u_b)^2$. Times are made nondimensional with respect to the characteristic eddy turnover time $\tau = h/u_\tau$. Dashed line: initial conditions with purely random disturbances; solid line: with superposed rollers as given in Eqn. (2.38).

The use of digital filtering technique rather than Eqn. (2.38), would give similar results, being of more difficult implementation. The flow field is therefor initialized using the incompressible laminar velocity profile to which organized fluctuations, as in Eqn. (2.38) are superposed, density and temperature profiles are set to uniform values. The laminar solution of the incompressible flow in channel pipe and duct that used for initialization are reported in the Appendix 5.4.

2.2 Governing equations in cylindrical coordinates

Let us consider the cylindrical system of coordinates in Fig. 2.2.

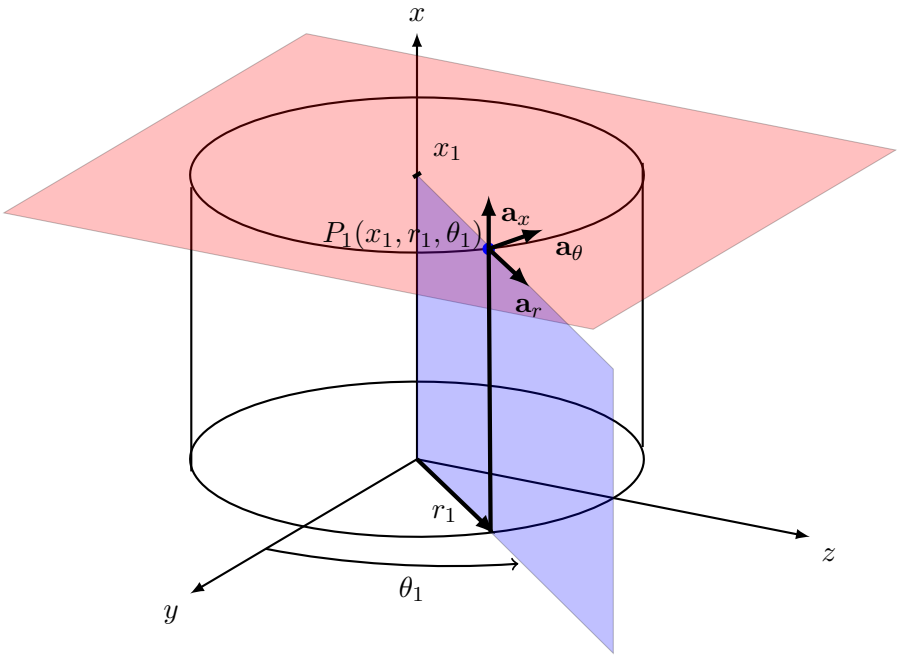

Figure 2.5: Cylindrical system of coordinates. The red plane $x = x_1$ indicates a slice in the $r\theta$ plane, while the blue one represents a slice in the xr plane.

Navier-Stokes equations for a compressible, ideal fluid in cylindrical coordinates with passive scalar transport can be written,

$$\frac{\partial \mathbf{w}}{\partial t} + \frac{1}{r}\left(\frac{\partial \mathbf{f}_x}{\partial x} + \frac{\partial \mathbf{f}_r}{\partial r} + \frac{1}{r}\frac{\partial \mathbf{f}_\theta}{\partial \theta}\right) - \frac{\partial \mathbf{f}_x^v}{\partial x} - \frac{1}{r}\frac{\partial r\, \mathbf{f}_r^v}{\partial r} - \frac{1}{r}\frac{\partial \mathbf{f}_\theta^v}{\partial \theta} + \mathbf{S_e} - \mathbf{S_v} = 0, \quad (2.39)$$

where $\mathbf{w}$ is the vector of the conservative variables, and $\mathbf{f}_i$, $\mathbf{f}_i^v$ $i = 1, 2, 3$ are the convective and viscous fluxes in the three coordinate directions,

$$\mathbf{w} = \begin{bmatrix} \rho \\ \rho u_j \\ \rho s \\ \rho \phi \end{bmatrix}, \quad \mathbf{f}_i = \begin{bmatrix} R u_i \\ R\, u_i\, u_j + P\, \delta_{ij} \\ R\, u_i\, s \\ R u_i \phi \end{bmatrix}, \qquad j = 1, 2, 3, \quad (2.40)$$

having introduced for convenience the variables $R = r\,\rho$, $P = r\,p$. u_i are the velocity components in x, r and θ, streamwise, radial and azimuthal direction, which will

also be denoted as $u = u_x$, $v = -u_r$, $w = u_\theta$. $s = C_v \log p/\rho^\gamma$ is the entropy per unit mass and ϕ the passive scalar field. $x \in [0, L_x]$, $r \in [0, R]$ and $\theta \in [0, 2\,\pi]$.
The viscous fluxes are

$$\mathbf{f}_x^v = \begin{bmatrix} 0 \\ \sigma_{xx} \\ \sigma_{xr} \\ \sigma_{x\theta} \\ q_x \\ J_x \end{bmatrix}, \quad \mathbf{f}_r^v = \begin{bmatrix} 0 \\ \sigma_{xr} \\ \sigma_{rr} \\ \sigma_{r\theta} \\ q_r \\ J_r \end{bmatrix}, \quad \mathbf{f}_\theta^v = \begin{bmatrix} 0 \\ \sigma_{x\theta} \\ \sigma_{r\theta} \\ q_{\theta\theta} \\ q_\theta \\ J_\theta \end{bmatrix}, \tag{2.41}$$

where σ_{ij} are the viscous stress components,

$$\sigma_{xx} = \mu \left(2\,\frac{\partial u_x}{\partial x} - \frac{2}{3}\Theta \right) \tag{2.42a}$$

$$\sigma_{xr} = \mu \left(\frac{\partial u_r}{\partial x} + \frac{\partial u_x}{\partial r} \right) \tag{2.42b}$$

$$\sigma_{x\theta} = \mu \left(\frac{\partial u_\theta}{\partial x} + \frac{1}{r}\frac{\partial u_x}{\partial \theta} \right) \tag{2.42c}$$

$$\sigma_{rr} = \mu \left(2\,\frac{\partial u_r}{\partial r} - \frac{2}{3}\Theta \right) \tag{2.42d}$$

$$\sigma_{r\theta} = \mu \left(\frac{\partial u_\theta}{\partial r} + \frac{1}{r}\frac{\partial u_r}{\partial \theta} - \frac{u_\theta}{r} \right) \tag{2.42e}$$

$$\sigma_{\theta\theta} = \mu \left(2\,\left(\frac{1}{r}\frac{\partial u_\theta}{\partial \theta} + \frac{u_r}{r} \right) - \frac{2}{3}\Theta \right), \tag{2.42f}$$

$$\tag{2.42g}$$

q_j is the heat flux vector,

$$q_x = \frac{k}{T}\frac{\partial T}{\partial x} \tag{2.43a}$$

$$q_r = \frac{k}{T}\frac{1}{r}\frac{\partial rT}{\partial r} \tag{2.43b}$$

$$q_\theta = \frac{k}{T}\frac{1}{r}\frac{\partial T}{\partial \theta}, \tag{2.43c}$$

$$\tag{2.43d}$$

and J_i is the diffusion flux vector,

$$J_x = \rho\alpha\frac{\partial\phi}{\partial x} \tag{2.44a}$$

$$J_r = \rho\alpha\frac{1}{r}\frac{\partial r\phi}{\partial r} \tag{2.44b}$$

$$J_\theta = \rho\alpha\frac{1}{r}\frac{\partial\phi}{\partial\theta}, \tag{2.44c}$$

and Θ is the dilatation,

$$\Theta = \frac{\partial u_x}{\partial x} + \frac{\partial}{\partial r}\left(r\frac{\partial u_r}{\partial r}\right) + \frac{1}{r}\frac{\partial u_\theta}{\partial\theta}. \tag{2.45}$$

The Eulerian and viscous source terms $\mathbf{S_e}$ and $\mathbf{S_v}$ are,

$$\mathbf{S}_e = \frac{1}{r}\begin{bmatrix} 0 \\ 0 \\ -\rho\, u_\theta^2 - p \\ \rho\, u_r\, u_\theta \\ 0 \end{bmatrix}, \quad \mathbf{S}_v = \begin{bmatrix} 0 \\ 0 \\ -\frac{\sigma_{\theta\theta}}{r} \\ \frac{\sigma_{r\theta}}{r} \\ \frac{\sigma_{lm}}{T}\frac{\partial u_l}{\partial x_m} - \frac{q_l}{T^2}\frac{\partial T}{\partial x_m} \end{bmatrix} \tag{2.46}$$

2.2.1 Space discretization

The introduction of the quantities R and P, in Eqn. (2.40) allows to discretize the convective terms as done for the Cartesian equations in Section 2.1.1. The convective terms are discretized through an energy-consistent, locally conservative, scheme of arbitrary order of accuracy [111], which guarantees preservation of the total kinetic energy from convection in the inviscid limit. The scheme was originally developed for Cartesian coordinates and successively extended to generalized curvilinear coordinates with smooth Jacobians [112]. Let us consider the 1D stencil in Fig. 2.2.1,

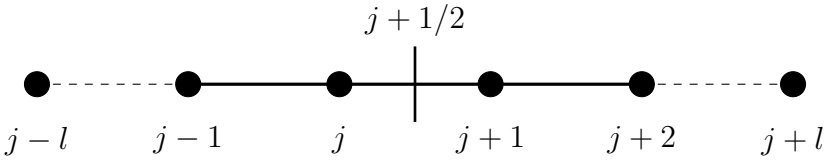

Figure 2.6: Sketch of the computational stencil in one direction. Computational nodes are denoted by bullets.

the numerical flux (see Eqn. (2.6)) in a generic coordinate direction (say r) for $2\,L$

order of accuracy is

$$\hat{f}^r_{j+1/2} = 2\sum_{l=1}^{L} a_l \sum_{m=0}^{l-1} \left(\widetilde{R, v, \varphi}\right)_{j-m,l}, \tag{2.47}$$

where φ is the transported quantity in the Euler equations, $\varphi = 1$ for the mass equation, $\varphi = u_j$ for the momentum, $\varphi = s$ for the entropy equation and ϕ for the passive scalar, and we used the three-point averaging operator introduced in Eqn. (2.8). The finite difference approximation of the Eulerian fluxes in Eqn. (2.39) at node (i, j, k) is

$$\mathbf{H}_{i,j,k} \approx \frac{1}{r}\left(\frac{\partial \mathbf{f}_x}{\partial x} + \frac{\partial \mathbf{f}_r}{\partial r} + \frac{1}{r}\frac{\partial \mathbf{f}_\theta}{\partial \theta}\right) + \mathbf{S}_e, \tag{2.48}$$

$$\begin{aligned}\mathbf{H}_{i,j,k} =& \frac{1}{r_j}\left[\frac{1}{\Delta x_i}\left(\hat{\mathbf{f}^x}_{i+1/2,j,k} - \hat{\mathbf{f}^x}_{i-1/2,j,k}\right) + \frac{1}{\Delta r_j}\left(\hat{\mathbf{f}^r}_{i,j+1/2,k} - \hat{\mathbf{f}^r}_{i,j-1/2,k}\right) + \right.\\ & \left.\frac{1}{r_j}\frac{1}{\Delta\theta_k}\left(\hat{\mathbf{f}^\theta}_{i,j,k+1/2} - \hat{\mathbf{f}^\theta}_{i,j,k-1/2}\right)\right] + \mathbf{S}_{ei,j,k}\end{aligned} \tag{2.49}$$

The Eulerian source terms in $\mathbf{S}_e$ do not pose any problem for discrete energy consistency because they do not appear in the kinetic energy equation. The discretization of the Eulerian terms as in Eqn. (2.49) thus allows to conserve the kinetic energy in the case of cylindrical coordinates. As for the Cartesian equations in Section 2.1.1 the viscous fluxes are expanded as Laplacians in each direction. Full expansion of the viscous fluxes into Laplacians is reported in the Appendix 5.3. The only noteworthy difference with the Cartesian discretization is the approximation of the Laplacians in radial direction, which are computed using staggered second order derivatives

$$\frac{\partial^2 f}{\partial r^2} + \frac{1}{r}\frac{\partial f}{\partial r} = \frac{1}{r}\frac{\partial}{\partial r}\left(r\frac{\partial f}{\partial r}\right) = \frac{1}{r_j}\frac{1}{\Delta r_j}\left(\frac{r_{j+1/2}(f_{j+1} - f_j)}{\Delta r_{j+1/2}} - \frac{r_{j-1/2}(f_j - f_{j-1})}{\Delta r_{j-1/2}}\right). \tag{2.50}$$

In our experience this approach shows better performances in the pole region due to the narrower stencil and to the fact that we let the axis coincide with an intercell [93], where the radial coordinate is identically zero, ($r_j = 0$ at $j = -1/2$, see Section 2.2.3 for a discussion of the axis treatment). The Laplacians in the streamwise and spanwise direction and first derivatives are computed using standard central finite differences approximations.

2.2.2 Time integration

Time integration of the Navier-Stokes equations in cylindrical coordinates is carried out using the ATI algorithm described in Section 2.1.2. In the case of cylindrical coordinates, simultaneous implicit treatment of both acoustic and viscous terms (AVTI) is mandatory in the azimuthal direction, since both viscous and acoustic limitations are restrictive at the axis. In the case of high-Reynolds-number simulations, the convective time step limitation in the azimuthal direction may also be relevant, as the azimuthal velocity component w is finite at the axis. In order to relax the convective limitation in θ direction, the azimuthal derivatives of the convective flux only are taken with coarsened resolution as the axis is approached. Towards the axis points are skipped and the effective resolution of the convective flux $\mathbf{f}_\theta^c$ (split as in Eqn. (2.12)) is reduced so as to relax the convective time step limitation in θ direction,

$$\left.\frac{\partial \mathbf{f}_\theta^c}{r\partial\theta}\right|_{j,k} = \sum_{l=1}^{L} a_l \frac{\mathbf{f}_{k+lm_j}^{\theta c} - \mathbf{f}_{k-lm_j}^{\theta c}}{m_j r_j \Delta\theta_k}, \tag{2.51}$$

where m_j is an integer chosen in such a way to set the azimuthal spacing at the axis equal to the minimum spacing in the radial direction $m_j \Delta\theta r_j = 2\Delta y_w$,

$$m_j = \min\left(N_z \Delta y_w/(\pi r_j), m_{max}\right). \tag{2.52}$$

In any case we do not use less than eight points $m_{max} = N_z/8$. We found this choice to be a good compromise between the accuracy near the axis and the maximum allowable time step. We limit ourselves to reduce the effective resolution of the convective derivatives only, while AVTI is used for acoustic and viscous terms. We found this approach to be more robust and accurate than reducing the effective resolution of all the azimuthal derivatives. The use of Eqn. (2.51) causes some check-boarding of the computational stencil near the axis with consequent odd-even decoupling, so that some filtering in the azimuthal direction is mandatory for that purpose. We use a low-pass filter with cut-off wavenumber changing along the radial coordinate. In particular we choose the cut-off wavenumber in such a way that $k_{co}/r = k_{max}/R$, where k_{max} is the maximum wavenumber. k_{co} will therefor be the integer such that,

$$k_{coj} = \min\left(k_{max}\frac{(r_j + r_0)}{R}, k_{max}\right), \tag{2.53}$$

where r_0 is a constant that avoids k_{co} to become too small. In our experience $r_0 = 0.1$ is a reasonable choice. Figure 2.7 shows k_{co} and m_j as a function of the distance from the wall $y = 1 - r$ for the pipe flow simulation P15, reported in Tab. 3.4. It is clear that the filter has no effect on the near wall region, where azimuthal derivatives are taken with full resolution.

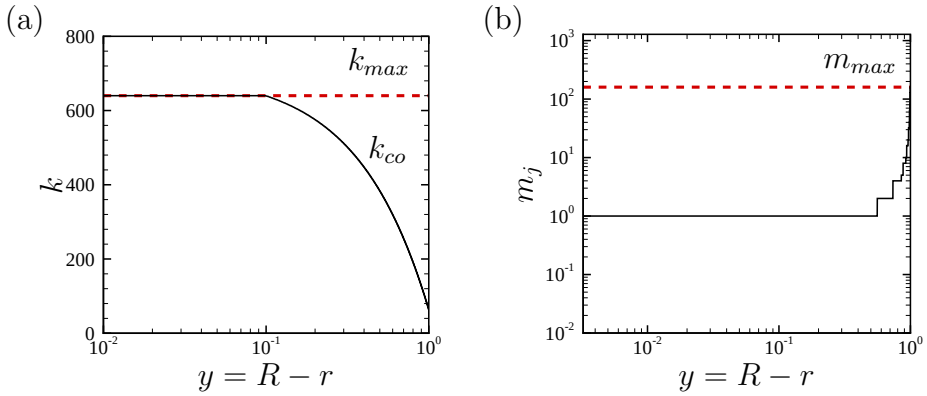

Figure 2.7: (a) Cut-off wavenumber k_{co} (Eqn. (2.53)) as a function of the distance from the wall $y = 1 - r$. The maximum wavenumber k_{max} is indicated by the red dashed line. (b) Index m_j of Eqn. (2.52) for coarsened derivatives as a function of the distance from the wall y.

2.2.3 Boundary closure

In pipe flow periodicity is imposed in the streamise and spanwise direction. The axis is treated according to Mohseni and Colonius [93], that is, the mesh is staggered along the radial direction and the first point (at $\Delta r/2$ from the axis) coincides with the intercell $j = -1/2$ (see Fig. 2.2.3a).

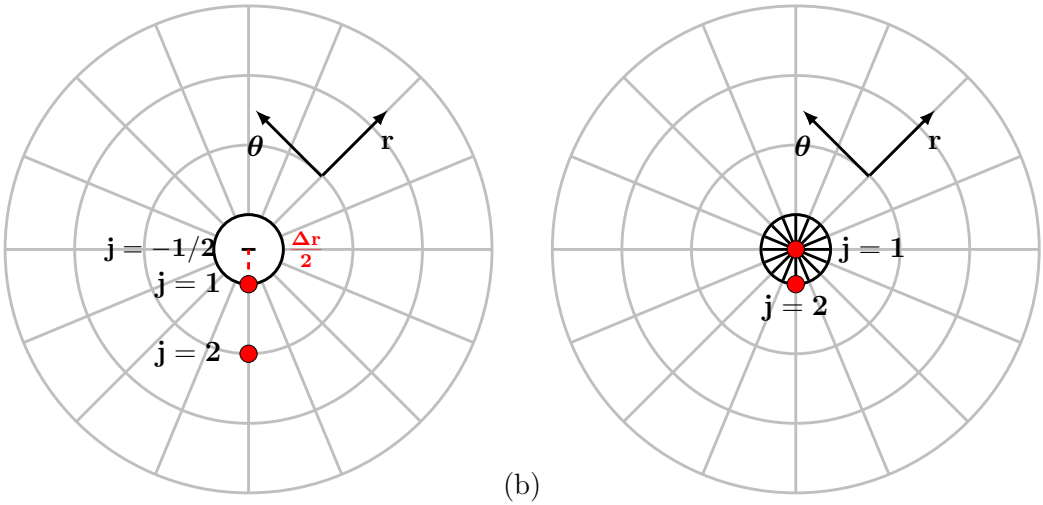

(a) (b)

Figure 2.8: Sketch of different axis treatments. (a) Approach by Mohseni and Colonius [93] in which the first point $j = 1$ is at distance $\Delta r/2$ from the axis. (b) Approach of Constantinescu and Lele [30] in which an ad hoc equation is solved at the axis.

This treatment is preferred with respect to other approaches (Constantinescu and Lele [30], Mitchell et al. [88], Fig. 2.2.3b) because of its simplicity and, above all, its the only one which allows to formally conserve the discrete kinetic energy. No numerical boundary conditions are needed at the axis. The exact values of the function at the opposite side of the axis can in fact be used,

$$\rho(i, 1-l, k) = \rho(i, l, k_\pi) \tag{2.54a}$$
$$u_x(i, 1-l, k) = u_x(i, l, k_\pi) \tag{2.54b}$$
$$u_r(i, 1-l, k) = -u_r(i, l, k_\pi) \tag{2.54c}$$
$$u_\theta(i, 1-l, k) = -u_\theta(i, l, k_\pi) \tag{2.54d}$$
$$s(i, 1-l, k) = s(i, l, k_\pi), \tag{2.54e}$$
$$\tag{2.54f}$$

with $i = 1, \ldots, N_x$, $l = 1, \ldots, N_g$ and $k = 1, \ldots, N_z$. k_π is the index that identify

the node at distance π from k. On *the other side* of the axis the polar velocity components change sign, as in Fig. 2.2.3.

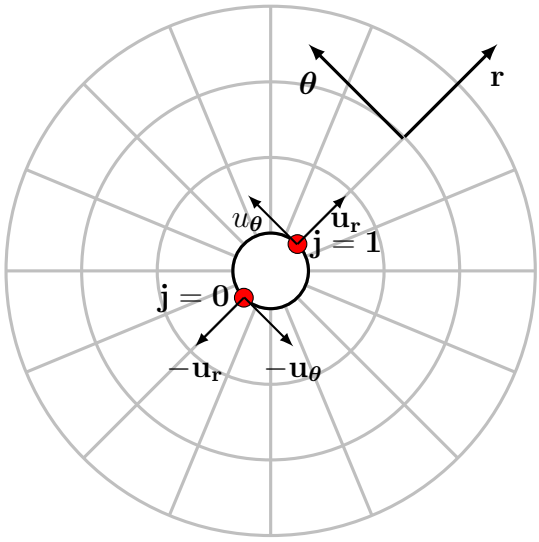

Figure 2.9: Sketch of the boundary conditions the axis. Quantities are copied from the *other side of the axis*, polar velocity components u_r and u_θ with opposite sign, as in Eqn. (2.54).

We also note that since the axis coincides with an intercell (see Fig. 2.2.3a), the numerical flux in the radial direction $\hat{\mathbf{f}}^r_{i,-1/2,k}$ in Eqn. (2.49) can be set to zero, for every i and k and for every time step. The idea is similar to the trick used by Verzicco and Orlandi [151] in the staggered case. The wall boundary is treated with the same approach described in Section 2.1.3.

2.3 Validation of the Cartesian solver

In this Section the DNS codes in Cartesian and cylindrical coordinates are validate, through a series of canonical test cases. The performance of the semi-implicit algorithm developed in Section 2.1.2 is tested through application to isotropic turbulence, channel and duct flow. The cylindrical solver is validated using Lamb dipole, inviscid and laminar pipe flow.

2.3.1 Isotropic turbulence

Numerical simulations of homogeneous isotropic turbulence have been frequently carried out to evaluate the properties of numerical schemes for turbulent flows [128].

DNS are here carried out in a triply periodic $(2\pi)^3$ box, discretized with 64^2 collocation points. At the initial time pressure and density are taken to be uniform, and solenoidal velocity perturbations are added according to the procedure introduced by Blaisdell [12], with prescribed three-dimensional energy spectrum

$$E(k) = 16\sqrt{\frac{2}{\pi}}\frac{u_0^2}{k_0}\left(\frac{k}{k_0}\right)^4 e^{-2(k/k_0)^2}, \tag{2.55}$$

where $k_0 = 4$ is the most energetic mode. The initial turbulent Mach number is given by $M_{t0} = \sqrt{3}u_0/c_0 = 0.3$, and the Reynolds number based on the Taylor microscale is $Re_\lambda = 2\rho_0 u_0/(\mu_0 k_0) = 30$. Time is made nondimensional with respect to the eddy turnover time $\tau = 2\sqrt{3}/(k_0 M_{t0} c_0)$. The results obtained with ATI and BW discretization in all space directions are shown in Figs. 2.10 and 2.11, respectively, at various Courant numbers. Stable results are obtained for CFL $\lesssim 5.1$ for ATI, and CFL $\lesssim 4.8$ for BW. Loss of stability at larger time steps is due to flux linearization and/or factorization errors, which prevent unconditional stability in practical computations [57]. The time behavior of turbulence kinetic energy (panel (a)) is well predicted at all Courant numbers up to the stability limit, whereas pressure fluctuations (panel (b)) are overdamped starting at CFL ≈ 3, in both ATI and BW. The different behavior is caused by the fact that pressure receives contributions of both hydrodynamic and acoustic nature. As seen in Section 2.1.2, and in particular Fig. 2.2 acoustic waves undergo significant damping at high Courant number.

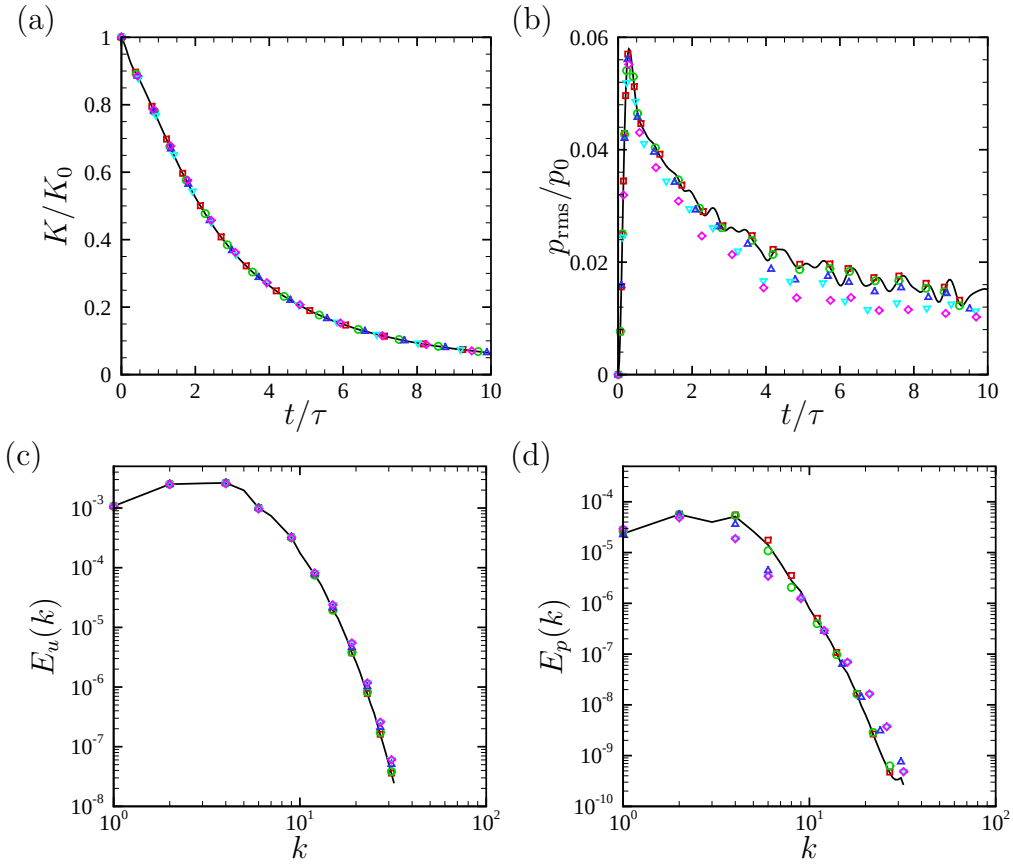

Figure 2.10: Numerical simulations of homogeneous isotropic turbulence at $M_t = 0.3$, $k_0 = 4$, $Re_\lambda = 30$, with ATI-XYZ scheme. Time history of turbulence kinetic energy (a), and pressure variance (b), and spectra of velocity (c) and pressure fluctuations (d) at $t/\tau = 5$. Solid lines denoted reference results obtained with explicit time discretization at CFL = 1. Symbols denote results obtained with ATI scheme at CFL = 1 (squares), CFL = 2 (circles), CFL = 3 (triangles), CFL = 4 (down-triangles), CFL = 5 (diamonds).

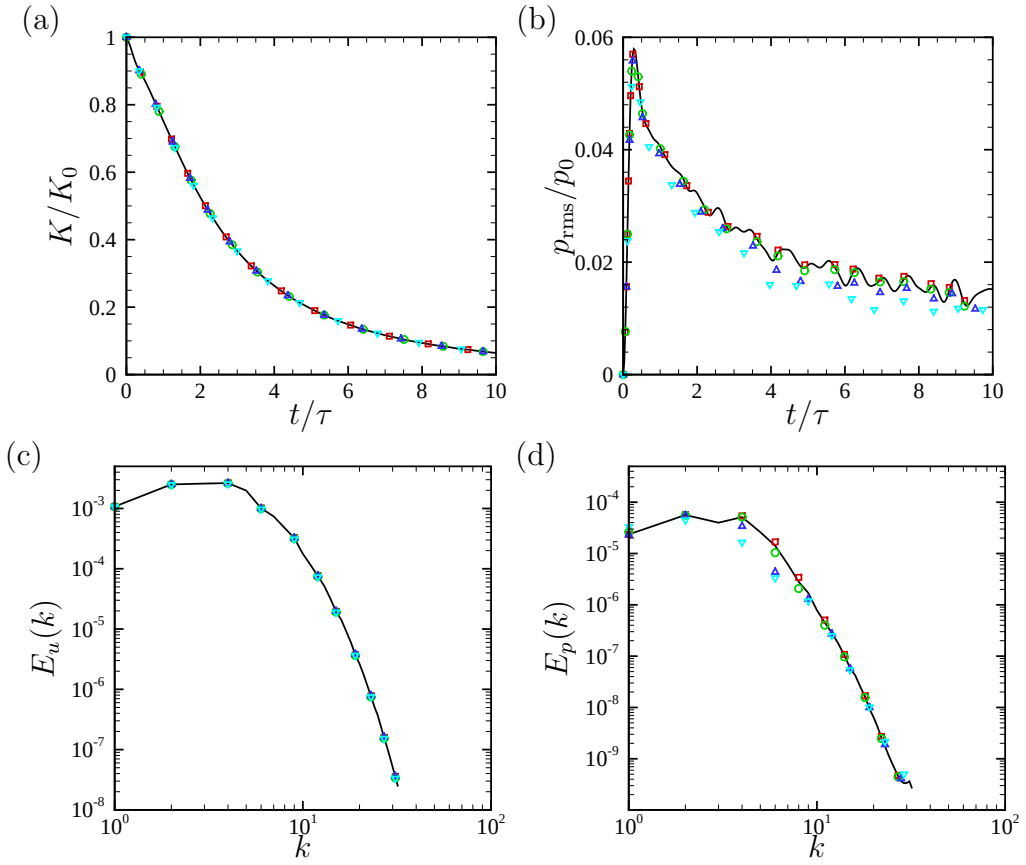

Figure 2.11: Numerical simulations of homogeneous isotropic turbulence at $M_t = 0.3$, $k_0 = 4$, $Re_\lambda = 30$, with BW-XYZ scheme. Time history of turbulence kinetic energy (a), and pressure variance (b), and spectra of velocity (c) and pressure fluctuations (d) at $t/\tau = 5$. Solid lines denoted reference results obtained with explicit time discretization at CFL = 1. Symbols denote results obtained with BW scheme at CFL = 1 (squares), CFL = 2 (circles), CFL = 3 (triangles), CFL = 4 (down-triangles),

This is even clearer in the velocity and pressure spectra, shown in panels (c) and (d), respectively. While velocity spectra are perfectly captured at all Courant numbers, pressure spectra undergo numerical damping, especially at intermediate wavenumbers, which is easily understood based on the amplification factors shown in Fig. 2.2. Given the similar performance of the two implicit methods for this test case, ATI is certainly preferable owing to its lower computational cost, which allows to achieve an effective speed-up over the explicit case (see Tab. 2.1) of about a factor of three, whereas BW yields almost the same efficiency.

2.3.2 Turbulent flow in planar channel

Channel flow is the simplest prototype of wall-bounded flows, and it has been studied by many authors in the incompressible [11, 71, 78], as well as in the compressible regime [28, 77, 91]. The controlling parameters are the bulk Mach number $M_b = u_b/c_w = 1.5$ (where u_b is the average velocity across the channel thickness, and c_w the sound speed at the wall temperature), and the bulk Reynolds number $Re_b = 2\rho_b u_b h/\mu_w = 6000$ (where ρ_b is the bulk density, μ_w the dynamic viscosity at the wall, and h the channel half height). Initial and boundary conditions used in all the simulations are described in Sections 2.1.3-2.1.4.

Case	M_b	M_0	Re_b	Re_τ	Δy_w^+	Δx^+	Δz^+	Δt_x^+	Δt_y^+	Δt_z^+	Δt_{yv}^+	Δt^+	CPU
CH01-EXPL	0.1	0.1	5790	180	0.60	8.80	3.90	0.053	0.0077	0.026	1.3	0.0077	1
CH01-ATI-XYZ	0.1	0.1	5790	180	0.60	8.80	3.90	0.053	0.0077	0.026	1.3	0.077	0.15
CH01-BW-XYZ	0.1	0.1	5790	180	0.60	8.80	3.90	0.053	0.0077	0.026	1.3	0.077	0.82
CH15a-EXPL	1.5	1.28	6000	220	0.70	10.8	4.80	0.32	0.11	0.27	1.2	0.099	1
CH15a-ATI-Y	1.5	1.28	6000	220	0.70	10.8	4.80	0.32	0.11	0.27	1.2	0.24	0.48
CH15a-BW-Y	1.5	1.28	6000	220	0.70	10.8	4.80	0.32	0.11	0.27	1.2	0.24	0.70
CH15b-EXPL	1.5	1.28	6000	220	0.15	10.8	4.08	0.32	0.11	0.27	0.062	0.021	1
CH15b-AVTI-Y	1.5	1.28	6000	220	0.15	10.8	4.80	0.32	0.11	0.27	0.062	0.21	0.13
CH15b-BWV-Y	1.5	1.28	6000	220	0.15	10.8	4.80	0.32	0.11	0.27	0.062	0.21	0.19

Table 2.2: Flow parameters for DNS of plane channel flow (CH). M_b and Re_b are the bulk Reynolds and Mach number, respectively. $M_0 = M_b\sqrt{T_w/T_b}$ is the reference Mach number, introduced when discussing Eqn. (1.1). The computational box dimension is $4\pi h \times 2h \times 4/3\pi$ for all flow cases. Δy_w^+ is the distance of the first grid point from the wall, and Δx^+, Δz^+ are the streamwise and spanwise grid spacings. The Δt_i^+ are the allowable time steps in the coordinate directions, estimated according to Eqns. (1.1),(1.3). Δt^+ is the time step actually used in the simulations. CPU is the cost to cover a unit time interval, compared to the standard fully explicit algorithm (EXPL).

The main flow parameters are listed in Tab. 2.2. Three flow cases have been considered, one at $M_b = 0.1$ (denoted as CH01), and two at $M_b = 1.5$ (denoted as CH15a-b), the latter two only differing in the distance of the first grid point from the wall. Reference DNS have been carried out with fully explicit time discretization, at CFL ≈ 1, which are used as a basis of comparison for the ATI and BW algorithms. In order to understand the effectiveness of the (semi-)implicit algorithms, in Tab. 2.2 we report the time step restrictions associated with the three coordinate directions, as estimated from Eqns. (1.1), (1.3), as well as the actual time step used in the DNS, all in wall units. As expected, in all flow cases the time step limitation in the wall-normal direction is the most restrictive. Although larger time steps are allowed on grounds of sole numerical stability, all DNS have been carried out at the maximum

time step for which accurate results are obtained, which corresponds to $CLF \approx 1$ for the fully explicit simulations. For ease of reference, the maximum time steps associated with accuracy and stability restrictions are also reported in Fig. 1.1(a) with circle and square symbols, respectively. As a first test, we consider flow at low subsonic Mach number (CH01), for which the explicit time advancement step is very small, hence we apply implicit treatment is all coordinate directions (XYZ). We find that, although the wall-normal time step restrictions can be removed, the allowed time step for accurate calculations cannot substantially larger than for the streamwise convective restriction (see Fig. 1.1(a)). This is probably due to inherent mesh anisotropy in DNS of wall-bounded flows. In fact, mesh spacing is over-resolved in the wall-normal direction, hence the relevant values of the reduced wavenumber kh are small, which allows to operate at high values of CFL with little error, recalling (see Fig. 2.2) that the dissipation error grows with both kh and CFL. On the other hand, the typical wall-parallel mesh spacings used in DNS are barely sufficient to resolve the smallest scales of turbulence, hence the typical reduced wavenumbers are higher, and time accuracy is a factor in that case. We find that both ATI and BW are capable of boosting the time step by about a factor of ten, with efficiency gain of 85% for ATI, and results almost indistinguishable from the fully explicit case (see below). Still, the time step is far from that allowed by incompressible solvers (again, see Fig. 1.1(a)). This issue will be further recalled in the concluding discussion. To show effectiveness in removing the wall-normal acoustic time limitation is supersonic flow calculations, in flow case CH15a the first grid point is placed sufficiently far from the wall that the viscous limitation is ineffective. Hence, the implicit algorithms are applied only in the wall-normal direction (Y), and viscous terms are handled explicitly. The ATI and BW algorithms are both found to effectively suppress the wall-normal acoustic time step limitation, and achieve the same maximum time step for accurate flow resolution, corresponding to about CFL = 2.4. Hence, accounting for the cost figures given in table 2.1, we find a speed-up of about a factor of two for the ATI algorithm, and 30% gain with BW. o prove effectiveness of the implicit treatment of the viscous terms proposed in Section (2.1.2), in flow case CH15b the first grid point is placed closer to the wall, in such a way that the viscous time limitation also becomes relevant, after the acoustic one. Both wall-normal time step restrictions are suppressed through use of the AVTI and BWV algorithms, hence the achieved time step is similar to flow case CH15a. Both algorithms here achieve CFL $\approx$ 10, at a cost which is a small fraction of the fully explicit algorithm. For the sake of comparison, in Figs. 2.12-2.14 we show the main statistics for the flow cases

listed in Tab. 2.2. As anticipated, excellent agreement is observed between implicit algorithms and the reference explicit solution, including pressure and temperature fluctuations, which is especially satisfactory.

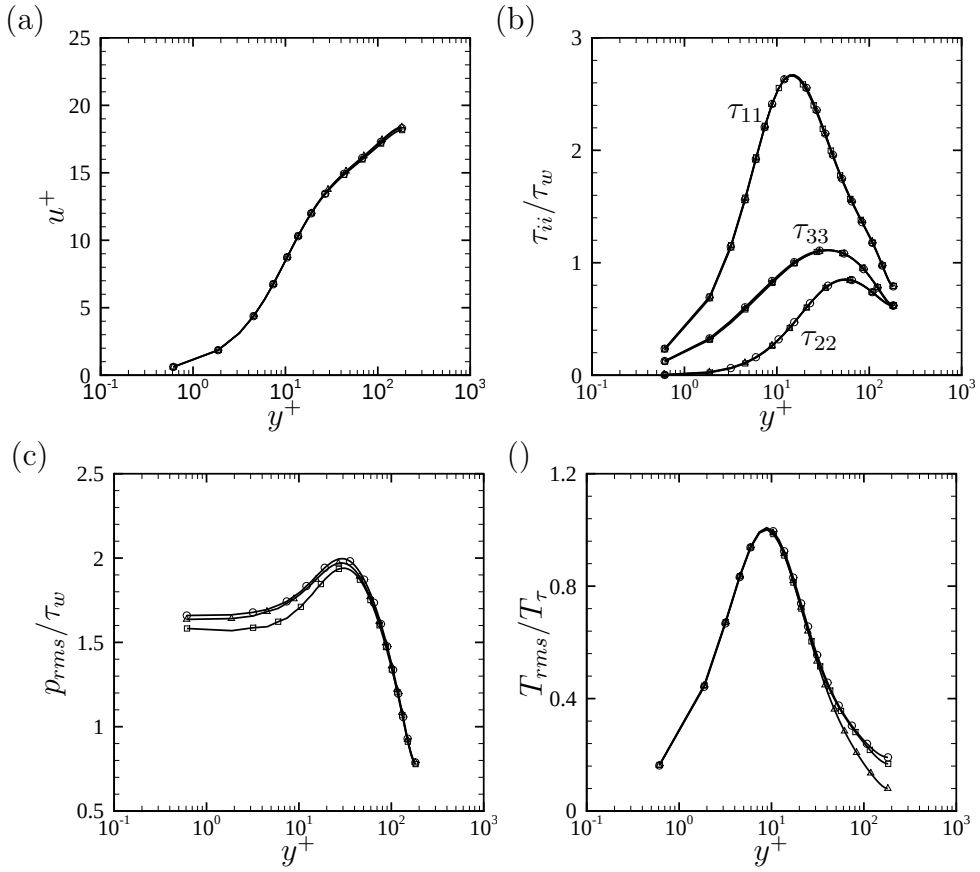

Figure 2.12: Flow statistics for DNS of flow case CH01 (see Tab. 2.2): mean velocity (a), Reynolds stresses (b), r.m.s. pressure (c) and r.m.s. temperature (d), for CH01-EXPL (squares), CH01-ATI-XYZ (circles), CH01-BW-XYZ (triangles). $T_\tau = q_w/(\rho_w c_p u_\tau)$ is the friction temperature.

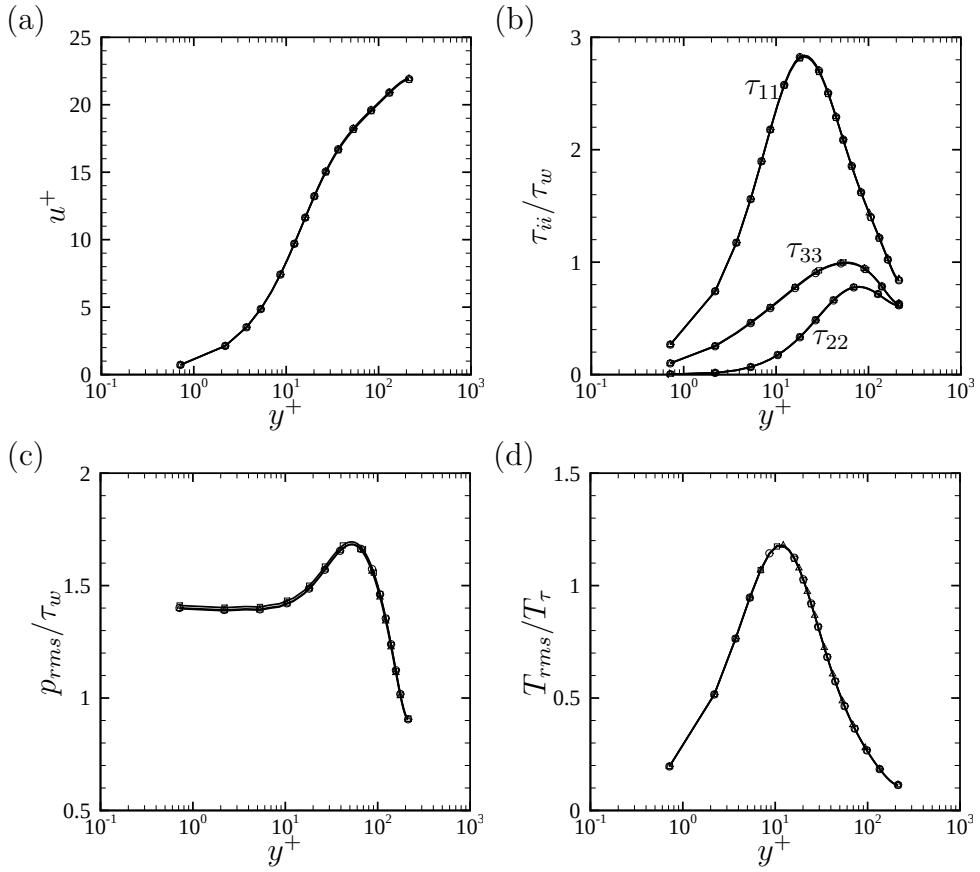

Figure 2.13: Flow statistics for DNS of flow case CH15a (see Tab. 2.2): mean velocity (a), Reynolds stresses (b), r.m.s. pressure (c) and r.m.s. temperature (d), for CH15a-EXPL (squares), CH15a-ATI-Y (circles), CH15a-BW-Y (triangles).

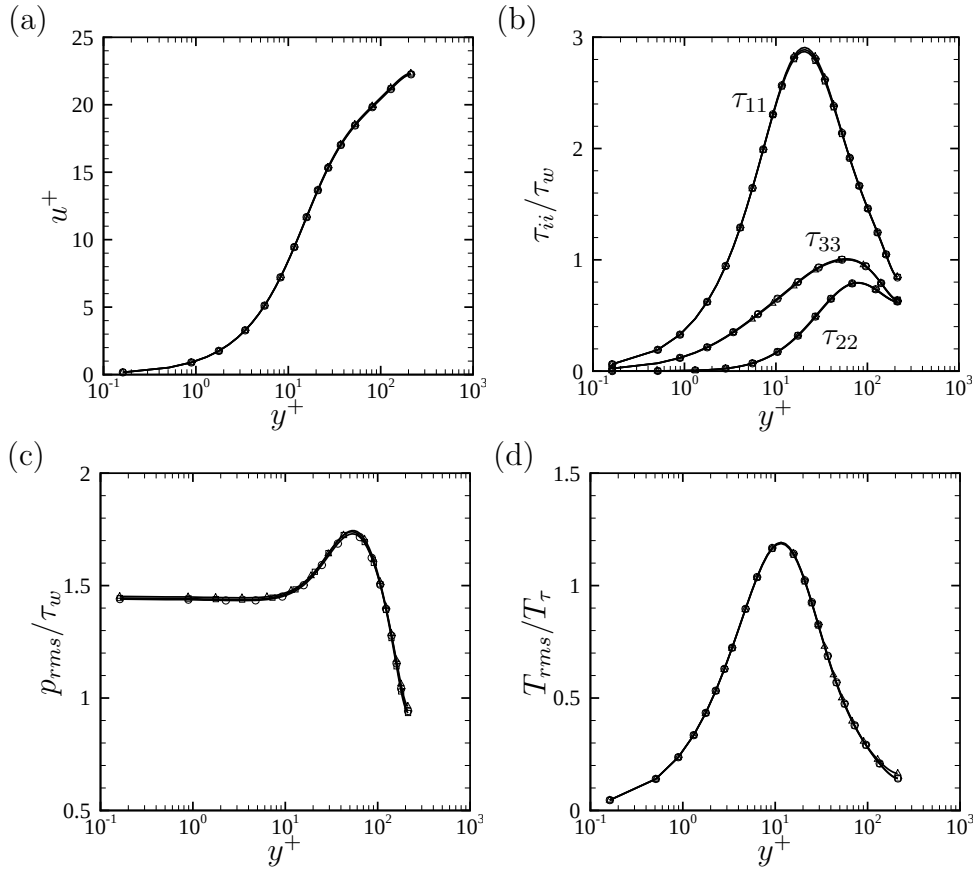

Figure 2.14: Flow statistics for DNS of flow case CH15b (see Tab. 2.2): mean velocity (a), Reynolds stresses (b), r.m.s. pressure (c) and r.m.s. temperature (d), for CH15b-EXPL (squares), CH15b-AVTI-Y (circles), CH15b-BWV-Y (triangles).

2.3.3 Turbulent flow in square duct

As a further step in complexity we consider the flow inside a straight duct with square cross-section. This flow has been the subject of several DNS studies in the incompressible regime [50, 63, 110], all limited to low Reynolds number. One of the main difficulties that arise when dealing with square duct flows is the long averaging time necessary to attain convergence of even the basic mean flow statistics, caused by the extremely long typical time scales of secondary corner eddies. In fact, Pinelli et al. [110] reported that an averaging time of about $8000h/u_b$ was needed to have symmetric statistics in the four quadrants of the cross section. Hence, it is clear that efficient numerical methods are needed to study turbulent compressible flow in ducts.

Case	M_b	M_0	Re_b	Re_τ	Δy_w^+	Δx^+	Δz^+	Δt_x^+	Δt_y^+	Δt_z^+	Δt_{yv}^+	Δt^+	CPU
DU02-EXPL	0.2	0.2	4410	150	0.66	8.40	0.66-3.20	0.094	0.019	0.019	1.69	0.018	1
DU02-ATI-XYZ	0.2	0.2	4410	150	0.66	8.40	0.66-3.20	0.094	0.019	0.019	1.69	0.18	0.15

Table 2.3: DNS dataset for square duct (DU) flow. M_b and Re_b are the bulk Reynolds and Mach number, respectively. $M_0 = M_b\sqrt{T_w/T_b}$ is the reference Mach number, introduced when discussing Eqn. (1.1). The computational box dimension is $8\pi h \times 2h \times 2h$. Δy_w^+ is the distance of the first grid point from the wall, and Δx^+,Δz^+ are the streamwise and spanwise grid spacings. The Δt_i^+ are the allowable time steps in the coordinate directions, estimated according to Eqns. (1.1),(1.3). Δt^+ is the time step actually used in the simulations. CPU is the cost to cover a unit time interval, compared to the standard fully explicit algorithm (EXPL).

Numerical simulations have been here carried out (see Tab. 2.3 for the main flow parameters) at the same Reynolds number as Pinelli et al. [110], and sufficiently low Mach number ($M_b = 0.2$) that direct comparison with incompressible data is possible. The duct length $L_x = 8h$ (where $2h$ is the length of each side of the duct), and the time window for collecting the flow statistics is the same used by Pinelli et al. [110]. As in plane channel flow, a spatially uniform forcing is applied to the momentum equation to maintain a time constant mass flow rate. Note that, unlike in channel flow, the mesh is also non-uniformly spaced in the z direction, hence a range of mesh spacings is reported in Tab. 2.3. A reference fully explicit numerical simulation has been carried out and used as a basis of reference for the ATI algorithm, here applied to all coordinate directions. As seen in Tab. 2.3, the corresponding CFL number is about unity. As in the case of plane channel, DNS were carried out at increasing values of CFL, until deviations from the reference data were found, to determine the maximum allowed time step for accuracy. It appears that accurate results of the semi-implicit algorithm are recovered up to CFL $\approx$ 10. Again, implicit treatment of the x direction is not capable of fully suppressing the corresponding time step limitation, owing to the emergence of accuracy issues. Similar to channel flow, use of the ATI algorithm allows for about 85% cost reduction. Figure 2.15 confirms that excellent matching of the flow statistics is found among DU02-ATI, DU02-EXPL and the data of Pinelli et al. [110], except for some differences in the wall-normal Reynolds stress and the pressure r.m.s., which may be due to the greater importance of acoustic waves in the presence of a fully confined flow geometry.

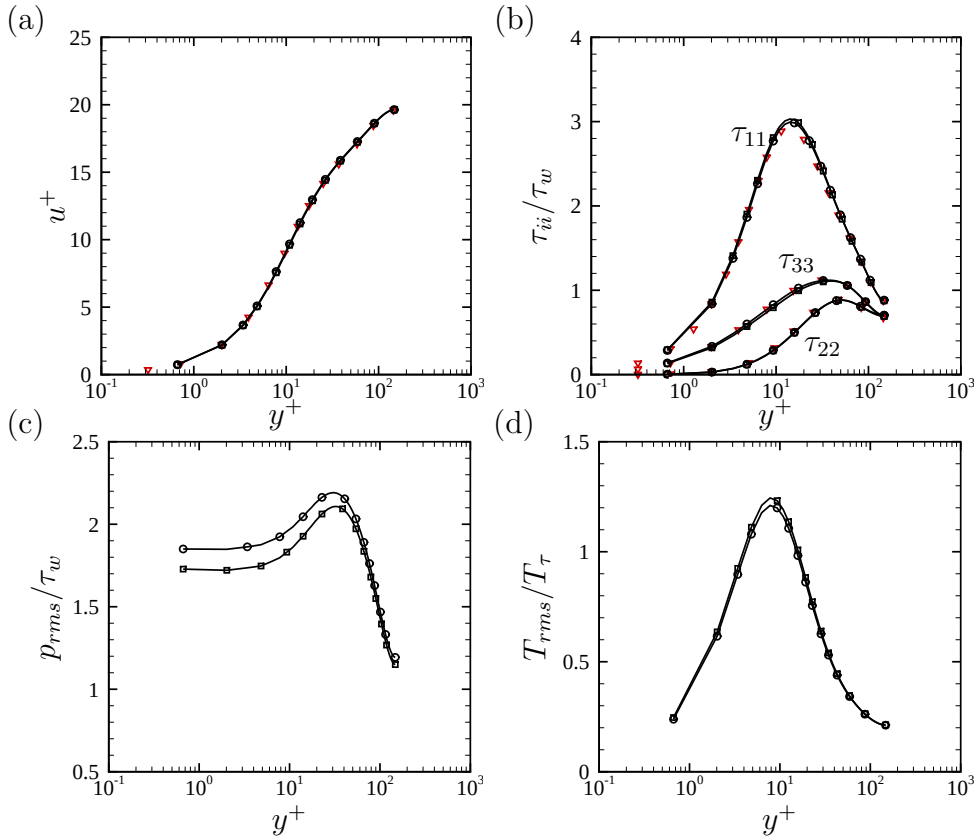

Figure 2.15: DNS of flow in square duct (see Tab. 2.3): mean velocity (a), Reynolds stresses (b), r.m.s. pressure (c) and r.m.s. temperature (d), for DU02-EXPL (squares), DU02-ATI-XYZ (circles). Triangle symbols denote reference incompressible DNS data [110].

2.4 Validation of the cylindrical solver

In order to test the kinetic energy conservation properties of the cylindrical solver we repeat the test case proposed by Morinishi et al. [96], considering the inviscid flow through an concentric annular pipe (see Fig. 2.4) and through a standard pipe.

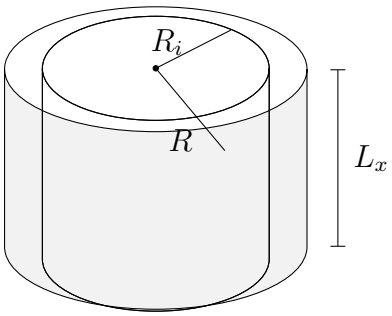

The size is $N_x \times N_y \times N_z = 16 \times 16 \times 32$ and the box dimensions are $L_x \times L_y \times L_z =$

$6\pi R \times R \times 2\pi R$. The mesh is uniform in the streamwise and azimuthal direction, with hyperbolic tangent stretching in the radial direction. In the case of the concentric annular pipe the inner radius is $R_i = 0.5R$. Inviscid wall boundary condition is imposed at the walls. The flow is initialized as in Section 2.1.4 and the bulk Mach number is $M_b = 0.1$. Figure 2.16 shows that turbulent kinetic energy for the explicit time integration with different order of spatial accuracy and for ATI-YZ with second order of accuracy. Kinetic energy is conserved both for the concentric annular pipe flow, Fig. 2.16a and the standard pipe flow configuration, Fig. 2.16b. We also note that despite the fact kinetic energy conservation cannot be proved in the case of implicit time integration, very good conservation properties are observed even at high CFL number. This extremely low damping observed also at high wavenumbers can be explained by the fact that the mesh is always over-resolved in the azimuthal direction, so that the reduced wavenumber kh is small and the amplification factor of the scheme is close to unity (recall Fig. 2.2).

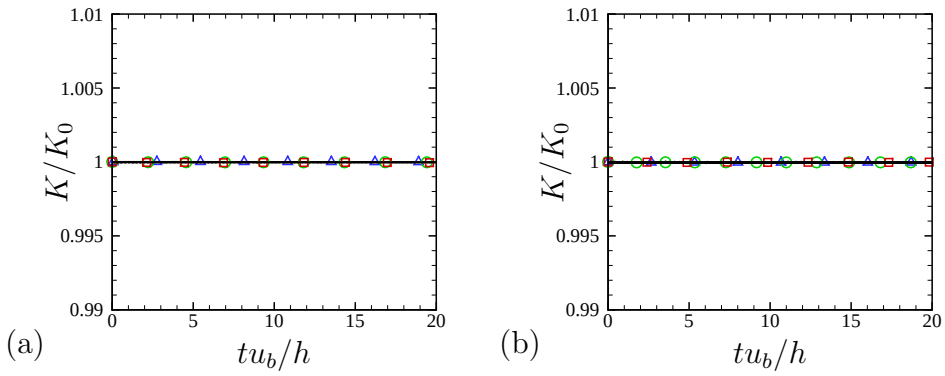

Figure 2.16: Normalized turbulent kinetic energy for inviscid annular pipe (a) and pipe (b). For the annular pipe the internal radius $R_i = 0.5R$. Explicit time integration with second order spatial discretization (black solid) is compared to fourth order (red squares) and sixth order (green circles). Implicit time discretization ATI-YZ (blue triangles) is also shown at CFL = 25 for the annular case and CFL = 450 for the pipe.

In order to validate the pole treatment introduced in Section 2.2.3 we use the Lamb dipole test case proposed by Verzicco and Orlandi [151]. We consider a dipole of radius r_v confined in a free-slip cylinder with radius $R = 2.5r_v$. The field is initialized

as follows,

$$
\begin{aligned}
&\frac{\rho(r,\theta)}{\rho_{ref}} = 1 \\
&\frac{u_\theta(r,\theta)}{u_v} = \begin{cases} \left[-C\left(J_0\left(\beta\hat{r}\right) - \frac{J_1(\beta\hat{r})}{\beta\hat{r}}\right)\right]\sin\theta & \hat{r} \leq 1, \\ -\frac{sin\theta}{\hat{r}^2} & \hat{r} > 1 \end{cases} \\
&\frac{u_r(r,\theta)}{u_v} = \begin{cases} \left(C\,\frac{J_1(\beta\hat{r})}{\beta\hat{r}}\right)\cos\theta & \hat{r} \leq 1, \\ -\frac{cos\theta}{\hat{r}^2} & \hat{r} > 1 \end{cases} \\
&\frac{p(r,\theta)}{p_{ref}} = \begin{cases} 1 + \frac{\gamma\,{M_v}^2}{2}\left\{1 - C^2\left[\frac{{J_1}^2(\beta\hat{r})}{(\beta\hat{r})^2} + \left({J_0}^2(\beta\hat{r}) + {J_1}^2(\beta\hat{r}) - 2, \frac{J_0(\beta\hat{r})J_1(\beta\hat{r})}{\beta\hat{r}}\right)\sin^2\theta\right]\right\} & \hat{r} \leq 1, \\ 1 - \frac{\gamma{M_v}^2}{2\hat{r}^2}\left(\frac{1}{\hat{r}^2} - 2\,cos(2\theta)\right) & \hat{r} > 1, \end{cases}
\end{aligned}
\tag{2.56}
$$

where J_0 and J_1 are Bessel functions of the first kind, β is the first positive zero of J_1 ($\beta \approx 3.8317$), $C = 2/J_0(\beta)$ and u_v is the maximum tangential velocity of the vortex. The vortex Mach number is defined as $M_v = u_v/c_{ref} = 0.1$. We consider two different initial positions of the dipole, the first one $x_0 = -r_v$, $y_0 = 0$ and $x_0 = -0.5\,r_v$, $y_0 = 0.5\,r_v$. The mesh and the Reynolds number are the same used by Verzicco and Orlandi [151], $N_y \times N_\theta = 96 \times 128$ and $Re_v = 2\,r_v u_v/\nu = 1000$. Figures 2.17-2.18 show the comparison between the second order discretization with implicit treatment of acoustic and viscous terms in the azimuthal direction AVTI-Z and the results of Verzicco and Orlandi [151] (panels a-b-c). The present treatment shows similar performances to the incompressible staggered flow solver, both for the asymmetric and symmetric case, Figs. 2.17 and 2.18, respectively. In the present case we continue the simulation after time $t^* = tu_v/r_v = 2$, when the vortex impact the wall, splits, and after half a revolution merges again. This cycle ends up with the vortex dissipation due to viscosity, after several passages over the axis.

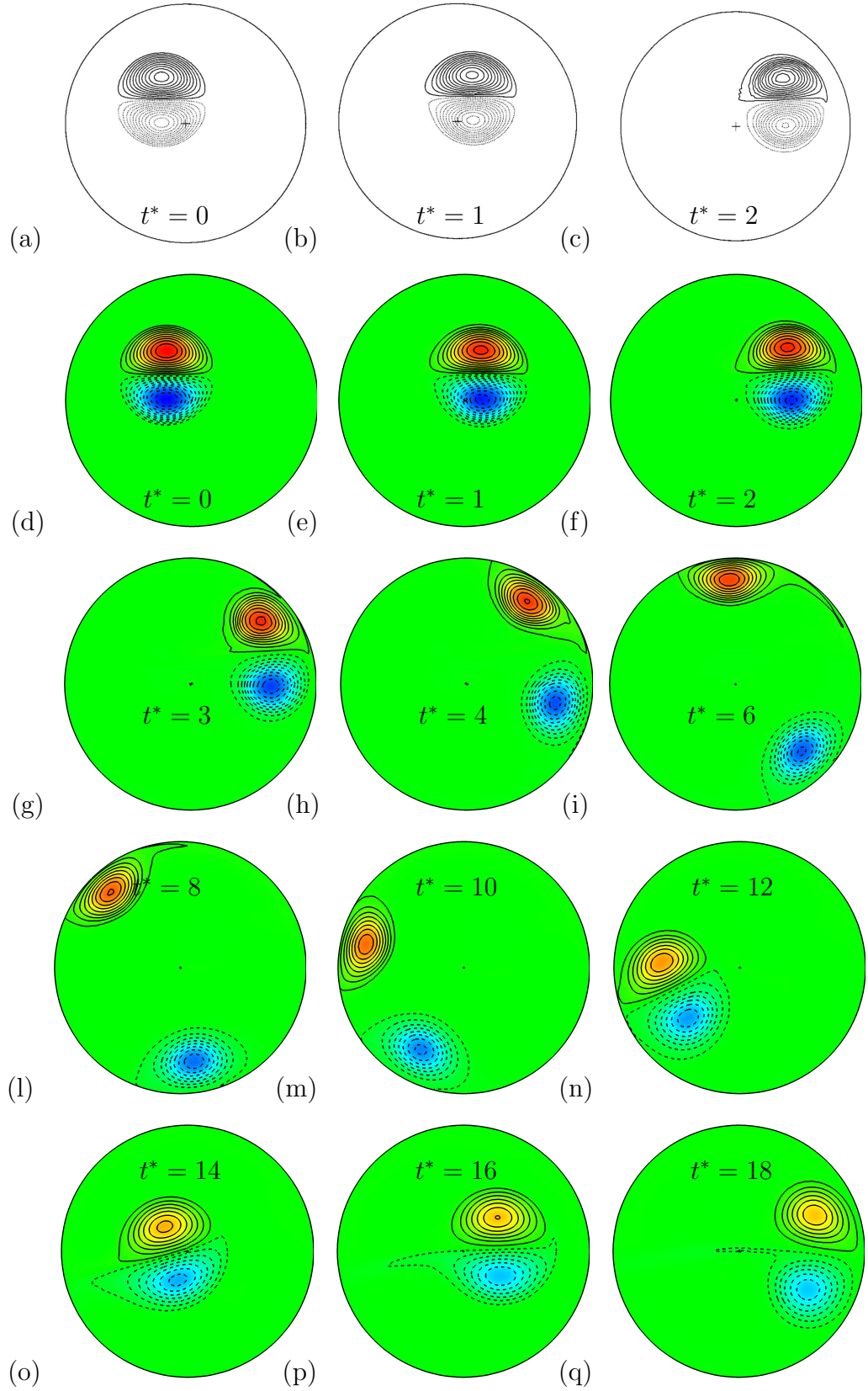

Figure 2.17: Vorticity field of Lamb dipole at vortex Mach number $M_v = 0.1$ and vortex Reynolds number $Re_v = 2r_v u_v/\nu = 1000$. Initial position of the vortex $x_0 = -r_v$ $y_0 = 0$, domain radius $R = 2.5\, r_v$ and mesh size $N_y \times N_z = 96 \times 128$. 22 vorticity contour levels between -1 and 1. Results are compared to Verzicco and Orlandi [151] (a)-(b)-(c).

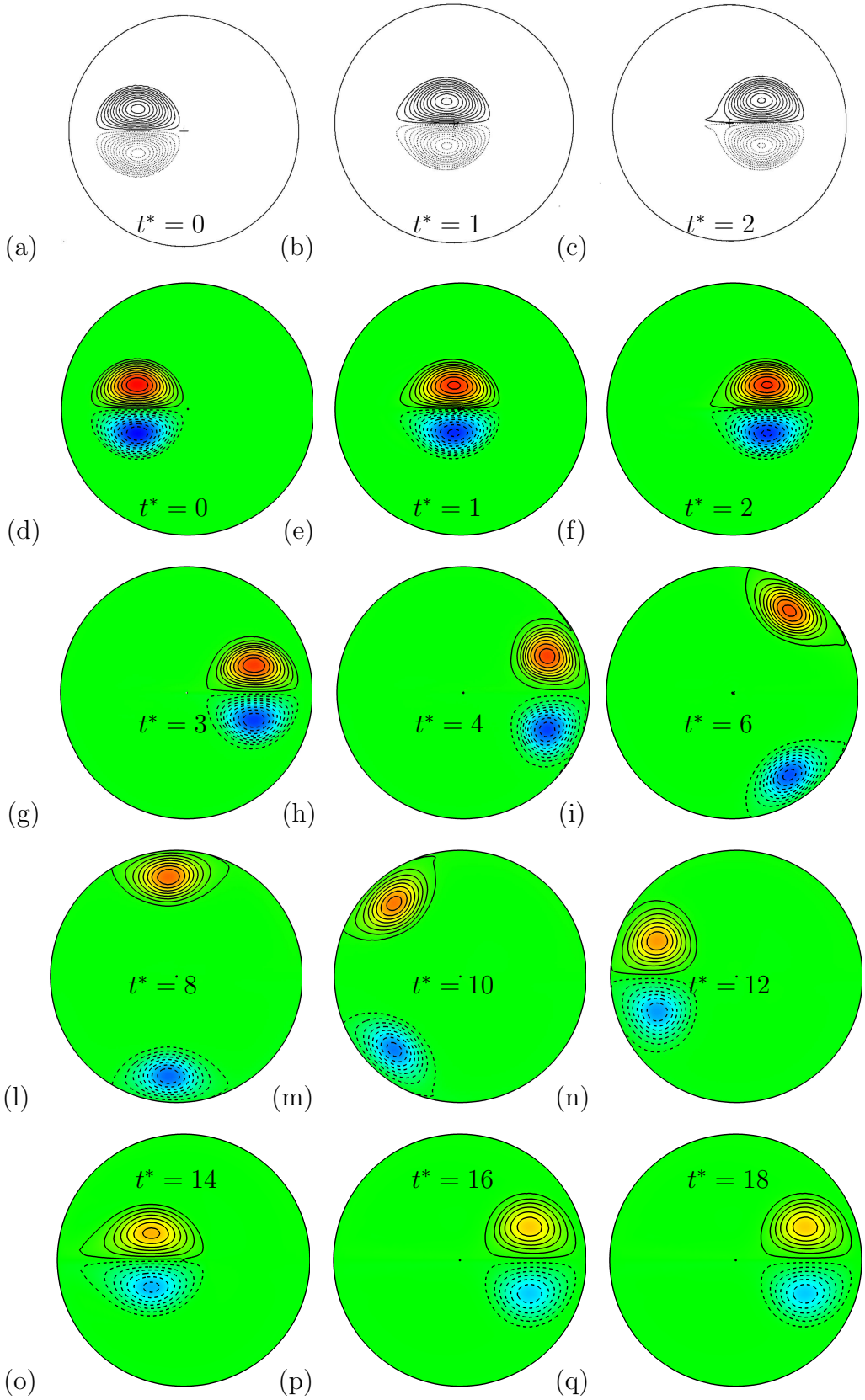

Figure 2.18: Vorticity field of Lamb dipole at vortex Mach number $M_v = 0.1$ and vortex Reynolds number $Re_v = 2\,r_v u_v/\nu = 1000$. Initial position of the vortex $x_0 = -r_v$ $y_0 = 0$, domain radius $R = 2.5\,r_v$ and mesh size $N_y \times N_z = 96 \times 128$. 22 vorticity contour levels between -1 and 1. Results are compared to Verzicco and Orlandi [151] (a)-(b)-(c).

Figures. 2.17-2.18 show that the accuracy of the axis treatment is similar to the one by Verzicco and Orlandi [151] and overall satisfactory. The numerical solver in cylindrical coordinates is validated in the case of laminar compressible pipe flow. Figure 2.19 shows the further result compared to the *e*xact solution, obtained by solving the equations for a laminar compressible pipe flow, as are reported in the Appendix 5.4. Figure 2.19 shows that the cylindrical solver is capable of reproducing the laminar compressible solution. . .

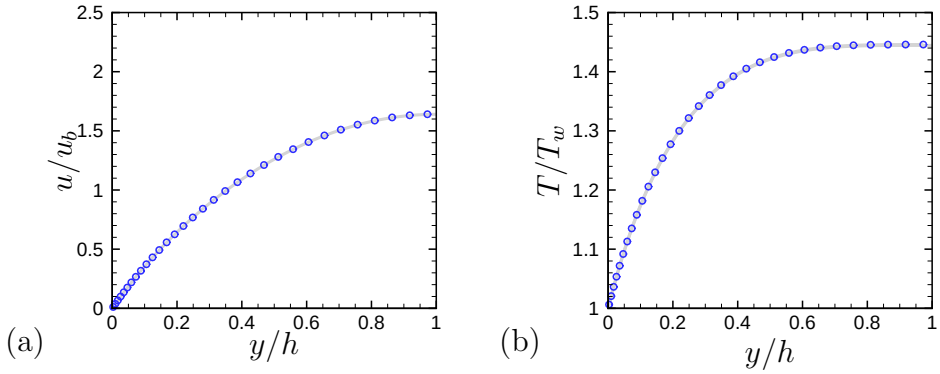

Figure 2.19: Supersonic laminar pipe flow at $M_b = u_b/c_w = 1.5$, where u_b is the bulk velocity and c_w the speed of sound at the wall. The solution obtained with the present solver (blue circles) is compared to the exact one (gray solid lines). Velocity and temperature profiles are show in panels (a)-(b), respectively.

Chapter 3

Results

In this chapter we report results of DNS of planar channel, pipe and duct flow, in Section 3.1-3.2 and 3.3 respectively. In the following chapter mean quantities are averaged according to Favre ($\phi = \widetilde{\phi} + \phi''$, $\widetilde{\phi} = \overline{\rho\phi}/\overline{\rho}$) where ϕ is a generic quantity. The superscript + denotes variables normalized in inner units, $u^+ = \widetilde{u}/u_\tau$ $y^+ = y/\delta_v$, where $u_\tau = \sqrt{\frac{\tau_w}{\rho_w}}$ and $\delta_v = \nu_w/u_\tau$ are the friction velocity and the viscous length scale respectively, while $\tau_w = \mu_w \frac{\mathrm{d}\widetilde{u}}{\mathrm{d}y}$ and ρ_w are the viscous stress and density at the wall. The Reynolds stress tensor components are $\tau_{ij} = \overline{\rho}\widetilde{u_i'' u_j''}$.

3.1 Compressible flow in planar channel

In this Section we present DNS of compressible channel flow. All supersonic simulations are performed using ATI-Y algorithm, while ATI-XYZ algorithm is used for the subsonic case, denoted as CH01. Details on the computational arrangement of the DNS are given in Tab. 3.1. For the sake of comparison, a set of incompressible channel DNS have been carried out so as to accurately reproduce the relevant friction Reynolds number for fair comparison of incompressible and compressible flow statistics (see the later discussion), whose details are reported in Tab. 3.2. The numerical algorithm used for the incompressible DNS is the same as in previous studies from our group [11].

Case	Re_b	M_b	Re_τ	$Re_{\tau H}$	$Re_{\tau B}$	N_x	N_y	N_z	Δx^+	Δz^+	M_τ	$-B_q$
CH01	5790	0.1	180	180	180	384	128	192	8.8	5.9	0.0063	9.7e-6
CH15A	6000	1.5	215	141	169	512	128	256	8.0	5.2	0.079	0.048
CH15B	15334	1.5	500	333	395	1024	256	512	9.2	6.1	0.072	0.042
CH15C	34000	1.5	1015	677	802	2048	512	1024	9.3	6.2	0.065	0.038
CH3	9760	3.	448	142	233	1024	256	512	8.2	5.5	0.11	0.14
CH15M	6000	1.5	218	141	169	120	180	120	23	7.6	0.079	0.048
CH15MF	6000	1.5	215	141	169	256	128	128	10	7.0	0.079	0.048

Table 3.1: Setup of compressible channel DNS. The computational box size is $6\pi h \times 2h \times 2\pi h$ for all flow cases, except case CH15M, which reproduces the DNS of Morinishi et al. [96], and CH15MF with improved spatial resolution, in which the box size is $4\pi h \times 2h \times 4/3\pi h$. N_i and Δx_i^+ are the number of points and the mesh spacing in the i-th coordinate direction, respectively. $M_\tau = u_\tau / c_w$ is the friction Mach number, and $B_q = q_w/(\rho_w C_p u_\tau T_w)$ is the heat flux coefficient. $Re_{\tau I}$ is the equivalent friction Reynolds number for Huangs' transformation (H), and Brun's transformation (B), as defined in Eqn. (3.12).

Case	Re_b	Re_τ	N_x	N_y	N_z	Δx^+	Δz^+
INC1	4272	140	384	128	192	6.9	4.6
INC2	5248	169	384	128	192	8.3	5.5
INC3	5790	180	384	128	192	8.8	5.9
INC4	7082	222	384	128	192	11	7.3
INC5	10074	299	768	192	384	7.3	4.9
INC6	13774	393	1024	256	512	7.2	4.8
INC7	20062	550	1024	256	512	10	6.7
INC8	25534	673	2048	512	1024	6.2	4.1
INC9	30800	796	2048	512	1024	7.3	4.9
INC10	39600	999	2048	384	1024	9.2	6.1

Table 3.2: Setup of incompressible channel DNS. The computational box size is $6\pi h \times 2h \times 2\pi h$ for all flow cases. Flow cases INC7-INC10 are taken from the dataset of Bernardini et al. [11], whereas all other simulations have been performed in the present study.

3.1.1 Instantaneous flow field

In this Section we qualitatively analyze the instantaneous flow field through snapshots of the channel flow in the cross-stream, wall-normal and wall-parallel planes. Figure 3.1 shows the velocity flow field for case CH15C on the three planes, forming a three dimensional view. The wall parallel plane xz, at $y+ = h/\delta_v = 15$ from the wall, clearly highlights the presence of low and high speed streaky structures elongated in the flow direction, similarly to what found in incompressible wall-bounded flows [75].

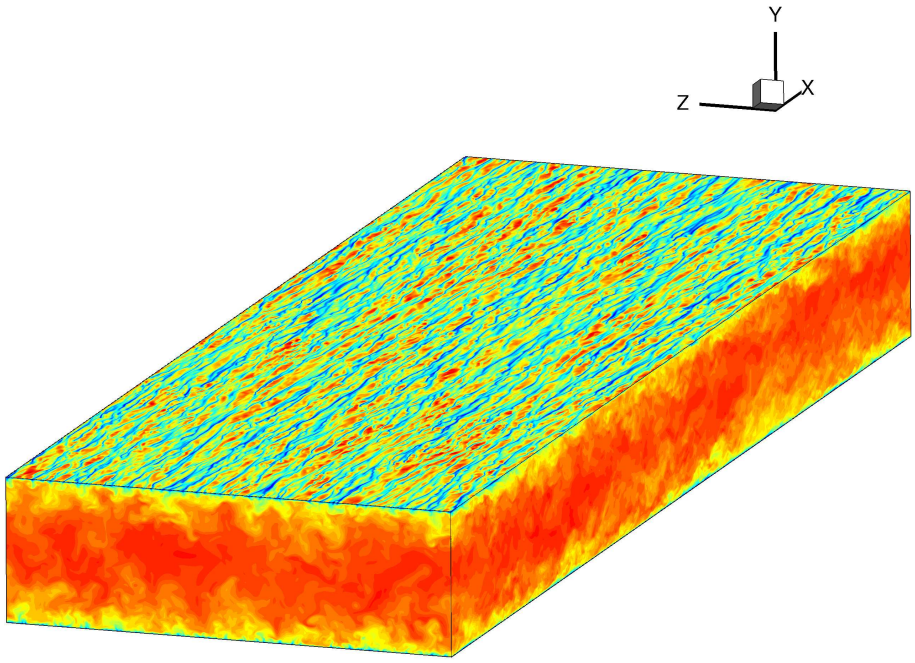

Figure 3.1: Instantaneous flow field of flow case CH15C. Streamwise velocity contours in the streamwise (xy), cross-stream (yz) and wall parallel (at $y^+ = 15$) planes are plotted.

Figure 3.2 shows the streamwise velocity fluctuations in the xz plane for flow cases CH15A,CH15B and CH15C at $y^+ = 15$. It is evident that near wall streaks are highly correlated in the streamwise direction x, while they have a better defined size in the spanwise direction. The spanwise length of the streaks definitely decreases with the Reynolds number, when scaled to the channel half width h, while it remains constant when scaled in wall units, $\lambda_z \approx 100\delta_v$ [75]. Further considering the velocity fluctuations in the wall normal plane allows to form a clearer qualitative picture of the flow field, Fig. 3.3. The streamwise velocity fluctuations field, Fig. 3.3a, shows large eddies spanning from the channel core down to the wall, as required by Townsend eddy attached hypothesis [140]. The wall-normal velocity fluctuations in Fig. 3.3b appear to be correlated to u' on the upper wall and anti-correlated on the lower wall, as found in the incompressible case [11]. On the other hand velocity fluctuations in the spanwise direction do not show a well defined structure.

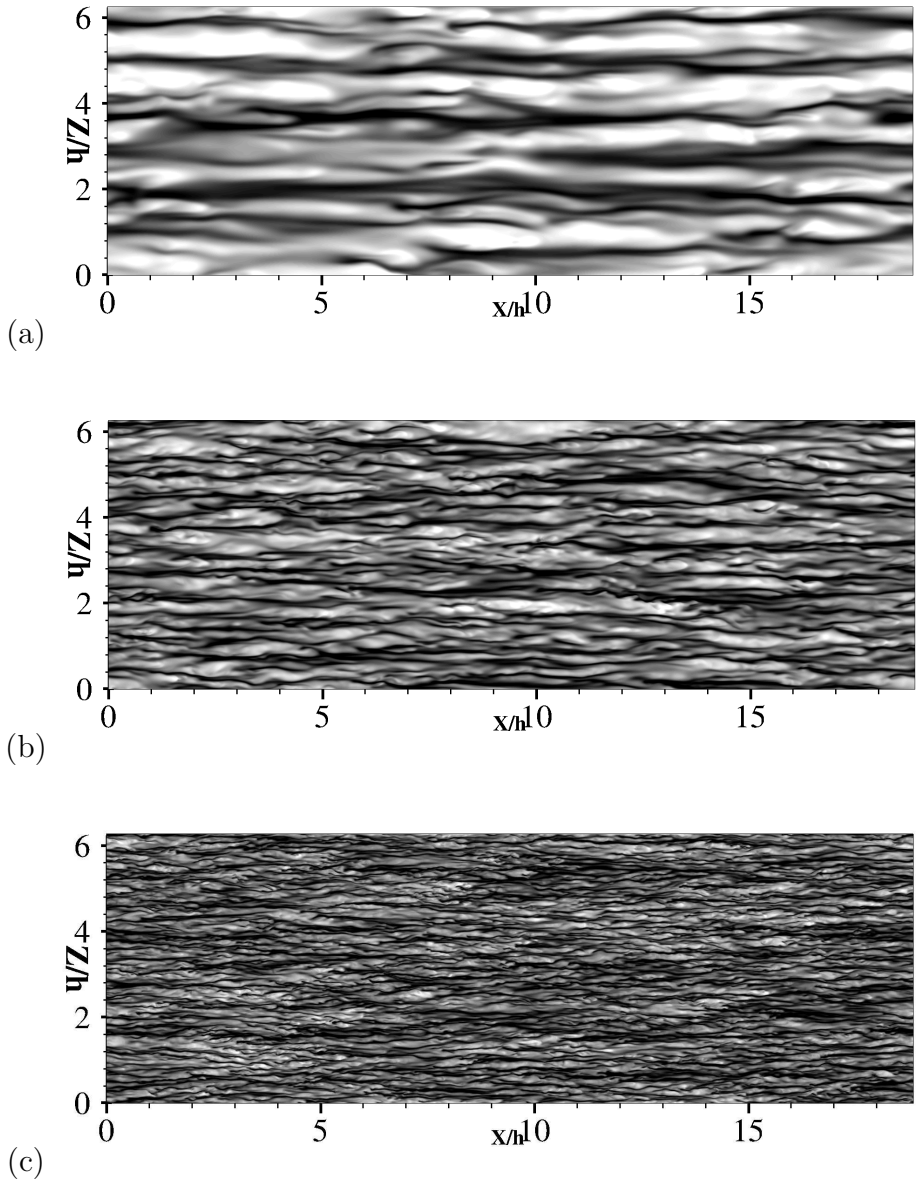

Figure 3.2: Instantaneous flow field of flow case CH15A(a), CH15(b), CH15C(c). Streamwise velocity fluctuations in the xz, wall parallel plane at $y^+ = 15$. Flow from left to right, 48 contour levels $-2 < u'/(\sqrt{\rho/\rho_w}u_{rms}) < 2$, from dark to light shades.

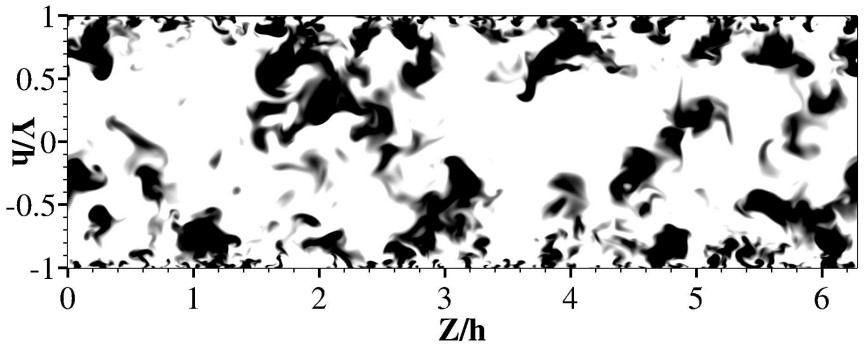

(a)

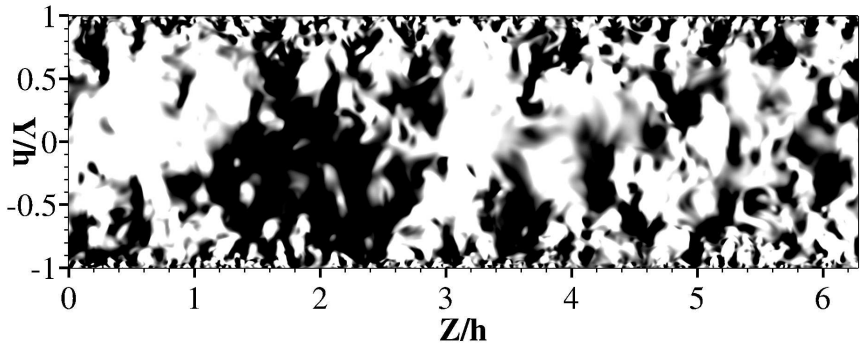

(b)

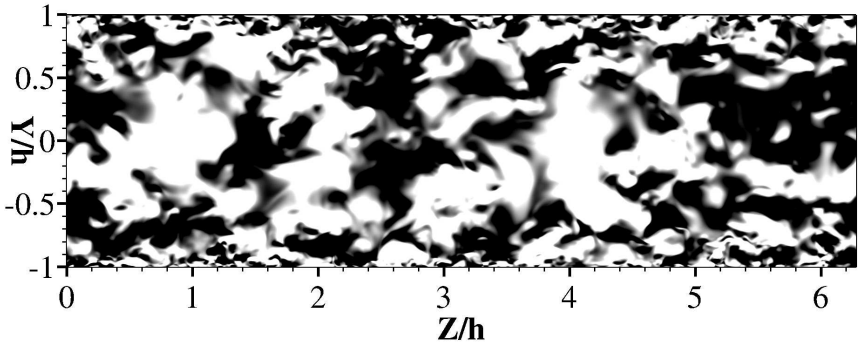

(c)

Figure 3.3: Instantaneous flow field of flow case CH15C velocity fluctuations u'(a) v'(b), and w'(c). Streamwise velocity fluctuations are normalized with their density scaled rms value, 48 contour levels $-0.5 < u_i'/(\sqrt{\rho/\rho_w}u_{irms}) < 0.5$, from dark to light shades.

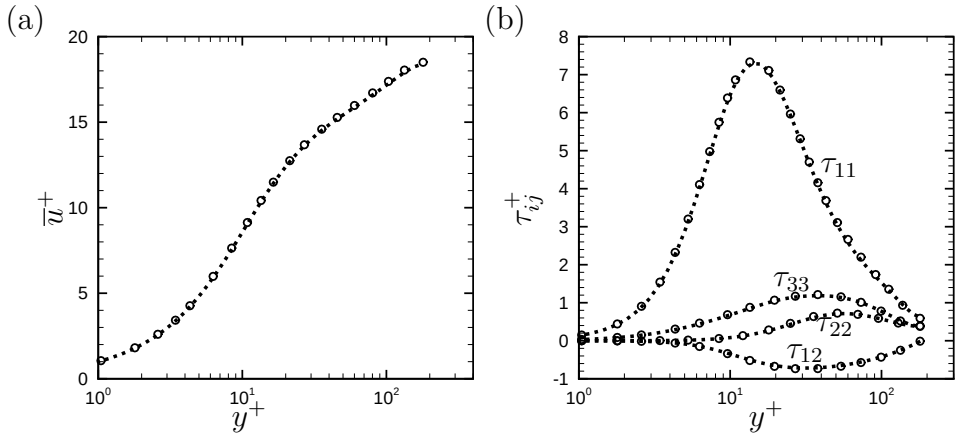

Figure 3.4: Performance in near-incompressible flow conditions: mean velocity profile (a) and Reynolds stresses (b) for flow case CH01 (circles) and INC3 (dots) (see Tabs. 3.1 and 3.2).

3.1.2 Compressibility transformations

The compressible solver is first tested in the nearly incompressible regime ($M_b = 0.1$, corresponding to flow case CH01 of Tab. 3.1), and compared with strictly incompressible data (flow case INC3 of Tab. 3.2) in Figure 3.4. Excellent agreement of the mean velocity and Reynolds stress distributions is recovered. The performance in the supersonic regime is tested by comparing our DNS data with reference data of Morinishi et al. [96], at $M_b = 1.5$, $Re_b = 6000$. Three DNS are presented in Fig. 3.5, one using the same set-up as all other DNS in terms of box size and resolution (CH15A), one in which the same box size and mesh resolution as Morinishi et al. [96] is used (labeled as CH15M), and one with same box size as Morinishi et al. [96], but improved resolution (labeled as CH15MF). Overall, very similar results are obtained for the various flow statistics, except for the peak of the streamwise Reynolds stress, which is known to be quite sensitive to mesh resolution. It appears that when using the same mesh resolution we very nearly match the results of Morinishi et al. [96]. However, refining the mesh has some impact on the streamwise Reynolds stress peak, which is underestimated by about 5% in the coarser computations. On the other hand, the effect of enlarging the computational box seems to be marginal at this modest Reynolds number.

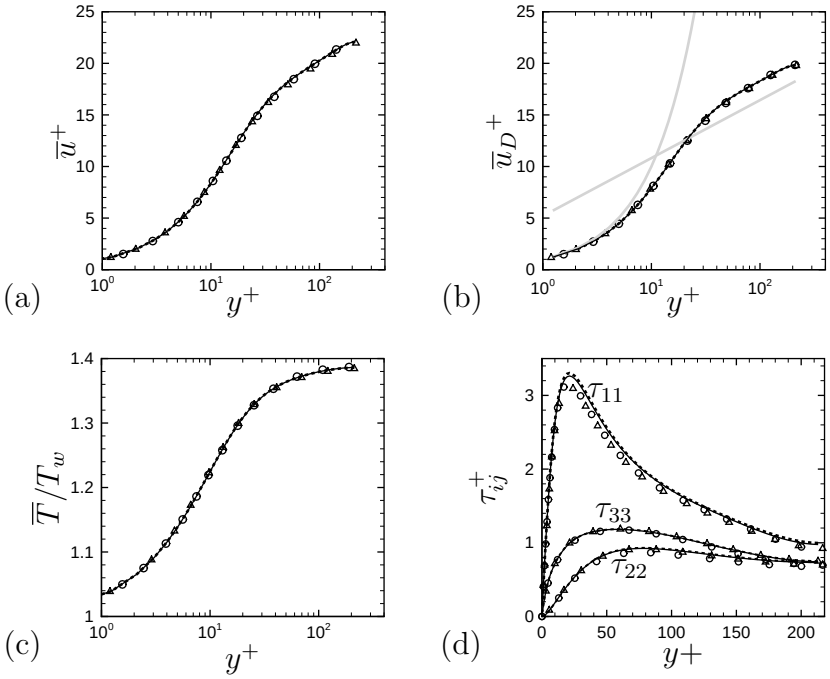

Figure 3.5: Comparison with DNS data of Morinishi et al. [96] (circles): mean velocity (a), van Driest-transformed velocity (b), mean temperature (c), and normal Reynolds stresses (d), for flow cases CH15A (solid), CH15M (triangles), CH15MF (dashed) (see Tab. 3.1), The thick gray lines in panel (b) denote the compound law-of-the-wall $u^+ = y^+$, $u^+ = 5.2 + \log y^+/0.41$.

Several propositions have been made in the past to remove compressibility effects from statistics of wall-bounded flows, starting from analytical transformations of the laminar boundary layer equations [59]. In laminar boundary layer flow, the Howarth-Dorodnitsyn transformation exactly accounts for variations of mean density and temperature through re-scaling of the wall-normal coordinate thus reducing the transformed boundary layer equations to the incompressible ones. The same mapping does not directly apply to channel flow as the momentum equation is not homogeneous, reducing to

$$\frac{\mathrm{d}}{\mathrm{d}y}\left(\mu\frac{\mathrm{d}u}{\mathrm{d}y}\right) + \frac{\tau_w}{h} = 0. \tag{3.1}$$

A solution of equation (3.1) can be found by introducing an effective velocity,

$$u_V = \int_0^u \frac{\mu}{\mu_w}\mathrm{d}u, \tag{3.2}$$

which satisfies the incompressible Poiseuille profile.

Transformation	Wall distance (f_I)	Mean velocity (g_I)	Stresses (φ_I)
Howarth [59]	$f_L = \frac{1}{N}$	$g_L = 1$	NA
Viscous sublayer	$f_V = 1$	$g_V = RN$	NA
van Driest [146]	$f_D = 1$	$g_D = R^{1/2}$	$\varphi_D = R$
Huang et al. [62]	$f_H = \frac{\mathrm{d}}{\mathrm{d}y}\left(\frac{y}{R^{1/2}N}\right)$	$g_H = R^{1/2}\left(1 + \frac{\tilde{u}}{R}\frac{\mathrm{d}R}{\mathrm{d}y}\frac{\mathrm{d}y}{\mathrm{d}\tilde{u}}\right)$	$\varphi_H = R$
Brun et al. [21]	$f_B = \frac{1}{RN}$	$g_B = \frac{1}{R^{1/2}N}\frac{y}{y_B}$	$\varphi_D = \frac{1}{RN^2}\left(\frac{y}{y_B}\right)^2$
Trettel and Larsson [141] (TL)	$f_T = \frac{\mathrm{d}}{\mathrm{d}y}\left(\frac{y}{R^{1/2}N}\right)$	$g_T = RN\frac{\mathrm{d}}{\mathrm{d}y}\left(\frac{y}{R^{1/2}N}\right)$	$\varphi_T = R$

Table 3.3: Transformation rules for wall distance, mean velocity and Reynolds stresses, according to equations (3.8), (3.19), with $N = \overline{\nu}/\nu_w$, $R = \overline{\rho}/\overline{\rho}_w$. See equation 3.8 for the definition of the mapping functions f_I, g_I.

The scenario is much more complicated in turbulent wall layers, in which no analytical transformation can be found to rigorously transform the governing equations to the incompressible ones. The only provable result pertains to the viscous sublayer, for which the mapping (3.2) still applies [129]. As regards the outer layer, the classical analysis is based on the work of van Driest [146]. Mean momentum balance in turbulent channel flow requires

$$\overline{\mu}\frac{\mathrm{d}\widetilde{u}}{\mathrm{d}y} - \bar{\rho}\widetilde{u''v''} = \overline{\rho}_w u_\tau^2 \left(1 - \eta\right), \tag{3.3}$$

where $\eta = y/h$ is the outer-scaled vertical coordinate. Away from the wall molecular viscosity is negligible, and further assuming $\eta << 1$, constancy of the turbulent stress follows, hence

$$-\widetilde{u''v''} \approx \left(\frac{\overline{\rho}_w}{\overline{\rho}}\right) u_\tau^2, \tag{3.4}$$

which shows that 'compressible' stresses should be scaled by the local mean density to recover the incompressible behavior. Mixing length modeling of the turbulent shear stress further leads to the classical overlap-layer equation

$$\frac{du_D}{dy} = \frac{u_\tau}{ky}, \tag{3.5}$$

in terms of the van Driest transformed velocity, defined as

$$u_D = \int_0^{\bar{u}} \left(\frac{\bar{\rho}}{\bar{\rho}_w} \right)^{1/2} \mathrm{d}\widetilde{u}. \tag{3.6}$$

Integration of (3.5) directly leads to a logarithmic layer for the transformed velocity field with the same slope as in the incompressible case, however with an additive constant which may in general vary with both Reynolds and Mach number. It should be noted that, assuming for simplicity a power-law expression for the molecular viscosity of the type $\mu \sim T^{0.76}$, it follows that the integrand of the viscous sublayer transformation (3.2) scales as $(\overline{\rho}_w/\overline{\rho})^{0.76}$, whereas in van Driest outer-layer transformation the scaling is about the inverse. Hence, it appears that van Driest transformation cannot collapse the entire wall layer, except for the case of an adiabatic wall, since $\overline{\rho}/\overline{\rho}_w \approx 1$ in the near-wall region [112]. This condition is asymptotically approached in channel flows as $Re_b \to \infty$, since the heat flux coefficients drops to zero (see table 3.1), hence it may be expected that the van Driest transformation recovers its accuracy in this limit. Failure of van Driest transformation was highlighted in previous works, in which alternative transformations were proposed to scale the whole inner layer. Empirical evidence [62] suggested that normalizing the mean velocity and Reynolds stress profiles with respect to suitable semi-local wall units based on the local density and viscosity, defined as

$$u_\tau^* = \sqrt{\tau_w/\overline{\rho}}, \quad \delta_v^* = \overline{\nu}/u_\tau^*, \tag{3.7}$$

yields better collapse of the flow statistics across the Mach number range. It can be readily shown [141] that using the local wall units defined in Eq. (3.7) is equivalent to introducing a mapping for the mean velocity and the wall distance, as given in Eqn. 3.8 below. Brun et al. [21] pointed out the importance of accounting for mean viscosity variations in the presence of high Mach number and/or hot/cold walls. Using arguments strictly applicable to the viscous sublayer, those authors proposed a set of transformation rules which includes a wall-normal stretching similar to the Howarth-Dorodnitsyn transformation. To gauge the validity of the various transformation rules, we preliminarily note that all of them can be cast in terms of mapping functions f_I, g_I for wall distance and mean velocity, defined as

$$y_I = \int_0^y f_I \, \mathrm{d}y, \quad u_I = \int_0^{\tilde{u}} g_I \, \mathrm{d}\tilde{u}, \tag{3.8}$$

where u_I and y_I denote the 'incompressible' values obtained from various transformations. Introducing these transformations into Eqn. (3.3), and assuming that the turbulent shear stress distribution obeys van Driest scaling, namely

$$-\overline{\rho}\widetilde{u''v''} = \overline{\rho}_w \tau_I(y_I), \tag{3.9}$$

we find

$$\frac{\overline{\mu}}{\mu_w}\frac{f_I}{g_I}\frac{\mathrm{d}u_I^+}{\mathrm{d}y_I^+} + \tau_I^+ = (1-\eta)\,. \tag{3.10}$$

Comparing Eqn. (3.10) with its incompressible counterpart then directly yields

$$\frac{\overline{\mu}}{\mu_w}\frac{f_I}{g_I} = 1, \tag{3.11}$$

which may be regarded as a constraint which defines a class of compressibility transformations which satisfy universality of the turbulent stresses. The mapping functions for wall distance and mean velocity corresponding to various compressibility transformations are listed in Tab. 3.3. Of course, the only existing transformation which satisfies the constraint given by Eqn. (3.11) is that for the viscous sublayer. A novel velocity transformation which also satisfies Eqn. (3.11), with the additional constraint that the transformed velocity profile collapses to the universal incompressible profile in the overlap layer, has been recently derived by Trettel and Larsson [141], and it is also listed in Tab. 3.3. It is interesting to note that the transformation rule for the wall-normal distance is identical to Huang's transformation (hence $y_T = y_H$). An important issue related to compressibility transformations is the definition of a suitable Reynolds number to compare the flow statistics across Mach numbers and with incompressible data. For instance, Coleman et al. [28] compared compressible channel statistics with the incompressible DNS of Kim et al. [71] at approximately the same friction Reynolds number, whereas Morinishi et al. [96] used a friction Reynolds number defined with the local viscous length scale at the channel centerline. We argue that the answer to the 'most relevant' Reynolds number should be given a-posteriori, based on the most successful transformation. For that purpose, we define a friction Reynolds number for the generic transformation as the ratio of the transformed wall-normal coordinate at

the channel centerline to the viscous length scale evaluated at the wall, hence

$$Re_{\tau I} = y_I(h)/\delta_v, \tag{3.12}$$

which clearly reduces to the conventional definition in the incompressible limit. In the following, in an attempt to evaluate the various compressibility transformations as fairly as possible, we compare the inner-scaled transformed distributions of the velocity statistics with incompressible DNS data at exactly the same relevant friction Reynolds number.

Mean velocity

As a preliminary check, in Fig. 3.6a we evaluate the viscous sublayer transformation given in Eqn. (3.2) for the case of compressible laminar flow at $M_b = 1.5$ and $M_b = 3$. It is clear that Eqn. (3.2) effectively maps the compressible velocity profiles to the incompressible parabolic Poiseuille distribution. Figure 3.6b further shows Eqn. (3.2) applied to flow case CH15C. In this case, satisfactory collapse to the incompressible distribution is recovered in the viscous sublayer up to $y^+ \approx 10$, with obvious deviations farther from the wall. The inner-scaled velocity distributions obtained from application of the compressibility transformations listed in Tab. 3.3 are compared in Figs. 3.7-3.10 with incompressible DNS data at the same relevant friction Reynolds number. For reference, the alleged universal incompressible wall law is also shown.

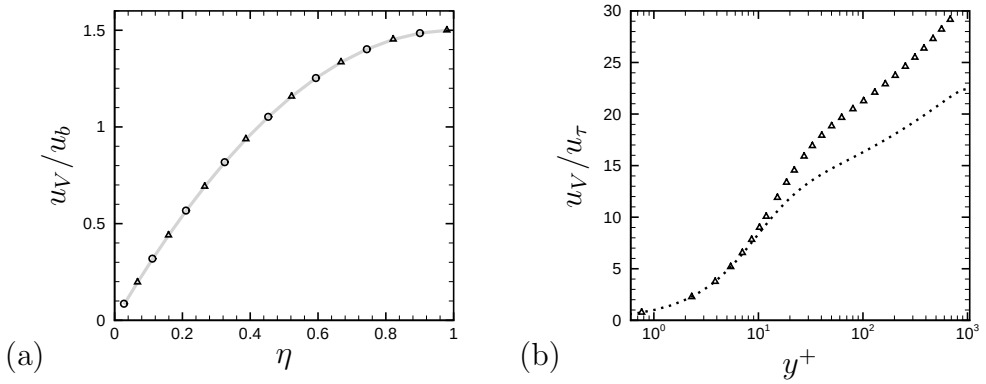

Figure 3.6: Assessment of laminar scaling, as from Eqn. (3.2): (a) laminar flow at $M_b = 1.5$ (triangles) and $M_b = 3$ (circles), compared with the parabolic Poiseuille profile (gray solid line); (b) comparison of flow case CH15C (triangles) with INC10 (dotted lines).

As also found in previous studies [28, 129], the van Driest transformation (Fig. 3.7) visibly undershoots the viscous sublayer linear distribution, especially in flow case CH3, and it overshoots the incompressible velocity distribution away from the wall, the crossing occurring at $y^+ \approx 30$. The van Driest transformation yields the correct slope of the log law in the overlap layer, but the additive constant is significantly overestimated at low Reynolds number, whereas it approaches the incompressible value at sufficiently high Reynolds number, as also noticed by Fernholz and Finley [40], Huang and Coleman [61], Spina et al. [134], and as probably due to the reduction in the heat flux coefficient (see Tab. 3.1). Unlike van Driest, Huang's transformation, shown in Fig. 3.8, performs well in the near-wall region, whereas it systematically overshoots the incompressible velocity profile in the outer layer, again approaching the incompressible behavior at sufficiently high Reynolds number. Brun's transformation (see Fig. 3.9) has an overall similar behavior as van Driest transformation, although absolute deviations in the outer layer are significantly smaller. The limitations of earlier transformations are apparently overcome by TL transformation (see Fig. 3.10), which yields collapse to the incompressible distributions across the Reynolds and Mach number range, throughout the wall layer.

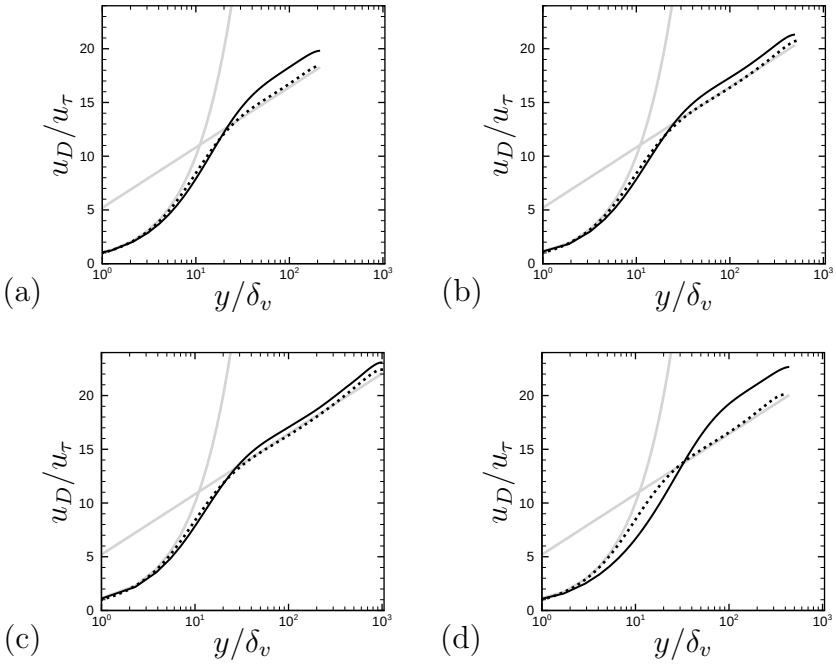

Figure 3.7: Mean velocity profiles transformed according to van Driest [146] (solid lines) for flow cases CH15A (a), CH15B (b), CH15C (c), CH3 (d), compared with incompressible DNS at matching $Re_{\tau D}$ (INC4, INC7, INC10, INC6, respectively, plotted with dotted lines). The thick gray lines denote the compound law-of-the-wall $u^+ = y^+$, $u^+ = 5.2 + \log y^+/0.41$.

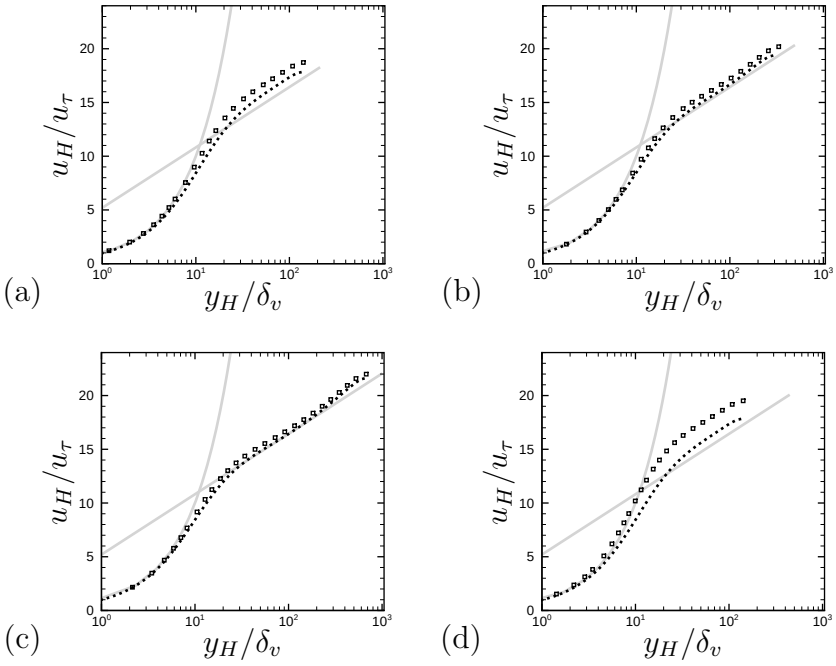

Figure 3.8: Mean velocity profiles transformed according to Huang et al. [62] (squares) for flow cases CH15A (a), CH15B (b), CH15C (c), CH3 (d), compared with incompressible DNS at matching $Re_{\tau H}$ (INC1, INC5, INC8, INC1, respectively, plotted with dotted lines). The thick gray lines denote the compound law-of-the-wall $u^+ = y^+$, $u^+ = 5.2 + \log y^+/0.41$.

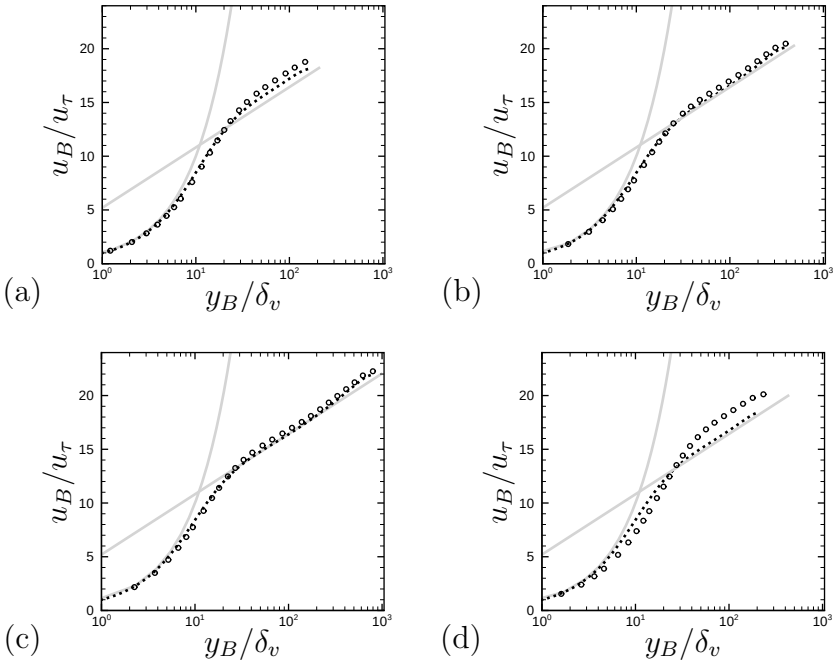

Figure 3.9: Mean velocity profiles transformed according to Brun et al. [21] (circles) for flow cases CH15A (a), CH15B (b), CH15C (c), CH3 (d), compared with incompressible DNS at matching $Re_{\tau B}$ (INC2, INC6, INC9, INC4, respectively, plotted with dotted lines). The thick gray lines denote the compound law-of-the-wall $u^+ = y^+$, $u^+ = 5.2 + \log y^+/0.41$.

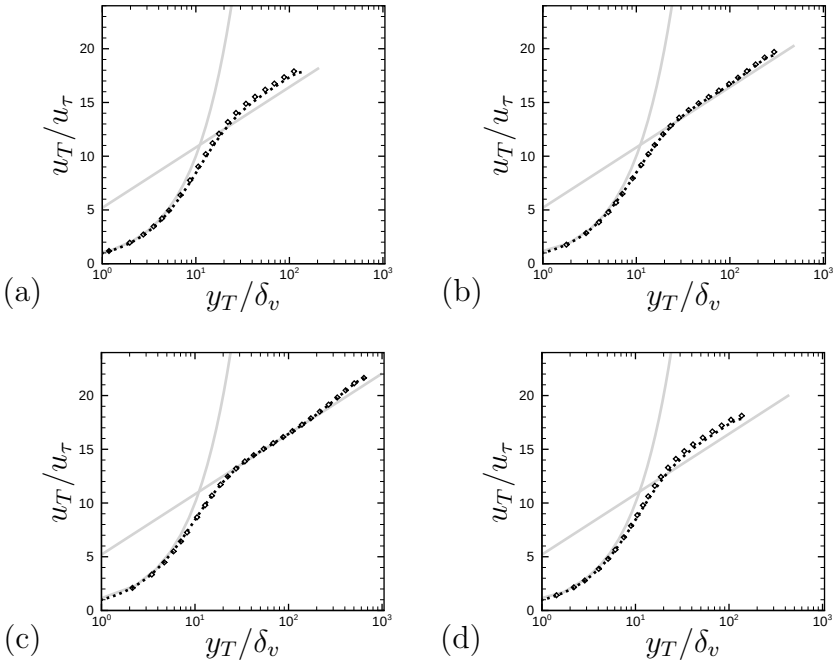

Figure 3.10: Mean velocity profiles transformed according to TL (diamonds) for flow cases CH15A (a), CH15B (b), CH15C (c), CH3 (d), compared with incompressible DNS at matching $Re_{\tau T}$ (INC1, INC5, INC8, INC1, respectively, plotted with dotted lines). The thick gray lines denote the compound law-of-the-wall $u^+ = y^+$, $u^+ = 5.2 + \log y^+/0.41$.

Closer scrutiny of the core part of the flow can be gained by inspecting the mean velocity profiles in defect form, as given in Fig. 3.11. A parabolic law for the core velocity profile of incompressible channels has recently been derived by Pirozzoli [115]. The derivation stems from the idea that the outer-layer turbulent eddies are not directly affected by the presence of the wall, and their size should hence scale with the channel height and with the typical eddy velocity scale (namely the friction velocity), whence it follows that the relevant eddy viscosity is

$$\nu_t = c_\mu u_\tau h, \tag{3.13}$$

where c_μ a suitable constant. This reasoning is easily extended to compressible flows on the token that in the presence of mean density variations the effective velocity scale is u_τ^* (as defined in Eqn. (3.7)) rather than u_τ, which yields the eddy viscosity

$$\nu_t = c_\mu^* u_\tau^* h, \tag{3.14}$$

where c_μ^* might differ from c_μ owing to compressibility effects. From Eqn. (3.3), neglecting the viscous term and using the eddy viscosity (3.14), one readily obtains

$$\frac{\mathrm{d}\widetilde{u}^+}{\mathrm{d}\eta} = \frac{1}{c_\mu^*}\left(\frac{\overline{\rho}_w}{\bar{\rho}}\right)^{1/2}(1-\eta)\,, \tag{3.15}$$

from which it follows that the van-Driest-transformed velocity should follow a universal parabolic law in the core part of the channel

$$u_D^+ - u_{De}^+ = -\frac{1}{2c_\mu^*}(1-\eta)^2\,, \tag{3.16}$$

where u_{De} is the transformed centerline velocity. Outer defect profiles obtained with van Driest transformation are given in Fig. 3.11, the other transformations yielding similar results, since density and viscosity variations in the outer layer are but moderate. Comparison with incompressible DNS (dotted lines) shows excellent agreement throughout the outer layer, irrespective of the Reynolds and Mach number. The DNS data are consistent with the prediction of Eqn. (3.16) around the channel centerline, the range of validity of the parabolic fit extending to about half of the flow domain at sufficiently high Reynolds number. No evident compressibility effects are observed on the parabolic law constant, which in fact coincides with its incompressible value.

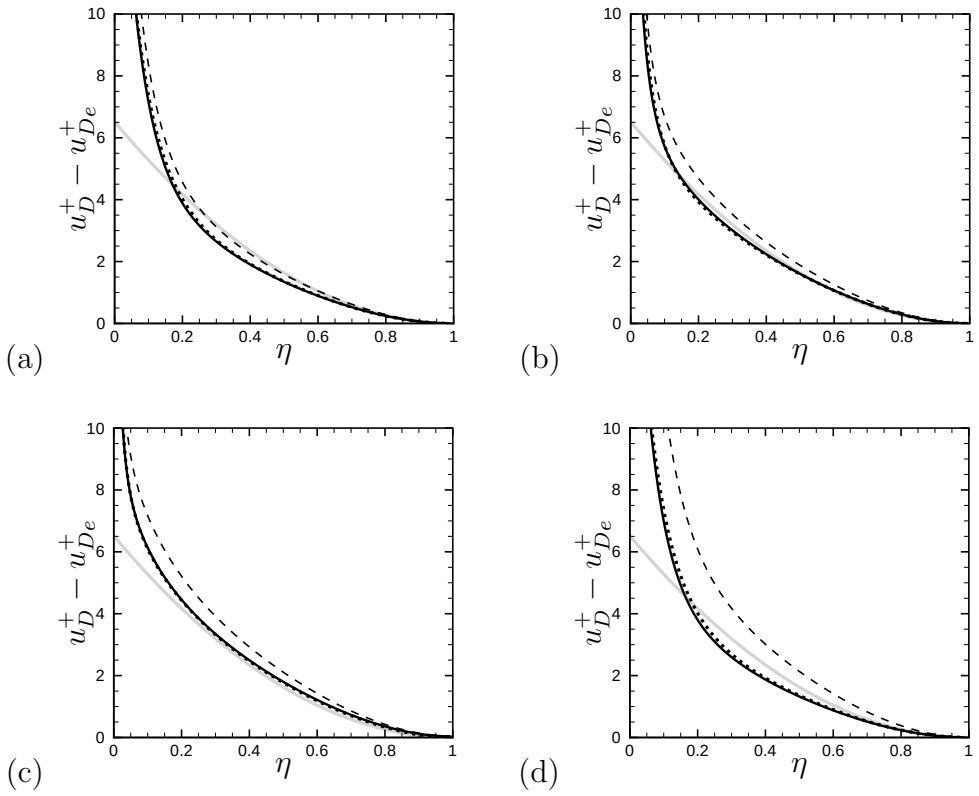

Figure 3.11: Van Driest-transformed defect velocity profiles for flow cases CH15A (a), CH15B (b), CH15C (c), CH3(d) (solid lines), compared with incompressible data from flow cases INC1-INC5-INC8-INC1 (dotted lines), at matching $Re_{\tau H}$. The dashed lines represent the untransformed velocity profiles. The 'e' subscript refers to properties at the channel centerline. The gray line represent Eqn. (3.15) with $c_\mu = 0.0767$.

Reynolds stresses and vorticity fluctuations

Here we discuss the validity of compressibility transformations as applied to the individual components of the Reynolds stress tensor, for which direct extension of the van Driest scaling yields

$$\tau_{Dij} = \frac{\overline{\rho}}{\overline{\rho}_w}\tau_{ij}. \tag{3.17}$$

The same assumption also subtends the scalings of Huang et al. [62] and Trettel and Larsson [141]. A different form of scaling was considered by Brun et al. [21], who applied the same scaling factor used for the mean velocity to scale the turbulence

velocity intensities, thus yielding

$$\tau_{Bii} = \frac{\overline{\rho}}{\overline{\rho}_w} \left(\frac{y}{y_B} \frac{\mu_w}{\overline{\mu}} \right)^2 \tau_{ii}, \tag{3.18}$$

for the diagonal Reynolds stress components. The scaling rules for the Reynolds stresses are summarized in Tab. 3.3, in the form of the ratio of the transformed to the untransformed stresses, namely

$$\varphi_I = \frac{\tau_I}{\tau}. \tag{3.19}$$

Figure 3.12 shows the van Driest-transformed Reynold stress components, compared with the corresponding incompressible distributions. As noticed in previous studies [28, 42], a mismatch between scaled compressible stresses and incompressible stresses is found in the inner layer, with clear difference in the amplitude of the streamwise stress and a shift in the position of peaks, whereas closer agreement is found in the outer layer. It is noteworthy that the in flow case CH15C (see panel c) a substantial layer with near-logarithmic variation of the spanwise stress is recovered [5], which is the symptom of the emergence of effects of scale separation, not attained in previous studies at lower Reynolds number. Figure 3.13 shows that Huang's scaling yields much better collapse of the compressible and incompressible stresses distributions, in terms of both the peak amplitude and the off-wall position. In fact, the shear stress and the wall-normal and spanwise velocity variances are almost perfectly matched, whereas differences remain for the amplitude of the streamwise turbulence intensity peak. Superior accuracy of Huang's scaling as compared to van Driest was also observed in previous studies [28, 96], but to our knowledge this is the first time that a comparison is carried out at precisely matching Reynolds number. Brun's scaling is tested for the Reynolds stress tensor components in Fig. 3.14. Note that, although the transformation (3.18) was originally meant for the normal stresses only, we also apply it to the shear stress. The transformed stresses shows reasonably good collapse on the incompressible simulations in the outer layer for flow cases CH15A-B-C, but they are less accurate in the near-wall region, similar to what observed for the van Driest transformation. As the Mach number is increased (panel d) Brun's transformation appears to fail both in the inner and in the outer layer. Interestingly, Brun's transformation seems to yield good prediction of the amplitude of the streamwise stress peak, although its positions is clearly shifted with respect to the 'correct' one. Trettel-Larsson (TL) transformation

for the Reynolds stresses is not shown here, being identical to Huang's.

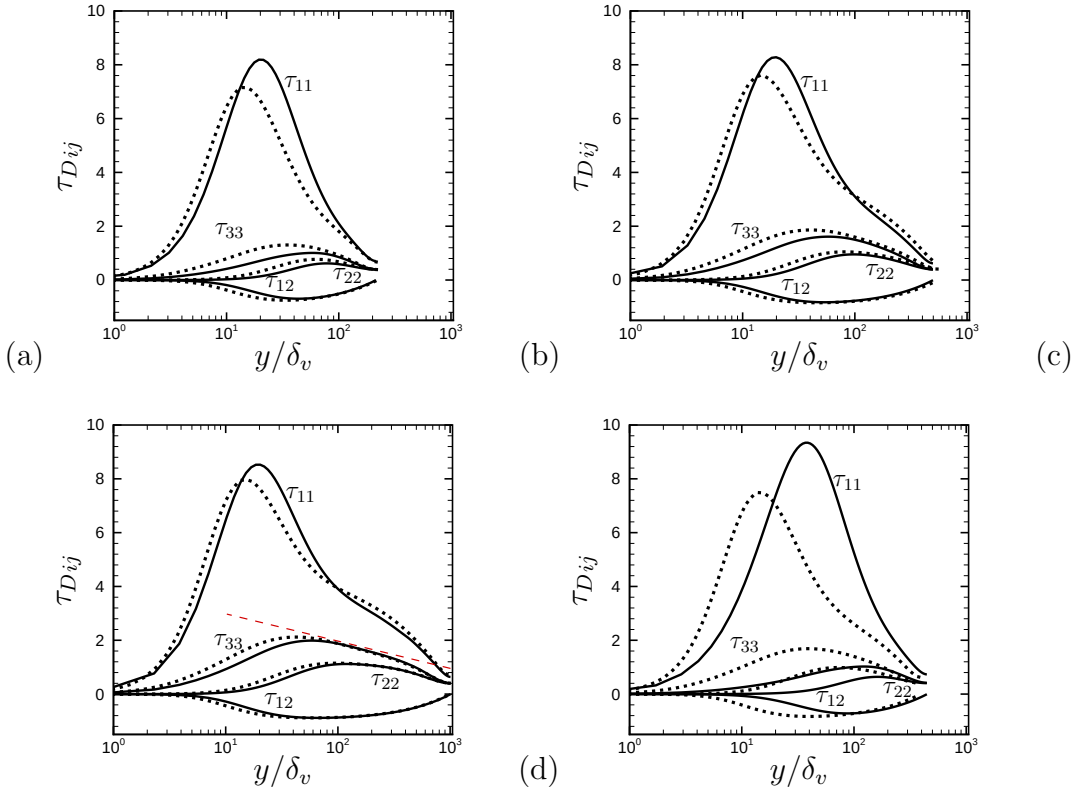

Figure 3.12: Reynolds stress components transformed according to van Driest [146] (solid lines) for flow cases CH15A (a), CH15B (b), CH15C (c), CH3 (d), and compared with incompressible DNS at matching $Re_{\tau D}$ (INC4, INC7, INC10, INC6, respectively, with dotted lines). The dashed line in panel (c) denotes a logarithmic fit of the data.

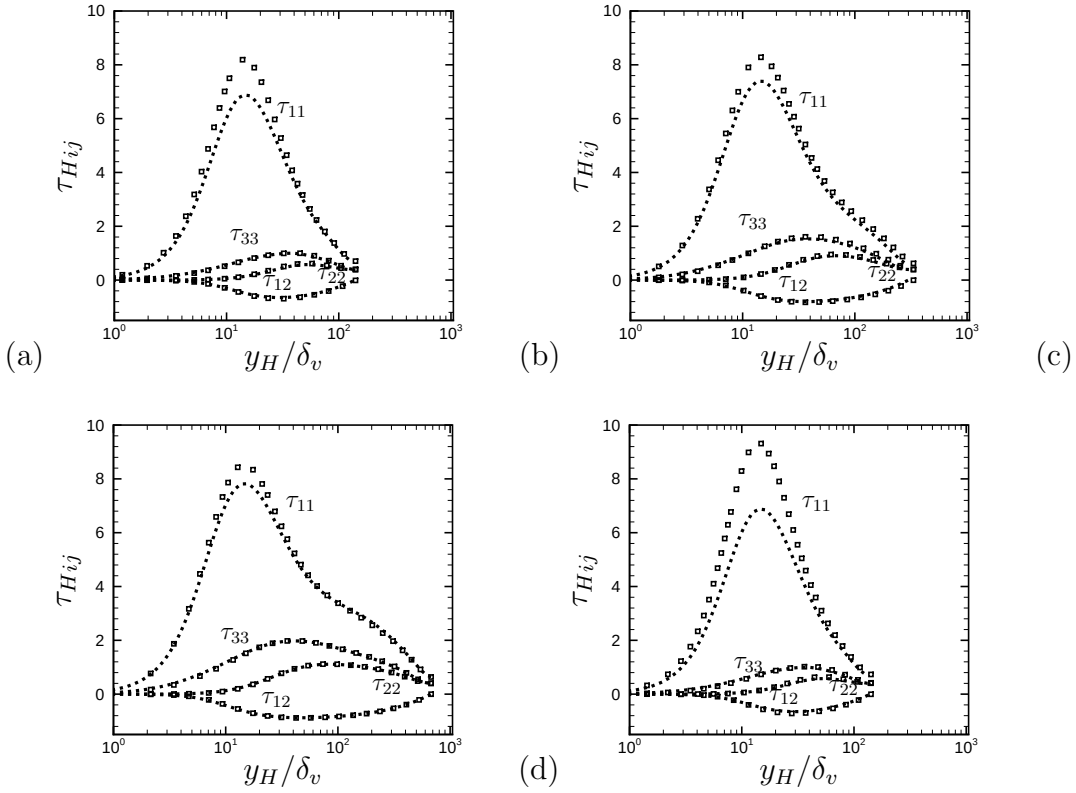

Figure 3.13: Reynolds stress components transformed according to Huang et al. [62] (squares) for flow cases CH15A (a), CH15B (b), CH15C (c), CH3 (d), compared with incompressible DNS at matching $Re_{\tau H}$ (INC1, INC5, INC8, INC1, respectively, with dotted lines).

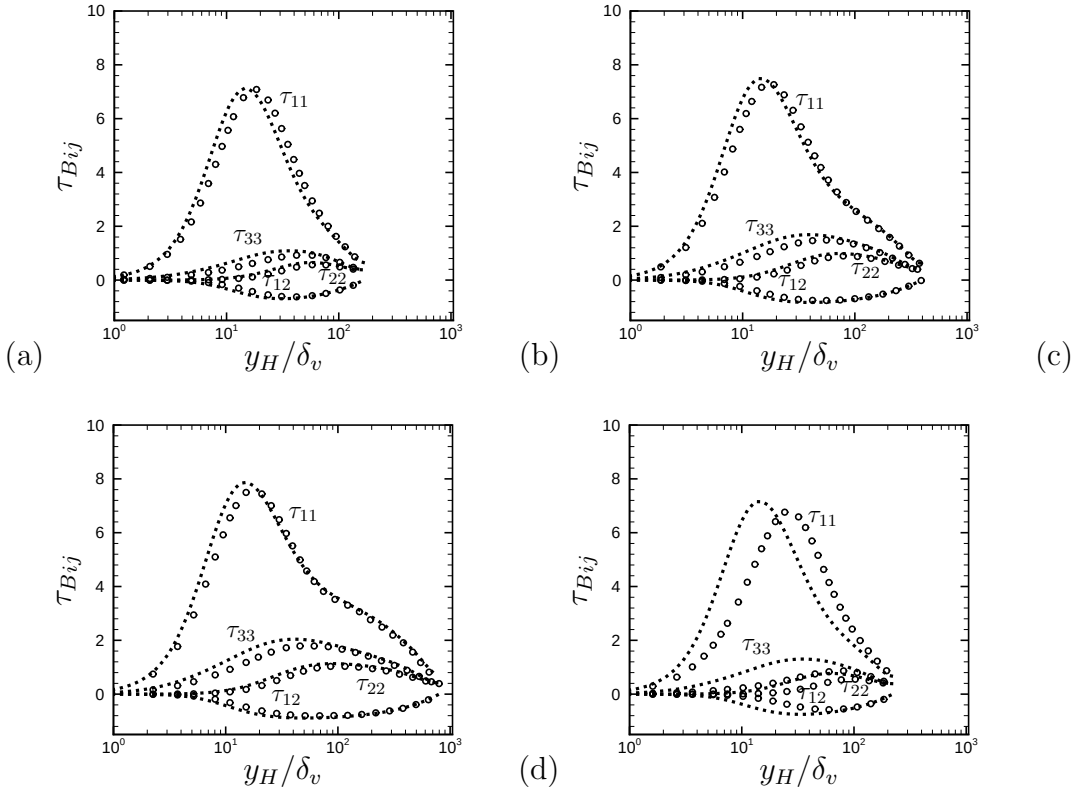

Figure 3.14: Reynolds stress components transformed according to Brun et al. [21] (circles) for flow cases CH15A (a), CH15B (b), CH15C (c), CH3 (d), compared with incompressible DNS at matching $Re_{\tau B}$ (INC2, INC6, INC9, INC4, respectively, with dotted lines).

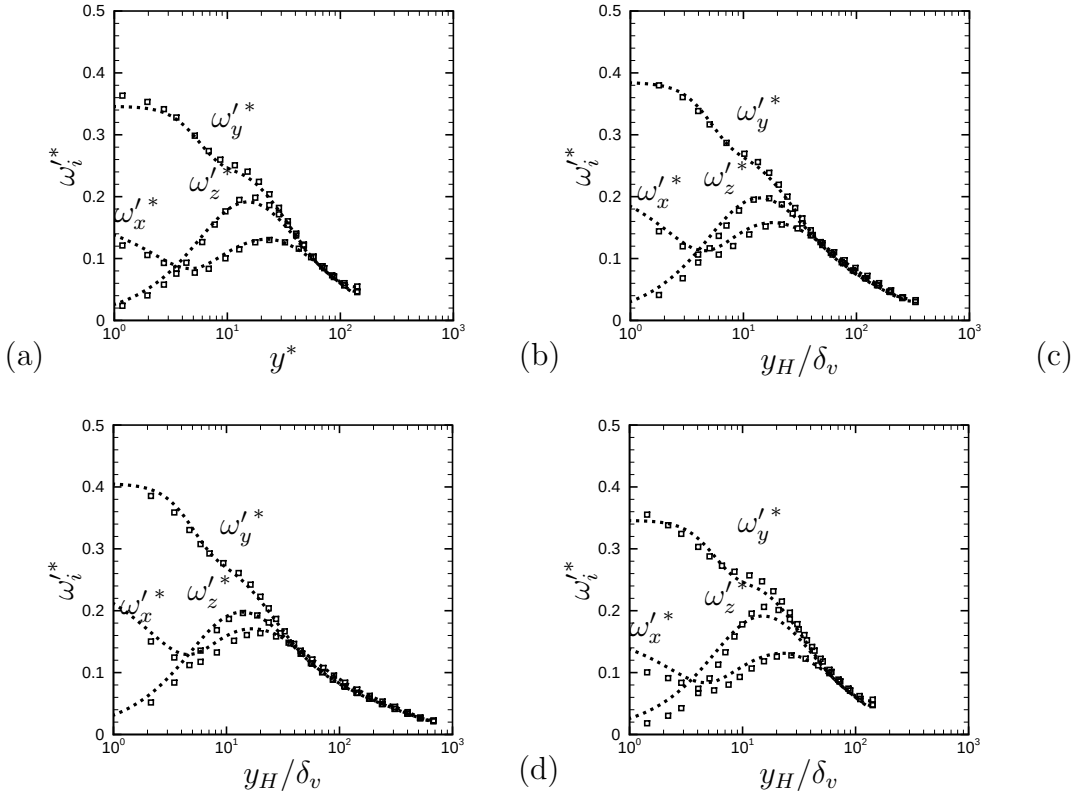

Figure 3.15: Vorticity fluctuations in semi-local scaling, $\omega_i'^* = \omega_i'\delta_v^*/u_\tau^*$ (squares) for flow case CH15A (a) CH15B (b) CH15C (c), CH3 (d), compared with incompressible DNS at matching $Re_{\tau H}$ (INC1, INC5, INC8, INC1, respectively, with dotted lines).

The vorticity fluctuation components are presented in Fig. 3.15, scaled in semi-local units, as defined in equation (3.7). The success in collapsing the various distributions is particularly impressive here, except perhaps for minor differences in the near-wall region for flow case CH3. This observation probably points to the physical fact that the small scales of fluid motion only depend on the local mean flow conditions, in terms of density and viscosity.

3.1.3 Mean temperature

The distribution of the mean temperature is of great importance in compressible boundary layers, as it obviously allows prediction of the heat transfer coefficient, but it is also necessary for accurate prediction of the skin friction coefficient, as an accurate temperature-velocity relation allows straightforward application of the inverse of the compressibility transformations of Tab. 3.3 to determine the mean

velocity profile in untransformed space [40]. A widely used temperature-velocity relationship was derived by Walz [156],

$$\frac{T}{T_w} = 1 + \frac{T_r - T_w}{T_w}\frac{\overline{u}}{\overline{u}_e} - r\frac{\gamma-1}{2}M_e^2\frac{T_e}{T_w}\left(\frac{\overline{u}}{\overline{u}_e}\right)^2, \tag{3.20}$$

where $T_r = T_e\left(1 + \frac{\gamma-1}{2}rM_e^2\right)$ is the recovery temperature, $r = 0.89$ is the recovery factor, and the subscript e denotes properties at the edge of the wall layer (the channel centerline in internal flow). Walz obtained Eqn. (3.20) from a simplified form of the energy equation [146, 147], based on several assumptions including neglect of turbulent dissipation and pressure-strain terms. Pirozzoli et al. [117] found good agreement between Eqn. (3.20) and DNS of a $M = 2.25$ boundary layer over an adiabatic wall. Duan et al. [35] carried out DNS of a supersonic boundary layer at $M = 5$ with different wall temperatures, finding good agreement between Eqn. (3.20) in adiabatic wall cases, but differences as the wall heat flux increases. Recently, Zhang et al. [165] derived a generalized Reynolds analogy by introducing a general recovery factor, which overcomes the limitations of Walz equation in the presence of non-adiabatic walls

$$\frac{T}{T_w} = 1 + \frac{T_{rg} - T_w}{T_w}\frac{u}{u_e} + \frac{T_e - T_{rg}}{T_w}\left(\frac{u}{u_e}\right)^2, \tag{3.21}$$

where $T_{rg} = T_e + r_g u_e^2/(2C_p)$, $r_g = 2C_p(T_w - T_e)/u_e^2 - 2Prq_w/(u_e\tau_w)$. Eqn. (3.21) explicitly takes into account the wall heat flux q_w, and it coincides with Walz relation in the case of adiabatic walls. Figure 3.16 provides a comparison between the channel flow DNS data and the predictions of Eqn. (3.20) and (3.21), which clearly shows superior performance of the latter, especially at higher Mach number. It is worth pointing out that Eqns. (3.20)-(3.21) have the same form for external and internal flows, but in the latter case the centerline values of temperature and velocity are not known a priori. As a consequence, these traditional temperature/velocity relations cannot be used to explicitly determine the friction coefficient, and their engineering relevance in this case is more limited

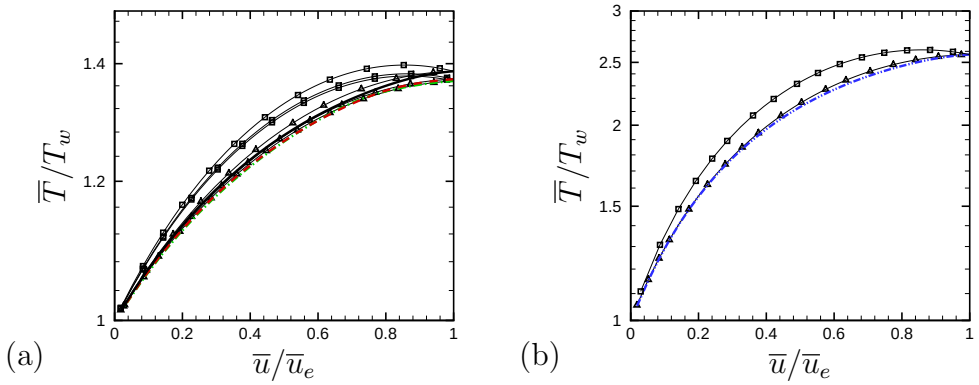

Figure 3.16: Temperature-velocity relationship: mean temperature as a function of mean velocity. In panel (a) flow cases CH15A (black, solid) -CH15B (red, dashed)-CH15C (green, dash-dotted), in panel (b) flow case CH3 (blue, dash-dot-dot) compared with Eqn. (3.20) (solid lines with square symbols) and with (3.21) (solid lines with triangle symbols), with $r = 0.89$.

3.1.4 Length scales

We now focus on the evaluation of the typical length scales in the outer wall layer. The integral length scales of a generic quantity φ in the i-th direction are defined as the integral of the two point correlation function,

$$\Lambda_\varphi^i = \int_{-\infty}^{\infty} C_{\varphi\varphi}\left(\Delta x_i\right) \mathrm{d}\Delta x_i. \tag{3.22}$$

As far as theory goes, the basic prediction of the attached eddy model for incompressible wall layers [108, 140], is that the typical length scales should increase linearly with the wall distance in the outer layer, which is consistent with the existence of a logarithmic layer in the mean velocity profile. A more refined assumption [89] is that the outer-layer length scales should scale with the local mean shear, as follows

$$\ell_m \sim u_\tau \left(\frac{\mathrm{d}\overline{u}}{\mathrm{d}y}\right)^{-1}, \tag{3.23}$$

which in fact predicts linear variation in the presence of a logarithmic mean velocity profile. A simple eddy-viscosity ansatz led Pirozzoli [114] to predict a rather different

scaling,

$$\ell_{12} \sim (u_\tau h)^{1/2} \left(\frac{\mathrm{d}\overline{u}}{\mathrm{d}y} \right)^{-1/2}, \tag{3.24}$$

which was shown to apply with greater accuracy than (3.23) far from the wall. The scaling (3.24) can be readily adapted to compressible flow on the token that the main compressibility effects are included in the variation of the local friction velocity, with the following result

$$\ell_{12}^* \sim (u_\tau^* h)^{1/2} \left(\frac{\mathrm{d}\tilde{u}}{\mathrm{d}y} \right)^{-1/2}. \tag{3.25}$$

In order to gauge the accuracy of the scaling given in Eqn. (3.25), we will focus on the spanwise spectral densities of u, defined such that

$$\widetilde{u''^2} = \int_0^\infty E_u(k_z)\, dk_z, \tag{3.26}$$

k_z is the Fourier wavenumber in the spanwise direction. This choice is motivated by the peculiar streaky pattern of the wall layer 'superstructures', which are relatively compact in the spanwise direction, whereas they are essentially infinite in the streamwise direction, and estimation of the actual length scale based on streamwise two-point correlations or one-dimensional spectra is prone to large uncertainties [65]. To account for the effect of turbulence intensity variation across the wall layer, we further consider the normalized spectral densities, defined as

$$\hat{E}_u(k_z) = E_u(k_z)/\widetilde{u''^2}. \tag{3.27}$$

Normalized spectral densities are related to the integral length scale Λ_u^z through the relation,

$$\Lambda_u^z = \lim_{k_z \to 0} \pi \hat{E}_u(k_z). \tag{3.28}$$

Figure 3.17 shows the spectra of u in pre-multiplied form, as a function of the spanwise wavelength $\lambda_z = 2\pi/k_z$, normalized with respect to either h or ℓ_{12}^*. The spectra at different stations, all laying in the outer layer $50/Re_{\tau H} \leq \eta \leq 0.7$, are shown and compared with the spectra from incompressible simulations at matching $Re_{\tau H}$, at $\eta = 0.4$. The outer-scaled spectra all show a distinct bump shape with

peak at $\lambda_z \approx h$, which is suggestive of eddies having a typical spanwise size of the order of the channel half-height, and increasing with the wall distance. When reported in terms of the length scale (3.25), spectra at all off-wall locations are found to collapse on another as well as on the incompressible spectra, with greater scatter in the low-Re flow case (CH15A), in which the lowest location is at the very lower edge of the outer layer. It is worth noting that this scaling also applies to the overlap region (albeit small in this case), as seen in the inset of Fig. 3.17e. Compressibility effects are further scrutinized in Fig. 3.18, which pertains to flow case CH3. In this case, wavelengths are scaled with respect to h (a), ℓ_{12} (b), and ℓ^*_{12} (c). Comparison of panels (b) and (c) clearly shows superior accuracy of the heuristic compressibility correction given in Eqn. (3.25), as compared to the baseline 'incompressible' scaling of Eqn. (3.24).

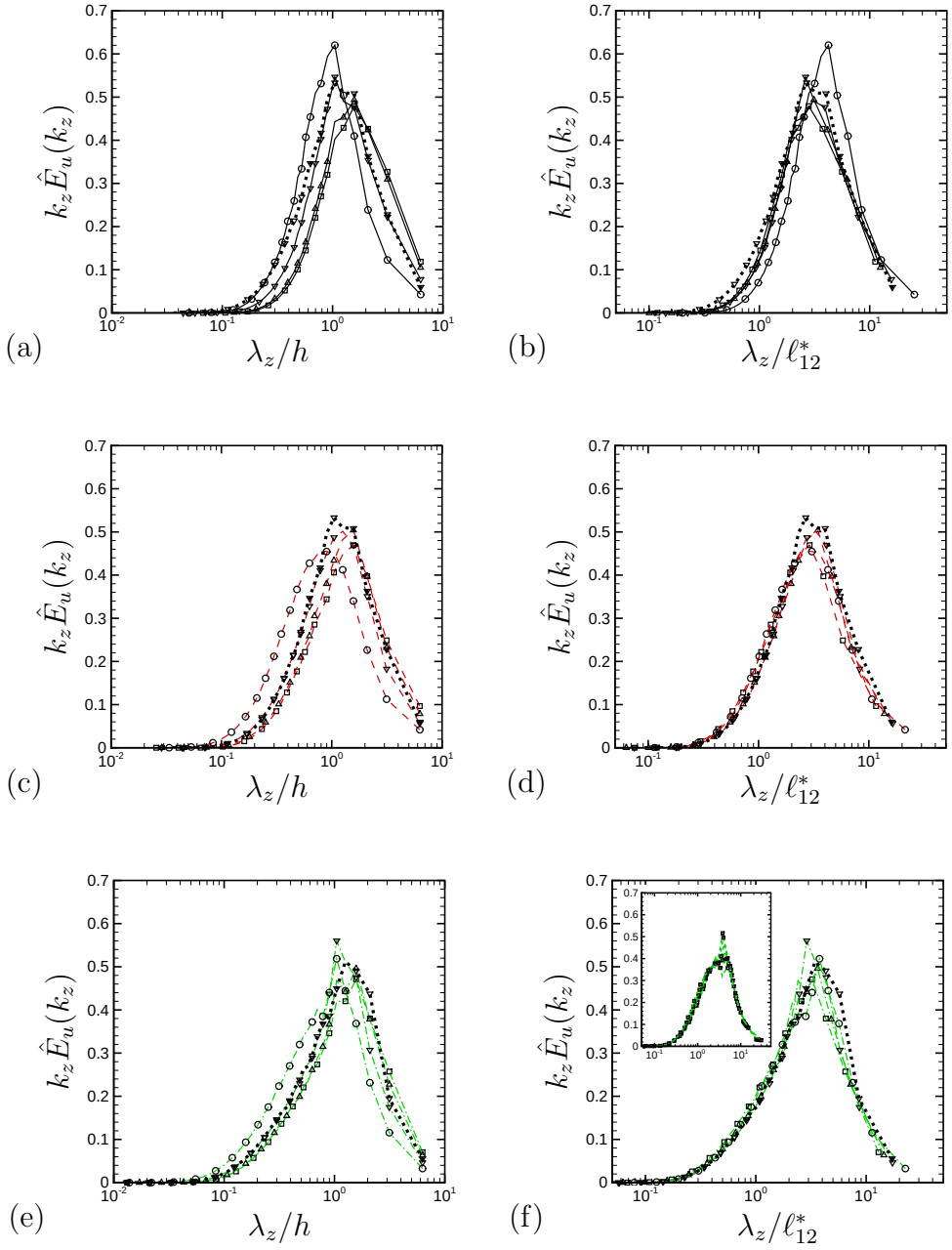

Figure 3.17: Pre-multiplied power spectral densities of u in spanwise direction as a function of λ_z/h (a-c-e) and λ_z/ℓ^*_{12} (b-d-f), for flow cases CH15A (a-b), CH15B (c-d), CH15C (e-f). Symbols denote different distances from the wall, namely $\eta = 0.2$ (circles), $\eta = 0.4$ (gradients), $\eta = 0.6$ (deltas), $\eta = 0.7$ (squares). The dotted lines with gradient symbols denotes the incompressible spectrum at $\eta = 0.4$ at matching $Re_{\tau H}$. The inset in panel (f) shows the spectra of CH15C at six stations in the logarithmic region between $y^+_H = 100$ and $y^+_H = 200$.

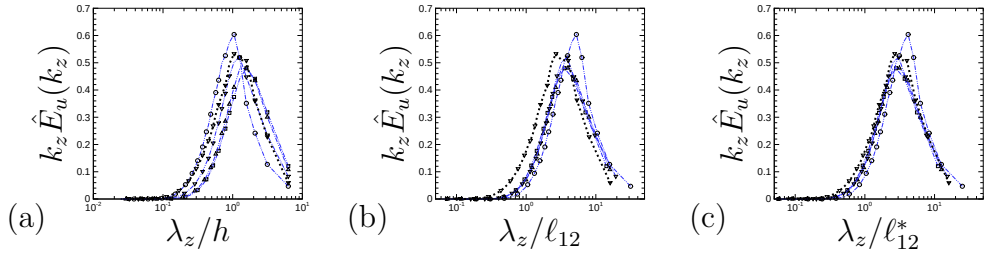

Figure 3.18: Pre-multiplied spectral densities in spanwise direction for the streamwise velocity component, as a function of λ_z/h (a), λ_z/ℓ_{12} (b) and λ_z/ℓ^*_{12} (c) for flow case CH3. Symbols denote different distances from the wall, namely $\eta = 0.2$ (circles), $\eta = 0.4$ (gradients), $\eta = 0.6$ (deltas), $\eta = 0.7$ (squares). The dotted lines with gradient symbols denotes the incompressible spectrum at $\eta = 0.4$ at matching $Re_{\tau H}$.

Overall, we believe that the data presented above convincingly support the validity of the theory developed by Pirozzoli [114], from which more general conclusions can be drawn. Using the identity $u^*_\tau = u_\tau \sqrt{\rho_w/\rho}$, and using van Driest transformation for the mean velocity, which as previously seen is quite accurate in the outer wall layer, Eqn. (3.25) becomes

$$\ell^*_{12}(y) \sim (u_\tau h)^{1/2} \left(\frac{\mathrm{d}u_D}{\mathrm{d}y} \right)^{-1/2}, \tag{3.29}$$

which coincides with the conventional length scale (3.24), applied to the transformed mean velocity profile. Since in the outer layer the transformed mean shear is the same at the same outer wall distance η, it follows that the typical spanwise length scales are not affected by compressibility. This is consistent with the previous Fig. 3.17, 3.18, which showed collapse with incompressible spectra and nearly identical distributions for flow cases CH15A and CH3 having very similar effective friction Reynolds number, and with previous experimental and DNS findings [112, 130].

3.2 Compressible flow in circular pipe

In this Section we present DNS of compressible pipe flow, at the same bulk Mach number of channel flow simulations and approximately the same friction Reynolds number Re_τ, as reported in Tab. 3.4.

Case	Re_b	M_b	Re_τ	$Re_{\tau H}$	N_x	N_y	N_z	Δx^+	Δz^+	M_τ	$-B_q$	$\Delta t_{av} u_\tau / h$
P02	5300	0.2	184	180	256	64	256	11	4.5	0.014	0.0011	21.4
P13	6362	1.3	235	164	320	96	320	7.3	4.6	0.075	0.040	13.2
P15A	6000	1.5	223	143	512	128	320	8.2	4.4	0.082	0.051	17.8
P15B	14600	1.5	521	334	1024	128	640	9.6	5.1	0.077	0.048	19.0
P15C	31500	1.5	1030	667	2048	256	1280	9.5	5.0	0.070	0.044	9.6
P3	10300.	3.	524	147	1024	128	640	9.6	5.1	0.12	0.15	15.7

Table 3.4: Setup of compressible pipe DNS. The computational domain length is $L_x = 6\pi R$ for all flow cases apart for P13 which reproduces the DNS by Ghosh et al. [52] with domain $L_x = 10R$. N_x, N_y, N_z and Δx^+, Δy^+, Δz^+ are the number of points and the mesh spacing in the streamwise, radial and azimuthal direction, respectively. $M_\tau = u_\tau / c_w$ is the friction Mach number, and $B_q = q_w / (\rho_w C_p u_\tau T_w)$ is the heat flux coefficient. $Re_{\tau H}$ is the equivalent friction Reynolds number for Huang's transformation (see Tab. 3.3 and Eqn. (3.12)) and Δt_{av} is the averaging time interval.

All simulations have been performed using AVTI-Z and ATI-Y algorithms while convective limitation in azimuthal direction is relaxed as described in Section 2.2.2. This allows to have a time step restriction comparable to the one of channel flow. An analysis similar to the one conducted for channel flow is performed for pipe. Attention is focused on compressibility transformations for velocity and Reynolds stresses. The detailed analysis on the accuracy of the compressibility transformations in Tab. 3.3 is not repeated for pipe flow, since an ad-hoc incompressible pipe flow database would be necessary. We limit ourself to test the TL transformation and use incompressible pipe flow data available in literature for comparison. In the case of pipe flow passive scalar transport at Schmidt number $Sc = 0.71 - 1$ is also investigated.

3.2.1 Instantaneous flow field

In this Section instantaneous flow visualizations of the pipe flow are qualitatively analyzed through snapshots of wall-parallel and cross-stream planes. Figure 3.19 shows a three dimensional visualization of the pipe flow case P15C, through simultaneous visualization of the cross-stream and wall-parallel plane at $y^+ = 15$. As for channel flow we note meandering streaky structures, elongated in the streamwise direction.

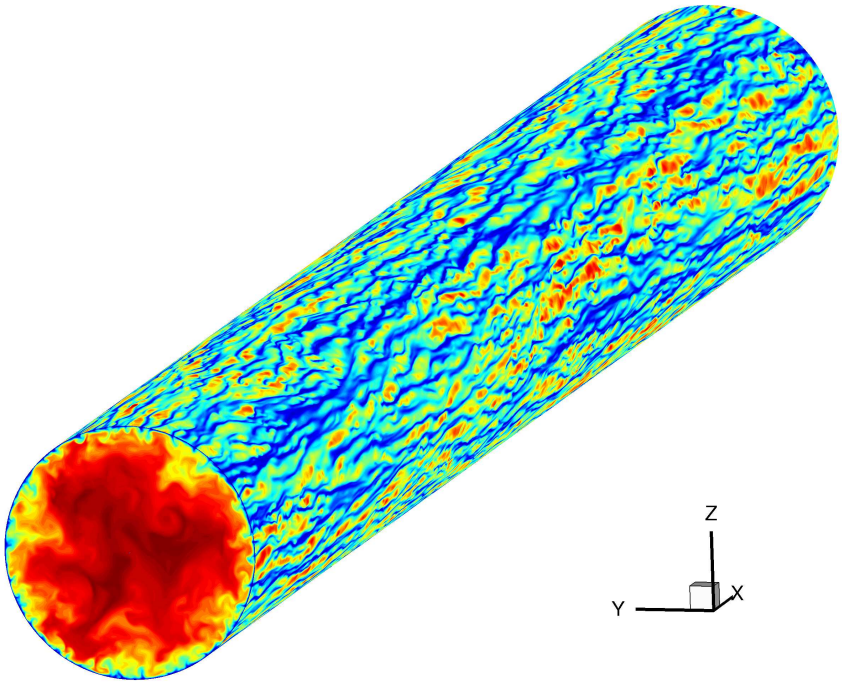

Figure 3.19: Instantaneous flow field of flow case P15C. Streamwise velocity contours in the streamwise (xy), cross-stream (yz) and wall parallel (at $y^+ = 15$) planes are plotted.

A closer look to the streaks, Fig. 3.20, for cases P15A, P15B and P15C highlights that the near wall-region of supersonic pipe flow is qualitatively similar to the one observed in channel flow, Fig. 3.2. The scrutiny of the velocity fluctuations allows to form a better picture of the qualitative behavior of the flow, Fig. 3.21. Streamwise velocity fluctuations indicate the presence of big eddies spanning half a pipe section, from the axis to the wall. In particular, it is clearly possible to identify three alternating low speed and high speed structures with an azimuthal size that decrease towards the pipe axis. Similar eddies were observed in the case of channel flow, Fig. 3.3, even if with their structure was more blurred. As for channel flow, it appears that the wall-normal velocity fluctuations are correlated to the streamwise ones, while a less clear organization can be observed for the azimuthal fluctuations.

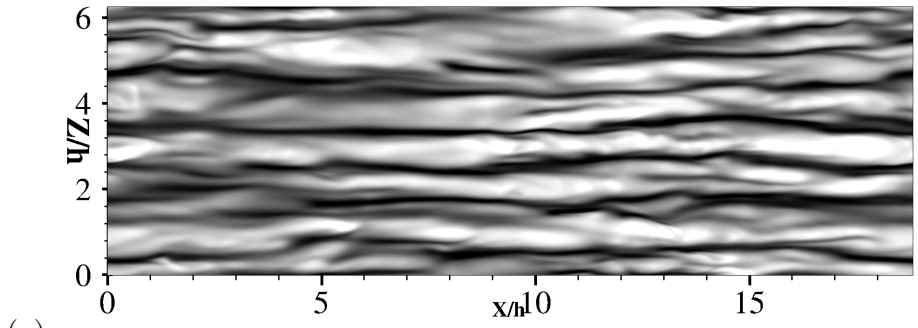

(a)

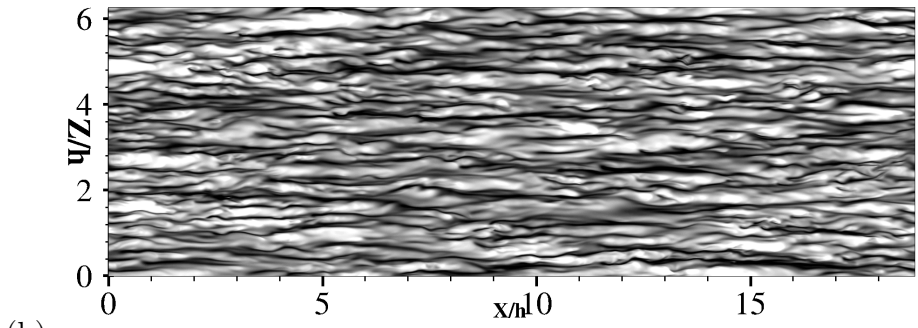

(b)

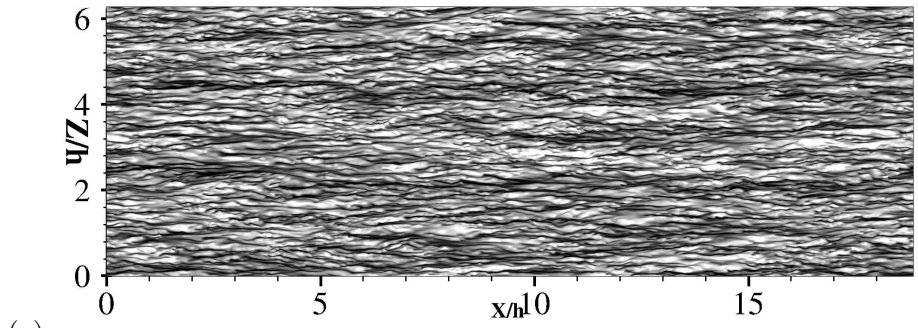

(c)

Figure 3.20: Instantaneous flow field of flow case P15A(a), P15(b), P15C(c). Streamwise velocity fluctuations in the xz, wall parallel plane at $y^+ = 15$. Flow from left to right, 48 contour levels $-2 < u'/(\sqrt{\rho/\rho_w}u_{rms}) < 2$, from dark to light shades.

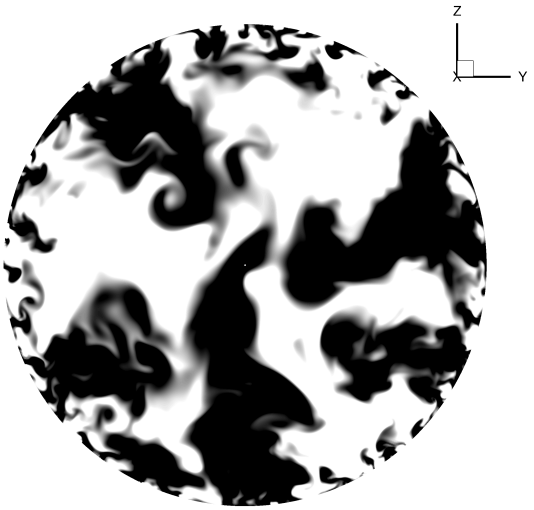

(a)

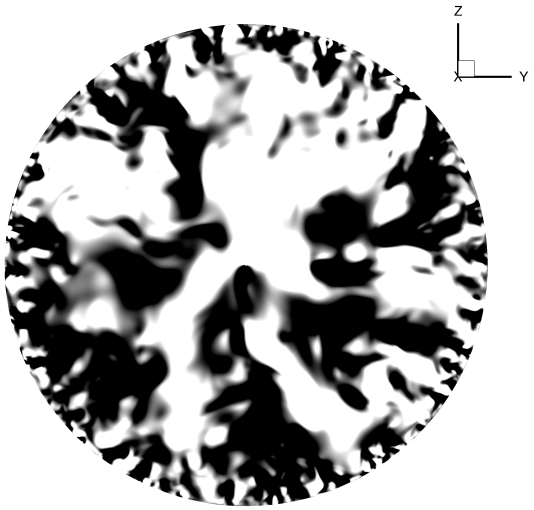

(b)

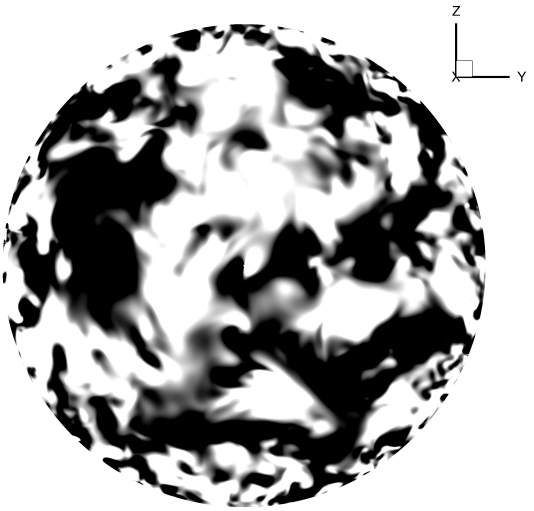

(c)

Figure 3.21: Instantaneous flow field of flow case CH15C in the cross-stream plane. Velocity fluctuations u'(a) v'(b), and w'(c), normalized with their density scaled rms value, 48 contour levels $-0.5 < u_i'/(\sqrt{\rho/\rho_w}u_{irms}) < 0.5$, from dark to light shades.

3.2.2 Compressibility transformations

As a first step the cylindrical solver is validated in the incompressible regime comparing case P02 in Tab. 3.4 to the data by Wu and Moin [160] at low Reynolds number. Figure 3.22 shows that agreement is satisfactory, both for mean velocity and turbulent stresses. The supersonic simulation by Ghosh et al. [52] is also reproduced (case P13 in Tab. 3.4), doubling the mesh resolution in x and θ with respect to Ghosh et al. [52]. Figure 3.23 shows the averaged van Driest velocity profile and turbulent stresses, together with Ghosh's mean statistics. Data are in good agreement except for a minor difference in the peak of τ_{11} which is known to be very sensitive to mesh resolution and numerical scheme. Another minor discrepancy is the value of the additive logarithmic constant, which is lower in the mean velocity profile by Ghosh et al. [52]. This can be explained by the fact that, for the same bulk Reynolds number, we obtain a slightly lower Reynolds number, $Re_\tau = 235$ rather than 245, reported by those authors. This can probably be attributed to the lower mesh resolution used by Ghosh et al. [52] in the azimuthal direction, $\Delta x^+ = 9.5$, $R\Delta\theta^+ \approx 12$.

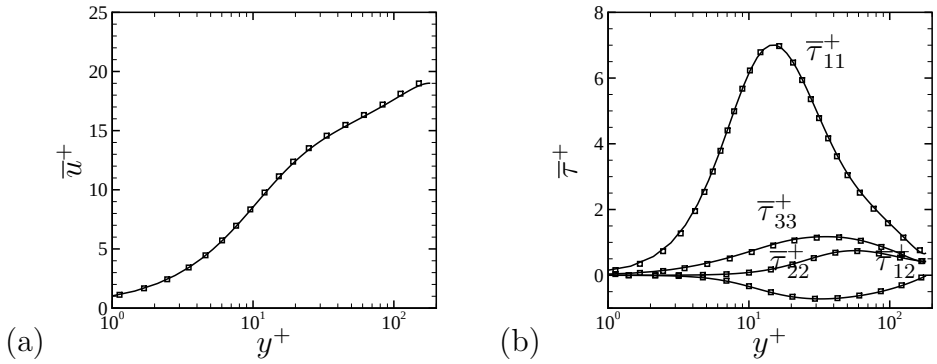

Figure 3.22: Comparison between P02 (black solid) and Wu and Moin [160] (squares). (a) Mean velocity u^+ (b) Turbulent stresses τ_{ij}

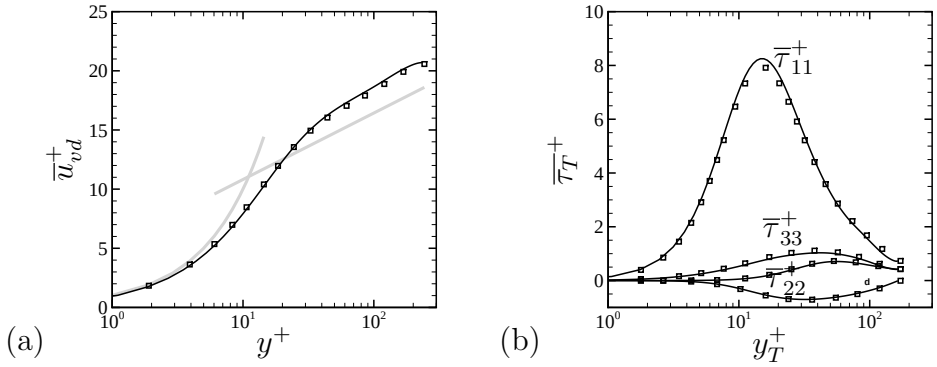

Figure 3.23: Comparison between P13 (black solid) and Ghosh et al. [52] (squares). (a) van Driest transformed velocity (b) Turbulent stresses transformed according to Huang. The thick gray lines in panel (a) represent the law of the wall $u^+ = y^+$, $u^+ = 1/k \log(y^+) + B$, $k = 0.41$, $B = 5.2$.

We note that the van Driest transformation is inaccurate, in the sense that the transformed profile does not collapse on the incompressible log-law, with an additive constant $B \approx 6$. This result is consistent to what found in Section 3.1 for the channel flow. The accuracy analysis on compressibility transformations performed in Section 3.1 for channel flow is expected to yield similar results in the case of pipe, so that we limit ourself to scrutinize the performance of TL transformation which is expected to be most accurate. The integrated mean momentum balance equation for pipe flow is in fact,

$$\overline{\mu}\frac{\mathrm{d}\widetilde{u}}{\mathrm{d}y} - \overline{\rho}\widetilde{u''v''} = \overline{\rho}_w u_\tau^2 \left(1 - \frac{y}{R}\right), \tag{3.30}$$

with $y = R - r$ the distance from the wall. Eqn. (3.30) is the same as in channel flow, Eqn. (3.3), hence the same arguments that led to the derivation of TL transformation also hold for pipe flow. Figure 3.24 shows the mean transformed velocity profile for compressible pipe flow (Tab. 3.4) and channel flow (Tab. 3.1) compared with incompressible pipe data. Flow cases P15A-CH15A and P3-CH3 are compared with incompressible data by Verzicco and Orlandi [151]. Cases P15C-CH15C are compared with data by Wu and Moin [160] at matching transformed Reynolds number, whereas no incompressible data at matching Re_τ are available for case P15B. Figures 3.24a-3.24d highlight major differences between compressible pipe and channel flow, starting from the buffer layer up to the core layer. In particular, pipe flow shows higher additive logarithmic constant than channel at low Reynolds number. These differences can be attributed to low Reynolds number effects, which

are stronger in pipe than in channel, mainly due to the geometrical confinement. Simulations P15B-P15C at higher Reynolds number, in Figs. 3.24b-3.24c, clearly show that as the Reynolds number increases near-wall similarity between pipe and channel flow is recovered, whereas a stronger wake region emerges in pipe flow. Variations from incompressible data can be observed for cases P15A-P3, which highlight limitations of TL transformation at low Reynolds number. This failure is also observed, although less evident, also in channel flow (see Fig. 3.10), which also confirms stronger persistency of low-Reynolds-number effects in pipe with respect to channel.

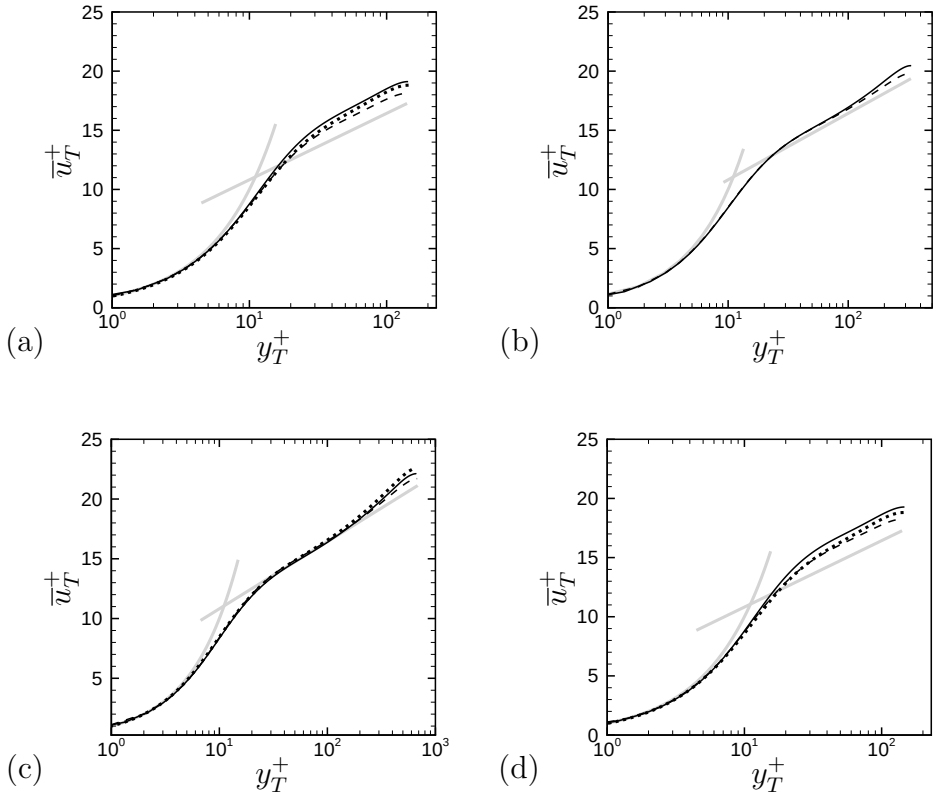

Figure 3.24: Mean velocity profile transformed according to TL. Pipe mean velocity (solid) is compared to channel mean velocity (dashed) at approximately matching $Re_{\tau H}$, for case P15A (a) P15B (b) P15C (c) P3 (d). Dotted lines in panels (a-c-d) represent incompressible data by Verzicco and Orlandi [151] at $Re_\tau = 140$ and by Wu and Moin [160] at $Re_\tau = 680$. Thick gray lines represent the law of the wall, $u^+ = y^+$, $u^+ = 1/0.41 \log(y^+) + 5.2$.

Similar conclusions can be drawn from scrutiny of the Reynolds stresses, transformed according to Huang, Fig. 3.25. The Reynolds stresses of pipe and channel flow show large similarities across the whole wall layer as the Reynolds

number increase. Ghosh et al. [52] found differences in the wall-normal velocity variance of supersonic pipe and channel flow, which are only minor in our case, Fig. 3.25a. At moderately high Reynolds number, Figs. 3.25b-c pipe and channel flow data are almost indistinguishable except for a minor difference in the streamwise variance peak, which is higher for the channel flow. This has also been observed by the recent study performed by Chin et al. [26], who observed considerable agreement in the Reynolds stresses of incompressible channel and pipe flow with a higher peak of the streamwise variance peak for the channel flow at $Re_\tau \approx 1000 - 2000$. Cases P15A-P3 in Fig. 3.25a-d show an opposite trend, with higher streamwise peak for the pipe flow. The different peak growth with Reynolds number between channel and pipe may be a hint of different outer/inner layer interaction in the two flows [1]. Comparison with the incompressible stresses from [151, 160] shows excellent agreement with increasing $Re_{\tau H}$, except for the streamwise variance peak which, as for the channel flow, is constantly higher than the incompressible one and seems the only genuine compressibility effect.

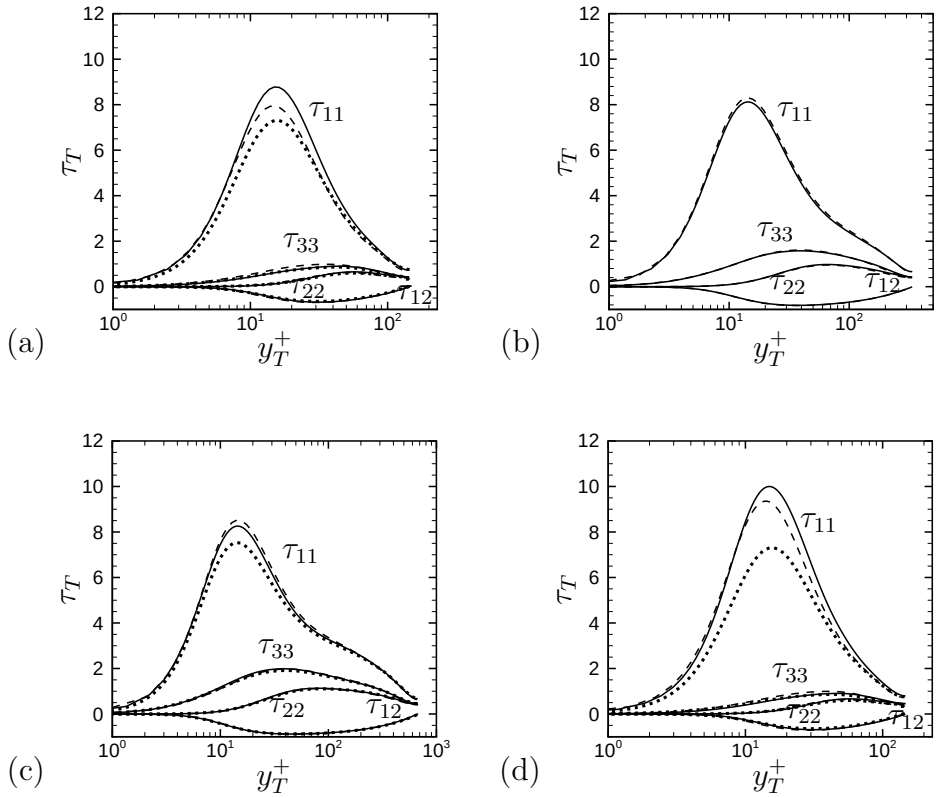

Figure 3.25: Streamwise turbulent stress transformed according to Huang. Pipe flow data (solid) are compared to channel flow (dashed) at approximately matching $Re_{\tau H}$, for case P15A (a) P15B (b) P15C (c) P3 (d). Dotted lines in panels (a-c-d) represent incompressible data by Verzicco and Orlandi [151] at $Re_\tau = 140$ and by Wu and Moin [160] at $Re_\tau = 680$.

Closer understanding of differences between pipe and channel can be gained from inspection of the core region. The fact that in the outer region turbulent eddies are scarcely influenced by the wall led Pirozzoli [115] to use the hypothesis of constant eddy viscosity in this region, which is used to derive a parabolic law for velocity in the core part of the channel. In Section 3.1 we showed that the van Driest transformed mean velocity profiles follow the universal parabolic law, given in Eqn. (3.16). Figure 3.26 shows the van Driest velocity profile in defect form as a function of $\eta = y/R$. Good agreement with the universal parabolic law is observed at high Reynolds number (Fig. 3.26c), although somehow better agreement was found for channel flow, recalling Fig. 3.11. The cause may be found in the fact that the constant c_μ was estimated [115] by fitting Princeton Superpipe data, at much higher Reynolds number than the present DNS. Although Eqn. (3.16) is formally derived for van Driest transformed velocity, TL transformation also follows

the incompressible parabolic law, since at the pipe core mean density gradients are small and TL transformation is close to van Driest.

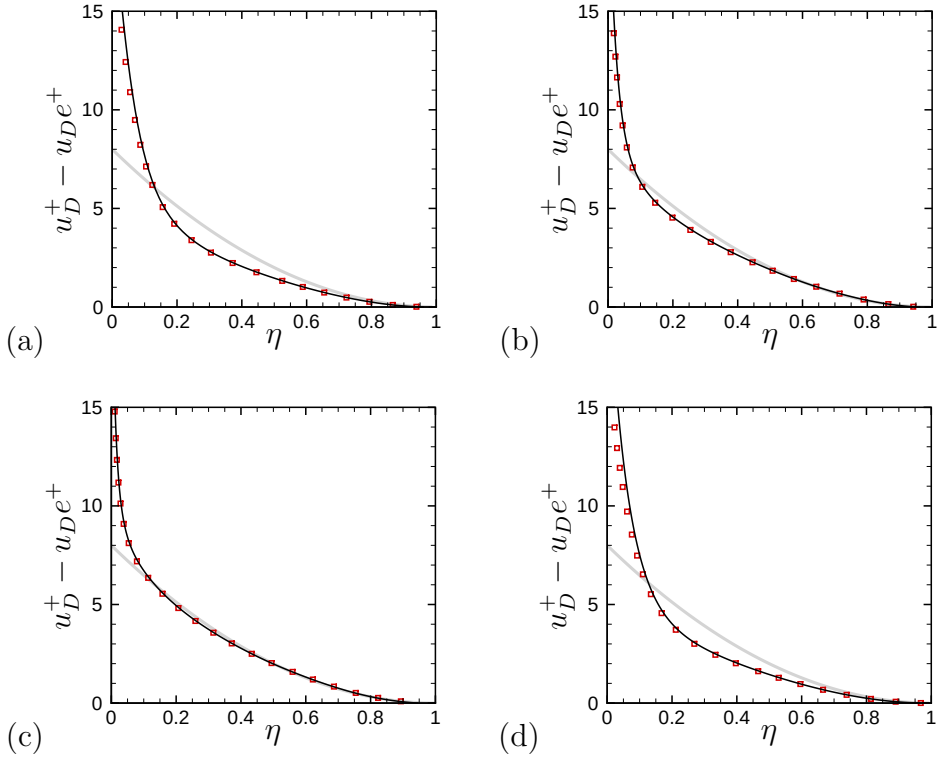

Figure 3.26: van Driest (black solid) and TL (red squares) transformed mean velocity as a function of $\eta = y/h$ for cases P15A (a), P15B (b), P15C (c) and P3 (d). The gray line represents Eqn. (3.16), with $c_\mu^* = 0.0625$. The subscript 'e' denotes properties at the pipe centerline.

3.2.3 Mean temperature and vorticity fluctuations

In Section 3.1 we showed that semi-local scaling can be used to map compressible vorticity fluctuations to *"incompressible"* ones with reasonable accuracy. Figure 3.27 shows mean vorticity fluctuations in semi-local scaling compared to compressible channel flow data. The agreement between vorticity fluctuations in pipe and channel is clear, except for P3-CH3, for which higher mean temperature variation occurs.

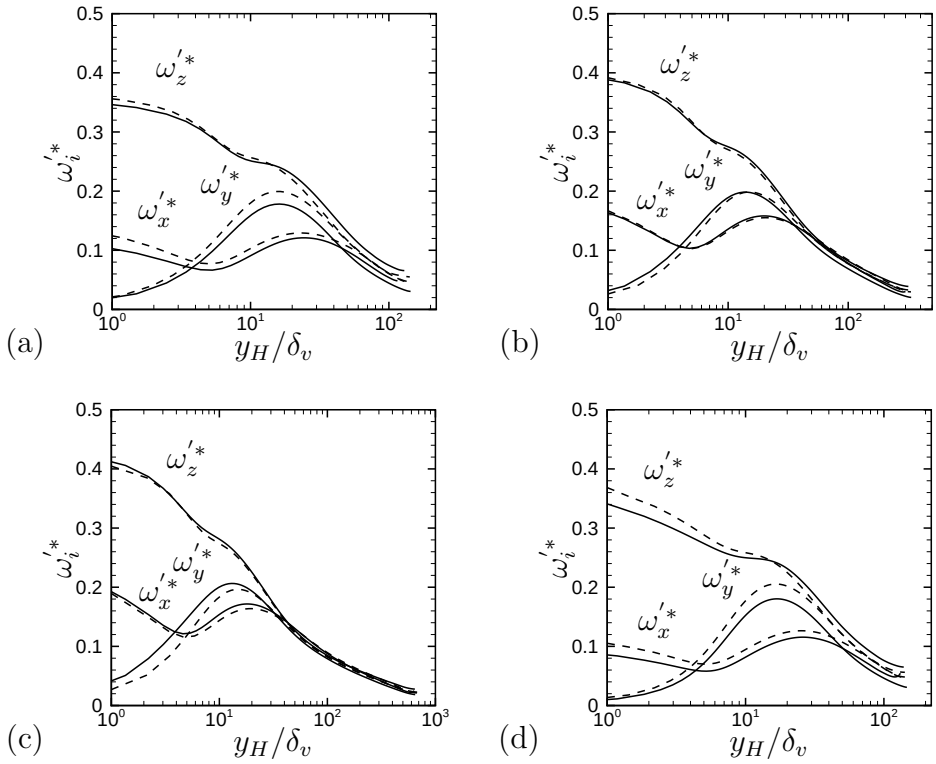

Figure 3.27: Vorticity fluctuations in semi-local scaling $\omega_i^{i*} = \omega_i^{'}\delta_v^* u_\tau^*$ for pipe (solid) and channel (dashed) flow, cases CH15A-P15A (a), CH15B-P15B (b), CH15C-P15C (c) and CH3-P3 (d).

A key point in the study of compressible wall-bounded turbulence is the temperature velocity relation. Successful definition of a relation between temperature and velocity in fact allows to use compressibility transformations the other way round (mapping incompressible velocity into compressible), thus leading to van Driest II like transformations for the friction coefficient. Classical Walz [156] relation, Eqn. (3.20), is known to be inaccurate in the case of isothermal boundary layer [35], while the relation obtained by Zhang et al. [165], Eqn. (3.21), explicitly take into account thermal wall flux and it has been tested for isothermal boundary layers [35, 165] and channel flow [91], proving its validity. Figure 3.28 shows the mean temperature profile as a function of velocity for pipe flow, compared to Zhang et al. [165] relation, Eqn. (3.21). The temperature-velocity relationship for channel flow is also shown for comparison. Maximum temperature in pipe flow is higher than in channel, for given bulk Mach number, meaning that circular geometry yields higher aerodynamic heating. Zhang's relation confirms its accuracy also in the case of pipe flow, with better agreement as the Reynolds number increases.

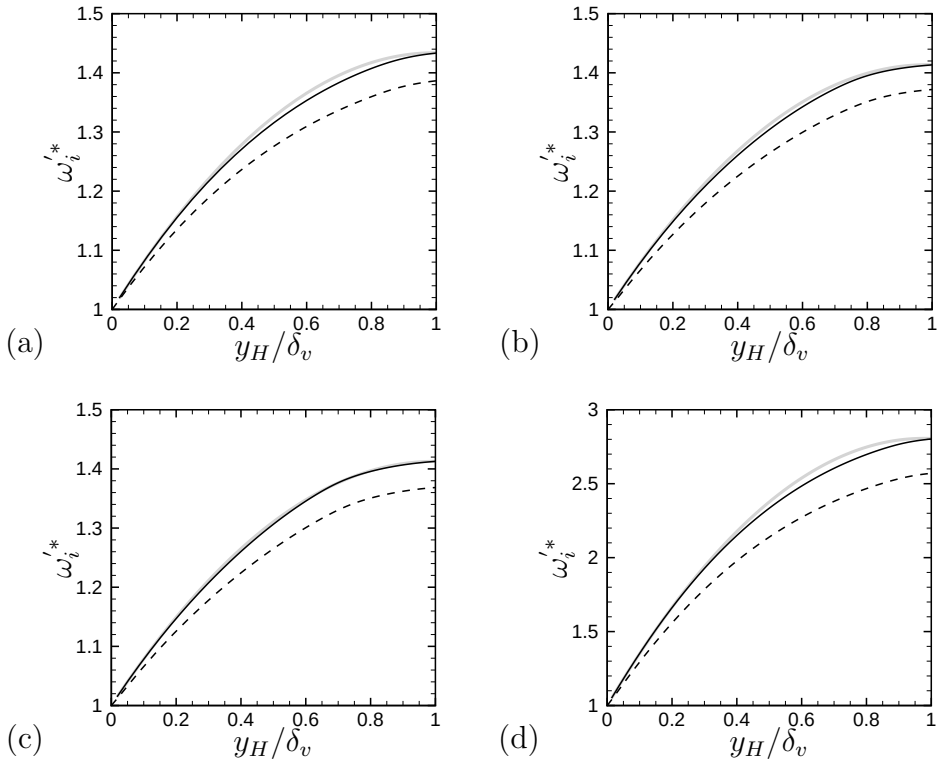

Figure 3.28: Temperature-velocity relationship: mean temperature as a function of mean velocity. Pipe flow (solid) is compared with channel (dashed). Thick gray line represents Zhang et al. [165] relation, Eqn. (3.21). Panel (a) P15A, (b) P15B, (c) P15C, (d)P3.

3.2.4 Length scales and velocity spectra

As pointed out in Section 3.1.4 the effect of compressibility on turbulent length scales is not well understood. Pirozzoli [114] proposed a scaling for the integral length scales in the outer part of the wall layer, which is based on local mean shear and local friction velocity, Eqn. (3.25). In this work we limit to study the integral length scale of the streamwise velocity through normalized spectral densities, Eqn. (3.27). Normalized spectral densities and integral length scales are related through Eqn. (3.28). Pirozzoli [119] recently performed a survey on the integral length scales in different wall-bounded turbulent flows using normalized energy spectra. As for pipe flow, this analysis is limited to experimental data, both in azimuthal and streamwise direction. It is known that obtaining spectra in the azimuthal direction is rather difficult, since Taylor hypothesis cannot be used, while spectra in the streamwise direction do not contain clear information on the integral length scales since momentum streaks in the flow direction are

essentially infinite [64]. Hence, DNS data may help to shed light on the scaling of the integral length scales. Figure 3.29 shows normalized spectra of the streamwise velocity at different stations from the wall all laying in the outer layer region, $50/Re_{\tau H} \leq \eta \leq 0.7$. Figures. 3.29a-d-g-l show that spectra at different wall stations have peaks which are spread out in terms of λ_z/R. For this purpose we introduce the wavenumber $\widetilde{k}_z = k_z \frac{R}{r}$, in which a geometric factor is taken into account, and the corresponding associated wavelength $\widetilde{\lambda}_z = 2\pi/\widetilde{k}_z$. Figures 3.29b-e-h-m clearly show that spectral peaks occur at the same normalized wavelength $\frac{\widetilde{\lambda}_z}{R} \approx 1$, that is energy containing eddies have size which scale as $\widetilde{\lambda}_z \sim R$, in the outer layer. In order to derive a scaling similar to Eqn. (3.25) for pipe flow we reason that at the pipe core large structures must shrink due to space limitations, and their size should diminish towards the axis. Ahn et al. [2], Lee et al. [78] also pointed out differences between large scale structures in pipe and channel flow, proving that their time decay is faster in pipe than in channel. For this reason we modify Eqn. (3.25) substituting h with r,

$$\ell_{12}^* \sim (u_\tau^* r)^{1/2} \left(\frac{\mathrm{d}\tilde{u}}{\mathrm{d}y} \right)^{-1/2}. \tag{3.31}$$

Figures 3.29c-f-i-n show streamwise velocity spectra as a function of $\frac{\widetilde{\lambda}_z}{\ell_{12}^*}$. Incompressible channel flow spectra (flow cases in Tab. 3.2) are also plotted for comparison. Apart for cases P15A-P3 which share a relatively low $Re_{\tau H}$ the agreement between compressible pipe and incompressible channel is striking, which support the validity of Eqns. 3.25-3.31 as scaling of the integral length scales for channel and pipe flow. The successful collapsing of the spectra in Figs. 3.29c-f-i-n imply that integral length scales are not affected by compressibility, as found for compressible channel flow also.

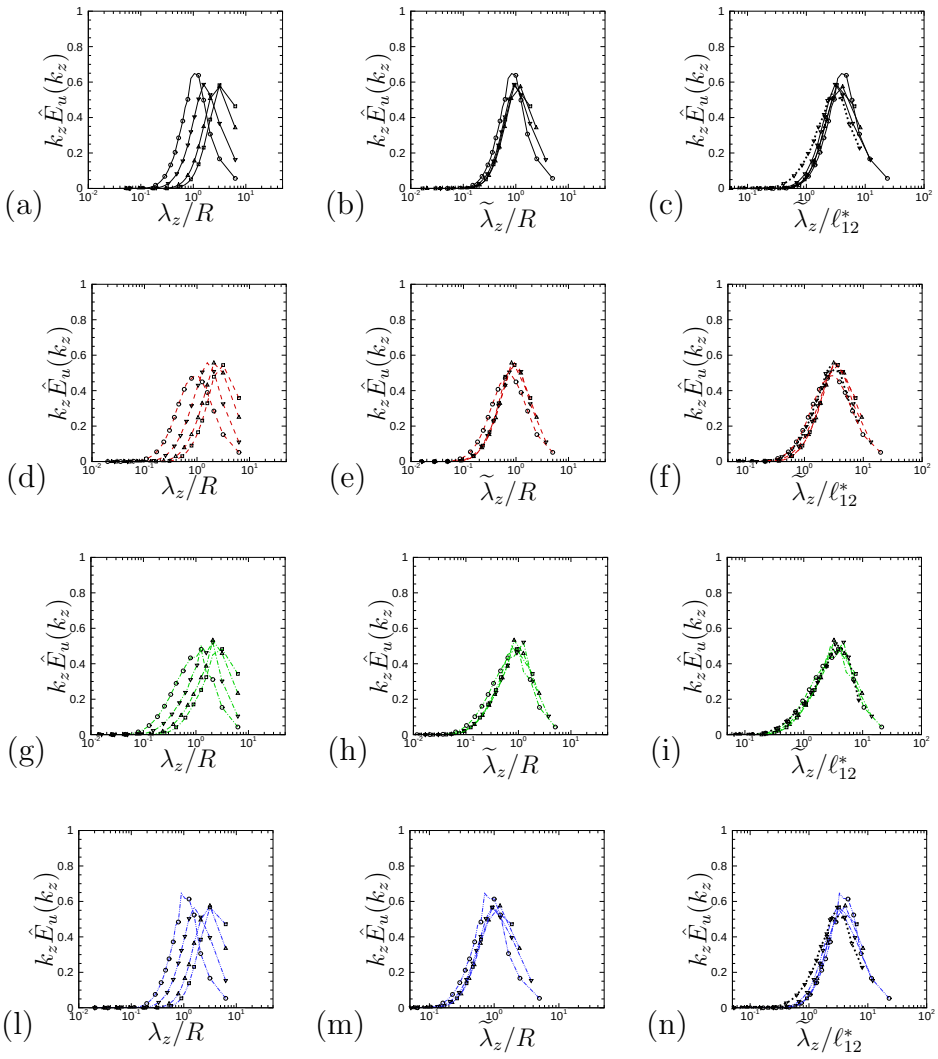

Figure 3.29: Pre-multiplied power spectral densities of u in azimuthal direction as a function of λ_z/h (a-d-g-l), $\widetilde{\lambda}_z/R$ (b-e-h-m) and $\widetilde{\lambda}_z/\ell^*_{12}$ (c-f-i-n). Symbols denote different distances from the wall, namely $\eta = 0.2$ (circles), $\eta = 0.4$ (gradients), $\eta = 0.6$ (deltas), $\eta = 0.7$ (squares). Dotted lines in figures (c-f-i-n) denote incompressible channel flow at matching $Re_{\tau H}$, at $\eta = 0.4$.

3.2.5 Passive scalar transport

In this Section we focus on passive scalar transport in compressible pipe flow. We consider two passive scalars with Schmidt number $Sc = 1, 0.71$ for each flow case in Tab. 3.4, so as to compare passive scalar flow statistics with velocity and temperature

profiles respectively. The mean passive scalar balance equation reads,

$$\overline{\rho\alpha}\frac{\mathrm{d}\widetilde{\phi}}{\mathrm{d}y} - \bar{\rho}\widetilde{\phi''v''} = \overline{\rho}_w\phi_\tau^2\left(1-\frac{y}{R}\right), \tag{3.32}$$

where $\alpha = \frac{\mu}{\rho Sc}$ is the passive scalar diffusivity and $\phi_\tau = \frac{\alpha_w}{u_\tau}\frac{\partial\widetilde{\phi}}{\partial y}\big|_w = \frac{\mu_w}{\rho_w u_\tau Sc}\frac{\partial\widetilde{\phi}}{\partial y}\big|_w$ is the friction scalar. It is clear that for $Sc = 1$ Eqn. (3.32) is identical to the mean momentum balance equation, (Eqn. (3.30)), upon substitution of ϕ with the streamwise velocity u. This observation leads to expect that TL transformation for velocity also applies to Eqn. (3.32), thus allowing to transform passive scalar values into their incompressible counterpart. Hence by analogy with Eqn. (3.8) we propose,

$$y_I = \int_0^y f_I\,\mathrm{d}y, \quad \phi_T = \int_0^{\widetilde{\phi}} g_T\mathrm{d}\widetilde{\phi}, \tag{3.33}$$

where f_T and g_T are the same functions used to transform mean velocity, reported in Tab. 3.3. Figure 3.30 shows mean passive scalar profiles transformed according to Eqn. (3.33), in wall units.

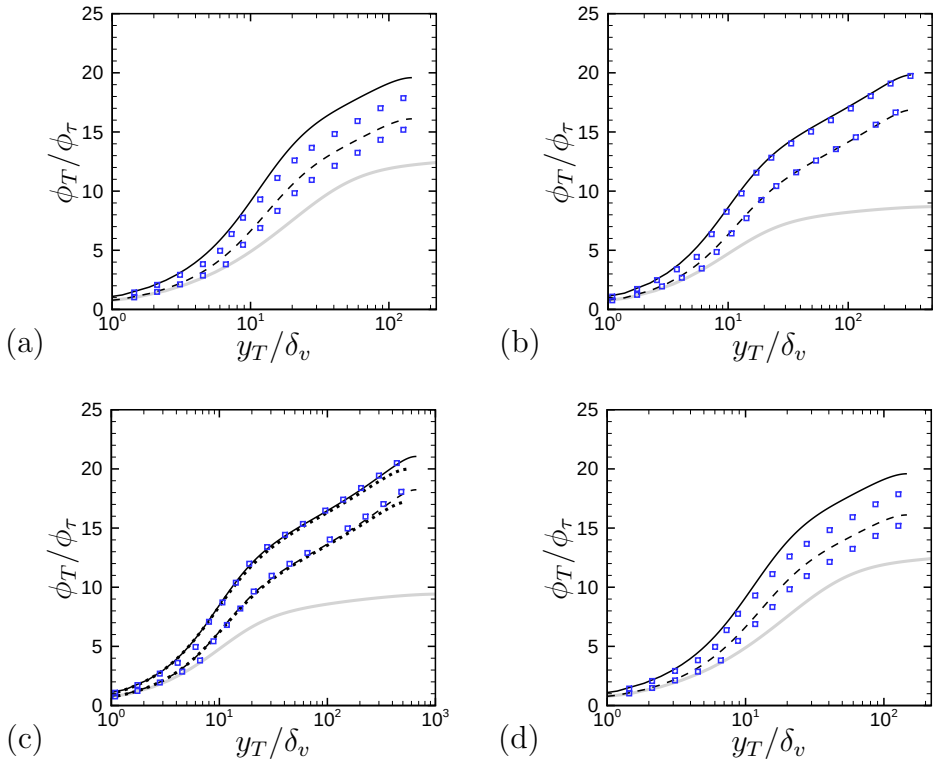

Figure 3.30: Mean values of passive scalars transformed according to TL, at Schmidt number $Sc = 1$ (solid) and $Sc = 0.71$ (dashed) for cases P15A (a), P15B (b), P15C (c), P3 (d). Kader [68] fit is also shown (blue squares). Dotted lines in panel (c) represents passive scalars in incompressible channel flow from Pirozzoli et al. [118] at corresponding Schmidt number and approximately matching Reynolds number. Thick gray lines indicate temperature profile in wall units, $T^+ = (T - T_w)/T_\tau$.

The transformed mean scalar distributions are also compared to incompressible passive scalar fits proposed by Kader [68] for internal flows. Kader's fits were obtained from high- Reynolds-number experiments, hence it is not surprising that they do not match low-Reynolds-number flow cases P15A-P3, Figs. 3.30a-d. On the other hand high-Reynolds-number data(P15B-P15C Figs. 3.30b-c) show satisfactory agreement at both Schmidt numbers. Figure 3.30c also reports passive scalar distributions from incompressible channel flow at matching $Re_{\tau H}$ from the database by Pirozzoli et al. [118]. Agreement with incompressible channel flow is also excellent except for the core region, where pipe flow exhibits stronger wake region. Temperature profiles in wall units are also shown in Fig. 3.30 to highlight differences between temperature and passive scalar profiles. The main differences are observed as the Mach number increases, Fig. 3.30d, as the relative importance of viscous dissipation increases with Mach number. The successful transformation of the mean

passive scalar profile also supports for the use of Huang's transformation for the passive scalar fluctuations. We define the transformed passive scalar fluctuations as,

$$\widetilde{\phi''^2}_H = \frac{\overline{\rho}}{\overline{\rho}_w}\widetilde{\phi''^2} \quad , \left(\widetilde{\phi''^2 u''^2}\right)_H = \frac{\overline{\rho}}{\overline{\rho}_w}\widetilde{\phi''^2 u''^2} \quad , \left(\widetilde{\phi''^2 v''^2}\right)_H = \frac{\overline{\rho}}{\overline{\rho}_w}\widetilde{\phi''^2 v''^2} \tag{3.34}$$

Figure 3.31 shows passive scalar fluctuations for flow case P15C in wall units scaled according to Eqn. (3.34). Transformed statistics are compared with passive scalar in incompressible channel flow [118] at approximately matching $Re_{\tau H}$. The main difference is found in the peak value of the fluctuations, as for the transformed streamwise velocity variance, Fig. 3.25. We reason that the difference in the peak is due to compressibility effects rather than differences between channel and pipe flow, which for velocity variances show similar peaks [78]. This is somehow a clue that pressure, which is absent in passive scalar transport, does not play any role in the breakdown of Huang's scaling for the streamwise velocity variance peak.

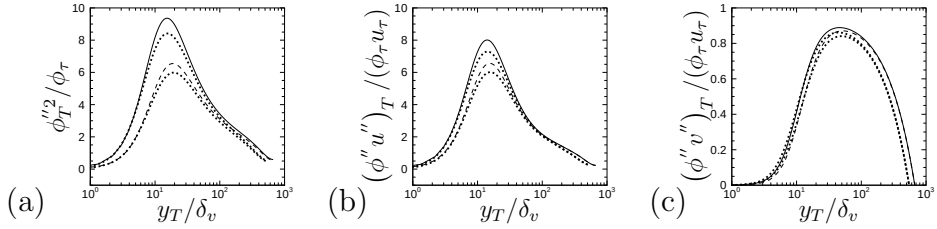

Figure 3.31: Passive scalars fluctuations transformed according to Huang, at Schmidt number $Sc = 1$ (solid) and $Sc = 0.71$ (dashed) for case P15C. Dotted lines represents passive scalars fluctuations in incompressible channel flow [118], at corresponding Schmidt number and approximately matching Reynolds number.

As done for the mean velocity we now focus our attention on passive scalar in the core part of the channel flow. Pirozzoli et al. [118] recently showed that a universal parabolic profile holds for passive scalar fields in the core part of incompressible channel flows. The same reasoning that led us to Eqn. (3.16) can be applied to passive scalar transport,

$$\phi_D^+ - \phi_{De}^+ = -\frac{1}{2c_\mu^*}\left(1-\eta\right)^2, \tag{3.35}$$

where ϕ_D is the passive scalar transformed according to van Driest. The subscript e denote quantities at the pipe axis. Eqn. (3.35) states that the van Driest transformed passive scalar follows the incompressible universal parabolic law derived by Pirozzoli

et al. [118]. Figure 3.32 shows the passive scalars at $Sc = 1, 0.71$ in defect form compared to Eqn. (3.35). All flow cases follow the universal parabolic law down to $\eta \approx 0.2 - 0.3$.

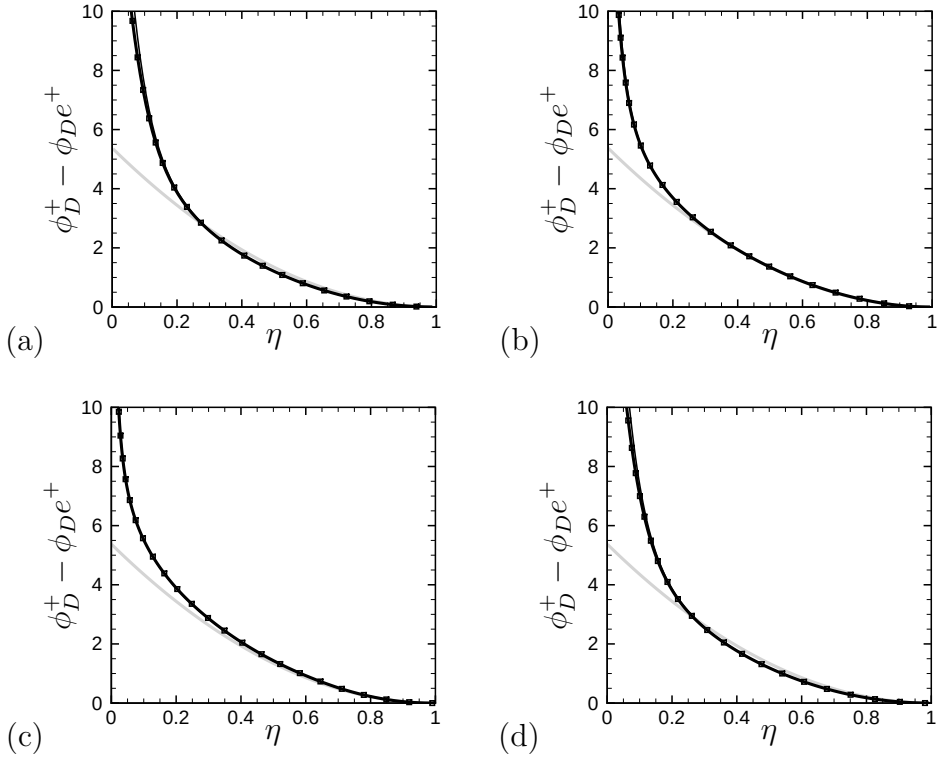

Figure 3.32: van Driest transformed mean scalar profiles as a function of $\eta = (1 - r)/R$ for flow cases P15A (a), P15B (b), P15C (c) and P3 (d), at Schmidt number $Sc = 1$ (solid) and $Sc = 0.71$ (squares). The gray line represents Eqn. (3.16), with $c_\mu^* = 0.093$. The subscript 'e' denotes quantities at the centerline.

The integral length scales of the passive scalar field are scrutinized through azimuthal spectral densities, Fig. 3.33. The spectra show that ϕ is highly correlated with the streamwise velocity, as they follow the same scaling as in Fig. 3.29. The peak of the spectral densities is located at $\widetilde{\lambda}_z \approx R$, which highlights that this is the size of energy containing eddies. The definition of the characteristic length l_{12}^* of Eqn. (3.29) is properly modified for passive scalar field,

$$\ell_{12}^*(y) \sim (\phi_\tau r)^{1/2} \left(\frac{\mathrm{d}\phi_D}{\mathrm{d}y} \right)^{-1/2}, \tag{3.36}$$

where ϕ_D is the mean passive scalar profile transformed according to van Driest. Figures 3.33(c-f-i-n) show that the integral length scales of the passive scalar grow

according to Eqn. (3.36), similarly to what found for velocity. Comparison with incompressible passive scalar spectra would be necessary to assess that Eqn. (3.36) takes into account compressibility effects, nevertheless since we have shown that compressibility transformations for velocity accurate hold also for passive scalars we expect a proper collapsing of the integral length scales as well.

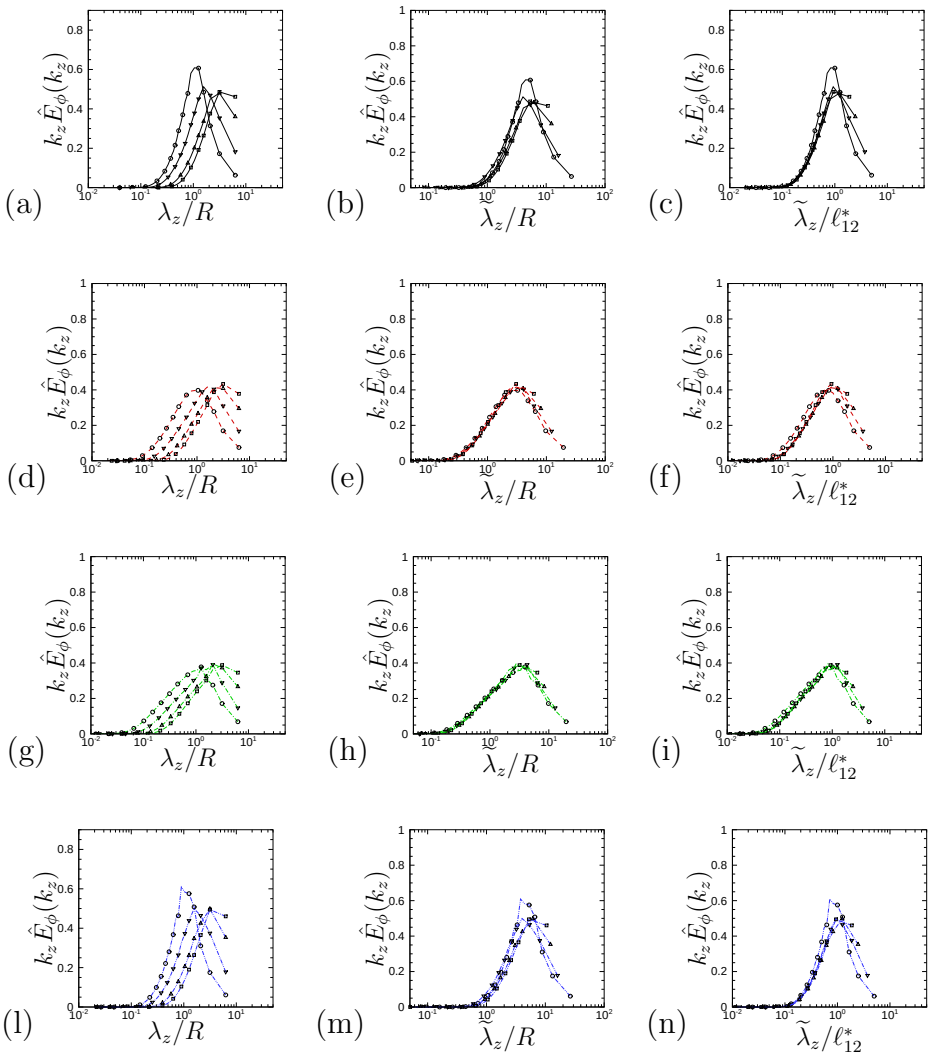

Figure 3.33: Pre-multiplied power spectral densities of the passive scaler ϕ at $Sc = 1$ in azimuthal direction as a function of λ_z/h (a-d-g-l), $\widetilde{\lambda}_z/R$ (b-e-h-m) and $\widetilde{\lambda}_z/\ell^*_{12}$ (c-f-i-n). Symbols denote different distances from the wall, namely $\eta = 0.2$ (circles), $\eta = 0.4$ (gradients), $\eta = 0.6$ (deltas), $\eta = 0.7$ (squares).

3.3 Compressible flow in rectangular duct

DNS of compressible rectangular duct flow have been carried out at three bulk Mach numbers, $M_b = 0.2, 1.5, 3$, (see Tab. 3.5). For the flow case at $M_b = 1.5$ we carried out DNS by changing the aspect ratio ($\mathit{Æ}$) in the range $\mathit{Æ} = 1 - 4$, whereas for the other flow cases only a square cross-section is considered. Fig. 3.34 indicates the duct flow geometry in the cross-stream section, with the notation that will be used in the following. The side length in y direction is fixed to $2h$, whereas the side length in z direction depends on the aspect ratio, $2h\mathit{Æ}$, and for this reason z coordinate will be reported in non-dimensional form $z/(h\mathit{Æ})$ in the following. Fig. 3.34 also shows red lines at constant $z/(h\mathit{Æ})$ which will be used as reference sections.

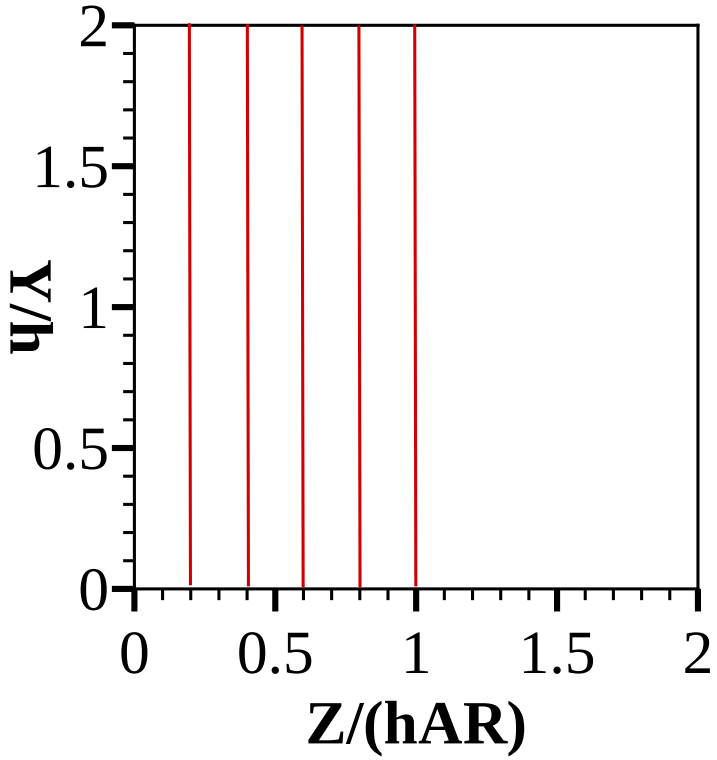

Figure 3.34: Sketch of the duct flow domain. The duct height in y direction is fixed, $2h$, whereas the spanwise width in z direction depends on the aspect ratio. Red lines indicate test sections at $z/(h\mathit{Æ}) = 0.2, 0.4, 0.8, 1$.

The maximum friction Reynolds number achieved is $Re_\tau \approx 1000$ at $M_b = 0.2$, which, to our knowledge, is the highest achieved so far [164]. Supersonic flow simulations are carried out using ATI-YZ algorithm, whereas ATI-XYZ is used for the subsonic DNS. As for plane channel and pipe flow attention is focused

on studying the validity of compressibility transformations in the case of three dimensional mean flow.

Case	$\mathcal{R}$	M_b	Re_b	Re_τ	$Re_{\tau H}$	N_x	N_y	N_z	M_τ	$-B_q$	$\Delta t_{av} u_\tau / h$
D02A-$\mathcal{R}$1	1	0.2	4410	150	145	512	128	128	0.082	0.001	702.0
D02B-$\mathcal{R}$1	1	0.2	40000	1054	1035	2048	512	512	0.0008	0.0008	64.4
D15-$\mathcal{R}$1	1	1.5	6000	228	102	512	128	128	0.082	0.045	264.2
D15-$\mathcal{R}$2	2	1.5	6000	224	101	512	128	256	0.081	0.046	336.2
D15-$\mathcal{R}$4	4	1.5	6000	221	100	512	128	512	0.080	0.047	354.5
D3 -$\mathcal{R}$1	1	3.	9760	483	54	1024	256	256	0.12	0.13	68.0

Table 3.5: Compressible duct flow dataset. $\mathcal{R}$ is the aspect ratio of the duct. $M_b = u_b/c_w$ and $Re_b = 2\rho_w u_b h/\mu_w$ the bulk Mach and Reynolds number respectively. $Re_\tau = h/\delta_v$ and $Re_{\tau H} = y_H(h)/\delta_v$ are the untransformed and transformed friction Reynolds number. N_i is the number of mesh points in the $i-$th direction, $M_\tau = u_\tau/c_w$ the friction Mach number and B_q the non-dimensional heat flux. Box dimensions are $6\pi h \times 2h \times 2h\mathcal{R}$ for all cases. Δt_{av} is the averaging time interval.

3.3.1 Instantaneous flow field

In this Section the instantaneous flow field of the duct flow is qualitatively described through the scrutiny of the cross-stream and streamwise planes. Figure 3.35 shows a three dimensional sketch of the duct flow case D02B-$\mathcal{R}$1, obtained through simultaneous visualizations of the cross-stream and streamwise planes at $y^+ = 15$. As in channel and pipe flow, Figs. 3.1-3.19, the streamwise velocity in the near wall region is characterize by streaky structures , elongated in the flow direction.

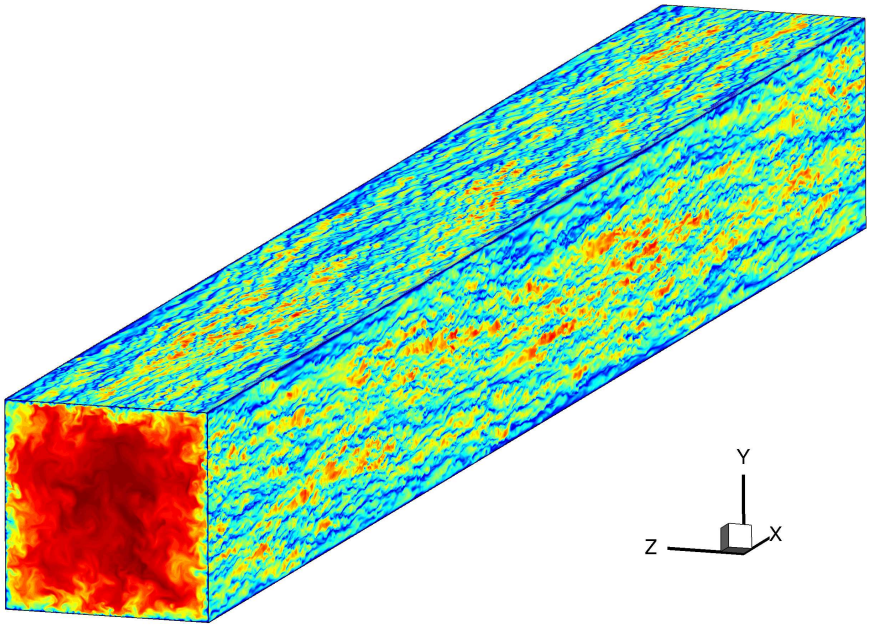

Figure 3.35: Instantaneous flow field of flow case D02B-$\mathcal{A}$1. Streamwise velocity contours in the cross-stream (yz) and wall-parallel (at $y^+ = 15$) planes are plotted.

Figure 3.36 shows the near wall streaks for the supersonic cases D15A-$\mathcal{A}$1, D15-$\mathcal{A}$2 and D15-$\mathcal{A}$4, with different aspect ratio. Velocity streaks observed in duct flow are qualitatively similar to channel and pipe flow, with the main difference that velocity goes to zero at the side walls. It seems that streaks are barely modified by the presence of the side walls, as variation from the classical streaky pattern only occurs very close to the sides. Figure 3.36a shows that for $\mathcal{A}$=1 the duct scarcely contains a couple of streaks, at this Reynolds number, whereas their number increases with the aspect ratio and the flow pattern of case D15-$\mathcal{A}$4 almost resembles the planar channel flow, Fig. 3.36.

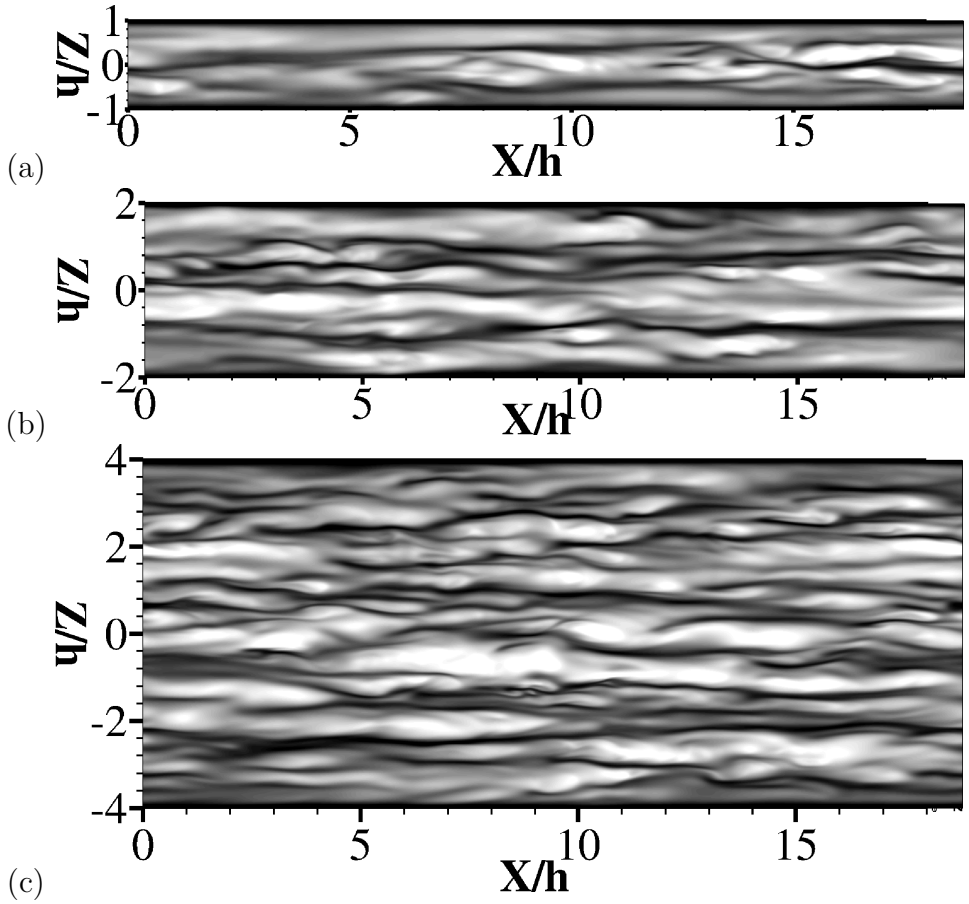

Figure 3.36: Instantaneous flow field of flow case D1515A-$\mathcal{A}$1(a), D15-$\mathcal{A}$2(b), D15-$\mathcal{A}$4(c). Streamwise velocity fluctuations in the xz, wall-parallel plane at $y^+ = 15$. Flow from left to right, 48 contour levels $-2 < u'/(\sqrt{\rho/\rho_w}u_{rms}) < 2$, from dark to light shades.

Figure 3.37 shows the mean velocity fluctuations in the cross-stream plane for flow case D02B-$\mathcal{A}$1. Streamwise velocity fluctuations are characterized by large eddies, which occupy the duct half section, from the core region down to the wall. The high correlation between the streamwise velocity fluctuations and the wall-normal ones, observed for channel and pipe flow is less evident for duct flow 3.37b. The spanwise velocity fluctuations w' in Fig. 3.37c do not show an organized structure and attached eddies [140] cannot be visualized.

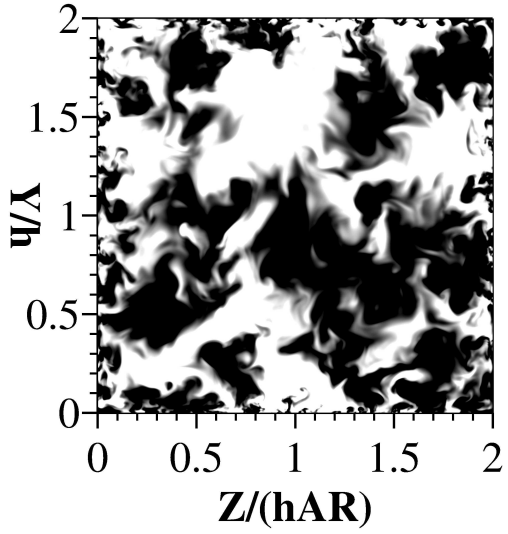

(a)

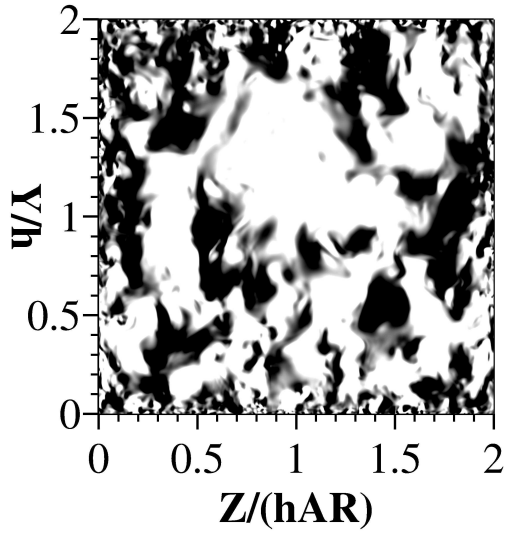

(b)

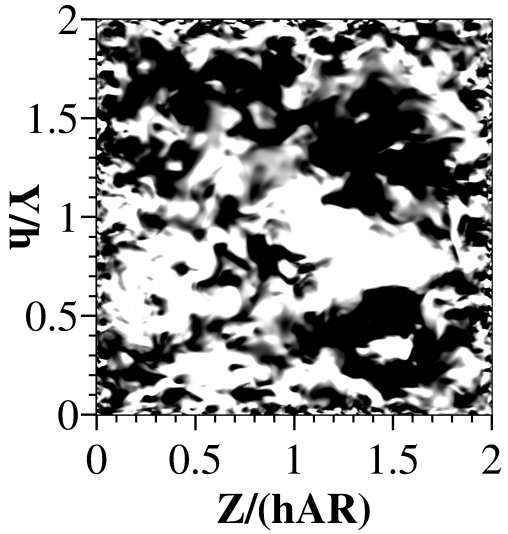

(c)

Figure 3.37: Instantaneous flow field of flow case D02B-$\mathcal{A}$R1 velocity fluctuations u'(a) v'(b), and w'(c). Streamwise velocity fluctuations are normalized with their density scaled rms value, 48 contour levels $-0.5 < u_i'/(\sqrt{\rho/\rho_w}u_{irms}) < 0.5$, from dark to light shades.

3.3.2 Compressibility transformations

In the case of rectangular duct flow both global and local wall units can be defined [50]. The global stress at the wall can be derived from mean momentum balance,

$$\tau_w = \rho_w u_\tau^2 = -\frac{1}{4} H \Pi, \tag{3.37}$$

where Π is the imposed pressure gradient, and $H = 4\frac{A}{P}$ the hydraulic diameter, A and P being the area and the perimeter of the duct section, respectively. The global viscous length scale is defined as $\delta_v = \nu_w/u_\tau$. Local friction velocity and viscous length scale can be defined based on the mean viscous stress at the wall, and denoted as $u_{\tau l}$ and δ_{vl} in the following. In order to test the validity of compressibility transformations, we reason on the mean momentum balance equation for the duct flow, which reads,

$$\frac{\partial \overline{\rho}\widetilde{u}\widetilde{v}}{\partial y} + \frac{\partial \overline{\rho}\widetilde{u}\widetilde{w}}{\partial z} = \frac{\partial}{\partial y}\left(\overline{\mu}\frac{\partial \widetilde{u}}{\partial y}\right) + \frac{\partial}{\partial z}\left(\overline{\mu}\frac{\partial \widetilde{u}}{\partial z}\right) - \frac{\partial \overline{\rho}\widetilde{u}\widetilde{v}}{\partial y} - \frac{\partial \overline{\rho}\widetilde{u}\widetilde{w}}{\partial z} - \Pi. \tag{3.38}$$

It is clear that the same arguments leading to the derivation of the TL transformation cannot be directly applied to Eqn. (3.38). Nevertheless, it is reasonable to assume that at the duct bisector $z/(Æh) = 1$, where $\frac{\partial}{\partial z} \approx 0$ and $v \approx 0$, the TL transformation still applies, since Eqn. (3.38) reduces to the mean momentum balance for planar channel flow. We first test TL transformation at the duct bisector, for the supersonic flow cases reported in Tab. 3.5. Figure 3.38 shows TL transformed velocity in local and global wall units, compared to transformed channel flow profiles and to the nearly incompressible duct flow data, D02A-$Æ1$. We note that the profiles scaled in global units do not follow the universal law of the wall $u^+ = y^+$ in the viscous sublayer. This result was also observed by Gavrilakis [50], but less evident in the incompressible case. We note in fact that the deviation from the universal law of the wall $u^+ = y^+$ becomes more evident as the Mach number increases. This deviation is small for case D02A-$Æ1$ (Fig. 3.38b) and it becomes evident for D3-$Æ1$ (Fig. 3.38d). Hence, in the following we will mainly use local wall units. Figure 3.38a shows that D02A-$Æ1$ profile is very close to the transformed planar channel case CH15A. The transformed duct velocity profile of case D15-$Æ1$ shows only minor differences with D02A-$Æ1$, while increasing the aspect ratio is sufficient to have nearly perfect agreement with CH15A, Fig. 3.38a. Major differences with the corresponding channel flow cases are found at $M_b = 3$, Fig. 3.38c-d. It is known that

increasing the Mach number, at fixed Reynolds number, causes relaminarization of the flow, with increased thickness of the viscous sublayer. In the case of a confined geometry, such as square duct flow, thickening of the viscous sublayer causes stronger side walls effects, so that the transformed mean velocity profile, differs from the incompressible case at matching local $Re_{\tau H} = y_T/\delta_{vl}$.

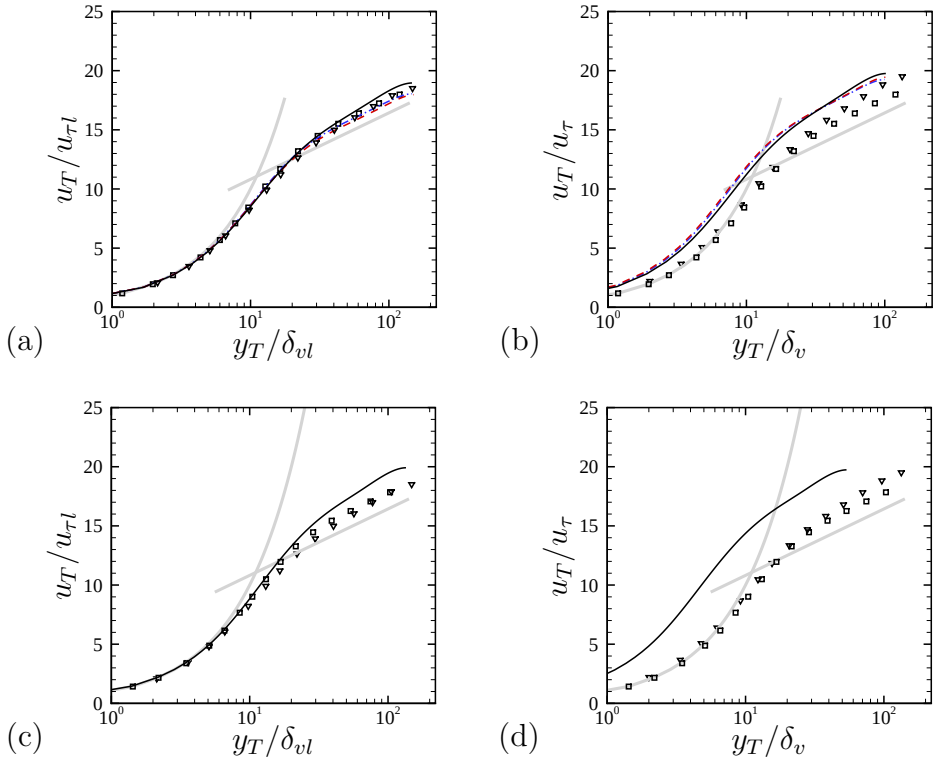

Figure 3.38: TL transformed velocity profile at duct bisector $z/(\mathcal{A}h) = 1$, for cases D15-$\mathcal{A}$1, D15-$\mathcal{A}$2, D15-$\mathcal{A}$4 (a-b) and M3-$\mathcal{A}$1 (c-d). Quantities in panels (a-c) and (b-d) are normalized by local and global wall units respectively. In panels (a-b) $\mathcal{A}$=1 (black solid) AR=2 (red dashed) AR=4 (blue dash-dotted). Gradient symbols represent case D02A-$\mathcal{A}$1. Square symbols represent planar channel flow data CH15A-CH3. Gray lines indicate the law of the wall $u^+ = y^+$, $u^+ = 1/0.41 \log(y^+) + 5.2$.

Although, accordingly to Eqn. (3.38), TL transformation should not hold approaching the wall, we test it to establish the minimum wall distance from which it can be applied. Figure 3.39 shows TL transformed velocity profile at different distances $z/(\mathcal{A}h)$ towards the wall, from which we note that different accuracy is found depending of the aspect ratio. For case D15-$\mathcal{A}$1 the transformation is reasonably accurate up to $z/(\mathcal{A}h) = 0.4$ (Fig. 3.39c), then it diverges from case D02A-$\mathcal{A}$1. Flow case D15-$\mathcal{A}$4 also follows with good accuracy the plane channel

profile up to $z/(\cancel{R}h) = 0.4$ (Fig. 3.39c), while minor divergence is observed at $z/(\cancel{R}h) = 0.2$ (Fig. 3.39d) It is surprising to note that the transformed velocity profile of $D3 - \cancel{R}1$ exhibits higher accuracy near the wall than at the duct center, probably owing to the fact that compressibility effects are smaller towards the side-wall.

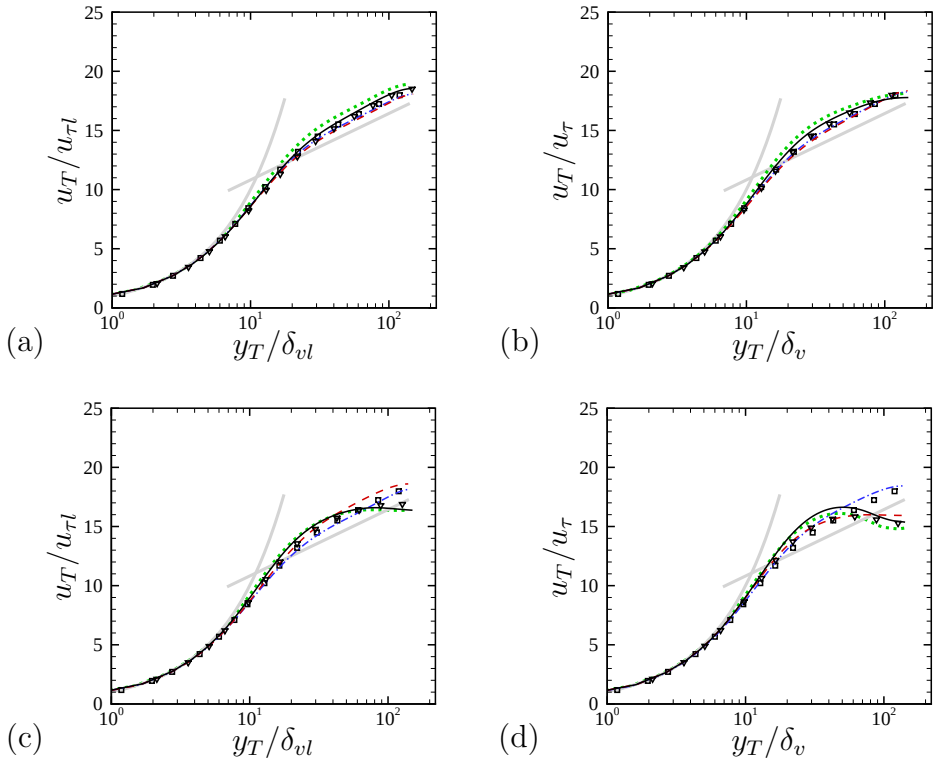

Figure 3.39: TL transformed velocity profile at $z/(h\cancel{R}) = 0.8$ (a), $z/(h\cancel{R}) = 0.6$ (b), $z/(h\cancel{R}) = 0.4$ (c), $z/(h\cancel{R}) = 0.2$ (d) from the wall, for cases D15-$\cancel{R}1$ (black solid), D15-$\cancel{R}2$ (red dashed), D15-$\cancel{R}4$ (blue dash-dotted) and D3-$\cancel{R}1$ (green dotted). Gradient and squares symbols represent case D02A-$\cancel{R}1$ and CH15A, respectively.

The overall picture that emerges from Fig. 3.39 is that TL transformation can be properly used in the whole duct section, with minor deviations from incompressible data. Velocity profiles of v/u_e and w/u_e, where u_e is streamwise velocity, at the duct centerline, are reported in outer units at different $z/(h\cancel{R})$ stations from the walls, Figs. 3.40-3.41. Surprisingly, v and w for cases D15-$\cancel{R}1$ and D02A-$\cancel{R}1$ are not very different, which is an evidence that compressibility affects on secondary motions are quite limited at $M_b = 1.5$. Some differences between D3-$\cancel{R}1$ and D02A-$\cancel{R}1$ are observed in the v and w profiles, at least towards the duct core (Figs. 3.40(a-b-c-d)). As the wall is approached (Figs. 3.40(e-f) and Fig. 3.41) the cross-stream velocity

components are in some way similar, for the same aspect ratio (cases D02A-$\mathcal{A}$1, D15-$\mathcal{A}$1 and D3-$\mathcal{A}$1) which seems a clue that secondary motions are insensitive to the Mach number. On the contrary, large differences are observed at different aspect ratios, cases D15-$\mathcal{A}$1, D15-$\mathcal{A}$2, D15-$\mathcal{A}$4, thus secondary motions are, as expected, affected by the shape of the cross-stream section.

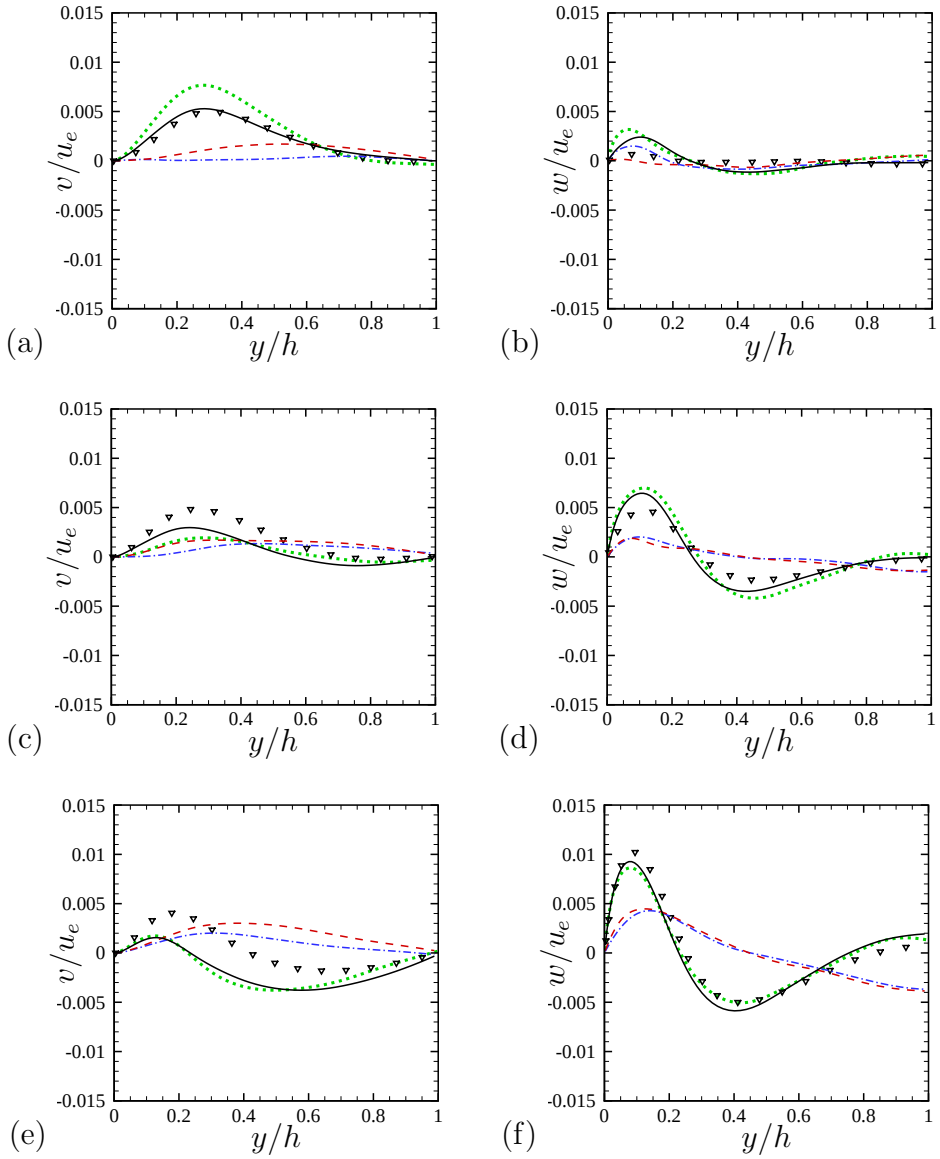

Figure 3.40: Velocity components in the cross-stream plane, v/u_e (a-c-e) and w/u_e (b-d-f). u_e is the centerline streamwise velocity. Profiles are taken at $z/(h\mathcal{A}) = 1$ (a-b), $z/(h\mathcal{A}) = 0.8$ (c-d), $z/(h\mathcal{A}) = 0.6$ (e-f) from the wall. Case D15-$\mathcal{A}$1 (black solid), D15-$\mathcal{A}$2 (red dashed), D15-$\mathcal{A}$4 (blue dash-dotted) D3-$\mathcal{A}$1 (green dotted) and D02A-$\mathcal{A}$1 (gradient symbols).

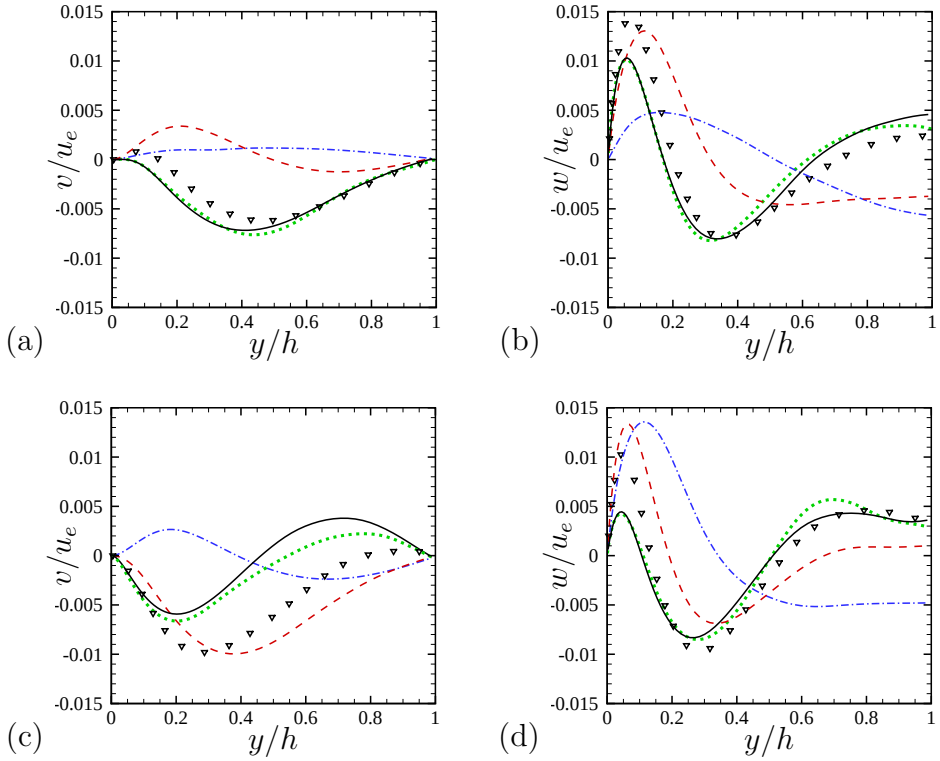

Figure 3.41: Velocity components in the cross-stream plane, v/u_e (a-c) and w/u_e (b-d). u_e is the centerline streamwise velocity. Profiles are taken at $z/(h\mathcal{R}) = 0.4$ (a-b), $z/(h\mathcal{R}) = 0.2$ (c-d) from the wall. Case D15-$\mathcal{R}1$ (black solid), D15-$\mathcal{R}2$ (red dashed), D15-$\mathcal{R}4$ (blue dash-dotted) D3-$\mathcal{R}1$ (green dotted) and D02A-$\mathcal{R}1$ (gradient symbols).

The accuracy of Huang transformation for Reynolds stresses can be gauged from inspection of Figs. 3.42-3.43-3.44, which show density-scaled velocity variances in direction x, y and z respectively at different wall stations $z/(h\mathcal{R})$. Figures 3.42(a-b), 3.43(a-b) 3.44(c-d) show that near the duct centerline, $z/(h\mathcal{R}) = 1$ and $z/(h\mathcal{R}) = 0.8$, density scaled variances collapse on the reference profiles of D02A-$\mathcal{R}1$. Consistently with what found for plane channel and pipe flow, the only discrepancy that can be observed is in the peak of the streamwise velocity variance of D15-$\mathcal{R}1$ and D3-$\mathcal{R}1$, which does not collapse on D02A-$\mathcal{R}1$ (Fig. 3.42a-b). On the other hand, we note the agreement of the streamwise velocity variance duct flow case D15-$\mathcal{R}4$ and planar channel case CH15A, also in the proximity of the wall Figs. 3.43(a-b-c-d) (the same was true for mean streamwise velocity, Fig. 3.39). This highlights that a relatively small aspect ratio ($\mathcal{R}$=4) is necessary for obtaining streamwise duct flow statistics resembling those of planar channel flow. The same conclusion does not hold for the velocity variances in the cross-stream plane, which

always differ from the plane channel case, especially for w, Fig. 3.44.

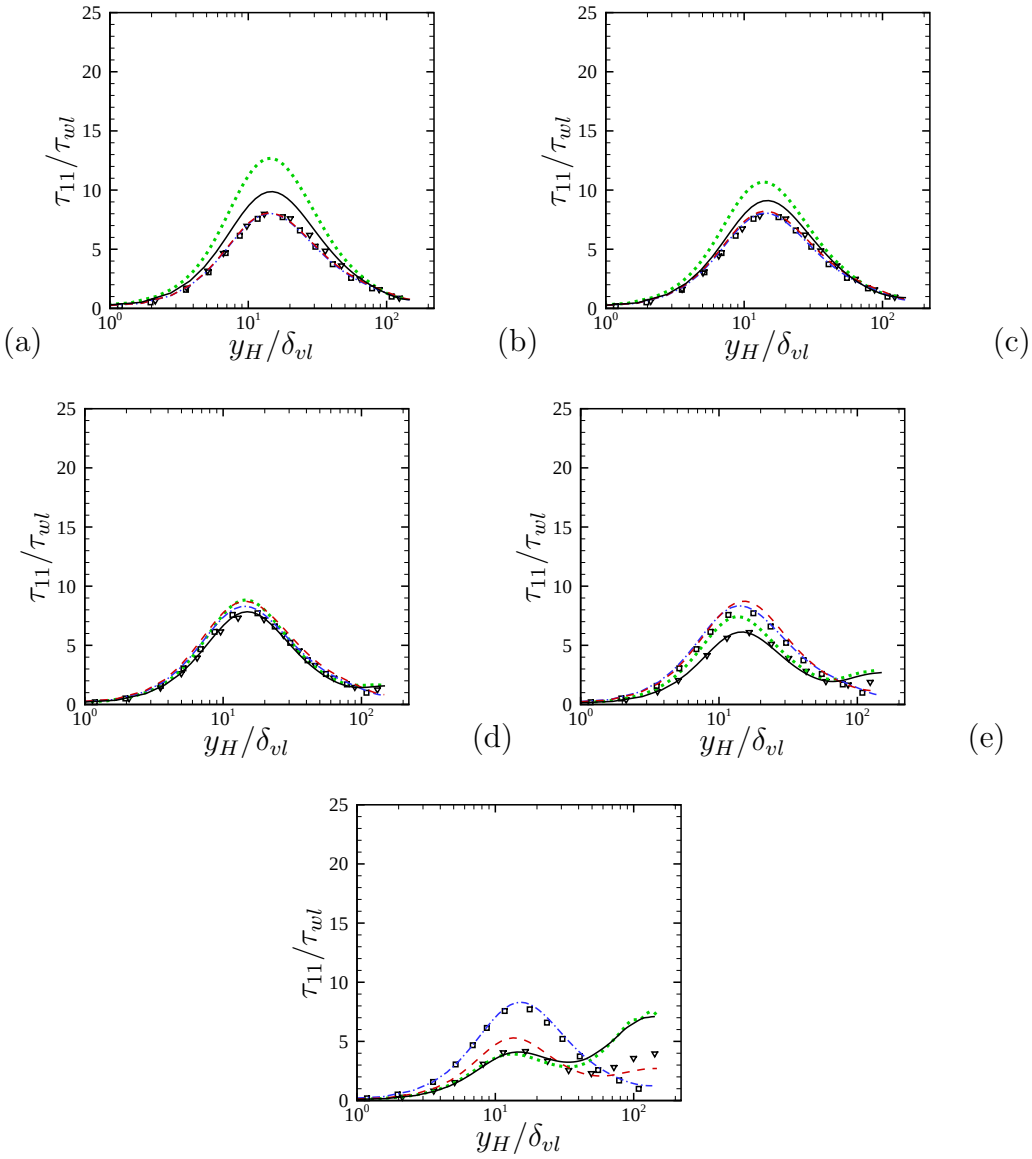

Figure 3.42: Streamwise velocity variance transformed according to Huang. Profiles are taken at $z/(h\mathcal{AR}) = 1$ (a), $z/(h\mathcal{AR}) = 0.8$ (b), $z/(h\mathcal{AR}) = 0.6$ (c), $z/(h\mathcal{AR}) = 0.4$ (d), $z/(h\mathcal{AR}) = 0.2$ (e) from the wall. Case D15-$\mathcal{AR}1$ (black solid), D15-$\mathcal{AR}2$ (red dashed), D15-$\mathcal{AR}4$ (blue dash-dotted), D3-$\mathcal{AR}1$ (green dotted), and D02A-$\mathcal{AR}1$ (gradients). Planar channel data CH15A are indicated by square symbols.

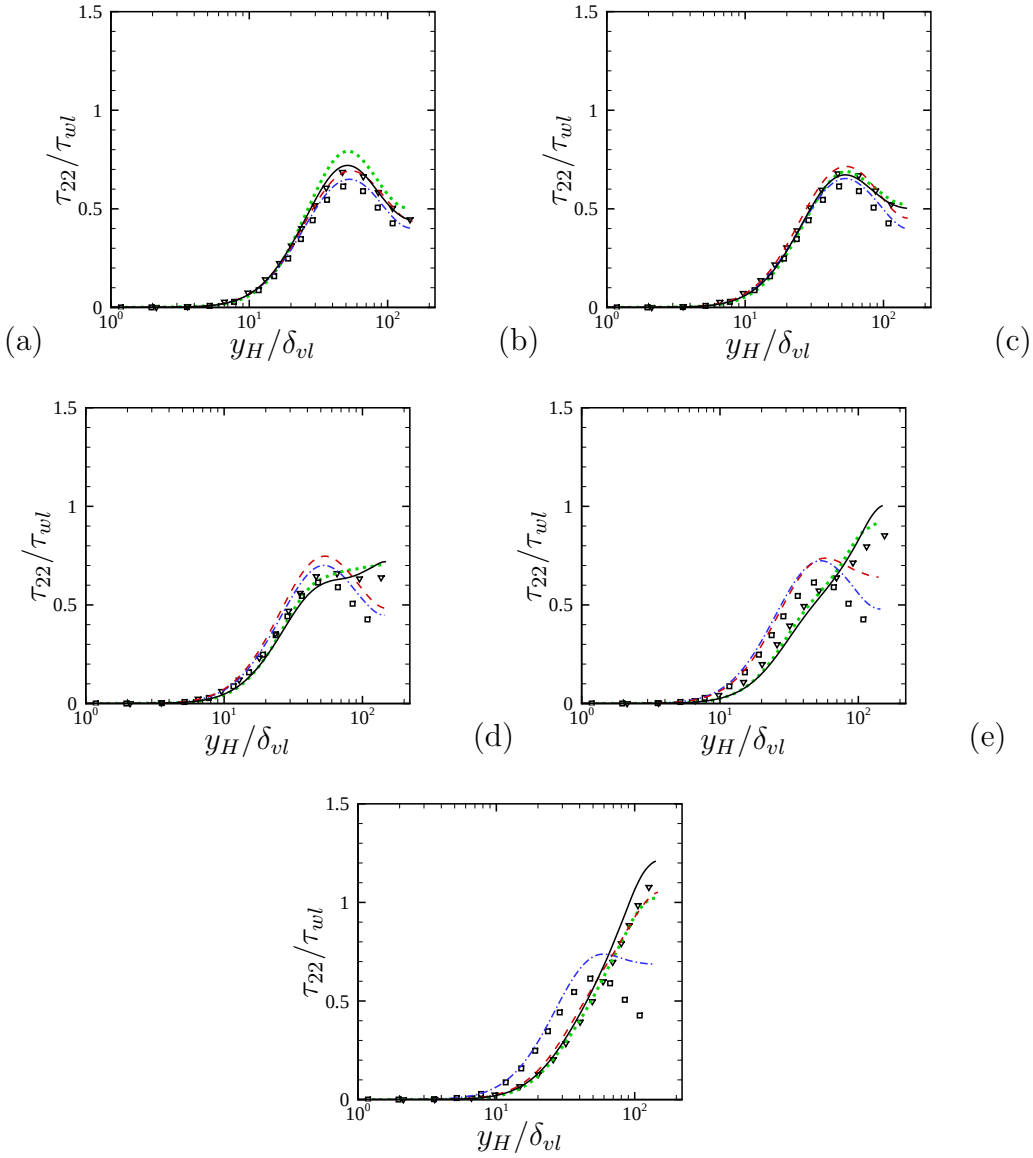

Figure 3.43: v velocity variance transformed according to Huang. Profiles are taken at $z/(h\mathcal{R}) = 1$ (a), $z/(h\mathcal{R}) = 0.8$ (b), $z/(h\mathcal{R}) = 0.6$ (c), $z/(h\mathcal{R}) = 0.4$ (d), $z/(h\mathcal{R}) = 0.2$ (e) from the wall. Case D15-$\mathcal{R}1$ (black solid), D15-$\mathcal{R}2$ (red dashed), D15-$\mathcal{R}4$ (blue dash-dotted), D3-$\mathcal{R}1$ (green dotted) and D02A-$\mathcal{R}1$ (gradients). Planar channel data CH15A are indicated by square symbols.

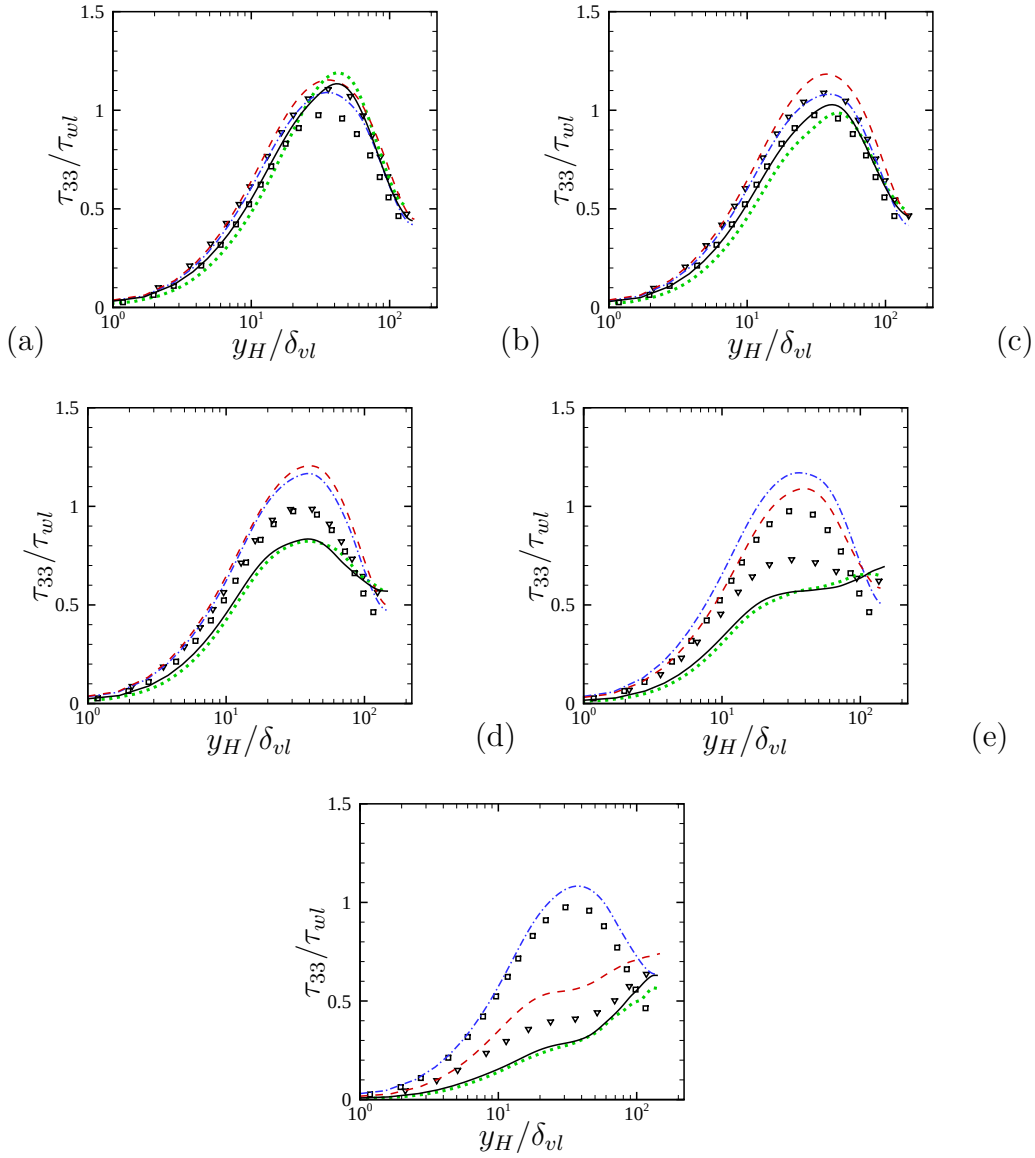

Figure 3.44: w velocity variance transformed according to Huang. Profiles are taken at $z/(h\mathcal{R}) = 1$ (a), $z/(h\mathcal{R}) = 0.8$ (b), $z/(h\mathcal{R}) = 0.6$ (c), $z/(h\mathcal{R}) = 0.4$ (d), $z/(h\mathcal{R}) = 0.2$ (e) from the wall. Case D15-$\mathcal{R}1$ (black solid), D15-$\mathcal{R}2$ (red dashed), D15-$\mathcal{R}4$ (blue dash-dotted), D3-$\mathcal{R}1$ (green dotted), D02A-$\mathcal{R}1$ (gradients). Planar channel data CH15A are indicated by square symbols.

3.3.3 Effect of Reynolds number variation

Although DNS of incompressible duct flow at different Reynolds number are available in literature [50, 63, 164], Reynolds number effects on the mean flow statistics have not been study systematically. For that purpose, we use flow cases D02A-$\mathcal{R}1$ and D02B-$\mathcal{R}1$ to analyze Reynolds number effects in duct flow. In order

to perform a complete study, additional DNS results in the friction Reynolds number range $Re_\tau = 150 - 1000$ would be necessary, although we believe that some Reynolds number trend can be inferred from these low and high Reynolds number simulations, D02A-$\cancel{R}1$ and D02B-$\cancel{R}1$. Figures. 3.45-3.46 show the mean velocity profiles in local and global wall units. As pointed out in Section 3.3.2 the profiles scaled in global wall units do not follow the viscous sublayer law, which indicates that near the wall the appropriate length scale is the local viscous length scale rather than the global one. The deviation in the incompressible case is only minor, but independent from the Reynolds number. The mean velocity profiles in global wall units (Figs. 3.45(a-b) 3.46(a-b)) roughly follow the log law, $u^+ = 1/k \log y^+ + B$ with $k = 0.41$ and $B = 5.1$, whereas in local wall units we find $B = 4.3$. We also note that the wake region is much stronger than in planar channel, starting at $y^+ \approx 200$ (Figs. 3.45(a-b)). It appears that differences between square duct and plane channel become more evident as the Reynolds number increases. The velocity at the duct bisector nearly matches the planar channel profile for case D02A-$\cancel{R}1$ (Fig. 3.45a), whereas case D02B-$\cancel{R}1$ differs substantially. This observation confirms that the large-scale structures, that emerge at higher Reynolds number, are strongly influenced by the duct corners. Approaching the wall in the z direction the velocity profile is not monotone and the wake region is driven downward, due to secondary vortices which bring low momentum fluid from the wall. We note that this velocity lag occurs at approximately the same position from the wall ($z/(\cancel{R}h) = 0.6$, Fig. 3.45e) for D02A-$\cancel{R}1$ and D02B-$\cancel{R}1$, but it becomes more intense as Reynolds number increases. This means that secondary vortices are intensified but barely move with the Reynolds number.

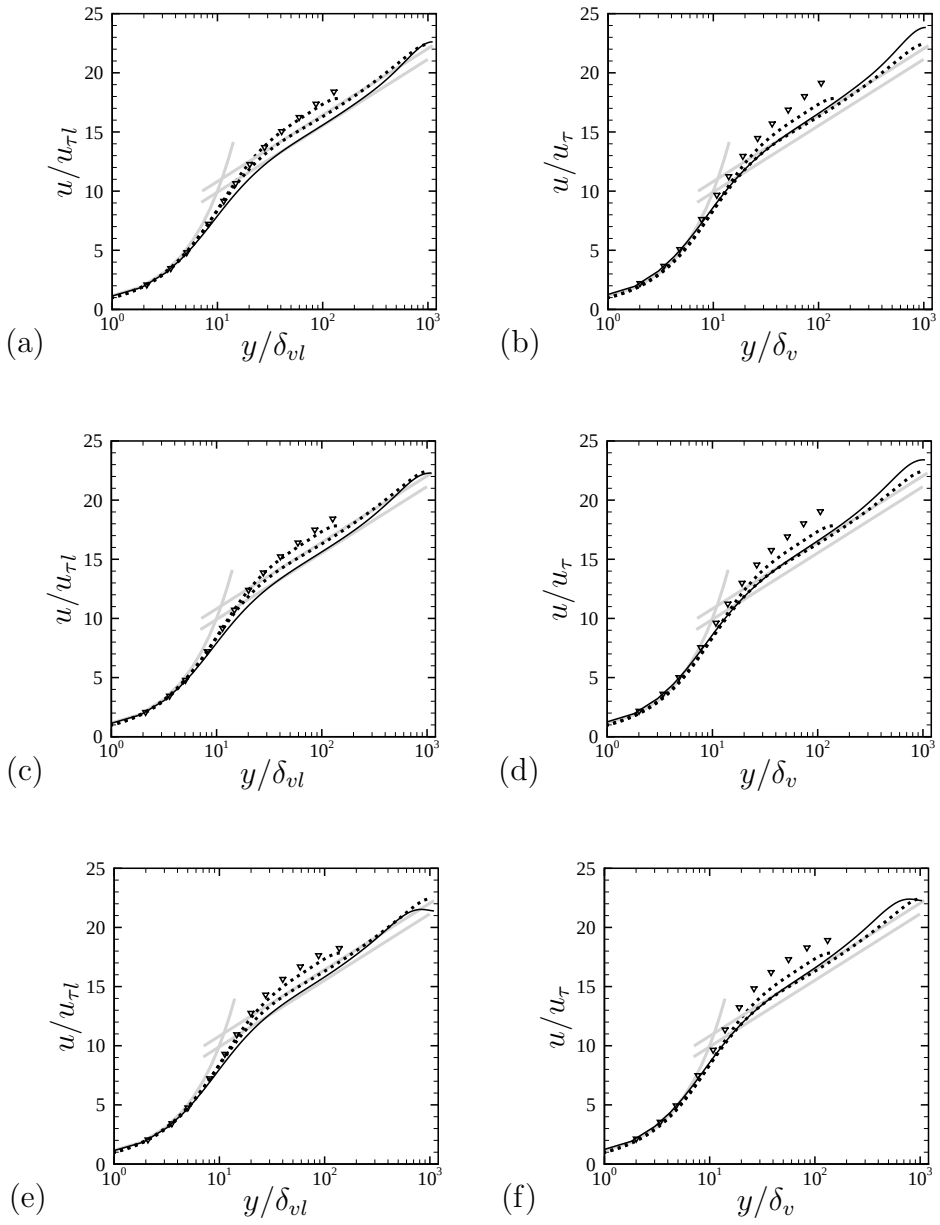

Figure 3.45: Streamwise velocity profile in local (a-c-e) and global wall units (b-d-f) at $z/(h\mathcal{AR}) = 1$(a), $z/(h\mathcal{AR}) = 0.8$ (b), $z/(h\mathcal{AR}) = 0.6$ from the wall, for cases D02B-$\mathcal{AR}1$ (black solid), D02A-$\mathcal{AR}1$ (gradients). Dotted lines represent incompressible planar channel data from Bernardini et al. [11] at $Re_\tau = 140 - 1000$. Gray lines represents the universal law of the wall, $u^+ = y^+$, $u^+ = 1/0.41 \log(y^+) + 5.2$ and $u^+ = 1/0.41 \log(y^+) + 4.3$.

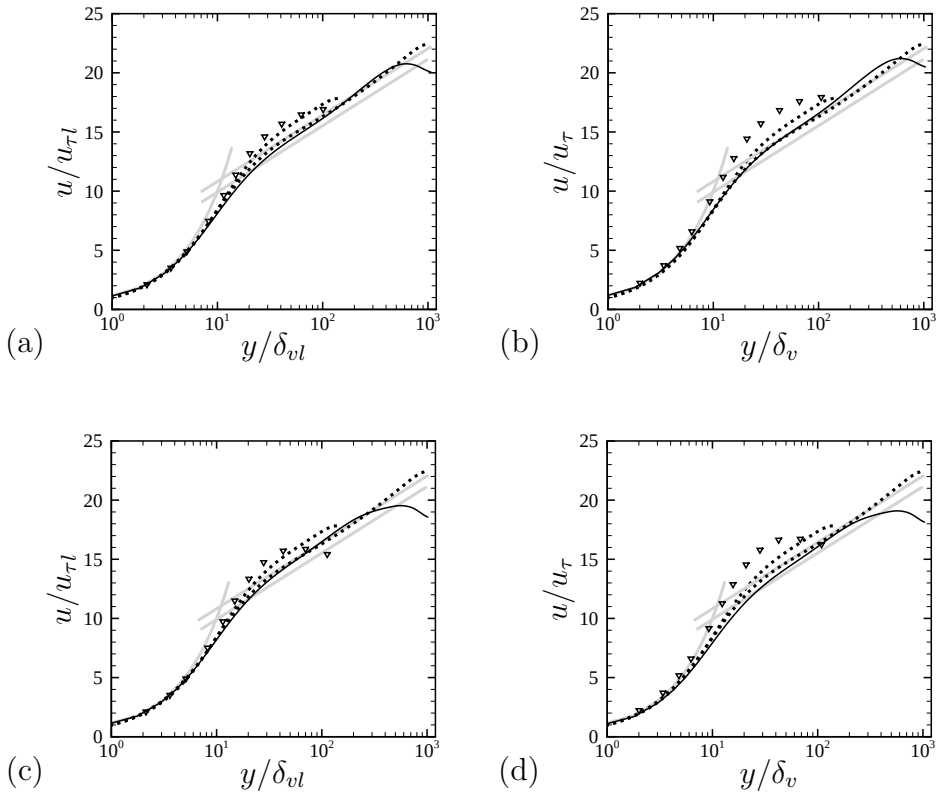

Figure 3.46: Streamwise velocity profile in local (a-c) and global wall units (b-d) at $z/(h\mathcal{R}) = 0.4$ (a-b), $z/(h\mathcal{R}) = 0.2$ (c-d) from the wall, for cases D02B-$\mathcal{R}1$ (black solid), D02A-$\mathcal{R}1$ (gradients). Gray lines represent the universal law of the wall, $u^+ = y^+$, $u^+ = 1/0.41 \log(y^+) + 5.2$ and $u^+ = 1/0.41 \log(y^+) + 4.3$.

A widely studied issue in wall-bounded turbulence is the scaling of turbulent fluctuations with the Reynolds number. Perfect inner scaling would yield insensitivity of the inner scaled statistics from the Reynolds number [90]. However many studies show that velocity fluctuations in channel and boundary layer increase with the Reynolds number [11, 54, 60, 74, 79, 84, 87]. This effect has been attributed to the increasing importance of inner/outer layer interaction of the wall parallel motions [4, 85]. Figure 3.47 shows the streamwise velocity variances in wall units for square duct D02A-$\mathcal{R}1$, D02B-$\mathcal{R}1$ and incompressible channel flow from [11]. The duct flow data seem to exhibit inverse trend in the growth of the velocity variance peak with Reynolds number and in particular we observe a lower peak for case D02A-$\mathcal{R}1$. The reason of this interesting result may be found in a different mechanism of inner/outer layer interactions, associated with spanwise motions in channel and duct flow. A possible explanation is given in the next Section, where secondary motions

are analyzed in more detail. We also note that the classical Reynolds number trend is recovered towards the wall, starting from $z/(h\mathcal{R})$ (Fig. 3.47c).

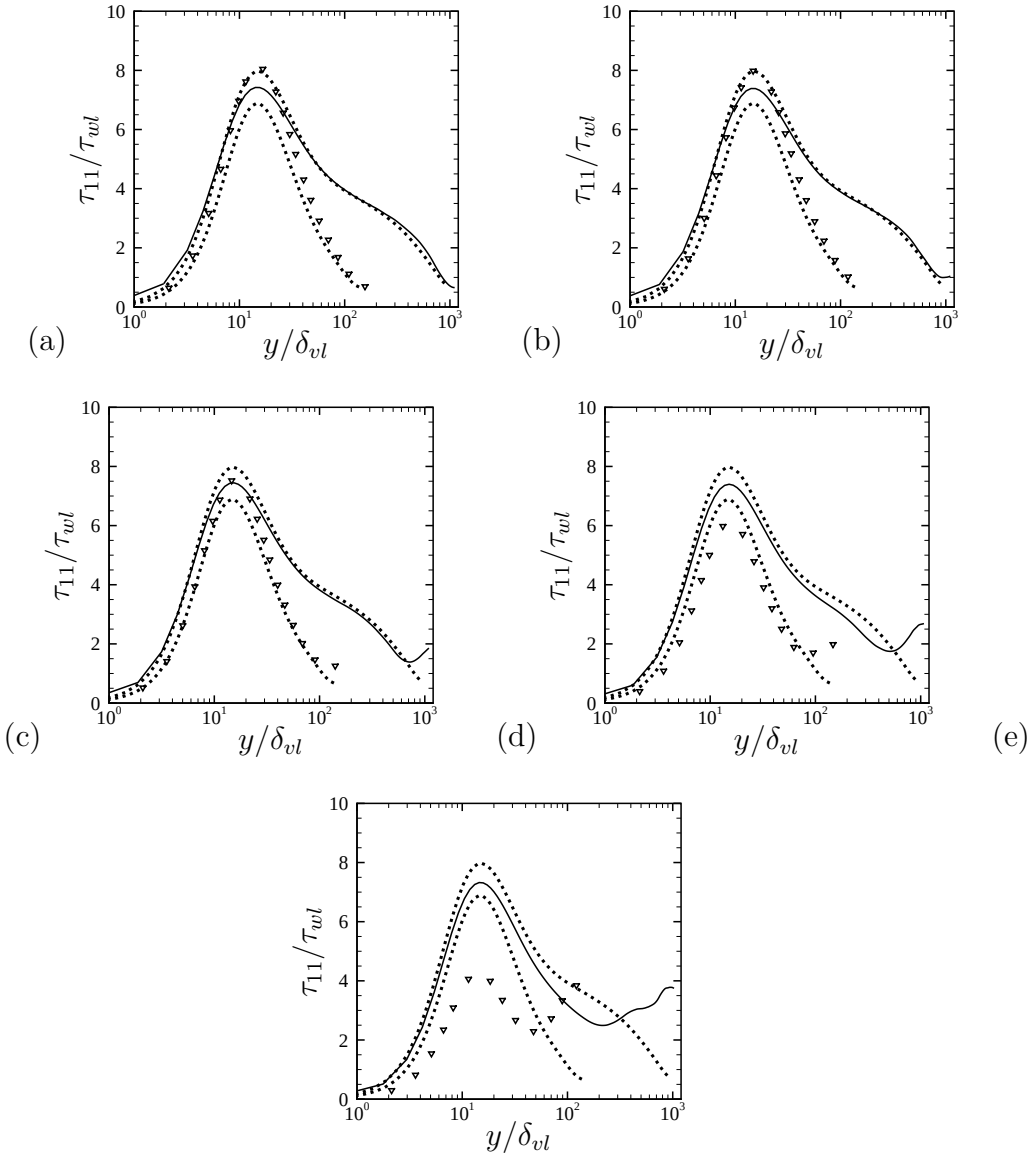

Figure 3.47: Streamwise velocity variance in local wall units at $z/(h\mathcal{R}) = 1$(a), $z/(h\mathcal{R}) = 0.8$ (b), $z/(h\mathcal{R}) = 0.6$ (c), $z/(h\mathcal{R}) = 0.4$ (d), $z/(h\mathcal{R}) = 0.2$(e) from the wall, for cases D02B-$\mathcal{R}1$ (black solid), D02A-$\mathcal{R}1$ (gradients). Incompressible channel flow simulations at $Re_\tau = 1000$ and $Re_\tau = 140$ are also reported (dotted lines) from the database by Bernardini et al. [11].

The velocity variances in y and z direction are reported in Figs. 3.48-3.49. Unlike the streamwise velocity variance, the Reynolds stresses τ_{22} and τ_{33} show trends similar to channel flow. Variances at the duct centerline are close to those found in

channels, with higher peak values (Figs. 3.48-3.49). We find evidence (Fig. 3.49a) of a logarithmic scale of the spanwise Reynolds stresses, according the attached eddy hypothesis [140],

$$\overline{w}^{'2}/u_\tau \approx B_3 - A_3 \log(y/h), \tag{3.39}$$

with constants $B_3 = 0.8$ and $A_3 = 0.5$, as found in incompressible channel flow at $Re_\tau \approx 2000$ [60].

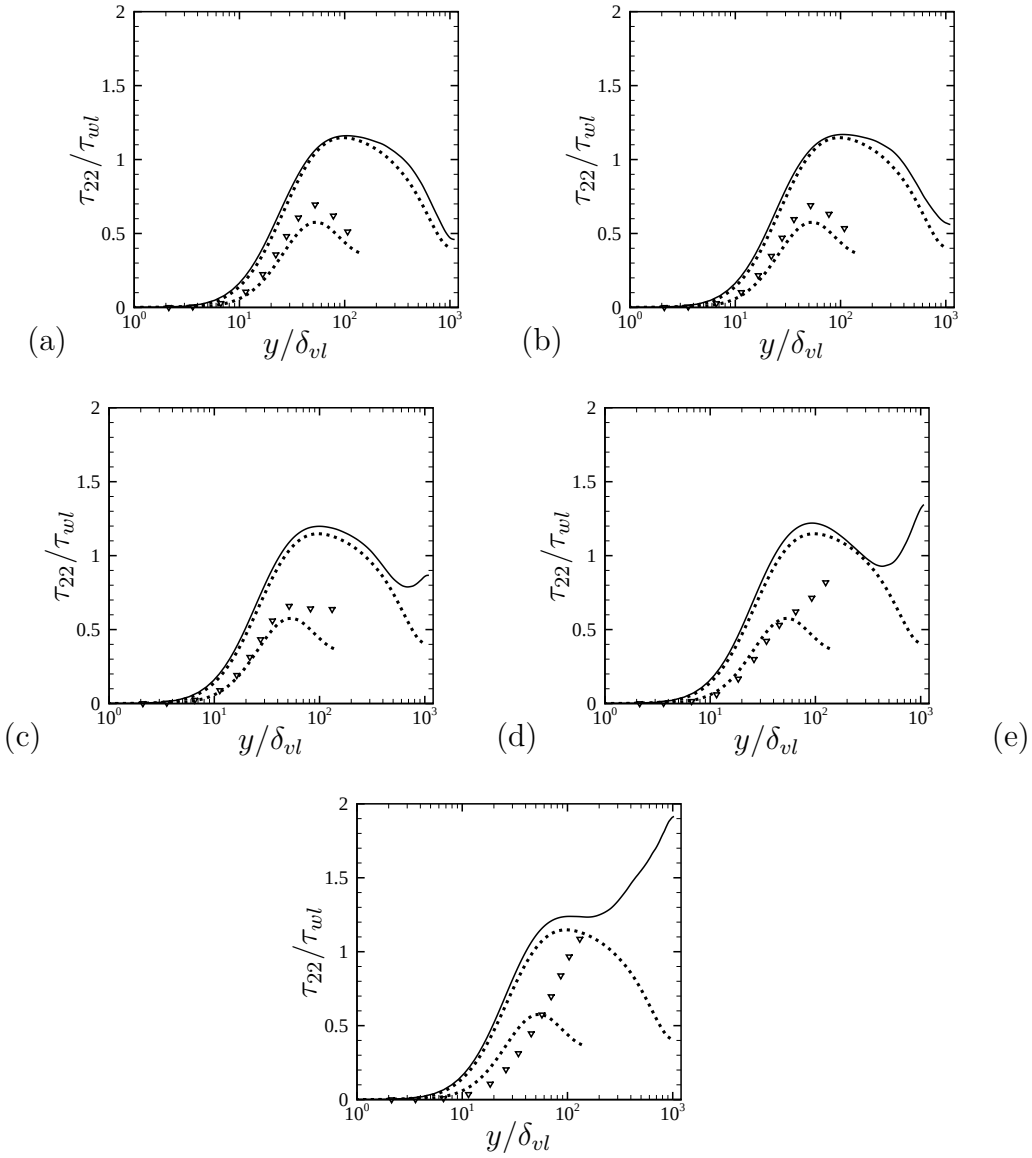

Figure 3.48: Velocity variance in direction y in local wall units at $z/(h\mathcal{R}) = 1$(a), $z/(h\mathcal{R}) = 0.8$ (b), $z/(h\mathcal{R}) = 0.6$ (c), $z/(h\mathcal{R}) = 0.4$ (d), $z/(h\mathcal{R}) = 0.2$(e) from the wall, for cases D02B-$\mathcal{R}1$ (black solid), D02A-$\mathcal{R}1$ (gradients). Incompressible channel flow simulations at $Re_\tau = 1000$ and $Re_\tau = 140$ are also reported (dottes lines) from the database by Bernardini et al. [11].

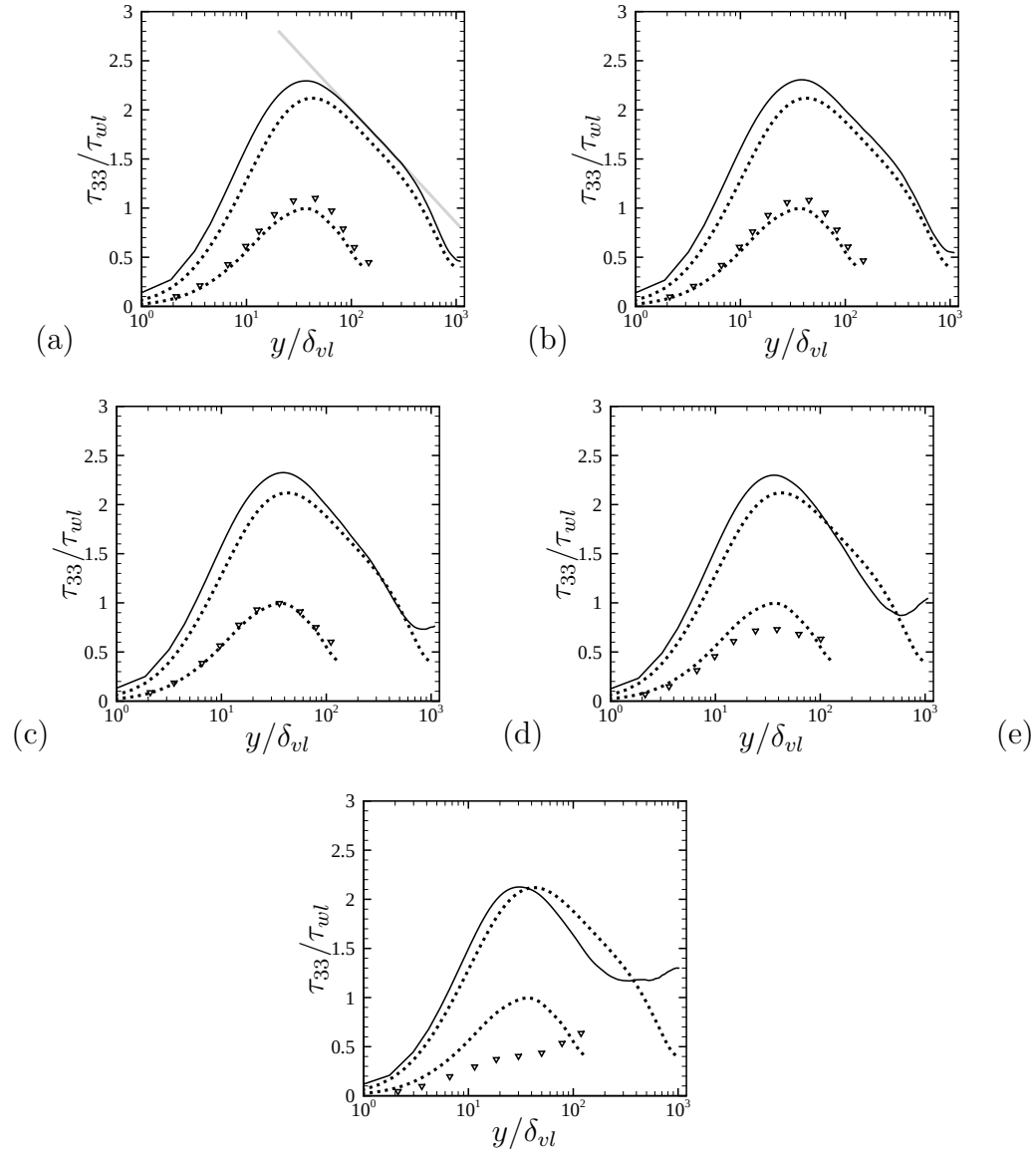

Figure 3.49: Velocity variance in direction z in local wall units at $z/(h\mathcal{AR}) = 1$(a), $z/(h\mathcal{AR}) = 0.8$ (b), $z/(h\mathcal{AR}) = 0.6$ (c), $z/(h\mathcal{AR}) = 0.4$ (d), $z/(h\mathcal{AR}) = 0.2$(e) from the wall, for cases D02B-$\mathcal{AR}1$ (black solid), D02A-$\mathcal{AR}1$ (gradients). Incompressible channel flow simulations at $Re_\tau = 1000$ and $Re_\tau = 140$ are also reported (dottes lines) from the database by Bernardini et al. [11]. Thick gray line in panel (a) refers to Eqn. (3.39), with $B_3 = 0.8$, $A_3 = 0.5$.

A close look to the cross-stream velocity components, Figs. 3.50-3.51, reveals large similarities of v and w between cases D02A-$\mathcal{AR}1$ and D02B-$\mathcal{AR}1$. As noticed in Section 3.3.2, concerning the effect of the Mach number, it seems that cross-stream velocity components are barely affected by the Reynolds number, for given aspect ratio.

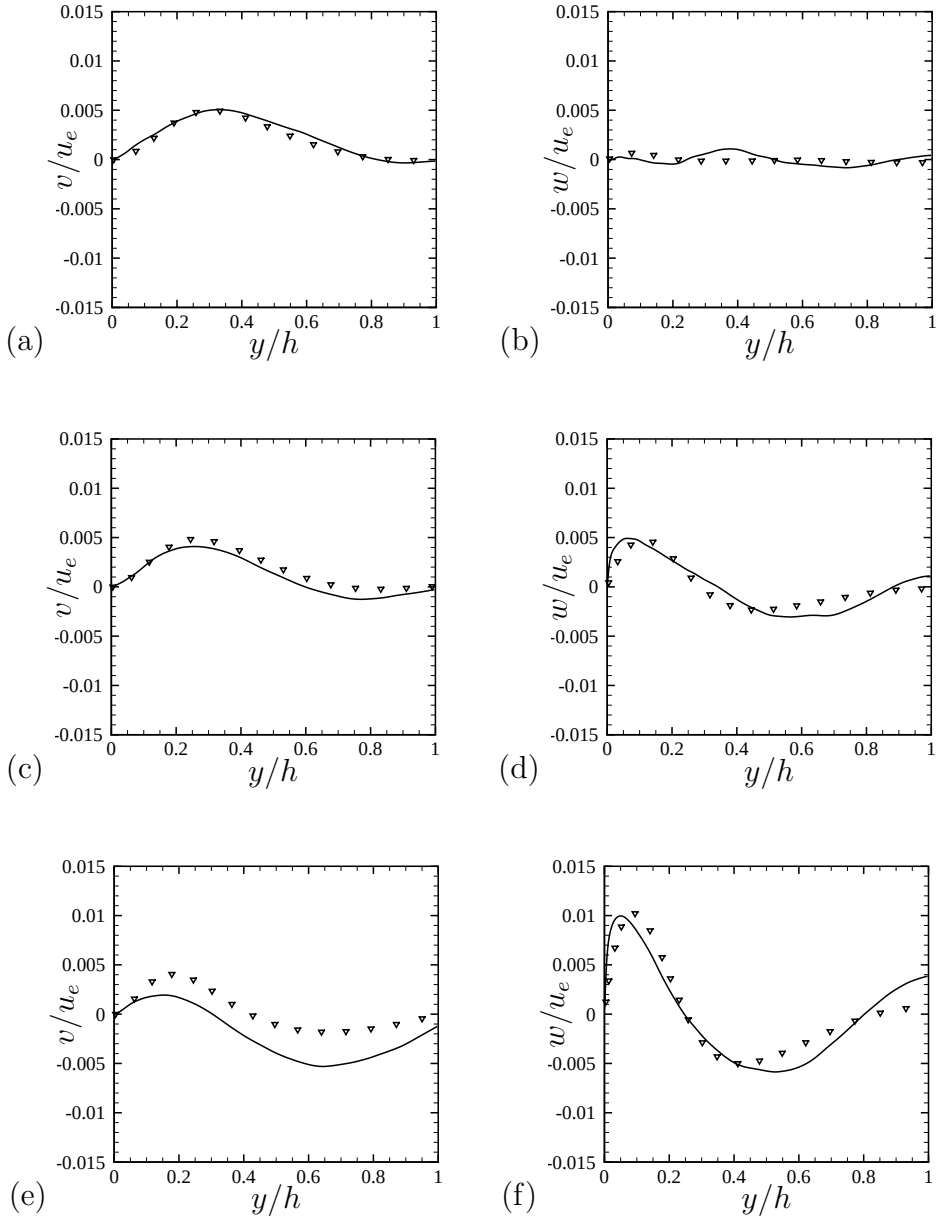

Figure 3.50: Mean velocity components in the cross-stream plane, v/u_e (a-c-e) and w/u_e (b-d-f). u_e is the centerline streamwise velocity. Profiles are taken at $z/(h\text{Æ}) = 1$ (a-b), $z/(h\text{Æ}) = 0.8$ (c-d) and $z/(h\text{Æ}) = 0.6$ (e-f) from the wall. Case D02B-Æ1 (black solid), D02A-Æ1 (gradients).

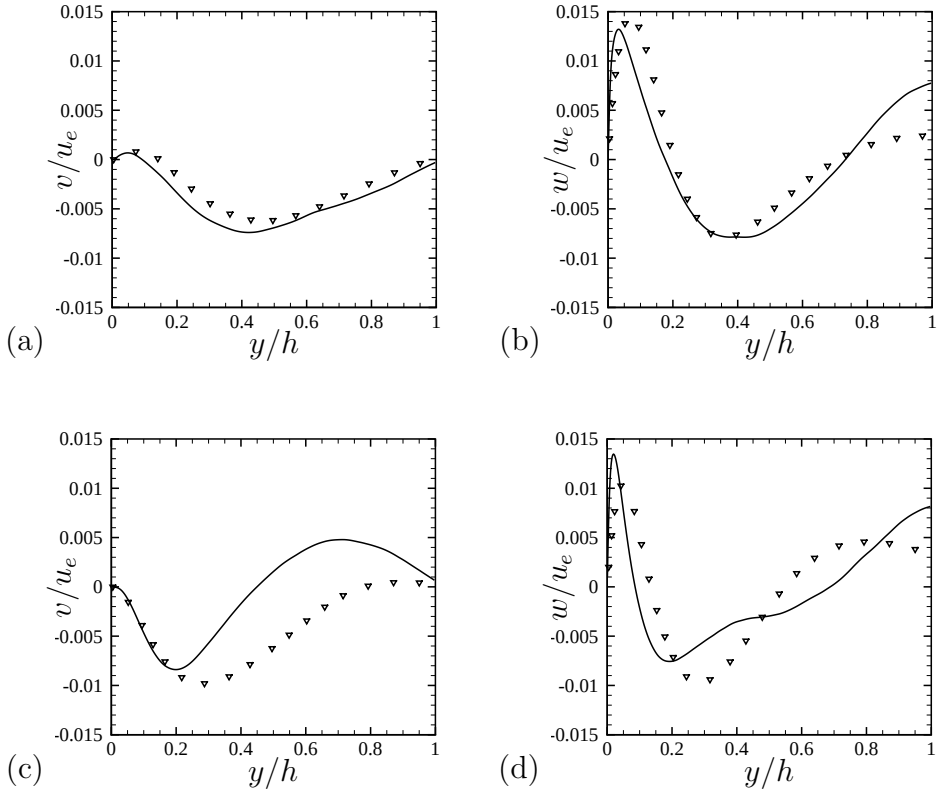

Figure 3.51: Mean velocity components in the cross-stream plane, v/u_e (a-c) and w/u_e (b-d). u_e is the centerline streamwise velocity. Profiles are taken at $z/(h\cancel{R}) = 0.4$ (a-b), $z/(h\cancel{R}) = 0.2$ (c-d) from the wall. Case D02B-$\cancel{R}1$ (black solid), D02A-$\cancel{R}1$ (gradients).

3.4 Secondary flows

As introduced in Section 1.3, rectangular duct flow is characterized by Prandtl secondary motions of second kind. In this Section we analyze the effect of Mach number, Reynolds number and aspect ratio on the mean secondary motions, by scrutiny of the mean statistics in the cross-stream section. Figures 3.52-3.53 show the mean velocity components averaged over the duct quadrants for all the flow cases. It is evident that the averaging time of flow cases D02B-$\cancel{R}1$ (Figs. 3.52 d-e-f) and D15-$\cancel{R}4$ (Figs. 3.52 h-i-l) is not sufficient to reach accurate convergence of the flow statistics, especially of the cross-stream velocity components. The information contained in the duct quadrant in Figs. 3.52-3.53 is clearly redundant, thus a good way to compress information is to plot z direction in outer units and y direction in wall units. Figure 3.54 shows the velocity variances with superposed mean velocity

vectors in the cross-stream, reported as function of the inner length scale y/δ_v and the outer length scale $z/(h\mathcal{R})$, for cases at different Mach number D02A-$\mathcal{R}$1, D15-$\mathcal{R}$1, D3-$\mathcal{R}$1. For these cases the center of the secondary vortices occur at $z(h\mathcal{R}) \approx 0.5$ and $y/\delta_v \approx 12$, and it is not affected by the Mach number. As we observed in Section 3.1.2 it seems that Prantdl secondary motions of second kind are insensitive to Mach number variation, at least in the range considered here. We further note that the center of the secondary vortex in inner units approximately corresponds to the distance at which maximum velocity fluctuations occur $y/\delta_v \approx 15$.

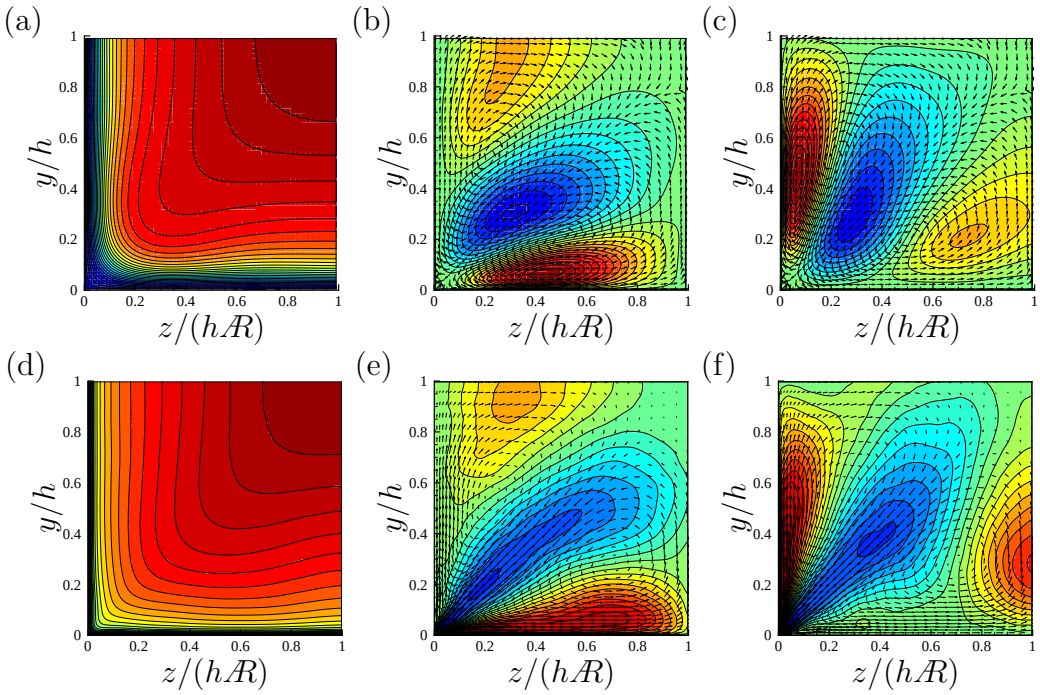

Figure 3.52: Mean velocity components, normalized with the streamwise centerline velocity u/u_c(a-d), v/u_c(b-e), w/u_c(c-f) for flow cases D02A-$\mathcal{R}$1 (a-b-c) and D02B-$\mathcal{R}$1 (e-f-g). 30 contours levels are shown in the range $0 \leq u/u_c \leq 1$, $-0.015 \leq v/u_c \leq 0.015$, $-0.015 \leq w/u_c \leq 0.015$. Vectors denote cross-stream velocity components.

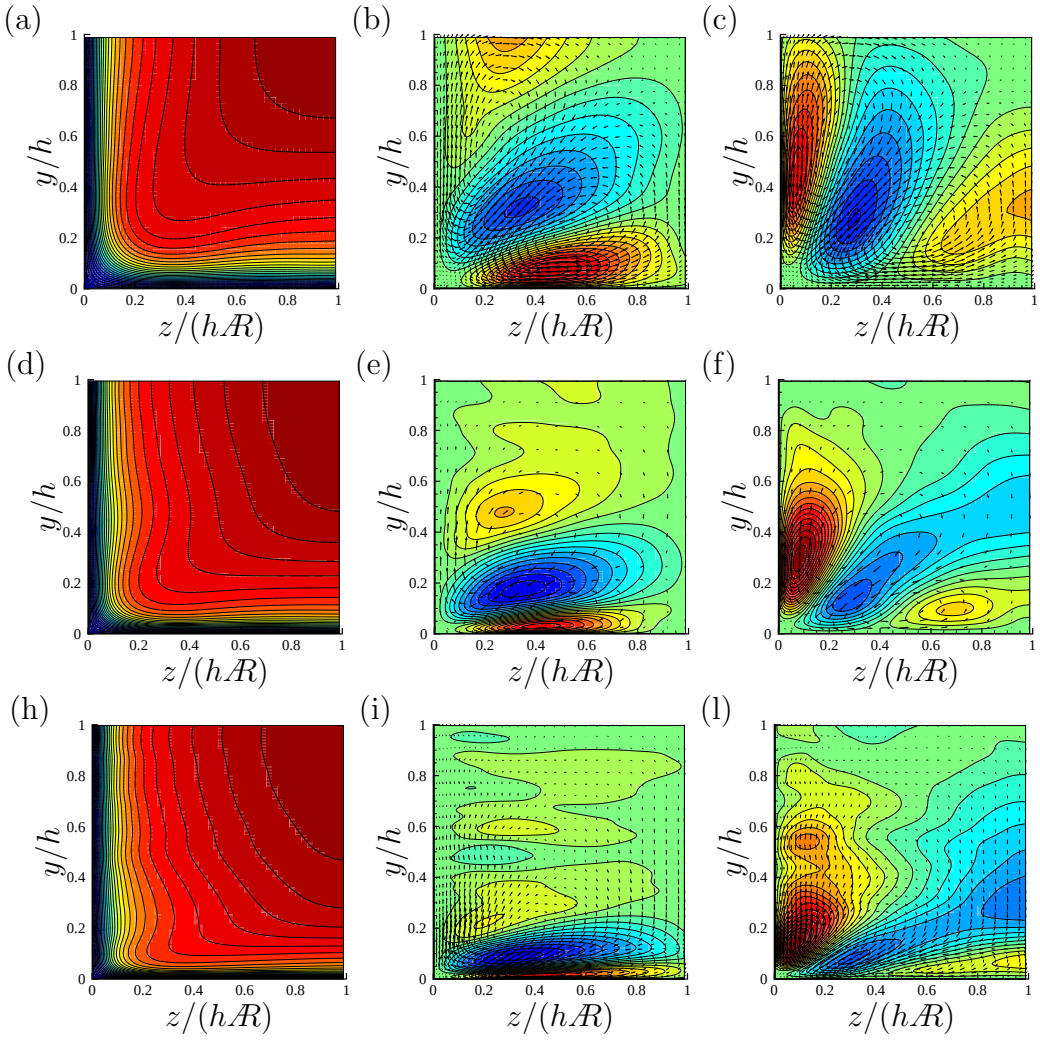

Figure 3.53: Velocity components in outer units y/h and $z/(h\mathcal{R})$, normalized with the streamwise centerline velocity u/u_c(a-d-h), v/v_c(b-e-i), w/w_c(c-f-l) for flow cases D15-$\mathcal{R}$1 (a-b-c), D15-$\mathcal{R}$2 (d-e-f) and D15-$\mathcal{R}$4 (d-e-f). 30 contours levels are shown in the range $0 \leq u/u_c \leq 1$, $-0.015 \leq v/u_c \leq 0.015$, $-0.015 \leq w/u_c \leq 0.015$. Vectors denote cross-stream velocity components.

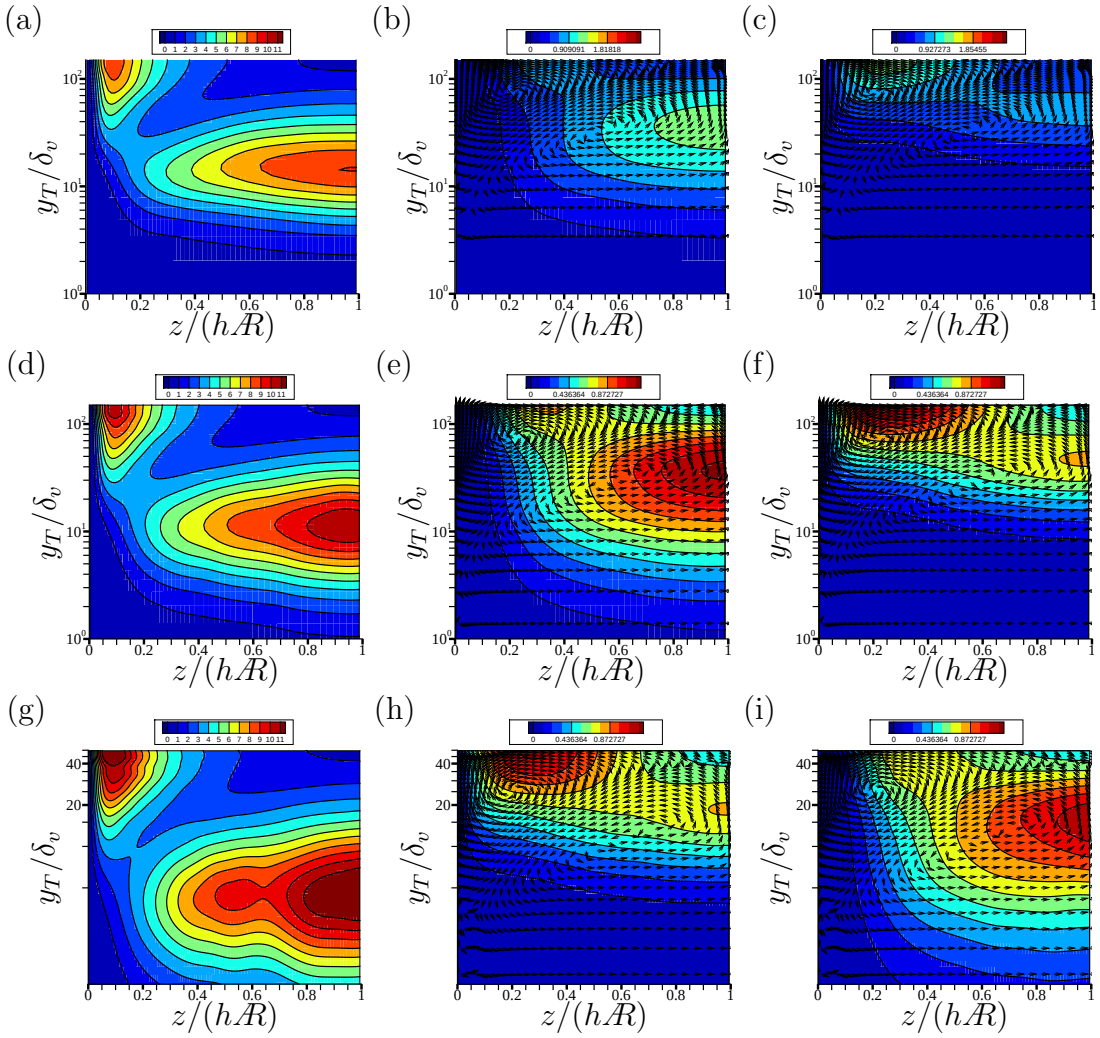

Figure 3.54: Velocity variances in global wall units, scaled according to TL. Vectors denote cross-stream velocity components. z direction is reported in outer units $z/(h\mathcal{R})$, whereas y is in global wall units y_T/δ_v. τ_{11}/τ_w (a-d-g), τ_{22}/τ_w (h-e-h), τ_{33}/τ_w (c-f-i), for cases D02A-$\mathcal{R}1$ (a-b-c), D15-$\mathcal{R}1$ (d-e-f), D3-$\mathcal{R}1$ (g-h-i.)

Figure.3.55 shows the effect of $\mathcal{R}$on secondary motions for given Mach number, flow cases D15-$\mathcal{R}1$, D15-$\mathcal{R}2$,D15-$\mathcal{R}4$. As the $\mathcal{R}$increase the secondary vortex center moves towards the side wall and for $\mathcal{R} = 4$ $z/(h\mathcal{R}) \approx 0.2$, whereas the position in inner units does not change $y/\delta_v =\approx 12$. Besides, increasing $\mathcal{R}$clearly reduces the vortex strength.

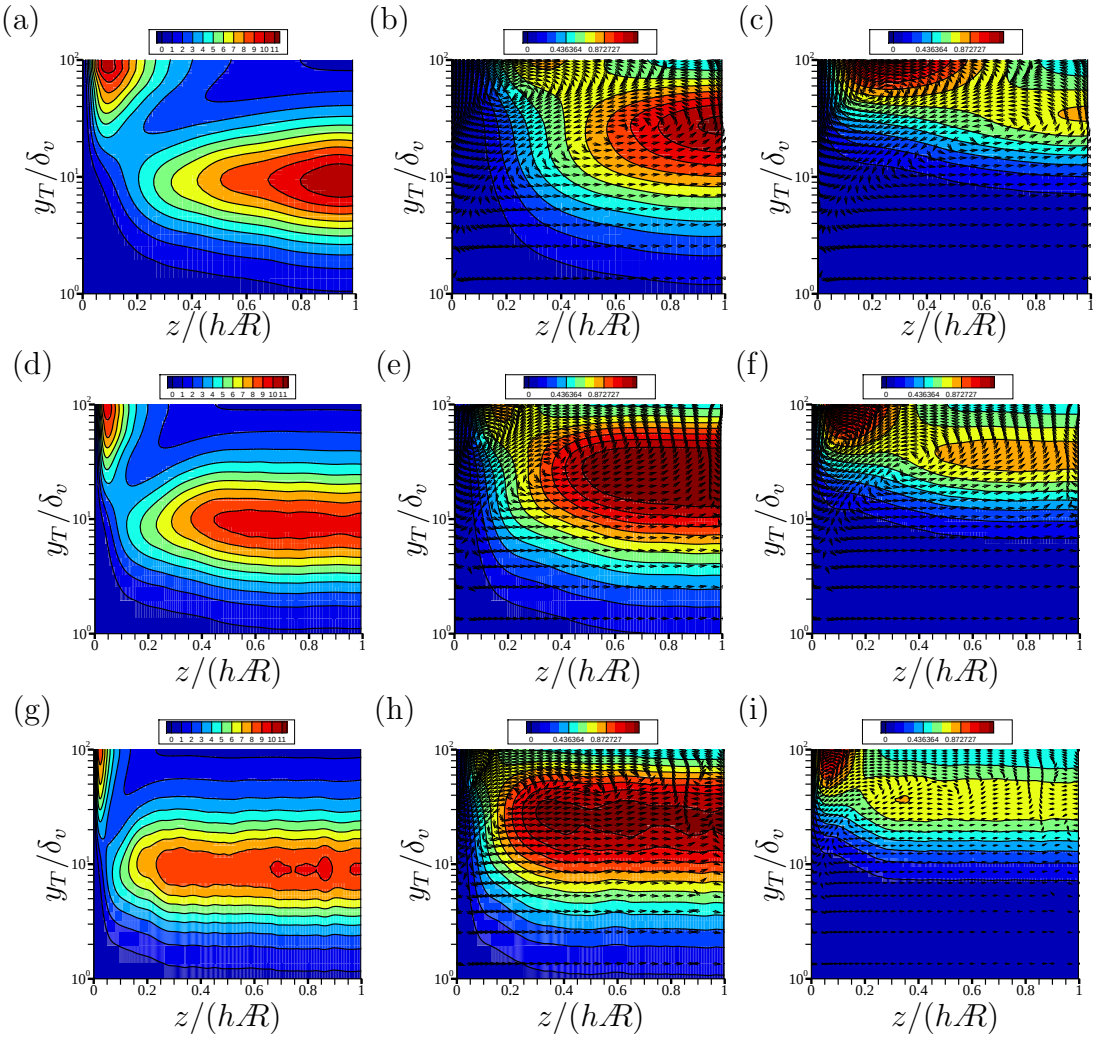

Figure 3.55: Velocity variances in global wall units, scaled according to TL. z direction is reported in outer units $z/(h\mathcal{R})$, whereas y is in global wall units y_T/δ_v. τ_{11}/τ_w (a-d-g), τ_{22}/τ_w (h-e-h), τ_{33}/τ_w (c-f-i), for cases D15-$\mathcal{R}$1 (a-b-c), D15-$\mathcal{R}$2 (d-e-f), D15-$\mathcal{R}$4 (g-h-i.)

The effect of the Reynolds number on secondary motions is studied through Fig. 3.56, which shows velocity variances with superposed mean velocity vectors in the cross-stream plane, for flow cases M02A$\mathcal{R}$1 and M02A$\mathcal{R}$. We note that the center of the secondary vortex is at the same position in outer units, $z/(h\mathcal{R}) \approx 0.5$ for the two flow cases, meaning that the effect of the Reynolds number variation on secondary motions is minor. On the contrary the position of the vortex in inner units changes, from $y/\delta_v \approx 12$ to $y/\delta_v \approx 110$, maybe clarifying the reason for the odd trend of the streamwise Reynolds number peak observed in Section 3.3.3. At low Reynolds number in fact, the center of the secondary vortex occurs approximately at the same position where τ_{11} reaches its maximum ($y/\delta_v \approx 15$), so that the higher

streamwise fluctuations peak at low Reynolds number may be due to the contribution of secondary motions.

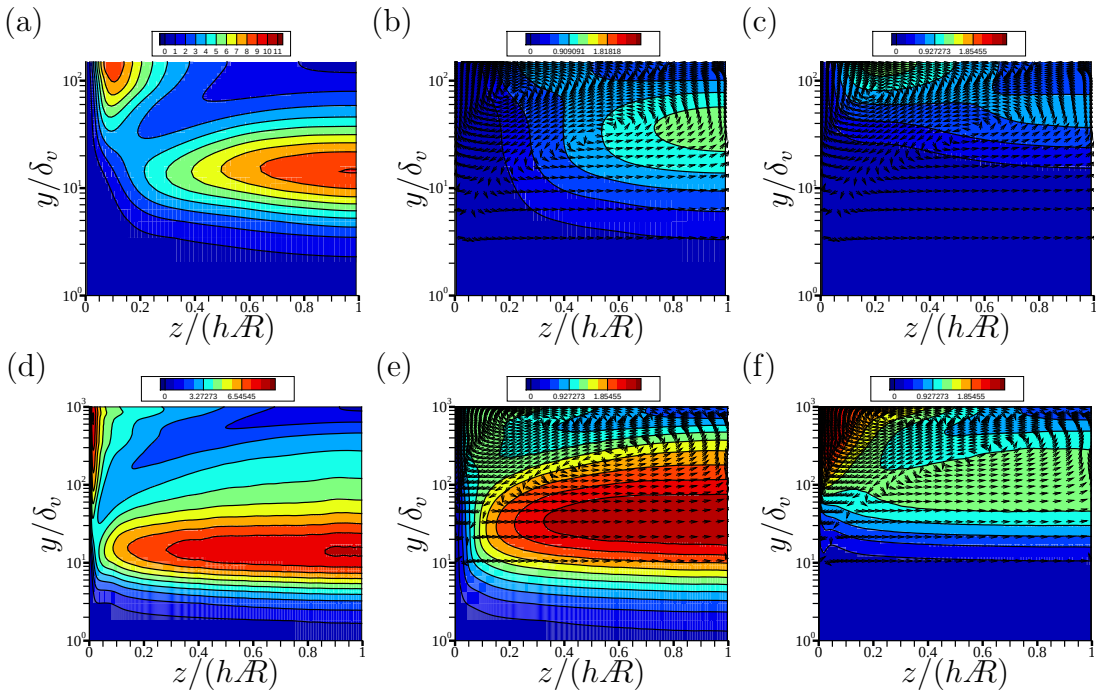

Figure 3.56: Velocity variances in global wall units. z direction is reported in outer units $z/(h\mathcal{R})$, whereas y is in global wall units y/δ_v. τ_{11}/τ_w (a-d), τ_{22}/τ_w (h-e), τ_{33}/τ_w (c-f), for cases D02A-$\mathcal{R}1$ (a-b), D02B-$\mathcal{R}1$ (d-e).

Chapter 4

Conclusions

The aim of this work was to investigate Mach and Reynolds number effects in compressible internal flows. The study has focused on physical and numerical issues which emerges in the numerical solution of turbulent compressible wall-bounded flows. DNS of compressible flows is more expensive than incompressible simulations, mostly owing to the acoustic time step restriction, which is always exceedingly restrictive at the wall. The need to overcome this difficulty led us to develop a novel semi-implicit treatment for the acoustic waves in the compressible N-S equations. This efficient semi-implicit algorithm has been used to perform DNS of internal flows with increasing geometrical complexity, namely planar channel, circular pipe and rectangular duct flow. The numerical solver has been used to perform DNS spanning a large range of Reynolds and Mach number, in order to clarify some basic issues which are not yet understood. We divide this concluding chapter into two parts, which summarize the key aspects of the recently developed numerical algorithm and the main physical findings.

4.1 Numerical issues

A novel semi-implicit algorithm for time-accurate solution of the compressible Navier-Stokes equations has been developed in Section 2.1.2, which is capable to operate efficiently all the way from low subsonic to supersonic flow conditions. The main features of the algorithm are as follows: i) use of the entropy transport equation instead of total energy conservation; ii) Beam-Warming-like linearization of the partial convective flux associated with acoustic propagation; iii) energy-consistent discretization of the convective derivatives in the explicit part of the

time-advancement operator; iv) semi-implicit treatment of viscous fluxes based on isolation of Laplacian terms; v) approximate factorization for implicit treatment of multiple space directions; vi) third-order accurate Runge-Kutta time integration, according to the algorithm proposed by Nikitin [100]. The main advantage of the algorithm is that, unlike the classical Beam-Warming scheme, it avoids the computationally expensive inversion of 5×5 block-banded matrices, but rather inversion of standard banded matrices (tridiagonal matrices in the case of second-order accurate space discretization) is sufficient. Specifically, a single banded matrix inversion is needed for implicit treatment of the convective terms, whereas five matrix inversions are needed if viscous terms are also handled implicitly. The cost overhead with respect to standard explicit algorithms (see Tab. 2.1) is quite modest, ranging from 20% to 30%, for each space direction to be handled implicitly. Modification of existing compressible flow solvers to incorporate the present method is relatively straightforward, as the explicit part of the algorithm is unchanged. The method nominally allows unconditional stability for low-Mach-number flows. However, flux linearization and approximate factorization reduce the stability margins, and CFL number is of the order of 5-10 are achieved in practical computations, which is probably less than achievable with iterative methods. However, compared to compressible flow algorithms based on pre-conditioning, the present method avoids use of inner time iterations, whose computational cost is difficult to estimate a-priori. Another possible shortcoming of the method is the use of the entropy equation, which is instrumental to achieve (approximate) separation of hydrodynamic from acoustic effects. While use of the entropy equation yields improved numerical stability, it also makes proper capturing of shock waves difficult, since the equations are not in conservation form. We have found that this issue can be fixed by locally reverting to a total energy formulation for the explicit time increment in the presence of shocks, as identified through a shock sensor [113]. The resulting time increments are then converted to the entropy increments, prior to application of the implicit operator. Although the algorithm herein developed has in principle much wider range of applications, the main focus of this work was on DNS of compressible wall-bounded flows, which is notoriously plagued by severe time step restrictions inherited from the wall-normal acoustic and viscous stability conditions. We have found that the wall-normal acoustic time limitation can be effectively removed through semi-implicit treatment. The same conclusion also applies to the viscous time step restriction, although the most efficient way to alleviate it is placing the first grid point sufficiently away from the wall $y^+ \approx 0.5 - 0.7$, and using suitable staggering [91], with no effect

of accuracy. The wall-parallel stability restrictions can also be suppressed through semi-implicit treatment. However, accuracy considerations lead to the practical rule (see Fig. 1.1) that the time step cannot be much larger than the one stemming from the streamwise time limitation. Hence, we suggest that in low-subsonic flow both the wall-normal and the spanwise convective terms are handled implicitly, whereas the streamwise terms should be evaluated explicitly. The resulting saving of computer time can be of the order of 85% with respect to a fully explicit solver with identical accuracy. In high subsonic or supersonic flow, implicit treatment of the wall-normal convective derivatives is sufficient, with typical savings of to order of 50%, in line with theoretical estimates. We foresee that the present technique can be fruitfully extended to numerical simulation of wall-bounded turbulent flows with time-accurate models, such as LES or DES [132]. In that case, given the higher aspect ratio of near-wall cells, higher gains are expected. Advantages with respect to classical algorithms based on Beam-Warming linearization are also expected for steady RANS applications. Indeed, although the present algorithm is in principle only capable of suppressing the acoustic time step limitation, it is found to be at least as stable as Beam-Warming in practical computations. As for cylindrical coordinates, we showed that successful conservation of the discrete kinetic energy can be achieved simply rewriting the equations in terms of the variables $R = r\rho$ and $P = rp$, which allows the straightforward application of the scheme developed by [112]. For cylindrical coordinates the use of the semi-implicit algorithm (ATI) is mandatory in the azimuthal direction, which in principle destroy the conservation of the kinetic energy. Nevertheless inviscid cases have shown that the solver retains its low dissipative character also in the semi-implicit case.

4.2 Flow physics

We have presented built a novel DNS database for compressible channel, pipe and rectangular duct flow, which includes flows at unprecedented Reynolds number, with the aim to shed some additional light on the structure of turbulence. Importantly, compressible channel data are directly compared with incompressible channel DNS data at precisely matching Reynolds number which allows to perform a fair comparison with incompressible data. In the case of pipe and duct flow, ad-hoc incompressible datasets have not been developed, and we have mainly relied on low data available in literature. As far as 'compressibility transformations' are concerned, we find the classical van Driest scaling to be inaccurate in representing

the full inner-layer velocity profile, especially in the presence of significant wall heat flux. Later transformations, including Huang and Coleman [61] and Brun et al. [21] yield some improvement, especially because they more faithfully reproduce the correct behavior in the inner layer. It appears that a recent transformation [141] well reproduces the behavior of the entire mean velocity profile, with the side consequence that fair comparison of inner-scaled velocity profiles across the Mach number range should be carried out at matching friction Reynolds number based on y_T as defined in Eqn. (3.8) + Tab. 3.3. Comparison with incompressible data has shown that the TL transformation is equally accurate for channel, pipe and duct flow. Notably, in the case of duct flow, the TL transformation for velocity is reasonably accurate for the whole duct cross section, although the formal derivation cannot be provided. Huang's (and consequently TL) transformations well perform for all the Reynolds stress components, with the partial exception of the peak of the streamwise turbulent stress, which as seen in many previous studies [55, 158] is higher than in the incompressible case. We believe that the study of a passive scalar field may help to shed light on this long-standing issue. In particular, since pressure does not appear in the passive scalar transport equation, the study of the passive scalar statistics may help in clarifying the role of pressure in the failure of Huang's scaling, if any. It seems in fact that pressure is not the cause of the unsuccessful transformation of the velocity variance peak, since the same failure appears for the passive scalar variance.

The outer-scaled mean velocity profile is reasonably well represented by all compressibility transformations, as density and viscosity variations are small. In particular, it is found that a universal parabolic profile well represents a substantial fraction of the wall layer, up to 50% at sufficiently high Reynolds number, which is characterized by a single, universal constant.

Study of the mean velocity/temperature relation shows a classical quadratic dependence, however with coefficients different than the classical Walz formula, and which explicitly depend of the wall heat flux [165].

Finally, we have scrutinized the behavior of the length scales associated with the streamwise velocity field, for which no consensus exists at present. Limiting ourselves to the spanwise length scales in channel and pipe flow, for which no ambiguity in the interpretation exists, we find that their dependence on wall distance, Reynolds and Mach number is well synthesized in formulas (3.25)-(3.31), which is rooted in crude mixing length arguments. The direct consequence is that, for fixed Reynolds number and wall distance, the length scales of the typical eddies should not vary

with the Mach number.

4.3 Future work

Some of the issues encountered in this work have not been analyzed in detail, and they are the subject of ongoing and future work. The compressibility transformations discussed in this work, together with the temperature velocity relation may lay the basis for the development of explicit approximations for the friction and heat flux coefficients in compressible internal flows, which are currently lacking. In turns out that deriving a counterpart of van Driest II transformation in the case of internal isothermal flows is not straightforward, in fact in the generalized temperature/velocity relation derived by Zhang et al. [165], temperature appears a function of the wall heat flux and the temperature at the channel center, which are not known a priori. For this reason, the compressibility transformations presented in this work are a valuable tool to understand and quantify compressibility effects, but their engineering applicability remains limited. We have shown that the compressibility transformation by Huang is accurate for all Reynolds stress components except for the streamwise velocity variance, which exhibits a higher peak value with respect incompressible data. Reasons for this remaining discrepancy may constitute an interesting topic for future research. In particular, we believe that the analysis of the budgets of the streamwise Reynolds stress may help to shed light on this issue. The study of duct flow case has revealed that the effect of the secondary flows is important also for high aspect ratios (e.g. $\mathcal{AR} = 4$), hence supersonic duct flow simulations at higher aspect ratio are currently being carried out. The effect of Reynolds number variation in duct flow is also an interesting topic and for that purpose we are carrying out DNS at $M_b = 0.2$ in the range range $Re_\tau = 150 - 1000$. We have shown that for channel and pipe flow the velocity profile in the core region can be well represented by a laminar-like profile (parabolic law in Eqn. 3.16), thus we may expect that a similar law holds for duct flow.

Chapter 5

Appendix

5.1 Non-uniform mesh spacing

In the case of wall bounded flow the mesh is usually uniform in the wall parallel directions x and z but its necessarily clustered towards the walls. For this reason the numerical space η, uniformly spaced, is mapped into the physical one $y(\eta)$. Several choices are possible for the stretching function, which can be found on Orlandi [102]. In the case of internal flows such as channel and duct the classical choice is

$$y(\eta) = \frac{\text{erf}\left(\beta\left(\eta - \frac{1}{2}\right)\right)}{\text{erf}\left(\frac{\beta}{2}\right)}, \tag{5.1}$$

where $\eta = (j-1)\,\Delta\eta$ for co-located walls and $\eta = (j-0.5)\,\Delta\eta$ for staggered walls, with $j = 1, \ldots, N_y$ and $\Delta\eta = l_y/N_y$. β is the stretching parameter. The error function in Eqn. (5.1) can be substituted by the hyperbolic tangent function, with similar behavior.

Derivative of a generic quantity f in the wall normal direction are therefor taken using the chain rule,

$$\frac{\partial f}{\partial y} = \frac{\partial f}{\partial \eta}\frac{\partial \eta}{\partial y}, \tag{5.2}$$

and the metric term $\frac{\partial \eta}{\partial y}$ is evaluated numerically with the same order of accuracy of $\frac{\partial f}{\partial \eta}$. A similar reasoning hold for second derivatives,

$$\frac{\partial^2 f}{\partial y^2} = \frac{\partial^2 f}{\partial \eta^2}\left(\frac{\partial \eta}{\partial y}\right)^2 + \frac{\partial f}{\partial \eta}\frac{\partial \eta}{\partial y}\frac{\partial^2 \eta}{\partial y^2}. \tag{5.3}$$

5.2 Jacobians of Navier-Stokes equations

In this Section we report the full Jacobians of the Navier-Stokes Eqns. (2.4) in the three coordinate direction, together with the acoustic ones.

$$\mathbf{A}_x = \frac{\partial \mathbf{f}_x}{\partial \mathbf{w}} = \begin{bmatrix} 0 & 1 & 0 & 0 & 0 \\ \frac{T}{\rho}\left(\gamma - \frac{s}{c_v}\right) - u^2 & 2u & 0 & 0 & \frac{p}{\rho C_v} \\ -uv & v & u & 0 & 0 \\ -uw & w & 0 & u & 0 \\ -us & s & 0 & 0 & u \end{bmatrix} \tag{5.4}$$

$$\mathbf{A}_y = \frac{\partial \mathbf{f}_y}{\partial \mathbf{w}} = \begin{bmatrix} 0 & 0 & 1 & 0 & 0 \\ -uv & v & u & 0 & 0 \\ \frac{T}{\rho}\left(\gamma - \frac{s}{c_v}\right) - v^2 & 0 & 2v & 0 & \frac{p}{\rho C_v} \\ -vw & 0 & w & v & 0 \\ -vs & 0 & s & 0 & v \end{bmatrix}. \tag{5.5}$$

$$\mathbf{A}_z = \frac{\partial \mathbf{f}_z}{\partial \mathbf{w}} = \begin{bmatrix} 0 & 0 & 0 & 1 & 0 \\ -uw & w & 0 & u & 0 \\ -vw & 0 & w & v & 0 \\ \frac{T}{\rho}\left(\gamma - \frac{s}{c_v}\right) - w^2 & 0 & 0 & 2w & \frac{p}{\rho C_v} \\ -ws & 0 & 0 & s & w \end{bmatrix}. \tag{5.6}$$

It is easy to obtain the acoustic Jacobians from the full ones (5.7)-(5.8)-(5.9)

$$\mathbf{A}_x^a = \frac{\partial \mathbf{f}_x^a}{\partial \mathbf{w}} = \begin{bmatrix} 0 & 1 & 0 & 0 & 0 \\ \frac{p}{\rho}\left(\gamma - \frac{s}{c_v}\right) & 0 & 0 & 0 & \frac{p}{\rho C_v} \\ 0 & 0 & 0 & 0 & 0 \\ 0 & 0 & 0 & 0 & 0 \\ 0 & 0 & 0 & 0 & 0 \end{bmatrix} \tag{5.7}$$

$$\mathbf{A}_y^a = \frac{\partial \mathbf{f}_y^a}{\partial \mathbf{w}} = \begin{bmatrix} 0 & 0 & 1 & 0 & 0 \\ 0 & 0 & 0 & 0 & 0 \\ \frac{p}{\rho}\left(\gamma - \frac{s}{c_v}\right) & 0 & 0 & 0 & \frac{p}{\rho C_v} \\ 0 & 0 & 0 & 0 & 0 \\ 0 & 0 & 0 & 0 & 0 \end{bmatrix}. \tag{5.8}$$

$$\mathbf{A}_z^a = \frac{\partial \mathbf{f}_z^a}{\partial \mathbf{w}} = \begin{bmatrix} 0 & 0 & 0 & 1 & 0 \\ 0 & 0 & 0 & 0 & 0 \\ 0 & 0 & 0 & 0 & 0 \\ \frac{p}{\rho}\left(\gamma - \frac{s}{c_v}\right) & 0 & 0 & 0 & \frac{p}{\rho C_v} \\ 0 & 0 & 0 & 0 & 0 \end{bmatrix}. \tag{5.9}$$

5.3 Viscous fluxes in cylindrical coordinates

In this Section the viscous fluxes in cylindrical coordinates in Eqn. (2.41) are expanded into Laplacians.

$$\frac{\partial \mathbf{f}_x^v}{\partial x} = \begin{bmatrix} 0 \\ V_{xx} \\ V_{xr} \\ V_{x\theta} \\ V_{xq} \end{bmatrix}, \frac{1}{r}\frac{\partial r \mathbf{f}_r^v}{\partial r} = \begin{bmatrix} 0 \\ V_{rx} \\ V_{rr} \\ V_{r\theta} \\ V_{rq} \end{bmatrix} \frac{1}{r}\frac{\partial \mathbf{f}_\theta^v}{\partial \theta} = \begin{bmatrix} 0 \\ V_{\theta x} \\ V_{\theta r} \\ V_{\theta\theta} \\ V_{\theta q} \end{bmatrix}, \tag{5.10}$$

with,

$$V_{xx} = \frac{\partial \mu}{\partial x}\sigma_{xx} + \mu\frac{\partial^2 u_x}{\partial x^2} \tag{5.11a}$$

$$V_{xr} = \frac{\partial \mu}{\partial x}\sigma_{xr} + \mu\frac{\partial^2 u_r}{\partial x^2} \tag{5.11b}$$

$$V_{x\theta} = \frac{\partial \mu}{\partial x}\sigma_{x\theta} + \mu\frac{\partial^2 u_\theta}{\partial x^2} \tag{5.11c}$$

$$\begin{aligned} V_{xq} = \frac{1}{T}\Bigg[\mu\left(\sigma_{xx}\frac{\partial u_x}{\partial x} + \sigma_{xr}\frac{\partial u_x}{\partial y} + \sigma_{x\theta}\frac{1}{r}\frac{\partial u_x}{\partial \theta}\right) + \\ \frac{\gamma}{(\gamma-1)Pr}\left(\frac{\partial \mu}{\partial x}\frac{\partial T}{\partial x} + \mu\frac{\partial^2 T}{\partial x^2}\right)\Bigg] \end{aligned} \tag{5.11d}$$

$$V_{rx} = \frac{\partial \mu}{\partial r}\,\sigma_{xr} + \mu\,\frac{\partial^2 u_x}{\partial r^2} + \frac{\tau_{xr}}{r} \tag{5.12a}$$

$$V_{rr} = \frac{\partial \mu}{\partial r}\,-\sigma_{\theta\theta} + \mu\,\frac{\partial^2 u_r}{\partial r^2} + \frac{\tau_{rr}}{r} \tag{5.12b}$$

$$V_{r\theta} = \frac{\partial \mu}{\partial r}\,\sigma_{r\theta} + \mu\,\frac{\partial^2 u_\theta}{\partial r^2} + \frac{\tau_{r\theta}}{r} \tag{5.12c}$$

$$\begin{aligned} V_{\theta q} = \frac{1}{T}\Bigg[\mu\left(\sigma_{rx}\,\frac{\partial v_x}{\partial x} + \sigma_{rr}\,\frac{\partial v_r}{\partial r} + \sigma_{r\theta}\,\frac{1}{r}\frac{\partial v_\theta}{\partial \theta}\right) + \\ \frac{\gamma}{(\gamma-1)Pr}\left(\frac{\partial \mu}{\partial r}\,\frac{\partial T}{\partial r} + \mu\left(\frac{\partial^2 T}{\partial r^2} + \frac{1}{r}\frac{\partial T}{\partial r}\right)\right)\Bigg] \end{aligned} \tag{5.12d}$$

$$V_{\theta x} = \frac{1}{r}\frac{\partial \mu}{\partial \theta}\,\sigma_{x\theta} + \mu\,\frac{1}{r^2}\frac{\partial^2 u_\theta}{\partial \theta^2} \tag{5.13a}$$

$$V_{\theta r} = \frac{1}{r}\frac{\partial \mu}{\partial \theta}\,\sigma_{r\theta} + \mu\,\frac{1}{r^2}\frac{\partial^2 u_r}{\partial \theta^2} - \frac{1}{r^2}\frac{\partial u_\theta}{\partial \theta} \tag{5.13b}$$

$$V_{\theta\theta} = \frac{1}{r}\frac{\partial \mu}{\partial \theta}\,\sigma_{\theta\theta} + \mu\,\frac{1}{r^2}\frac{\partial^2 u_\theta}{\partial \theta^2} + \frac{1}{r^2}\frac{\partial u_r}{\partial \theta} \tag{5.13c}$$

$$\begin{aligned} V_{\theta q} = \frac{1}{T}\Bigg[\mu\left(\sigma_{\theta x}\,\frac{\partial u_\theta}{\partial x} + \sigma_{\theta r}\,\frac{\partial u_\theta}{\partial r} + \sigma_{\theta\theta}\,\frac{1}{r}\frac{\partial w_\theta}{\partial \theta}\right) + \\ \frac{\gamma}{(\gamma-1)Pr}\left(\frac{1}{r}\frac{\partial \mu}{\partial \theta}\,\frac{1}{r}\frac{\partial T}{\partial \theta} + \mu\,\frac{1}{r^2}\frac{\partial^2 T}{\partial \theta^2}\right)\Bigg] \end{aligned} \tag{5.13d}$$

Note that only the derivative of the velocity gradient tensor is considered, while the other contributions are neglected.

5.4 Equations for laminar internal flows

We report the equation for laminar compressible internal flows. In the compressible case, no analytical solution to the equations can be found, nevertheless the system constitute a set of ordinary differential equations that can be easily solved numerically, with the appropriate boundary conditions. IN the incompressible limit the problem is known as Poiseuille flow and it reduces to solution of classic Poisson equation.

5.4.1 Planar channel

The compressible equations for the laminar flow in a planar straight channel are,

$$\frac{\mathrm{d}}{\mathrm{d}\,y}\left(\mu\frac{\mathrm{d}\,u}{\mathrm{d}\,y}\right)+\Pi=0 \qquad momentum \tag{5.14a}$$

$$\frac{1}{T}\frac{\mathrm{d}}{\mathrm{d}\,y}\left(k\frac{\mathrm{d}\,T}{\mathrm{d}\,y}\right)+\frac{\mu}{T}\frac{\mathrm{d}^2\,u}{\mathrm{d}\,y^2}=0 \qquad entropy \tag{5.14b}$$

$$\frac{\mathrm{d}}{\mathrm{d}\,y}\left(k\frac{\mathrm{d}\,T}{\mathrm{d}\,y}\right)+u\frac{\mathrm{d}}{\mathrm{d}\,y}\left(\mu\frac{\mathrm{d}\,u}{\mathrm{d}\,y}\right)+\mu\frac{\mathrm{d}^2\,u}{\mathrm{d}\,y^2}+\Pi u=0 \qquad total\,energy, \tag{5.14c}$$

where of course entropy and total energy equations are interchangeable. In the incompressible limit analytical solution can be found for $-h \leq y \leq h$,

$$u(y)=\frac{3}{2}u_b\left(1-\frac{y^2}{h^2}\right) \tag{5.15}$$

where $u_b=\frac{2}{3}\frac{\Pi h^2}{2\mu}$.

5.4.2 Rectangular duct

In case of square duct with square section the analytical solution for $-a \leq y \leq a$,$-b \leq z \leq b$ is [159],

$$u(y,z)=\frac{12u_b}{\pi Q}\sum_{i=1}^{\infty}(-1)^{(i-1)/2}\left[1-\frac{cosh(i\pi z/2a)}{cosh(i\pi b/2a)}\right]\frac{\cos\left(i\pi y/2a\right)}{i^3} \tag{5.16}$$

with,

$$Q=1-\frac{192a}{\pi^5 b}\sum_{i=1}^{\infty}\frac{\tanh\left(i\pi b/2a\right)}{i^5}, \tag{5.17}$$

and $u_b=\frac{4a^2}{3\mu}\Pi Q$

5.4.3 Circular pipe

The compressible equations for a compressible laminar circular pipe are,

$$\frac{1}{r}\frac{\mathrm{d}}{\mathrm{d}\,r}\left(r\mu\frac{\mathrm{d}\,u}{\mathrm{d}\,r}\right)+\Pi=0 \qquad momentum \tag{5.18a}$$

$$\frac{1}{rT}\frac{\mathrm{d}}{\mathrm{d}\,r}\left(rk\frac{\mathrm{d}\,T}{\mathrm{d}\,r}\right)+\frac{\mu}{rT}\frac{\mathrm{d}^2\,u}{\mathrm{d}\,r^2}=0 \qquad entropy \tag{5.18b}$$

$$\frac{1}{r}\frac{\mathrm{d}}{\mathrm{d}\,r}\left(rk\frac{\mathrm{d}\,T}{\mathrm{d}\,r}\right)+u\frac{1}{r}\frac{\mathrm{d}}{\mathrm{d}\,r}\left(r\mu\frac{\mathrm{d}\,u}{\mathrm{d}\,r}\right)+\mu\frac{\mathrm{d}^2\,u}{\mathrm{d}\,r^2}+\Pi u=0 \qquad total\,energy, \tag{5.18c}$$

where entropy and total energy equations are interchangeable. In the incompressible limit analytical solution can be found, and the resulting velocity profile for $0 \leq r \leq R$ is,

$$u(r)=2u_b\left(1-\frac{r^2}{R^2}\right) \tag{5.19}$$

where $u_b=\frac{1}{2}\frac{\Pi R^2}{4\mu}$.

Bibliography

[1] J. Ahn, J.H. Lee, S.J. Jang, and H.J. Sung. Direct numerical simulations of fully developed turbulent pipe flows for re_τ= 180, 544 and 934. *Int. J. Heat Fluid Flow*, 44:222–228, 2013.

[2] J. Ahn, J.H. Lee, J. Lee, J-H Kang, and H.J. Sung. Direct numerical simulation of a 30r long turbulent pipe flow at $re_\tau = 3008$. *Phys. Fluids (1994-present)*, 27(6):065110, 2015.

[3] J.C. Del Alamo and J. Jiménez. Estimation of turbulent convection velocities and corrections to Taylor's approximation. *J. Fluid Mech.*, 640:5–26, 2009.

[4] J.C. Del Alamo, J. Jiménez, P. Zandonade, and R.D. Moser. Scaling of the energy spectra of turbulent channels. *J. Fluid Mech.*, 500:135–144, 2004.

[5] R. Baidya, J. Philip, N. Hutchins, P. Monty J, and I. Marusic. Measurements of streamwise and spanwise fluctuating velocity components in a high Reynolds number turbulent boundary layer. In *In Proc. 18th Australasian Fluid Mech. Conference*, page 7, 2012.

[6] T.J. Barth and J.L. Steger. A fast efficient implicit scheme for the gasdynamics equations using a matrix reduction technique. AIAA paper 1985-0085, 1985.

[7] M. Batista. A cyclic block-tridiagonal solver. *Advances in Engineering Software*, 37(2):69–74, 2006.

[8] R.M. Beam and R.F. Warming. An implicit finite-difference algorithm for hyperbolic systems in conservation-law form. *J. Comput. Phys.*, 22(1):87–110, 1976.

[9] R.M. Beam and R.F. Warming. An implicit factored scheme for the compressible Navier-Stokes equations. *AIAA J.*, 16(4):393–402, 1978.

[10] M. Bernardini, S. Pirozzoli, M. Quadrio, and M. Orlandi. Turbulent channel flow simulations in convecting reference frames. *J. Comput. Phys.*, 232:1–6, 2013.

[11] M. Bernardini, S. Pirozzoli, and P. Orlandi. Velocity statistics in turbulent channel flow up to $re_\tau = 4000$. *J. Fluid Mech.*, 742:171–191, 2014.

[12] G.A. Blaisdell. Numerical simulation of compressible homogeneous turbulence. 1991.

[13] G.A. Blaisdell, E.T. Spyropoulos, and J.H. Qin. The effect of the formulation of nonlinear terms on aliasing errors in spectral methods. *Appl. Numer. Math.*, 21(3):207–219, 1996.

[14] J.B. Boersma. A staggered compact finite difference formulation for the compressible Navier-Stokes equations. *J. Comput. Phys.*, 208(2):675–690, 2005.

[15] C. Bogey and C. Bailly. Computation of a high Reynolds number jet and its radiated noise using large eddy simulation based on explicit filtering. *Computers & fluids*, 35(10):1344–1358, 2006.

[16] C. Bogey, N. De Cacqueray, and C. Bailly. Finite differences for coarse azimuthal discretization and for reduction of effective resolution near origin of cylindrical flow equations. *J. Comput. Phys.*, 230(4):1134–1146, 2011.

[17] C. Bogey, O. Marsden, and C. Bailly. Large-eddy simulation of the flow and acoustic fields of a Reynolds number 105 subsonic jet with tripped exit boundary layers. *Phys. Fluids (1994-present)*, 23(3):035104, 2011.

[18] P. Bradshaw. Compressible turbulent shear layers. *Annu. Rev. Fluid Mech.*, 9(1):33–52, 1977.

[19] Peter Bradshaw. Turbulent secondary flows. *Annual review of fluid mechanics*, 19(1):53–74, 1987.

[20] M. Breuer and W. Rodi. Large-eddy simulation of turbulent flow through a straight square duct and a 180 bend. In *Direct and large-eddy simulation I*, pages 273–285. Springer, 1994.

[21] C. Brun, M.P. Boiarciuc, M. Haberkorn, and P. Comte. Large eddy simulation of compressible channel flow. *Theor. Comp. Fluid Dyn.*, 22(3-4):189–212, 2008.

[22] S. Bühler, L. Kleiser, and C. Bogey. Simulation of subsonic turbulent nozzle jet flow and its near-field sound. *AIAA J.*, 52(8):1653–1669, 2014.

[23] S. Bühler, D. Obrist, and L. Kleiser. Laminar and turbulent nozzle-jet flows and their acoustic near-field. *Phys. Fluids (1994-present)*, 26(8):086103, 2014.

[24] P.G. Buning, D.C. Jespersen, H. Thomas, W.M. Chan, J.F. Slotnick, S.E. Krist, and K.J. Renze. OVERFLOW user,Äôs manual. *NASA Langley Research Center*, 1998.

[25] V. Casulli and D. Greenspan. Pressure method for the numerical solution of transient, compressible fluid flows. *Int. J. Num. Meth. Fluids*, 4(11):1001–1012, 1984.

[26] C. Chin, J.P. Monty, and A. Ooi. Reynolds number effects in DNS of pipe flow and comparison with channels and boundary layers. *Int. J. Heat Fluid Flow*, 45:33–40, 2014.

[27] C. Chin, H.C-H Ng, H.M Blackburn, J.P. Monty, and A. Ooi. Turbulent pipe flow at $re_\tau \approx 1000$: A comparison of wall-resolved large-eddy simulation, direct numerical simulation and hot-wire experiment. *Comp. & Fluids*, 122: 26–33, 2015.

[28] G.N. Coleman, J. Kim, and R.D. Moser. A numerical study of turbulent supersonic isothermal-wall channel flow. *J. Fluid Mech.*, 305:159–183, 1995.

[29] T. Colonius and S. K. Lele. Computational aeroacoustics: progress on nonlinear problems of sound generation. *Progr. Aero. Sci.*, 40:345–416, 2004.

[30] G.S. Constantinescu and S.K. Lele. A highly accurate technique for the treatment of flow equations at the polar axis in cylindrical coordinates using series expansions. *J. Comput. Phys.*, 183(1):165–186, 2002.

[31] A. Demetriades and W.R. Martindale. Experimental determination of one-dimensional spectra in high-speed boundary layers. *Phys. Fluids*, 26(2):397–403, 1983.

[32] O. Desjardins, G. Blanquart, G. Balarac, and H. Pitsch. High order conservative finite difference scheme for variable density low Mach number turbulent flows. *J. Comput. Phys.*, 227(15):7125–7159, 2008.

[33] J. Douglas. On the Numerical Integration of $\frac{\partial^2 u}{\partial x^2} + \frac{\partial^2 u}{\partial y^2} = \frac{\partial u}{\partial t}$ by Implicit Methods. *J. Soc. Ind. Appl. Math*, 3(1):42–65, 1955.

[34] L. Duan and M.P. Martin. Direct numerical simulation of hypersonic turbulent boundary layers. Part 4. Effect of high enthalpy. *J. Fluid Mech.*, 684:25–59, 2011.

[35] L. Duan, I. Beekman, and M.P. Martin. Direct numerical simulation of hypersonic turbulent boundary layers. Part 2. Effect of wall temperature. *J. Fluid Mech.*, 655:419–445, 2010.

[36] L. Duan, I. Beekman, and M.P. Martin. Direct numerical simulation of hypersonic turbulent boundary layers. Part 3. Effect of Mach number. *J. Fluid Mech.*, 672:245–267, 2011.

[37] J.G.M. Eggels, F. Unger, M.H. Weiss, J. Westerweel, R.J. Adrian, R. Friedrich, and F.T.M. Nieuwstadt. Fully developed turbulent pipe flow: a comparison between direct numerical simulation and experiment. *J. Fluid Mech.*, 268: 175–210, 1994.

[38] K. El, K. George, P. Schlatter, A. Noorani, P. Fischer, G. Brethouwer, and A.V. Johansson. Direct numerical simulation of turbulent pipe flow at moderately high Reynolds numbers. *Flow, Turb. and Comb.*, 91(3):475–495, 2013.

[39] A. Favre. The mechanics of turbulence. *Gordon and Breach, New York*, 1964.

[40] H.H. Fernholz and P.J. Finley. A critical commentary on mean flow data for two-dimensional compressible turbulent boundary layers. AGARDograph 253, 1980.

[41] H. Foysi and R. Friedrich. DNS of passive scalar transport in turbulent supersonic channel flow. In *High Perfor. Comput. Sci. and Engin.*, pages 107–117. Springer, 2005.

[42] H. Foysi, S. Sarkar, and R. Friedrich. Compressibility effects and turbulence scalings in supersonic channel flow. *J. Fluid Mech.*, 509:207–216, 2004.

[43] J.B. Freund, S.K. Lele, and P. Moin. Direct simulation of a supersonic round turbulent shear layer. *AIAA paper*, pages 97–0760, 1997.

[44] J.B. Freund, P. Moin, and S.K. Lele. Compressibility effects in a turbulent annular mixing layer. Part 2. Mixing of a passive scalar. *J. Fluid Mech.*, 421: 269–292, 2000.

[45] K. Fukagata and N. Kasagi. Highly energy-conservative finite difference method for the cylindrical coordinate system. *J. Comput. Phys.*, 181(2):478–498, 2002.

[46] N. Furuichi, Y. Terao, Y. Wada, and Y. Tsuji. Friction factor and mean velocity profile for pipe flow at high Reynolds numbers. *Phys. Fluids (1994-present)*, 27(9):095108, 2015.

[47] B. Ganapathisubramani, N.T. Clemens, and D.S. Dolling. Large-scale motions in a supersonic turbulent boundary layer. *J. Fluid Mech.*, 556:271–282, 2006.

[48] T.B. Gatski and J.-P. Bonnet. *Compressibility, turbulence and high speed flow*. Academic Press, 2013.

[49] J. Gaviglio. Reynolds analogies and experimental study of heat transfer in the supersonic boundary layer. *Intl J. Heat Mass Transfer*, 30:911–926, 1987.

[50] S. Gavrilakis. Numerical simulation of low-Reynolds-number turbulent flow through a straight square duct. *J. Fluid Mech.*, 244:101–129, 1992.

[51] S. Ghosh and R. Friedrich. Effects of distributed pressure gradients on the pressure-strain correlations in a supersonic nozzle and diffuser. *J. Fluid Mech.*, 742:466–494, 2014.

[52] S. Ghosh, H. Foysi, and R. Friedrich. Compressible turbulent channel and pipe flow: similarities and differences. *J. Fluid Mech.*, 648:155–181, 2010.

[53] S. Ghosh, S. Mahapatra, A. Dubey, A. Thagela, and R. Friedrich. Les of supersonic turbulent flow in nozzles and diffusers. *Int. J. Heat Fluid Flow*, 2016.

[54] D.B. De Graaff and J.K. Eaton. Reynolds-number scaling of the flat-plate turbulent boundary layer. *J. Fluid Mech.*, 422:319–346, 2000.

[55] S.E. Guarini, R.D. Moser, K. Shariff, and A. Wray. Direct numerical simulation of a supersonic turbulent boundary layer at Mach 2.5. *J. Fluid Mech.*, 414:1–33, 2000.

[56] F.E. Ham, F.S. Lien, and A.B. Strong. A fully conservative second-order finite difference scheme for incompressible flow on nonuniform grids. *J. of Comput. Phys.*, 177(1):117–133, 2002.

[57] C. Hirsch. *Numerical computation of internal and external flows: The fundamentals of computational fluid dynamics*. Butterworth-Heinemann, 2007.

[58] A.E. Honein and P. Moin. Higher entropy conservation and numerical stability of compressible turbulence simulations. *J. Comput. Phys.*, 201(2):531–545, 2004.

[59] L. Howarth. Concerning the effect of compressibility on laminar boundary layers and their separation. *Proc. Roy. Soc. (London) A*, 194(1036):16–42, 1948.

[60] S. Hoyas and J. Jiménez. Scaling of the velocity fluctuations in turbulent channels up to $\mathrm{Re}_\tau = 2003$. *Phys. Fluids*, 18(1):011702, 2006.

[61] P.G. Huang and G.N. Coleman. van Driest transformation and compressible wall-bounded flows. *AIAA J.*, 32(10):2110–2113, 1994.

[62] P.G. Huang, G.N. Coleman, and P. Bradshaw. Compressible turbulent channel flows: DNS results and modeling. *J. Fluid Mech.*, 305:185–218, 1995.

[63] A. Huser and S. Biringen. Direct numerical simulation of turbulent flow in a square duct. *J. Fluid Mech.*, 257:65–95, 1993.

[64] N. Hutchins and I. Marusic. Evidence of very long meandering features in the logarithmic region of turbulent boundary layers. *J. Fluid Mech.*, 579:1–28, 2007.

[65] N. Hutchins and I. Marusic. Evidence of very long meandering features in the logarithmic region of turbulent boundary layers. *J. Fluid Mech.*, 579:1–28, 2007.

[66] E. Isaacson and H.B. Keller. *Analysis of numerical methods*. Courier Corporation, 1994.

[67] J. Jiménez and R.D. Moser. What are we learning from simulating wall turbulence? *Phil. Trans. R. Soc. of Lond. A*, 365(1852):715–732, 2007.

[68] B.A. Kader. Temperature and concentration profiles in fully turbulent boundary layers. *Int. J. Heat Mass Transf.*, 24(9):1541–1544, 1981.

[69] C.A. Kennedy and A. Gruber. Reduced aliasing formulations of the convective terms within the Navier-Stokes equations for a compressible fluid. *J. Comput. Phys.*, 227(3):1676–1700, 2008.

[70] J. Kim and P. Moin. Application of a fractional-step method to incompressible Navier-Stokes equations. *J. Comput. Phys.*, 59(2):308–323, 1985.

[71] J. Kim, P. Moin, and R. Moser. Turbulence statistics in fully developed channel flow at low Reynolds number. *J. Fluid Mech.*, 177:133–166, 1987.

[72] B. Kjellström and S. Hedberg. Calibration experiments with a DISA hot-wire anemometer. Technical report, AB Atomenergi, 1968.

[73] M. Klein, A. Sadiki, and J. Janicka. A digital filter based generation of inflow data for spatially developing direct numerical or large eddy simulations. *J. Comput. Phys.*, 186(2):652–665, 2003.

[74] J.C. Klewicki and R.E Falco. On accurately measuring statistics associated with small-scale structure in turbulent boundary layers using hot-wire probes. *J. Fluid Mech.*, 219:119–142, 1990.

[75] S.J. Kline, W.C. Reynolds, F.A. Schraub, and P.W. Runstadler. The structure of turbulent boundary layers. *J. Fluid Mech.*, 30(04):741–773, 1967.

[76] L.S.G. Kovasznay. Turbulence in supersonic flow. *J. Aero. Sci.*, 1953.

[77] R. Lechner, J. Sesterhenn, and R. Friedrich. Turbulent supersonic channel flow. *J. Turbul.*, 2(1), 2001.

[78] J. Lee, J. Ahn, and H.J. Sung. Comparison of large-and very-large-scale motions in turbulent pipe and channel flows. *Phys. Fluids (1994-present)*, 27(2):025101, 2015.

[79] M. Lee and R.D. Moser. Direct simulation of turbulent channel flow layer up to $\mathrm{Re}_\tau = 5200$. *J. Fluid Mech.*, 774:395–415, 2015.

[80] S.K. Lele. Compact finite difference schemes with spectral-like resolution. *J. Comput. Phys.*, 103(1):16–42, 1992.

[81] S.K. Lele. Compressibility effects on turbulence. *Annu. Rev. Fluid Mech.*, 26: 211–254, 1994.

[82] R.K. Madabhushi and S.P. Vanka. Large eddy simulation of turbulence-driven secondary flow in a square duct. *Phys. Fluids A: Fluid Dynamics (1989-1993)*, 3(11):2734–2745, 1991.

[83] M.P. Martín and G.V. Candler. A parallel implicit method for the direct numerical simulation of wall-bounded compressible turbulence. *J. Comput. Phy.s*, 215(1):153–171, 2006.

[84] I. Marusic and G.J. Kunkel. Streamwise turbulence intensity formulation for flat-plate boundary layers. *Phys. Fluids (1994-present)*, 15(8):2461–2464, 2003.

[85] R. Mathis, N. Hutchins, and I. Marusic. Large-scale amplitude modulation of the small-scale structures in turbulent boundary layers. *J. Fluid Mech.*, 628: 311–337, 2009.

[86] B.J. Mckeon, J. Li, W. Jiang, J.F. Morrison, and A.J. Smits. Further observations on the mean velocity distribution in fully developed pipe flow. *J. Fluid Mech.*, 501:135–147, 2004.

[87] M.M. Metzger, J.C. Klewicki, K.L. Bradshaw, and R. Sadr. Scaling the near-wall axial turbulent stress in the zero pressure gradient boundary layer. *Phys. Fluids*, 13(6):1819–1821, 2001.

[88] B.E. Mitchell, S.K. Lele, and P. Moin. Direct computation of the sound generated by vortex pairing in an axisymmetric jet. *J. Fluid Mech.*, 383: 113–142, 1999.

[89] Y. Mizuno and J. Jiménez. Mean velocity and length-scales in the overlap region of wall-bounded turbulent flows. *Phys. Fluids*, 23(8), 2011.

[90] S. Mochizuki and F.T.M Nieuwstadt. Reynolds-number-dependence of the maximum in the streamwise velocity fluctuations in wall turbulence. *Exp. Fluids*, 21(3):218–226, 1996.

[91] D. Modesti and S. Pirozzoli. Reynolds and Mach number effects in compressible turbulent channel flow. *Int. J. Heat Fluid Flow*, 59:33–49, 2016.

[92] D. Modesti and S. Pirozzoli. An efficient semi-implicit solver for direct numerical simulation of compressible flows at all speeds. *arXiv preprint arXiv:1608.08513*, 2016.

[93] K. Mohseni and T. Colonius. Numerical treatment of polar coordinate singularities. *J. Comput. Phys.*, 157(2):787–795, 2000.

[94] Y. Morinishi, S. Tamano, and K. Nakabayashi. A DNS algorithm using B-spline collocation method for compressible turbulent channel flow. *Comput. Fluids*, 32(5):751–776, 2003.

[95] Y. Morinishi, S. Tamano, and K. Nakabayashi. Direct numerical simulation of compressible turbulent channel flow between adiabatic and isothermal walls. *J. Fluid Mech.*, 502:273–308, 2004.

[96] Y. Morinishi, O.V. Vasilyev, and T. Ogi. Fully conservative finite difference scheme in cylindrical coordinates for incompressible flow simulations. *J. Comput. Phys.*, 197(2):686–710, 2004.

[97] M.V. Morkovin. Effects of compressibility on turbulent flows. In *Mécanique de la Turbulence*, pages 367–380. A. Favre, 1962.

[98] V. Moureau, C. Bérat, and H. Pitsch. An efficient semi-implicit compressible solver for large-eddy simulations. *J. Comput. Phys.*, 226(2):1256–1270, 2007.

[99] S. Nagarajan, S.K. Lele, and J.H. Ferziger. A robust high-order compact method for large eddy simulation. *J. Comput. Phys.*, 191(2):392–419, 2003.

[100] N. Nikitin. Third-order-accurate semi-implicit Runge-Kutta scheme for incompressible Navier-Stokes equations. *Int. J. Numer. Meth. Fl.*, 51(2):221–233, 2006.

[101] N. Nikitin. Finite-difference method for incompressible Navier-Stokes equations in arbitrary orthogonal curvilinear coordinates. *J. Comput. Phys.*, 217(2):759–781, 2006.

[102] P. Orlandi. *Fluid flow phenomena: a numerical toolkit*, volume 55. Springer Science & Business Media, 2012.

[103] P. Orlandi and M. Fatica. Direct simulations of turbulent flow in a pipe rotating about its axis. *J. Fluid Mech.*, 343:43–72, 1997.

[104] P. De Palma, M.D. De Tullio, G. Pascazio, and M. Napolitano. An immersed-boundary method for compressible viscous flows. *Computers & fluids*, 35(7): 693–702, 2006.

[105] S.A. Pandya, S. Venkateswaran, and T.H. Pulliam. Implementation of preconditioned dual-time procedures in overflow. *AIAA paper*, 72:2003, 2003.

[106] A. Patel, J.W.R. Peeters, B.J. Boersma, and R. Pecnik. Semi-local scaling and turbulence modulation in variable property turbulent channel flows. *Phys. Fluids (1994-present)*, 27(9):095101, 2015.

[107] A. Patel, B.J. Boersma, and R. Pecnik. The influence of near-wall density and viscosity gradients on turbulence in channel flows. *arXiv preprint arXiv:1607.04015*, 2016.

[108] A.E. Perry and I. Marusic. A wall-wake model for the turbulence structure of boundary layers. Part 1. Extension of the attached eddy hypothesis. *J. Fluid Mech.*, 298:361, 1995.

[109] C.D. Pierce. *Progress-variable approach for large-eddy simulation of turbulent combustion*. PhD thesis, Citeseer, 2001.

[110] A. Pinelli, M. Uhlmann, A. Sekimoto, and G. Kawahara. Reynolds number dependence of mean flow structure in square duct turbulence. *J. Fluid Mech.*, 644:107–122, 2010.

[111] S. Pirozzoli. Generalized conservative approximations of split convective derivative operators. *J. Comput. Phys.*, 229(19):7180–7190, 2010.

[112] S. Pirozzoli. Stabilized non-dissipative approximations of Euler equations in generalized curvilinear coordinates. *J. Comput. Phys.*, 230(8):2997–3014, 2011.

[113] S. Pirozzoli. Numerical methods for high-speed flows. *Annu. Rev. Fluid Mech.*, 43:163–194, 2011.

[114] S. Pirozzoli. On the size of the energy-containing eddies in the outer turbulent wall layer. *J. Fluid Mech.*, 702:521–532, 2012.

[115] S. Pirozzoli. Revisiting the mixing-length hypothesis in the outer part of turbulent wall layers: mean flow and wall friction. *J. Fluid Mech.*, 745:378–397, 2014.

[116] S. Pirozzoli and M. Bernardini. Turbulence in supersonic boundary layers at moderate Reynolds number. *J. Fluid Mech.*, 688:120–168, 2011.

[117] S. Pirozzoli, F. Grasso, and T.B. Gatski. Direct numerical simulation and analysis of a spatially evolving supersonic turbulent boundary layer at M= 2.25. *Phys. Fluids*, 16:530–545, 2004.

[118] S. Pirozzoli, M. Bernardini, and P. Orlandi. Passive scalars in turbulent channel flow at high Reynolds number. *J. Fluid Mech.*, 788:614–639, 2016.

[119] Sergio Pirozzoli. On the Size of the Eddies in the Outer Turbulent Wall Layer: Evidence from Velocity Spectra. In *Progress in Wall Turbulence 2*, pages 3–15. Springer, 2016.

[120] T.J. Poinsot, A.C. Trouve, D.P. Veynante, S.M. Candel, and E.J. Esposito. Vortex-driven acoustically coupled combustion instabilities. *J. Fluid Mech.*, 177:265–292, 1987.

[121] T.H. Pulliam. Solution methods in computational fluid dynamics, 1986.

[122] T.H. Pulliam and D.S Chaussee. A diagonal form of an implicit approximate-factorization algorithm. *J. Comput. Phys.*, 39(2):347–363, 1981.

[123] M.D. Salas and A. Iollo. Entropy jump across an inviscid shock wave. *Theor. Comp. Fluid Dyn.*, 8(5):365–375, 1996.

[124] R.D. Sandberg. An axis treatment for flow equations in cylindrical coordinates based on parity conditions. *Computers & Fluids*, 49(1):166–172, 2011.

[125] R.D. Sandberg, N.D. Sandham, and V. Suponitsky. Dns of compressible pipe flow exiting into a coflow. *Int. J. Heat Fluid Flow*, 35:33–44, 2012.

[126] V.A. Sandborn. A review of turbulence measurements in compressible flow. 1974.

[127] P. Schlatter and R. Örlü. Assessment of direct numerical simulation data of turbulent boundary layers. *J. Fluid Mech.*, 659:116, 2010.

[128] M. Shoeybi, M. Svärd, F.E. Ham, and P. Moin. An adaptive implicit-explicit scheme for the DNS and LES of compressible flows on unstructured grids. *J. Comput. Phys.*, 229(17):5944–5965, 2010.

[129] A.J. Smits and J.-P. Dussauge. *Turbulent shear layers in supersonic flow, 2nd Edn.* American Istitute of Physics, 1996.

[130] A.J. Smits, E.F. Spina, A.E. Alving, R.W. Smith, E.M. Fernando, and J.F. Donovan. A comparison of the turbulence structure of subsonic and supersonic boundary layers. *Phys. Fluids A*, 1(11):1865–1875, 1989.

[131] R.M.C. So, H.S. Zhang, GT.B. atski, and C.G. Speziale. Logarithmic laws from compressible turbulent boundary layers. *AIAA J.*, 32(11):2162–2168, 1994.

[132] P.R. Spalart. Strategies for turbulence modelling and simulations. *Int. J. Heat Fluid Flow*, 21:252–263, 2000.

[133] P.R. Spalart, R.D. Moser, and M.M. Rogers. Spectral methods for the Navier-Stokes equations with one infinite and two periodic directions. *J. Comput. Phys.*, 96(2):297–324, 1991.

[134] E.F. Spina, A.J. Smits, and S.K. Robinson. The physics of supersonic turbulent boundary layers. *Annu. Rev. Fluid Mech.*, 26:287–319, 1994.

[135] J.L. Steger. Coefficient matrices for implicit finite difference solution of the inviscid fluid conservation law equations. *Comput. Meth. Appl. Mech. Eng.*, 13:175–188, 1978.

[136] P.A. Subbareddy and G.V Candler. A fully discrete, kinetic energy consistent finite-volume scheme for compressible flows. *J. Comput. Phys.*, 228(5):1347–1364, 2009.

[137] K. Takeishi, G. Kawahara, H. Wakabayashi, M. Uhlmann, and A. Pinelli. Localized turbulence structures in transitional rectangular-duct flow. *J. Fluid Mech.*, 782:368–379, 2015.

[138] S. Tamano and Y. Morinishi. Effect of different thermal wall boundary conditions on compressible turbulent channel flow at M= 1.5. *J. Fluid Mech.*, 548:361–373, 2006.

[139] E. Tavakoli, B. Lessani, and R. Hosseini. High-order pole-treatment in cylindrical coordinates for incompressible flow simulations with finite-difference collocated schemes. *J. Comput. Phys.*, 296:1–24, 2015.

[140] A.A. Townsend. *The Structure of Turbulent Shear Flow. 2nd edn.* Cambridge University Press., 1976.

[141] A. Trettel and J. Larsson. Effect of cooling on compressible wall-turbulence. In *67th Annu. Meet. APS Div. Fluid Dyn.*, volume 59 of *Bull. Am. Phys. Soc.*, Nov. 2014. URL `http://meetings.aps.org/link/BAPS.2014.DFD.L26.5`.

[142] A. Trettel and J. Larsson. Mean velocity scaling for compressible wall turbulence with heat transfer. *Phys. Fluids (1994-present)*, 28(2):026102, 2016.

[143] E. Turkel. Review of preconditioning methods for fluid dynamics. *Appl. Numer. Math.*, 12:257–284, 1993.

[144] E. Turkel. Preconditioning techniques in computational fluid dynamics. *Annu. Rev. Fluid Mech.*, 31(1):385–416, 1999.

[145] M. Uhlmann, A. Pinelli, G. Kawahara, and A. Sekimoto. Marginally turbulent flow in a square duct. *J. Fluid Mech.*, 588:153–162, 2007.

[146] E.R. van Driest. Turbulent boundary layer in compressible fluids. *J. Aero. Sci.*, 18:145–160, 1951.

[147] E.R. van Driest. The turbulent boundary layer with variable Prandtl number. No. Amer. Avia., Inc. AL-1914, 1954.

[148] E.R. van Driest. The problem of aerodynamic heating. *Aeronaut. Engng Rev.*, 15(10):26–41, 1956.

[149] M.S. Vázquez and O. Métais. Large-eddy simulation of the turbulent flow through a heated square duct. *J. Fluid Mech.*, 453:201–238, 2002.

[150] S. Venkateswaran and C.L. Merkle. Dual Time stepping and Preconditioning for Unsteady Computations. 1995.

[151] R. Verzicco and P. Orlandi. A finite-difference scheme for three-dimensional incompressible flows in cylindrical coordinates. *J. Comput. Phys.*, 123(2): 402–414, 1996.

[152] R. Vichnevetsky and J. B. Bowles. *Fourier analysis of numerical approximations of hyperbolic equations*. SIAM, Philadelphia, 1982.

[153] R. Vinuesa, A. Noorani, A. Lozano-Durán, G.K.E. Khoury, P. Schlatter, P.F. Fischer, and H.M. Nagib. Aspect ratio effects in turbulent duct flows studied through direct numerical simulation. *J. Turbulence*, 15(10):677–706, 2014.

[154] C. Wagner, T.J. Hüttl, and R. Friedrich. Low-Reynolds-number effects derived from direct numerical simulations of turbulent pipe flow. *Comp. & Fluids*, 30 (5):581–590, 2001.

[155] C. Wall, C.D. Pierce, and P. Moin. A semi-implicit method for resolution of acoustic waves in low Mach number flows. *J. Comput. Phys.*, 181(2):545–563, 2002.

[156] A. Walz. Compressible turbulent boundary layers with heat transfer and pressure gradient in flow direction. *J. Res. Natl. Bur. Stand.*, 63, 1959.

[157] L. Wei and A. Pollard. Interactions among pressure, density, vorticity and their gradients in compressible turbulent channel flows. *J. Fluid Mech.*, 673: 1–18, 2011.

[158] L. Wei and A. Pollard. Direct numerical simulation of compressible turbulent channel flows using the discontinuous Galerkin method. *Comput. Fluids*, 47 (1):85–100, 2011.

[159] F.M. White and I. Corfield. *Viscous fluid flow*, volume 3. McGraw-Hill New York, 2006.

[160] X. Wu and P. Moin. A direct numerical simulation study on the mean velocity characteristics in turbulent pipe flow. *J. Fluid Mech.*, 608:81–112, 2008.

[161] X. Wu, J.R. Baltzer, and R.J. Adrian. Direct numerical simulation of a $30r$ long turbulent pipe flow at $re_\tau = 685$: large-and very large-scale motions. *J. Fluid Mech.*, 698:235–281, 2012.

[162] M.V. Zagarola and A.J. Smits. Mean-flow scaling of turbulent pipe flow. *J. Fluid Mech.*, 373:33–79, 1998.

[163] M.V. Zagarola, A.E. Perry, and A.J. Smits. Log laws or power laws: The scaling in the overlap region. *Phys. Fluids (1994-present)*, 9(7):2094–2100, 1997.

[164] H. Zhang, F.X. Trias, A. Gorobets, Y. Tan, and A. Oliva. Direct numerical simulation of a fully developed turbulent square duct flow up to $Re_\tau = 1200$. *Int. J. Heat Fluid Flow*, 54:258–267, 2015.

[165] Y.S. Zhang, W.T. Bi, F. Hussain, and Z.S. She. A generalized Reynolds analogy for compressible wall-bounded turbulent flows. *J. Fluid Mech.*, 739: 392–420, 2014.